

Validation of the Composite Propeller Application and flexible propeller design space exploration

MSc Thesis

Jeroen van Bemmelen

June 26, 2022



Validation of the Composite Propeller Application and flexible propeller design space exploration

MSc Thesis

by

J.S. van Bommel

To obtain a master degree of science at the Delft University of Technology, in Marine
Technology

To be defended publicly on Wednesday July 6, at 2.00 PM.

Student number: 4359402
Document number: MT.21/22.033.M
Project duration: October 6, 2021 - July 6, 2022

| | | |
|-------------------|-----------------------------------|-----------------|
| Thesis committee: | Prof. Dr. Ir. T.J.C van Terwisga, | TU Delft, MARIN |
| | Dr. Ir. H.C.J. van Wijngaarden, | MARIN |
| | Ir. H.C. Neatby, | DRDC, TU Delft |
| | Dr. Ir. L. Pahlavan, | TU Delft |
| | Ir. K. Visser, | TU Delft |

Preface

Before you lies my thesis *Validation of the Composite Propeller Application and flexible propeller design space exploration* to obtain a Master of Science degree from the Delft university of technology in Marine technology. When I started studying Marine technology in 2015, I had little knowledge of the marine industry, but have always felt drawn to the elegance of ships. Whilst visiting Monaco with my parents as a little kid, I clearly remember the impression these super yachts made on me. And at that moment I knew that I wanted to study Marine Technology. A part of me thought that studying Marine technology would enable me one day to own such ships which, with the knowledge I have obtained through my study, is a ridiculous idea. It nevertheless was that moment I decided to study Marine engineering which turned out to be the best decision I ever made.

Whilst writing this preface, and reflecting of the process of enrolling for Marine Technology seven years ago, and finishing my time as a student with the nine months of working on this thesis. I started with very little knowledge about engineering in general, and even more so for propellers. This gap of knowledge was still present when starting this thesis mainly because propeller design is very niche, and the tricks of the trade are kept secret. Right now I feel confident to say I have gained a thorough understanding of marine propellers and especially with respect to flexibility which can be used. After writing this thesis, I hope to one day see composite marine propeller used throughout the industry.

This thesis would not have been realized without Tom van Terwisga, my professor and supervisor from the Delft university of technology who has brought me into contact with MARIN and allowed me to work on this assignment in the first place. For that I am very thankful. Throughout this project, I have had endless discussions with Erik van Wijngaarden from MARIN and Holly Neatby from DRDC Canada. I would like to thank them both for these endless discussions and their guidance of this project. Lastly, I would also like to Klaas Visser and Pooria Pahlavan for evaluating this thesis and completing my thesis committee.

J.S. van Bommel
June 26, 2022

Summary

Marine propellers are used to propel the vast majority of ships as it is the most efficient and relatively straightforward way to propel vessels. Marine propellers are conventionally made from Nickel-Aluminium-Bronze alloys (*NAB*), which have superior corrosion and strength to stiffness properties. These metal propellers are assumed to be rigid and deformation of the blades during operation is neglected. In current research, (but literature on the topic is found from the 1980s onward) it is suggested to design propellers from more flexible materials such as composites. This to exploit the flexibility of propellers to tailor the performance. A potential benefit from this flexibility is to relieve the blades from large pressures by large blade deformations to mitigate the risk of propeller cavitation. This potential has also been noticed by Maritime Research Institute Netherlands (*MARIN*) and combined with other players from the maritime industry who perform research together under the umbrella organisation Cooperative Research Ships (*CRS*). Within the *CRS*, research is performed in every thinkable field of the maritime industry by all involved members. The working group studying a wide variety of topics concerning composite propellers is known as *COMPROP*.

To simulate a presumably rigid propeller, Boundary Element Methods- (*BEM*) or Computational Fluid Dynamics (*CFD*) codes can be used to predict the flow around a propeller blade and calculate the corresponding pressures, lift and drag forces. When flexibility and corresponding deformations can no longer be neglected in the solution, these methods do not suffice anymore. Therefore *MARIN* developed the Composite Propeller Application (*ComPropApp*) which uses Fluid-Structure Interaction (*FSI*) in which either one of the two mentioned flow solvers is coupled with a Finite Element Method (*FEM*) to link the found pressures on the blade to the corresponding deformation. This process is iterated until a converged solution is reached. The *ComPropApp* uses a coupled *BEM-FEM* solver in which the *BEM* solver is an in house and well validated code known as *PROCAL*, the *FEM* solver is provided by Lloyd's Register (*LR*) and is known as *VAST/TRIDENT*.

This research aims to study two topics concerning composite marine propellers:

1. Validation of the unsteady *FSI*- and Stress Analysis modules of the *ComPropApp* by comparing simulations with experiments executed at *MARIN*. The unsteady *FSI* module can simulate the time-dependent deformation of a propeller in a non-uniform wake field. This is not possible in the validated steady *FSI* module
2. Exploration of the design space of flexible marine propellers. To identify which parameters are influential in flexible propeller design.

Validation of the Unsteady *FSI* module

The validation of the *ComPropApp*'s unsteady *FSI* module starts with grid studies to ensure the solutions are independent of the considered amount of nodes or panels. Thereafter, the steady *FSI* module was validated with experimental data found in literature on the open water performance of the Wageningen c4-40 propeller. With the confidence that the steady *FSI* module is simulating the deformation and performance accurately, the unsteady *FSI* module is validated. From initial tests in a simple sinusoidal wake field, it was shown that there was a discrepancy between the deformation magnitude in the Unsteady *FSI*- and Stress Analysis module. Yet the average deformation component was equal for both modules for all simulations. By systematic modification of all involved parameters, it was concluded that the bug must be in the modal analysis procedure in the Unsteady *FSI* code since it showed non-physical attributes whilst altering the damping ratio (ζ), material density (ρ) and Young's Modulus (E). This error was then located and turned out to be in the process of the Fourier Transform when computing the complex conjugate vectors. This also explained why the average deformation was equal for all simulations, as this average deformation component (the 0-vector) has no complex conjugate. After the modifications in the code, both modules showed equal deformation.

With these initial tests in a simple sinusoidal wake field validated, now the *ComPropApp* can be used to compare simulations with experiments. The *COMPROP* working group executed a series of experiments in the cavitation tank at *MARIN* with a flexible c4-40 propeller. This model propeller was constructed from SikaBlock M980 (a polyurethane foam). From static loading tests, time-dependent deformation in the material was observed in the form of unrecoverable creep. Material sample testing also showed a large discrepancy between the Young's modulus given by the manufacturer and by testing. There is also the suspicion that the material is slightly anisotropic. All these material observations led to the conclusion that the material is unsuitable for these types of validation experiments as the current *FEM* module in the *ComPropApp* cannot model these material properties. Therefore it is advised to select a different material, or at least validate that these material properties are insignificant to the results.

The experimental setup in the cavitation tunnel was as follows: a Digital Image Correlation (*DIC*) system captures the deformation of black dots on the blade with a method known as ensemble averaging. This means that

no real-time deformation within a revolution is recorded, only the average of 40 revolutions per blade position. Thus no conclusions can be done on the possible vibrations happening within a revolution. As the vibrations visible in the experimental data is an average thus is most likely uncertainty due to different flow conditions per revolution. The largest uncertainty in the experimental data is shown before the wake peak. It is thought that this area is most affected by the different inflow conditions per revolution as the blade starts to deform here. Furthermore, could it be that an asymmetrically in the used ship model locally accelerates flow here even further.

When the experiments are simulated with the ComPropApp, it was shown that the deformations through both methods were in quite good agreement. Only in the wake peak, a slight difference between both methods exists. The simulations (both Unsteady FSI and Stress Analysis), tend to overestimate the deformation. It is believed that this happens because a relatively little amount of points per revolution is considered (36 points per revolution). This leads to very large instantaneously loading in the wake peak as the simulation passes through this wake peak in only 2 data points. It is thought that refining this mesh would lead to better agreement between simulation and experiment. It was also observed that this error becomes larger for cases with larger blade loading. This hints that this suspicion is correct.

This grid could not be refined because beyond 36 points as the ComPropApp becomes quickly divergent and exponentially time-consuming. For 72 data points, the ComPropApp was unable to converge the simulation thus this could not be investigated. Therefore it is key that further research looks into the numerical stability of the system. This divergence also causes vibrations in the simulations. It is uncertain whether this smoothens out over time to become converged or whether they are actual resonance frequencies. It was chosen not to analyze these vibrations since they could not be validated. In the first place due to the ensemble average results of the experiments. Secondly, is it a more efficient study when the numerical stability and computational time of the ComPropApp have been improved.

A final test showed that hydrodynamic damping is not yet added to the simulations. The simulations were vibrating at the dry frequencies which should not happen since water adds damping to the system. In theory, an unsteady FSI simulation should slowly add this effect to the simulation but this was not observed. It might therefore be beneficial to compute the wet eigenfrequencies and mode shapes beforehand with estimation methods.

Design space exploration of flexible marine propellers

With the validation of ComPropApp completed, the second part of this report explores the design space of flexible marine propellers. Due to the above-mentioned problems with the Unsteady FSI module, it was chosen to use the steady FSI module to analyze the effect of propeller geometry parameters on the performance.

To initially assess the risk of cavitation of a propeller, a parameter is introduced named the cavitation area (A_{CAV}). This is the sum of all negative pressure coefficients (C_{PN}) on the nodes larger than -1. This way, all nodes which have a risk of cavitation contribute to a single number expressing the risk of cavitation. It should be noted that this number can only be used to compare large series of propellers in equal conditions with each other. No firm conclusions on whether a propeller will show cavitation can be made. Only the risk of cavitation relative to the other propellers is expressed in this number.

First, single parameters were altered and the effects were observed. Increasing the propeller pitch showed a large improvement in the propeller efficiency and suction side pressure distribution. On the downside, the pressure side pressures rapidly increase. Skew was shown to relieve pressure on both sides of the blade but is paid with an efficiency decrease. Decreasing the chord length relieves pressure on the suction side, but much higher pressures on the pressure side are observed. The last parameter is camber which does not affect the efficiency but is well capable of reducing pressure on both sides of the blade when the camber is reduced.

After these single parameter modifications, all parameters are altered simultaneously. The method chosen was Latin Hypercube Sampling (*LHS*). In which a number of x propellers is generated whilst dividing the range of all parameters in x intervals. This way all propellers are unique. It was chosen to use this method to cover a large area with a minimum number of simulations. In total 65 unique propeller geometries were generated. From this LHS space, it is immediately visible that the connection between parameters and performance is less pronounced compared to altering a single parameter. But the study was capable to draw many conclusions on the design space of propellers:

- Pitch is the most effective parameter in increasing open water efficiency.
- Increasing pitch and skew are the most effective parameters to reduce suction side cavitation.
- Reducing the risk of pressure side cavitation is best achieved by increasing skew and increasing chord length.

- Almost all propellers with desirable performance had a large skew and high pitch value. The two downsides of this are the larger pressure side pressures, and the higher stresses experienced due to both parameters. These larger pressures can be relieved by reducing camber and increasing the chord length
- Propellers with a large blade deformation have a high pitch setting and low chord length.
- Propellers with a large bending deformation are propellers with a low chord length and high skew, thus for future studies where anisotropy can be applied, this can be exploited to optimize the amount of de-pitching can be achieved.
- Unwanted tip pressures can be reduced by applying a positive rake in the tip region. This results in lower pressure side pressures on the complete blade. This is achieved without sacrificing the suction side cavitation risk or the efficiency significantly.

The pressure area numbers to assess initial cavitation risk was deemed very successful for the suction side pressures (A_{SUC}). This conclusion is based on visual inspection of the generated propellers and comparing the suction side area numbers. The pressure side pressures however (A_{PRES}), showed room for improvement. This is caused by pressures at the leading edge and hub of the propeller. It is known that BEM codes tend to show numerical artefacts in the form of unrealistically high pressures in this area. Therefore, sometimes large pressure area numbers arise whilst visual inspections show acceptable pressure distributions and vice versa. To make more meaningful conclusions with a single number, a follow-up study into these numerical artefacts could improve this pressure area number.

The tip also shows this numerical artefact from time to time. But by neglecting the pressures at 0.99R it was shown that the tip pressures can be accurately quantified with such a pressure area number ($A_{PRES,TIP}$). Of the 65 propellers, 2 propellers were reaching all three criteria (lower suction side area than the bronze c4-40, lower pressure side area than the bronze c4-40 and higher efficiency than the c4-40). Additionally, one propeller was improved with the above-mentioned tip rake to show the effectiveness of that parameter. Thus a total of three potential propellers were identified.

Up till that point, it has not been proven that flexibility does indeed influences the propeller performance. One could take the deformed geometry of a propeller and construct it out of a NAB-alloy to get the same steady performance. This was validated for the three potential propellers. As the unsteady FSI module was not used, the performance over a complete revolution could unfortunately not be tested.

In a minor demonstration, it is shown that from those three potential propellers, two of those showed much more favourable performance in terms of cavitation risk and propeller efficiency in a lower advance ratio, thus imitating the wake peak. The third one showed a significant decrease in performance. Thus concluding that a well-designed open water propeller does not instantly yield a well-performing propeller for the in-behind condition. The main differing parameter between those three propellers was the significantly longer chord length of the worst propeller. Thus this seems like an important parameter to allow the propeller to de-pitch in the wake peak to obtain a favourable setting.

Contents

| | | |
|----------|---|-----------|
| 1 | Introduction | 1 |
| 2 | Marine Propellers | 3 |
| 2.1 | Introduction | 3 |
| 2.2 | Propeller geometry | 3 |
| 2.3 | Propeller performance | 6 |
| 2.3.1 | Wake field | 7 |
| 2.4 | Cavitation | 7 |
| 2.4.1 | Types of Cavitation | 8 |
| 2.4.2 | Cavitation design considerations | 9 |
| 2.5 | Propeller strength and vibration | 10 |
| 2.5.1 | Propeller Strength and fatigue | 10 |
| 2.5.2 | Propeller vibrations | 10 |
| 2.5.3 | Mode shapes and frequencies | 11 |
| 2.6 | Composite Propellers | 12 |
| 2.6.1 | Stacking sequence | 13 |
| 2.7 | conclusions | 13 |
| 3 | The ComPropApp | 14 |
| 3.1 | Introduction | 14 |
| 3.2 | PROCAL and Boundary element method | 14 |
| 3.2.1 | PROCAL | 14 |
| 3.2.2 | Green's Theorem | 15 |
| 3.2.3 | Discretization | 15 |
| 3.2.4 | Fluid added mass and Hydrodynamic damping | 17 |
| 3.2.5 | Friction Coefficients | 18 |
| 3.2.6 | Cavitation modelling in PROCAL/ComPropApp | 19 |
| 3.3 | Vast/Trident and Finite element method | 19 |
| 3.3.1 | Finite Element Method in General | 19 |
| 3.3.2 | FEM in Vast/Trident | 20 |
| 3.3.3 | Conversion to frequency domain | 20 |
| 3.3.4 | Wet mode shapes | 21 |
| 3.4 | FSI and CompropApp | 21 |
| 3.4.1 | Steady FSI analysis | 22 |
| 3.4.2 | Modal Analysis | 22 |
| 3.4.3 | Unsteady FSI Analysis | 22 |
| 3.4.4 | Stress Analysis | 22 |
| 3.4.5 | Coupling Procedure | 22 |
| 4 | Grid Study and open water validation study | 25 |
| 4.1 | Introduction | 25 |
| 4.2 | Grid Study | 26 |
| 4.2.1 | BEM convergence | 26 |
| 4.2.2 | FEM convergence | 27 |
| 4.2.3 | Tip Cut-off value | 28 |
| 4.3 | Open water diagram and convergence | 29 |
| 4.3.1 | Steady FSI convergence | 29 |
| 4.3.2 | Unsteady FSI convergence | 29 |
| 4.3.3 | Open water diagram | 30 |
| 4.4 | Blade Deformation | 32 |
| 4.5 | Conclusions | 34 |
| 5 | Non-uniform wake field validation | 35 |
| 5.1 | ComPropApp before modifications | 35 |
| 5.2 | Systematic testing of the ComPropApp | 36 |
| 5.2.1 | Altering the number of Modes | 38 |
| 5.2.2 | Altering Stiffness | 39 |
| 5.2.3 | Altering Mass | 41 |
| 5.2.4 | Altering Damping Ratio | 42 |

| | | |
|----------|---|------------|
| 5.2.5 | Conclusions from systematic series | 43 |
| 5.2.6 | Code repair | 43 |
| 5.3 | ComPropApp after modifications | 43 |
| 6 | Validation of the COMPROP2 experiments | 46 |
| 6.1 | Experimental Setup | 46 |
| 6.2 | Material models | 48 |
| 6.2.1 | SikaBlock M700 | 48 |
| 6.2.2 | SikaBlock M980 | 49 |
| 6.2.3 | Manufacturing tolerances | 50 |
| 6.3 | Damping ratio and material property determination | 51 |
| 6.4 | Experimental Data | 52 |
| 6.5 | Comparison experiment and simulation | 54 |
| 6.5.1 | Convergence issues | 54 |
| 6.5.2 | Open water wake validation | 54 |
| 6.5.3 | Validation of experiment C038 (smallest deflection) | 55 |
| 6.5.4 | Validation of experiment C038 (Largest deflection) | 57 |
| 6.5.5 | Validation of experiment C036 (medium deflection) | 58 |
| 6.5.6 | More blade positions in experiment C036 | 59 |
| 6.6 | Conclusions and recommendations | 60 |
| 7 | Design study: design of flexible propellers | 62 |
| 7.1 | Introduction | 62 |
| 7.2 | Parameter identification & Methodology | 62 |
| 7.2.1 | Parameter identification | 62 |
| 7.2.2 | PROPART and propeller geometry modification | 63 |
| 7.3 | Deformation standard c4-40 Propeller | 63 |
| 7.4 | Cavitation area Criterion | 65 |
| 7.5 | Single parameter variations | 67 |
| 7.5.1 | Pitch | 67 |
| 7.5.2 | Skew | 69 |
| 7.5.3 | Rake | 71 |
| 7.5.4 | Chord length | 72 |
| 7.5.5 | Camber | 75 |
| 7.5.6 | Young's Modulus | 77 |
| 7.5.7 | Conclusions | 78 |
| 7.6 | Multi variate design space | 79 |
| 7.7 | Results of the multi variate design exploration | 80 |
| 7.7.1 | Open water efficiency | 80 |
| 7.7.2 | Suction side cavitation | 81 |
| 7.7.3 | Pressure side cavitation | 82 |
| 7.7.4 | Maximum Stress | 83 |
| 7.7.5 | Blade and pitch angle Deformation | 84 |
| 7.8 | Optimum Propellers | 88 |
| 7.8.1 | Best suction side propellers | 90 |
| 7.8.2 | Best pressure side propellers | 91 |
| 7.8.3 | Best efficiency propellers | 91 |
| 7.9 | Tip pressure reduction | 94 |
| 7.9.1 | Lowering pitch at the tip | 95 |
| 7.9.2 | Rake | 96 |
| 7.10 | Conclusions | 98 |
| 8 | Non-uniform wake field demonstration | 100 |
| 8.1 | Introduction | 100 |
| 8.2 | Wake peak performance | 100 |
| 8.3 | Conclusion | 107 |
| 9 | Conclusions | 108 |

| | |
|---|------------|
| 10 Further research and recommendations | 110 |
| 10.1 the Composite Propeller Application | 110 |
| 10.2 Design of flexible marine Propellers | 111 |
| A Latin Hypercube Sampling design space | 112 |

1 Introduction

Marine propellers have been optimized to function to the needs of the ship. From the early days with Archimedes Screws, to state-of-the-art Controllable Pitch propellers, engineers have been trying to design propellers which yield the most efficient propulsion for marine vessels. Until now, propellers for large merchant vessels have almost exclusively been made from metals, namely Nickel-Aluminium-Bronze Alloys (*NAB-Alloys*). These alloys have superior fatigue and strength characteristics compared to other metals. Recently there has been a growing interest in the use of other materials to construct propellers. One important group of these materials are composites. They consist of a fibre (carbon or glass fiber) and a matrix (epoxy or other resins).

Even though these composite materials are less strong compared to metals, they have properties which show potential for usage in Marine Propellers. Firstly, the material is far less dense compared to NAB-Alloys, which reduces the weight of the propeller, and reduces inertia needed to rotate the propeller. Secondly, composite materials are anisotropic, which means the stiffness of a material is not equal in all directions. Thus deformation is also direction-dependent. Another beneficial property of composites is the superior corrosion behaviour in salt water compared to metals. And lastly, the use of composite propellers has shown improvements in reducing propeller noise and cavitation. This is due to the larger deformations, which can be tailored such that it relieves pressure on the blade.

Cavitation is the collapse of vapour bubbles on the propeller, which happens when the local pressure drops below the vapour pressure of water. This phenomenon significantly damages propeller blades and generates a lot of noise. This noise is partly carried through a vessel in terms of structural vibrations: the so-called structure-borne noise. And partly reflected as underwater noise. This underwater noise has a signature sound profile which allows sonar systems to identify and intercept naval vessels. Thus the interest in limiting underwater noise by the use of composite propellers has been of interest for naval engineers for some time [1].

Research shows that marine wildlife (whales and other large mammals) are significantly impacted by this radiated underwater noise. This has raised concerns under wildlife protection agencies as whale populations have significantly dropped in areas with a lot of merchant vessels. [2]. It is therefore expected that the International Marine Organization (*IMO*), which decides on new maritime regulations for all United Nations member states, to regulate the amount of underwater noise allowable for merchant ships. Thus the interest in composite marine propellers has grown significantly for merchant ships to propel vessels with acceptable levels of noise, without compromising propulsive efficiency. This growing interest has resulted in the first classification society Bureau Veritas, publishing guidance notes for composite marine propellers in October 2020 [3].

The Maritime Research Institute Netherlands (*MARIN*) is a company also showing interest in this field of research. They have joined forces with players from all fields of the industry to conduct research into composite propellers. This joint investigation project is called COMPROP and is a working group within the larger cooperative naval research initiative called Cooperative Research Ships (*CRS*), which studies all thinkable aspects of maritime technology for over 50 years. MARIN has been involved in the COMPROP working group by developing a simulation tool called the Composite Propeller Application (*ComPropApp*).

This tool uses a Boundary element method (*BEM*) known as PROCAL to predict the hydrodynamic behaviour, this code has been developed by MARIN. Its main advantage over CFD codes (*Computational Fluid Dynamics*) is the computational speed, but the main disadvantage is that it is not always able to capture all complex flow phenomena such as vortex cavitation and turbulence.

For conventional metal propellers, the deformation is considered negligible small. For composite propellers, this deformation can no longer be neglected as it becomes large enough to affect the performance. The influence of deformation on the resulting pressure distribution is what needs to be studied. To calculate the connection between pressures and resulting deformations and vice versa, the BEM code is coupled with a Finite Element Method (*FEM*) known as VAST/TRIDENT. This was developed by Lloyd's Register (*LR*), another member of the CRS.

Thus the structural- and hydrodynamic solutions are coupled. This is a branch of physics known as Fluid Structure Interaction (*FSI*). The ComPropApp makes use of a BEM-FEM coupled FSI scheme and can execute four types of simulations.

1. **Steady FSI:** In this first module only open water computations can be performed. This is done in the time domain where the propeller loading is gradually increased until convergence is reached.
2. **Modal Analysis:** This module is used to calculate the eigenfrequencies and mode shapes of the propellers. This is required for the Unsteady FSI and Stress Analysis modules.
3. **Unsteady FSI:** In this module, modal analysis is used to perform non-uniform inflow simulations with propellers in the frequency domain. this is valid as the loading and deformations are periodical for each

revolution. This way, for each considered blade position within a revolution the deformation and pressure is calculated. The unsteady FSI module keeps iterating for each blade position until the residual of the modal forces of two iterations is below an user specified value and is said to be converged.

4. **Stress Analysis:** In the last module, the loading of the last revolution of the unsteady FSI analysis is communicated to perform a stand-alone finite element analysis. This should, when all mathematics and physics are applied correctly result in an equal deformation as provided by the unsteady FSI module.

The steady FSI analysis is validated and known to accurately simulate deformation and performance of flexible propellers in open water. The unsteady FSI- and Stress analysis do however show differences in the propeller deformation and propeller performance. This report has two goals:

1. Validation of the unsteady FSI- and Stress Analysis modules of the ComPropApp. First, the error in the code must be found and modified. Later on the Unsteady FSI- and Stress Analysis can be validated by comparing simulations with experiments executed at MARIN which were conducted on behalf of the COMPROP working group. These experiments contained a in-behind ship model, thus a non-uniform wake field is introduced.
2. Exploration of the design space of flexible marine propellers. Besides validation of the application, the second goal is to identify propeller geometry parameters which influence the deformation and performance of propellers.

The structure of this thesis is as follows: In chapter 2, the working principles of marine propellers are investigated. From literature, parameters are identified which could be altered in the propeller design study. Before the validation starts, in chapter 3, the physics and mathematics behind the ComPropApp are explained. This is necessary to understand how errors can be explained and solved.

The validation of the ComPropApp has been divided into three separate chapters: First in chapter 4, the steady FSI module is validated. This module executes simulations in the time domain and can be used to simulate propeller behaviour in open water. The open water propeller is compared with found performance in literature on the same propeller. Grid studies are executed to ensure the solutions are independent of the grid sizes. Afterwards, in chapter 6, a non-uniform sinusoidal wake field is introduced in the unsteady-FSI module. This is to test whether the Fourier transform is applied correctly. This module simulates the propeller in the frequency domain and uses a Fourier transform scheme to calculate the periodical motion of the propeller.

When the working principles of the unsteady FSI module are validated, in chapter 6, the experiments conducted at MARIN as part of the COMPROP working group with a model flexible propeller are compared to simulations to prove that the ComPropApp is capable of simulating the deformation of flexible marine propellers. Before the comparison start, the material and experimental are discussed.

When the validation is finished, the tool can be used with confidence to explore the design space of flexible marine propellers. The design space of conventional propellers is already a very complex and correlated. With the introduction of flexibility (and for composite propellers anisotropy as well) this space becomes even more complex.

In chapter 7, the influence of propeller geometry parameters on the hydrodynamic and structural performance is explored and the possible advantageous effects of these parameters on the cavitation behaviour is examined. First, single parameters are altered to explore the effects of these changes. Later on, in a multi-variable analysis, all parameters will be modified simultaneously. In chapter 8, the designed propellers are used in a demonstration of how they can reduce the pressures (and thus possible cavitation and noise emission) by de-pitching in the wake peak. This thesis will be finalized with a conclusion and recommendations in chapters 9 and 10.

2 Marine Propellers

2.1 Introduction

The goal of this chapter is to get familiar with all terminology and performance parameters of marine propellers. In section 2.2, the geometry of the propeller is explained. Subsequently, in section 2.3 the hydrodynamic performance of propellers is explained in terms of delivered thrust, torque and efficiency. Hereafter, in section 2.4, the phenomenon of propeller cavitation and design considerations concerning cavitation prevention will be discussed. Later on, in section 2.5 the strength of propellers and propeller vibrations will be discussed. Finally, composites as propeller material are discussed in section 2.6. Throughout this chapter, the book *Marine Propellers and Propulsion*, (*J. Carlton 2019*) has been used extensively. [4]

2.2 Propeller geometry

It is the specific combination of parameters that make a propeller unique both in terms of appearance and performance. These parameters are chosen such that the propeller fits the ship to ensure the best combination of thrust, torque, speed and other mission requirements. This whilst minimizing fuel usage, vibration and cavitation.

Before the parameters are discussed, it is needed to establish a coordinate system that will be used. It was chosen to adopt the coordinate system from *J. Carlton (2019)*. This coordinate system is the industry standard frame established at the International Towing Tank Conference (*ITTC*) in 1963 [5]. In this reference frame, the positive x -direction moves along the with the ship (upstream), the y -direction is positive to starboard and the positive z -direction moves vertically downward. Rotation is positive when rightward. The coordinate system is shown in figure 2.1.

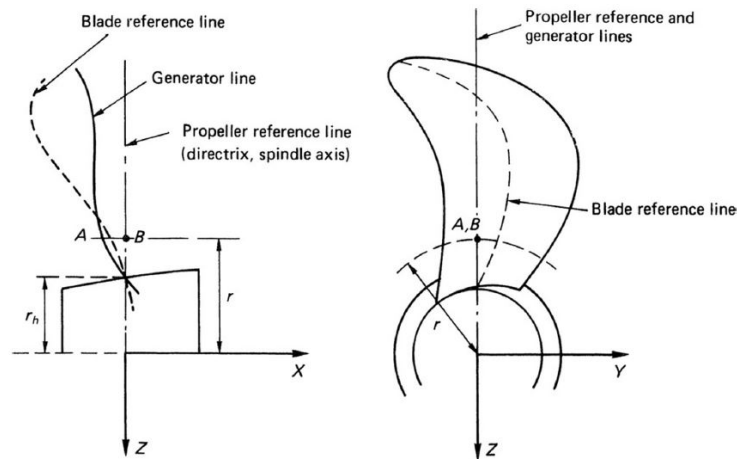


Figure 2.1: Established reference frame for propellers. (*Source: J Carlton (2019) [4]*)

Propeller Diameter

The most obvious parameter is the propeller diameter (D) and in general, it can be stated that the bigger the propeller diameter is, the more thrust it will generate. The propeller diameter is limited by the total space it can occupy beneath the hull, and most classification societies require a minimum amount of *tip clearance* (around 15 % of propeller diameter as a minimum value). This is done because water must flow freely alongside the propeller. Too little space between propeller and hull would result in unwanted noise and pressure pulses from propeller to hull. Therefore, composite propellers might reduce the required tip clearance requirements from societies, as less noise and vibration are being thought to be transmitted.

Pitch

A propeller blade makes an angle with the shaft. For each pitch angle, the water encounters the blade with another angle of attack (α). This angle can vary largely throughout different vessels as for every load and speed, a different propeller pitch is beneficial. Vessels with multiple operational profiles are therefore equipped with Controllable Pitch Propellers (*CPP*), which can alter the blades to the desired pitch.

Besides efficiency, the pitch also influences the cavitation properties of the propeller in off-design conditions. A study by Vrijdag et. al (2010) [6], showed that by altering the pitch during an accelerating manoeuvre of a naval vessel. Significantly less tip vortex cavitation was observed. Composite propellers can be seen as a

self-twisting propellers, which passively adjusts the pitch when loaded by hydrodynamic forces whilst sailing. This is achieved due to the flexibility of composites compared to metals. The effects of this pitch adjustment have been studied extensively. Liu and Young (2009 and 2010) [7], [8] for example, stated that the potential benefits are improved efficiency and cavitation reduction, The authors showed higher efficiency in off-design conditions compared to a rigid NAB-propeller.

Skew

Skew, defined with angle $\theta_s(x)$, is the angle when the directrix (see figure 2.1) and the line which is drawn between the shaft center and the michord point. The skew varies along the blade, and the propeller skew (θ_{sp}) is defined as the greatest skew along the blade. The definition is shown in figure 2.2, here the two main types of skew; balanced and biased are clarified.

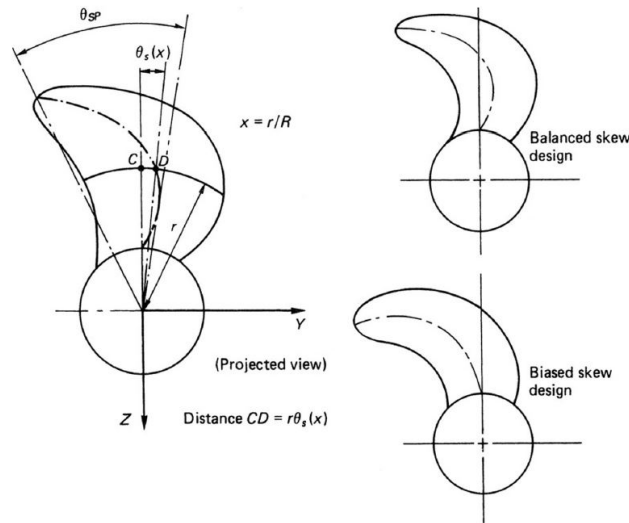


Figure 2.2: Propeller Skew. (Source: J Carlton (2019) [4])

Early studies into the effects of skewed propellers showed a delay in cavitation inception and erosion and lower induced vibrations [9]. In more recent numerical studies, Also hydrodynamic improvement in the form of 20 % thrust gains have been claimed in a study by Wang (2018) investigating 4 similar propellers whilst only increasing the skew angle. This study was performed with a CFD code [10]. It should be noted that an increase in thrust does not necessarily means an increase in efficiency. A study by Ghasseni and Ghadimi (2011) using a BEM method also claimed hydrodynamic gains for a highly skewed underwater vehicle [11]. These studies were, however, all performed on assumed rigid propellers, The effect of deformation might influence the results as it is believed that skew greatly influences the deformation of propellers. Young (2007), showed with a BEM study that increased skew leads to a lower natural frequency of the blade and increases the bending and torsional flexibility of a blade. This leads to higher observed stress levels in highly skewed propellers. But this also indicates the possibility to reduce noise and cavitation. [12].

Rake

Where skew is curving in the yz -plane, rake curves in the xy -plane. As seen in figure 2.3, this curvature can either be upstream (positive rake) or downstream (negative). The application and effects of rake to propellers are less studied compared to skew. Some studies have shown improvement in hydrodynamic performance, noise and cavitation characteristics. A CFD study conducted by Hayati et al. (2011) [13] showed efficiency improvements for higher propeller loads when increasing the forward rake angle. Hayati also observed an improvement in flow characteristics (less vibration and noise) for backward rake angles, yet those angles decreased the propeller efficiency. A study by Gaggero et al. (2016) [14], also showed a much more uniform blade loading when applying rake to propellers to induce a higher tip loading.

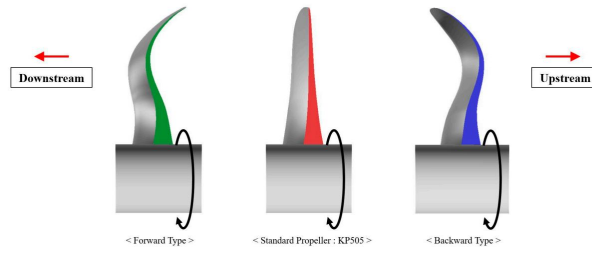


Figure 2.3: Propeller Rake. (Source: Kang et al. (2019) [15])

Blade area ratio

The blade-to-area ratio (A_E/A_0) can be defined as the fraction of area used for the propeller blade. The total open water area available A_0 is calculated with equation 2.1. The propeller area is defined differently throughout literature. Carlton (2019) [4] describes four commonly found definitions for which the most used is the expanded blade area (A_E) for its simplicity as it is easily computed with equation 2.2, and numerically calculated by applying the Simpson's rule, or other numerical integration methods. The three main ways of describing the blade area are shown in figure 2.4.

$$A_0 = \frac{\pi D^2}{4} \quad (2.1)$$

$$A_E = Z \int_{r_n}^R c dr \quad (2.2)$$

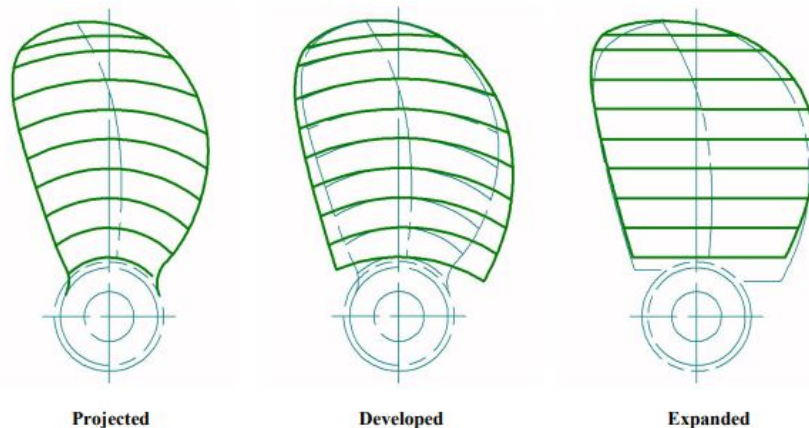


Figure 2.4: Different ways of defining the blade area. (Source: HydroComp Inc (2007) [16])

Propeller design process

As discussed above, many parameters influence the overall propeller performance. To complicate the process even more, the mission profile of a vessel also dictates whether a propeller is a good fit. It is in the nature of the industry (and engineering in general) to be very secretive about good propeller design. This is obvious, as they are very expensive and knowledge is scarce.

A popular approach to propeller design, which has been made possible by the increase in computational speed and space is propeller parametrization. In this process, large quantities of propellers are generated with minor alterations. Through optimization algorithms, an optimal propeller can be generated for specific ships with their operational profile. Thus without knowing which exact combination of skew, pitch rake, etc. leads to the optimum propeller, it is still generated. This approach to propeller design can lead to significant savings. A 3 % efficiency gain for a reference case was obtained by Foeth and Lafeber (2013) comparing 1250 propellers with a Boundary Element Method [17]. Even though, for this project, analyzing 1250 propellers for a test case must be deemed out of scope. It could still be possible to select some of the discussed propeller parameters and target one optimization parameter (vibration reduction or efficiency gain for example) to investigate the design space of flexible marine propellers.

2.3 Propeller performance

A propeller's performance is most commonly expressed in terms of delivered thrust, required torque and the propeller efficiency. For analysis purposes, the thrust and torque are non-dimensionalized with formulas 2.3 and 2.4. in which T and Q are the total thrust and torque, ρ is the fluid density, n is the rotational speed and D the propeller diameter. To analyze this over a non-dimensional speed range of a vessel, advance ratio J is introduced, and is formulated as in equation 2.5. Herein, V_a is known as the advance speed of a ship. This is lower than the observed ship speed (V_s) because hull-fluid interaction decelerates water, thus the propeller works with a lower speed than the ship speed. The relation between ship speed and advance speed is shown in equation 2.6. Here, w denotes the wake factor which is a factor describing how much lower the inflow velocity is compared to the ship speed.

$$K_T = \frac{T}{\rho n^2 D^4} \quad (2.3)$$

$$K_Q = \frac{Q}{\rho n^2 D^5} \quad (2.4)$$

$$J = \frac{V_a}{nD} \quad (2.5)$$

$$V_a = (1 - w)V_s \quad (2.6)$$

Propeller performance is best described in an open water diagram (*OWD*). This depicts the thrust- and torque coefficients and the open water propeller efficiency (η_0) over the advance ratio range (commonly from 0 (bollard pull condition) to around 1.5 (full speed)). For systematic propeller series such as the Wageningen B- or C-series for example, this is done for all possible pitch ratios (P/D). The pitch values are commonly selected as the P/D ratio at 70% of the propeller diameter. This way, ship designers can select the best screw for a wide range of vessels.

The propeller efficiency in open water (η_0) is a function of thrust and torque and is calculated as in equation 2.7. An explanatory *OWD* is shown in figure 2.5. Here the enormous effect of the pitch ratio on propeller efficiency is visible.

$$\eta_0 = \frac{K_T J}{K_Q 2\pi} \quad (2.7)$$

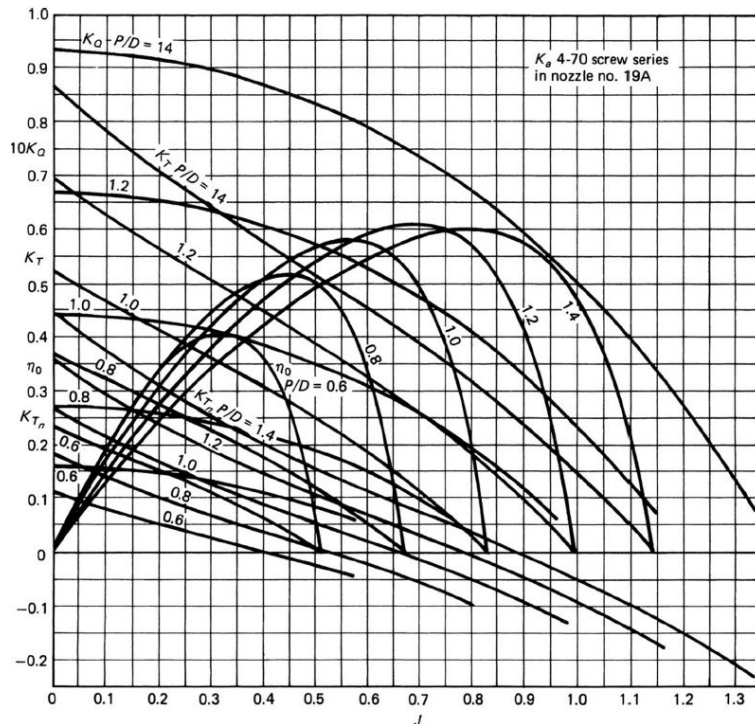


Figure 2.5: Open water diagram. (Source, J. Carlton (2019) [4])

Open water diagrams can be established by experiments or numerical studies. This is done by propeller manufacturers but this data is not made publicly available. One can create an open water diagram by performing several open water tests and fitting a curve through all data points, or one can perform numerical simulations to obtain data on propellers.

2.3.1 Wake field

Another method to look at the performance of propellers is by examining the propeller's wake field. The wake field shows the flow velocity and direction at the propeller plane. This is different for different types of vessels and how propellers modify this wake field. The wake velocity v_a is normally non-dimensionalized with the ship speed v_s , such that a propeller in open water encounters a uniform wake field with a velocity of 1 (equal to the ship speed). In reality, due to streamlining effects and the formation of a boundary layer because of friction of the hull form, the propeller encounters a non-uniform wake field. This non-uniform wake field is very a complex phenomenon to describe analytically because of all interactions taking place between fluid, hull and propeller. Experimental studies are performed using Particle Image Velocimetry (*PIV*). This is an optical method to analyze flow. Numerical experiments are executed with CFD techniques with turbulence models to capture the tip vortex effects and generate more accurate flow fields. In this study however, propeller analysis is performed with a boundary element method which is not accurate in performing wake field studies. This is due to the fact that viscous effects have large effects on the ship wake. It is possible to couple CFD and BEM software where a CFD code creates an inflow wake field. This can then be adopted by the BEM software to calculate propeller characteristics in non-uniform inflow conditions. This method has been tested and proven accurate by Rijpkema et al. (2013). [18]. This results in large savings in computational time with a thrust difference of 2 - 3 %.

2.4 Cavitation

Cavitation is the occurrence of vapour bubbles in a fluid which occur when the static pressure is below the fluid's vapour pressure. When these bubbles are exposed to high velocities and close to the propeller surface. Then, these vapour bubbles can explode, causing shock waves which lead to erosion and high noise levels. Cavitation is almost always present in marine propellers and unavoidable to some degree. Multiple types of cavitation are distinguished. The most common types will be explained in this section. A more complete overview of types of cavitation is shown in figure 2.6

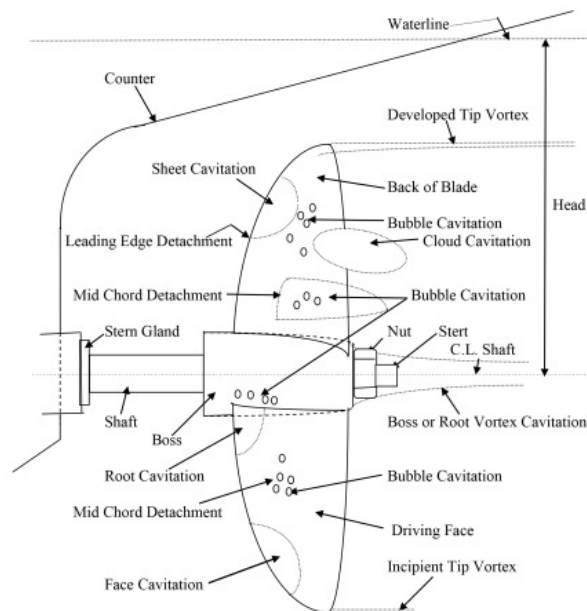


Figure 1 Various Types of Cavitation

Figure 2.6: Types of cavitation. (Source: *iims* (2015) [19])

2.4.1 Types of Cavitation

Sheet cavitation

Sheet cavitation occurs at the leading edge of the suction side of the propeller. As the name suggests, it forms a visible sheet on the blade. It arises because of the large suction pressure (negative pressure) build-up whilst rotating. Sheet cavitation is a relatively stable form of cavitation with little erosive effects. Only when model tests show unstable effects, measures should be taken from an erosion point of view.

Whilst some cavitation effects can not be modelled with boundary element methods, such as vortex cavitation types, boundary element methods can predict and model sheet cavitation. This is possible in the used PROCAL BEM code and has been tested by Bosschers et. al (2008) [20]. They succeeded to achieve similar sheet cavitation patterns from simulation and experiment. This is shown in figure 2.7. That research investigated hull pressure pulses generated by a rigid metal propeller, which is a completely different type of calculation then with a flexible propeller simulations in the ComPropApp. It can not be stated with certainty that cavitation is accurately modelled on flexible propellers as well. Mainly because it is believed that the deformed propeller geometry influences cavitation behaviour as well.

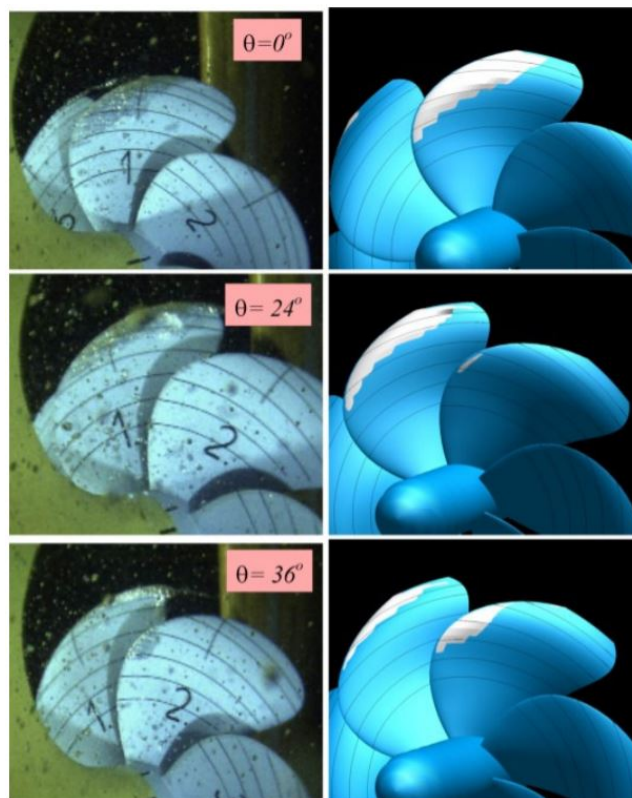


Figure 2.7: Sheet cavitation showing similarities between experiment and simulation. (Source: Bosschers et. al (2008) [20])

Cloud cavitation

Cloud cavitation is observed after stable cavitation and is thus frequently found after sheet cavitation. It consists of small cavities. This type should be taken seriously as it has the potential to cause severe erosion to the propeller [4]. Unfortunately, this can not be modelled by potential flow methods (BEM), and thus the possible occurrence and effects shall not be included in this research.

Hub vortex cavitation

Hub vortex cavitation starts at the hub and is visible as a "rope" behind the hub with strands equal to the number of blades. This type is stable and as it moves away from the propeller, no erosion is expected from this type of cavitation. It does however induce noise.

A study by Abdel-Maksoud et. al (2004) observed a high dependency on the thrust loading coefficient K_T [21]. The study also showed that the hub form affects the formation of hub vortex cavitation. A solution to decrease this type of cavitation is the use of propeller boss cap fins, which are known to reduce the propeller noise and increase propeller efficiency as it recovers rotational losses. [22]

Tip Vortex cavitation

Whereas hub vortex cavitation is seen behind the hub, tip vortex cavitation is shown a short distance behind the propeller blade tip. When it is first observed, the vortex is "unattached", but through higher blade loading and higher cavitation number, the vortex attaches to the propeller tip. A CFD study performed by Hu et. al (2021) [23] Showed that the larger skew angles resulted in smaller cavity sizes and reduced tip vortex cavitation intensity. It is also suspected that less susceptibility to sheet cavitation also resulted from this increase in skew.

Leading edge vortex cavitation

This type of cavitation distinguishes itself from tip vortex cavitation by the fact that it occurs at the inner radii of the blade since the blade loading is commonly the highest in this region. Especially in highly skewed propellers. This vortex will coincide with the tip vortex to form one trailing vortex. These effects are rather complex, and can not be captured by Boundary element codes.

Propeller-Hull Vortex (PHV)

This type of cavitation consists of cavitating vortices between the propeller tip and hull. These are a great source of radiated noise to the propeller hull and occur more frequently when the tip clearance is not sufficient. Then the propeller becomes "starved" of water. As discussed in section 2.2 composite propeller might be able to reduce the susceptibility of PHV cavitation.

2.4.2 Cavitation design considerations

The main parameter to consider whilst designing a propeller is the cavitation number (σ). This is the fraction of static pressure to dynamic pressure. It should always be known to which relative pressure (p_0) the cavitation number is calculated. This could be the pressure at the shaft, the pressure far away from the shaft, which is assumed unaffected, or any other pressure. p_v denotes the water vapour pressure. The two reference pressures named here make the most sense from a physical point of view.

The two most common expressions, the free stream-based cavitation number σ_0 and the rotational speed-based cavitation number σ_p are shown in equations 2.8 and 2.9 respectively.

$$\sigma_0 = \frac{p_0 - p_v}{\frac{1}{2}\rho v_a^2} \quad (2.8)$$

$$\sigma_p = \frac{p_0 - p_v}{\frac{1}{2}\rho(\pi \times nD)^2} \quad (2.9)$$

The inflow velocity of the water also plays an important role in propeller design. This is shown in another tool used by propeller designers known as a cavitation bucket. A basic explanatory cavitation bucket diagram is shown in figure 2.8. Here the relation between the angle of attack (α , describing the blade's pitch and speed), and the cavitation number is shown. This, in relation to which type of cavitation is expected to occur. This is different for each propeller-ship combination, and can be obtained through experiments, Ebrahimi et al. (2021) [24] for example, investigated the connection between the rotational-based cavitation number, different pressures and cavitation for Wageningen B-series propellers, and showed that cavitation occurs around a cavitation number of 6.

One should however never trust solely on the cavitation numbers for proper propeller design with respect to cavitation or acoustic performance for that matter. As correctly stated by Šarc et. al (2017) [25]. He shows a wide variety of optimum cavitation numbers through a literature survey for similar experiments with flat plates. Furthermore are other parameters such as geometry, gas quality and temperature shown to influence on cavitation and pressure distribution as well. Thus the cavitation bucket can be used as a quick initial tool. But for conclusive remarks on a propeller, other techniques have to be used.

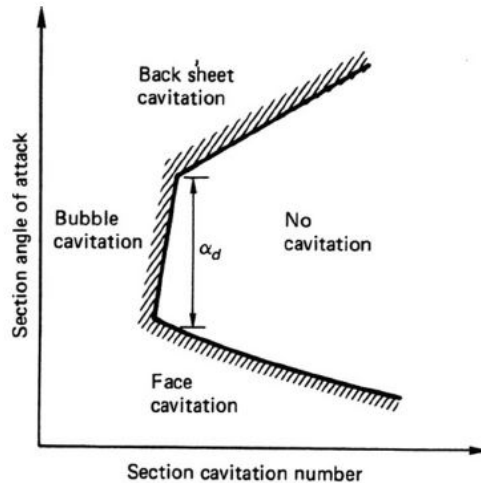


Figure 2.8: Cavitation bucket. (Source, J. Carlton (2019) [4])

2.5 Propeller strength and vibration

2.5.1 Propeller Strength and fatigue

A propeller experiences forces and moments during operation and should be designed so that it will not deform plastically over its operational lifetime. For properly designed conventional metal propellers, these strengths are far below the yield stress and should not cause problems, except for fatigue. In the early days it was done with cantilever beam methods (see chapter 19 from Carlton [4], which can still be done to quickly gain insight into the propeller loading. It is however, a limited method because it assumes an average section thickness. Thus errors are expected for propellers with non-linear thickness distributions.

Another limitation of cantilever beam methods is the inapplicability for highly skewed propellers and other complex three-dimensional geometries. Highly skewed propellers redistribute stress asymmetrically and increase the maximum principal stress found in the blade. This was shown in a BEM-FEM coupled study by Ghassemi (2012) for a composite propeller [26]. The paper also noted a decrease in efficiency for an increased skew angle over the complete advance ratio. This seems contradictory with the results for another test case by the same author where hydrodynamic gains were observed. [11].

Besides strength, propellers should also be evaluated on their fatigue. Whereas stress is experienced instantly and loads larger than the yield strength of the propeller's material could potentially break a propeller. Fatigue is an unavoidable material phenomenon which slowly deteriorates the material's strength over time. It is initiated by small microscopic cracks, which slowly develop into macroscopic failure. The fatigue lifetime is influenced by the number of stress cycles and the average level of stress. This is however an extremely complex and not well-understood topic in material science. The same goes for estimating the lifetime of marine propellers, this is even more complex for composite marine propellers. Some papers can be found ([27] for example), but the data these papers deliver seem unverifiable.

2.5.2 Propeller vibrations

A propeller, like all man-made structures, vibrates during operation. How much a blade vibrates is dependent on material properties and the geometry of the propeller. These parameters decide in which shape a propeller tends to vibrate under operation, the so-called *mode shapes*. These properties also determine the frequency in which the object tends to vibrate. This is called the *eigenfrequency*.

Propellers vibrate during operation and can be divided into two categories: low-frequency vibrations (the propeller turns with a rotational speed, causing a blade passing frequency (*BPF*) for example. These vibrations can excite the shafting line of a marine vessel. On the other hand, high-frequency vibrations are caused by the complex shape and resulting mode shapes of the propeller. Another high-frequency vibration might be the result of rapidly exploding cavities on the propeller structure. This also causes a phenomenon called *Propeller singing*.

This "singing" occurs through a wide range of ships, from slow large vessels to high-speed crafts. It happens mostly in off-design conditions. It is known that for two "identical" propellers, one might induce singing vibrations and the other does not. Showing how higher-order mode shapes are extremely sensitive to minimal production tolerances. [4] The effects of propeller vibration are plentiful. First the noise- and vibration levels are negatively affecting the comfort on board. Secondly, the vibrations cause noise which is an important aspect

of naval vessel design. Since naval vessels are trying to sail as silent as possible to avoid detection. Thirdly, the vibrations may also induce fatigue of the propeller blade.

2.5.3 Mode shapes and frequencies

When a blade is excited freely (stretching out a mass-spring system and letting it vibrate freely) with a force. It will vibrate in a unique pattern and frequency. This uniqueness is caused by the geometric and material properties of the propeller blade. The shapes and frequencies can be determined experimentally and have been done as early as 1949 by Grinstead and Burrill [28] for a flat plate propeller blade. These results are shown in figure 2.9, here the mode shapes were visualized with sand patterns. When a realistic propeller blade, with varying thickness, asymmetrical outlines and the twist of the blade is investigated, more complex shapes are observed but there are similarities with the flat symmetrical blades from Burrill as well.

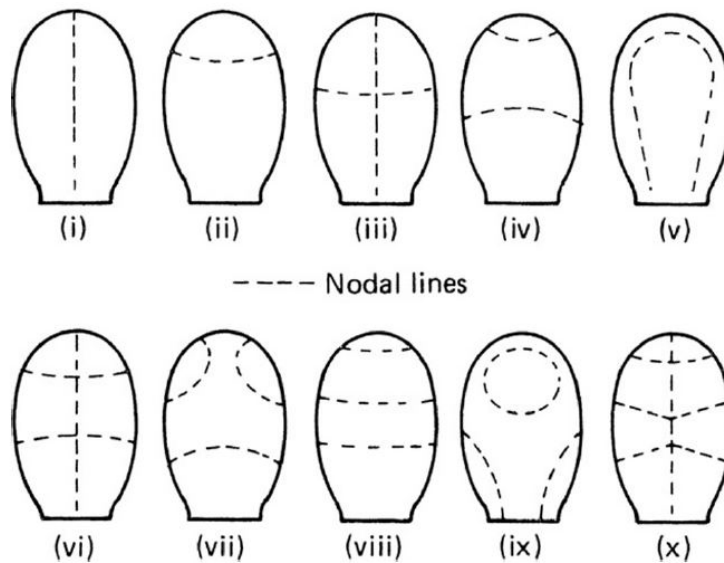


Figure 2.9: First ten modeshapes for the first ten blade frequencies by Grinstead and Burrill (1949). [28]

These early experiments investigated vibrations in air. Submerging a blade in water impacts the frequencies significantly and in less extent, the mode shapes as well. This is caused by the added mass of water around the propeller which is much denser compared to air, therefore more inertia is required to vibrate. Figure 2.10 shows the different shapes of the same propeller in water and air. Table 2.1 shows the corresponding frequencies of the first five shapes. A is known as the frequency reduction ratio. The table shows that there is no clear connection between the frequency in air and water. Even though it can be stated that for higher frequencies the effect of added mass becomes smaller.

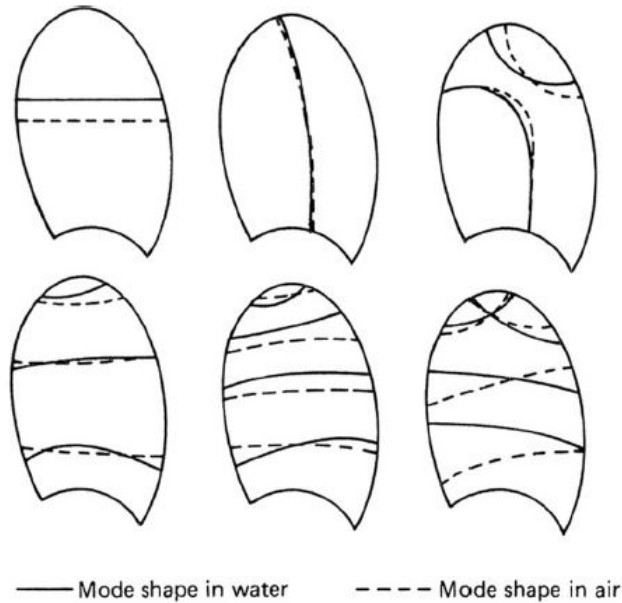


Figure 2.10: Difference in mode shapes in water and air, Burrill 1949. [28]

Table 2.1: Frequencies of the first five modes in figure 2.10, Modified from Burrill (1949). [28]

| Mode | Frequency [Hz] | | Λ [-] |
|------|----------------|-------|---------------|
| | air | water | |
| 1 | 230 | 161 | 0.700 |
| 2 | 400 | 265 | 0.662 |
| 3 | 670 | 490 | 0.731 |
| 4 | 710 | 625 | 0.880 |
| 5 | 1020 | 1000 | 0.980 |

Besides experimental determination, the finite element analysis can also determine the mode shapes and natural frequencies with accuracy. Although, there are some issues with adequately representing the effect of immersing the blade in water as stated by Carlton (2019) [4]. Therefore the preferred method is the use of dry mode shapes.

The main difference between the two is the inclusion of fluid through which an object has to move and accelerate. The difference in results, in terms of vibration and deformation, has to be examined. In theory, when modal analysis is applied correctly, the effect of added mass should be slowly added to the system, giving a fairer representation of the physics compared to estimation before-hand. literature is found stating deformations are different for dry and wet analysis. Loukogeorgaki et al. (2014) [29] showed different deformations for two large floating structures, and improvements for the wet mode shapes with respect to the experimental deformations. The wet and dry natural frequencies for an elastic marine propeller were investigated in a paper by Li et al. (2017) [30] and showed significant differences as well, but similar mode shapes. However, no connection is made to the resulting propeller vibrations or deformations, thus this is inconclusive. This might be an interesting research topic how these different approaches simulate blade vibration and deformation compared to the experimental data.

A Composite propeller will have different mode shapes and frequencies compared to a metallic counterpart. Lin et al. (2008) [31] showed lower frequencies for composite propellers compared to metallic propellers in water, but higher frequencies in air for composite propellers. This can be attributed to the relative weight of the propeller to the added mass of water. This is much higher for the composite propeller.

2.6 Composite Propellers

In the introduction, it was discussed why composite propellers became a point of interest for marine engineers. This section will discuss the points of interest in using composites as opposed to NAB-Alloys. The main differences being the anisotropy, and the lower Young's modulus of the material.

These two material properties are causing an effect called *bend-twist coupling*. This means that the propeller can passively adjust its pitch by bending due to the hydrodynamic loading on the blade. This is caused firstly

because of the lower material strength and secondly, the twisting is the result of the material's anisotropic behaviour. This effect is shown in a study paper by Lin et al. (2009) [32]. The blade is pre-deformed, and whilst loaded due to the hydrodynamic loading, the blade "pitches" itself to the desired pitch. This is shown in figure 2.11.

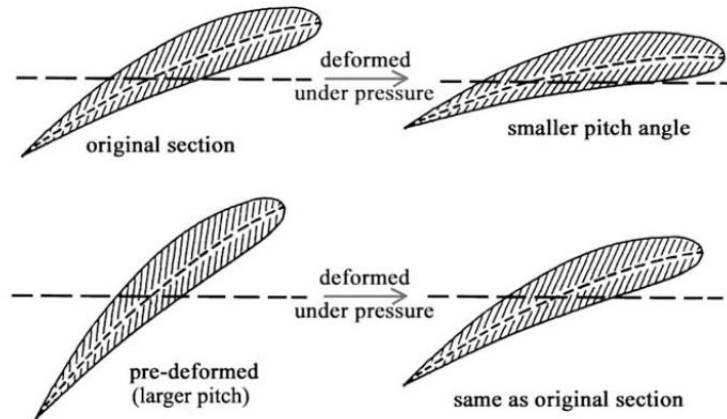


Figure 2.11: Visualization of the working mechanism of passive pitch adjustment. (Source: Lin et al. (2019) [32])

2.6.1 Stacking sequence

Composite objects consist of multiply layers of fibre (carbon or glass for example). Each layer or ply can have a different orientation (30,45,90 or 0 degrees are most common). These fibre directions causes that the layer is much stronger in one direction compared to another. By altering this sequence of fibre orientation, the strength and stiffness of the end product can be tailored in every direction which causes the anisotropy of composite materials. The stacking sequence (orientation of each sheet) of composites has a great influence on the strength of the final product. This is because the fibre orientation determines how stress is distributed in the propeller blade. Numerous studies have been performed on how this stacking sequence affects the overall propeller strength.

Maung et al. (2021) [33] studied composite propeller optimization by using a Generic algorithm approach (design optimization method where an optimum is found under given constraints). The optimized version used curved fibre paths and yielded 15 % less maximum deflection, whilst generating the same twist angle compared to a benchmark composite propeller. Thus the passive pitch adjusting mechanics remained intact.

A study by Blasques et al. (2010) [34] showed that by optimizing the stacking sequence for maximum efficiency, a 4.7 % efficiency increase was achieved compared to an identical metal propeller. The optimization did not include cavitation and vibration effects, thus whether the propeller is realistic was not completely validated.

2.7 conclusions

Throughout this chapter, several important parameters were identified which can be used in the to be executed design study. Pitch, skew and rake all had influence on pressure distributions, stress distributions, and the propeller efficiency. All these parameters should lead to the final goal of reducing the cavitation behaviour of the flexible propellers. It was concluded that some types of cavitation are not modelled in BEM methods (and thus in the ComPropApp). Thus no firm conclusions on cavitation behaviour can be done. Besides, even the the types which can be modelled in the ComPropApp (Sheet cavitation) was only verified on rigid propellers. As it is thought that flexibility greatly influences these results. It is chosen to not model cavitation in the design study. Instead it will be chosen to solely focus on the pressure distributions and make conclusions based on those pressures.

In this report, the *composite* propeller changed with a *flexible* propeller. Mainly because the experiments at MARIN were performed with a flexible isotropic material so the validation has to be performed with an equal material in the simulations. The ComPropApp is already used to analyze composite propeller models. But this is less straightforward, and for a design space study too time consuming. Therefore it is selected to perform this study on a isotropic solid as well. Thus, no study can be done on bend-twist coupling, and the even more complex deformations happening in anisotropic structures. But, the material used in the COMPROP2 experiments, and used in the design study is definitely flexible enough to enable de-pitching of the propellers as was shown in figure 2.11.

3 The ComPropApp

3.1 Introduction

To analyze the interaction between the fluid flow and the solid propeller blade, the ComPropApp studies Fluid-Structure interaction (*FSI*), which is a branch of hydro-elasticity. The interaction between hydrodynamics and structural deformation can not be neglected for flexible propellers. For metal propellers the deformation can be assumed to be zero, this can not be assumed for flexible propellers as the deformation components are large enough to influence the performance of the propeller. Software packages that are able to perform FSI simulations can be divided into two types: Partitioned FSI methods and Monolithic FSI methods.

The latter contains software simultaneously calculating the structural and hydrodynamic response of the system within a single system of equations. The partitioned FSI method, uses a separate calculation for the hydrodynamic- and structural response. ComPropApp is a partitioned method. The advantage of a partitioned FSI method is the ability to choose the hydrodynamic and structural code of preference which is not possible in a monolithic code. The disadvantage of the partitioned FSI method is the requirement of a numerical coupling scheme between the two obtained solutions, which most likely will cause another level of unwanted numerical errors and uncertainty.

The ComPropApp uses an in-house Boundary Element Method code developed by MARIN to obtain the hydrodynamic solution of the flow around the propeller known as PROCAL. This will be explained in section 3.2. The structural solution is obtained through the Finite Element software provided by Lloyd's Register which is a partner in the CRS. This software is known as Vast/Trident and will be discussed in section 3.3.

In section 3.4 the composite propeller application will be discussed. It will be shown what types of simulations can be performed and which data can be retrieved from those simulations. The numerical coupling scheme will be explained as well.

3.2 PROCAL and Boundary element method

A boundary element method is in the broadest sense a solver for partial differential equations, in the case of potential flow, it solves the pressures and flow velocities. The method is significantly faster compared to computational fluid dynamics (*CFD*) but it does exclude viscosity effects, these can be added to the solution in the form of empirical formulations. However, turbulence and cavitation effects are rejected in the solution. Nonetheless, when one knows where and how to use it. It can still be a very powerful tool in analyzing marine propellers. This is discussed in relation to the ComPropApp in the thesis by P. Maljaars (2018). [35]

3.2.1 PROCAL

In a Boundary element method code, the disturbed velocity potential Φ is solved. The total velocity in the domain is described by equation 3.1. In which \mathbf{x} is the position vector in Cartesian coordinates, t is the time and \mathbf{v}_0 is the relative inflow speed to the propeller, which can be written as equation 3.2 considering the ship's effective wake velocity \mathbf{v}_w and the propellers angular velocity θ .

$$\{\mathbf{v}\}(\mathbf{x}, t) = \{\mathbf{v}_0\}(\mathbf{x}, t) + \nabla\Phi(\mathbf{x}, t) \quad (3.1)$$

$$\{\mathbf{v}_0\}(\mathbf{x}, t) = \{\mathbf{v}_w\}(\mathbf{x}, t) - \{\theta\} \times \{\mathbf{x}\} \quad (3.2)$$

For potential flow methods, the flow is assumed incompressible (constant density) and irrotational which means the Laplace condition for flow (as shown in equation 3.3) is satisfied.

$$\nabla^2\Phi(\mathbf{x}, t) = 0 \quad (3.3)$$

Then, the fluid pressure p is related to velocity and potential disturbance according to Bernoulli's law:

$$\frac{\partial\Phi}{\partial t} + \frac{1}{2}|\{\mathbf{v}\}|^2 + \frac{p}{\rho} + gz = \frac{p_{ref}}{\rho} + \frac{1}{2}|\{\mathbf{v}_0\}|^2 \quad (3.4)$$

in which ρ is the fluid density, g is the gravitational constant and p_{ref} is the (undisturbed) pressure upstream, which can be calculated as in equation 3.5. where z is the distance between the free surface and the center of the shaft.

$$p_{ref} = p_{atm} + \rho gz \quad (3.5)$$

On the boundaries of the fluid: S_B at the propeller surface and S_W for the wake sheet, certain boundary conditions have to be implied. The wetted body surface is considered to be impenetrable, thus no velocity

of flow can happen perpendicular in the direction to the surface, in mathematical terms this is written as in equation 3.6 for a deforming and vibrating blade.

$$\nabla\Phi \cdot \mathbf{n}(\mathbf{x}, \delta) = -\mathbf{v}_0 \cdot \mathbf{n}(\mathbf{x}, \delta) + \frac{\partial\delta}{\partial t} \cdot \mathbf{n}(\mathbf{x}, \delta) \quad (3.6)$$

δ denotes the blade deformation. The first part of the right hand side of equation 3.6 is the surface velocity on the normal of the propeller blade, the second part is the vibrating velocity of the blade itself. The wake sheet S_W is an imaginary part of the flow, the path the propeller blade has travelled through the fluid. This fictional component is a surface with zero thickness. Then a kinematic boundary condition must be applied stating the wake sheet is a stream surface of the flow, thus no velocity can escape through this sheet. This is formulated as in equation 3.7.

$$\mathbf{v} \cdot \mathbf{n} = 0 \quad (3.7)$$

As the wake sheet has zero thickness, it can not yield a pressure difference over this wake sheet. This dynamic boundary condition is shown in equation 3.8 and is known as the Kutta-Condition:

$$\Delta p = p^+ - p^- = 0 \quad (3.8)$$

And the final boundary condition states that there should be no flow fluctuations at the outer panels of the domain, thus:

$$\nabla\phi \rightarrow 0 \quad (3.9)$$

3.2.2 Green's Theorem

The relation between the velocity potential function (ϕ) and any point in the domain is based on Green's third identity: the potential formulation by Morino (1975) [36]. the velocity potential for any point \mathbf{a} in domain Ω is given by equation 3.10. \mathbf{b} is a point on the fluid boundary domain and $\epsilon(x)$ is a constant for each point in the domain and is defined as shown in equation 3.11. Furthermore, is Green's function defined as $G(\mathbf{a}, \mathbf{b})$ for the applied 3D flow case. Herein \mathbf{n}_b is the outward normal at \mathbf{b} . Equation 3.10 could be interpreted as an equation that gives the potential at point \mathbf{a} . Which is induced by the distribution of sources and dipoles on the surfaces with the strengths being the fractions in the formulas.

$$\epsilon(\mathbf{a})\phi(\mathbf{a}, t) = \int_{S_B} \left[\phi(\mathbf{b}) \frac{\partial G(\mathbf{a}, \mathbf{b})}{\partial \mathbf{n}_b} - G(\mathbf{a}, \mathbf{b}) \frac{\partial \phi(\mathbf{b}, t)}{\partial \mathbf{n}_b} \right] dS + \int_{S_w} \left[\Delta\phi(\mathbf{b}, t) \frac{\partial G(\mathbf{a}, \mathbf{b})}{\partial \mathbf{n}_b} - G(\mathbf{a}, \mathbf{b}) \Delta \left(\frac{\partial \phi(\mathbf{b}, t)}{\partial \mathbf{n}_b} \right) \right] dS \quad (3.10)$$

$$\epsilon(x) = \begin{cases} 4\pi, & \mathbf{a} \text{ in } \Omega \\ 2\pi, & \mathbf{a} \text{ on smooth } S_B \\ 0, & \mathbf{a} \text{ interior to } S_B \end{cases} \quad (3.11)$$

Green's function $G(\mathbf{a}, \mathbf{b})$ is defined as in equation 3.12.

$$G(\mathbf{a}, \mathbf{b}) = \frac{1}{r(\mathbf{a}, \mathbf{b})}, \quad r(\mathbf{a}, \mathbf{b}) = |\mathbf{r}| = |\mathbf{a} - \mathbf{b}| \quad (3.12)$$

If point \mathbf{a} is on \mathbf{b} , then the last term in the second integral of equation 3.10 is zero. This condition can vary in time since the blade vibrates, therefore \mathbf{a} and \mathbf{b} have to become time-dependent to transform 3.10 into an unsteady and time-variant form. This is shown in equation 3.13.

$$2\pi\Phi(\mathbf{a}(t), t) = \int_{S_{B(t)}} \left[\phi(\mathbf{b}(t), t) \frac{\partial G(\mathbf{a}, \mathbf{b})}{\partial \mathbf{n}_b} - \frac{\partial \phi(\mathbf{b}, t)}{\partial \mathbf{n}_b} G(\mathbf{a}, \mathbf{b}) \right] dS + \int_{S_W(t)} \Delta\phi(\mathbf{b}(t), t) \frac{\partial G(\mathbf{a}, \mathbf{b})}{\partial \mathbf{n}_b} dS \quad (3.13)$$

3.2.3 Discretization

The Morino formulation in equations 3.10 and 3.13 are solved for each panel S_B and S_W in PROCAL on the defined collocation point. The total number of panels in PROCAL is defined by N_{total} and leads to a system of N equations, where the source and dipole elements are the only unknowns. PROCAL only models one propeller blade and hub section and uses propeller symmetry to extrapolate the results for a complete propeller to save computational time. As stated in the Thesis by P. Maljaars [35] this approach can be questioned due to time-varying deformations. An experiment executed on a propeller showed however that this does not influence the results significantly (within the accuracy requirement of 5% tip deflection, as used by the author). PROCAL defines a couple of different components, which are shown in figure 3.1.

- N_{surfs} : number of surfaces, for a propeller this is 2 (Blade and Hub)
- N_{sym} : number of symmetries, for a propeller this equals the number of blades.
- N_i : number of panels in stream-wise direction of the propeller and hub
- N_j : number of panels in radial direction of the propeller and hub
- N_{wi} : number of panels in stream-wise direction of the wake sheet
- N_{wj} : number of panels in radial direction of the wake sheet

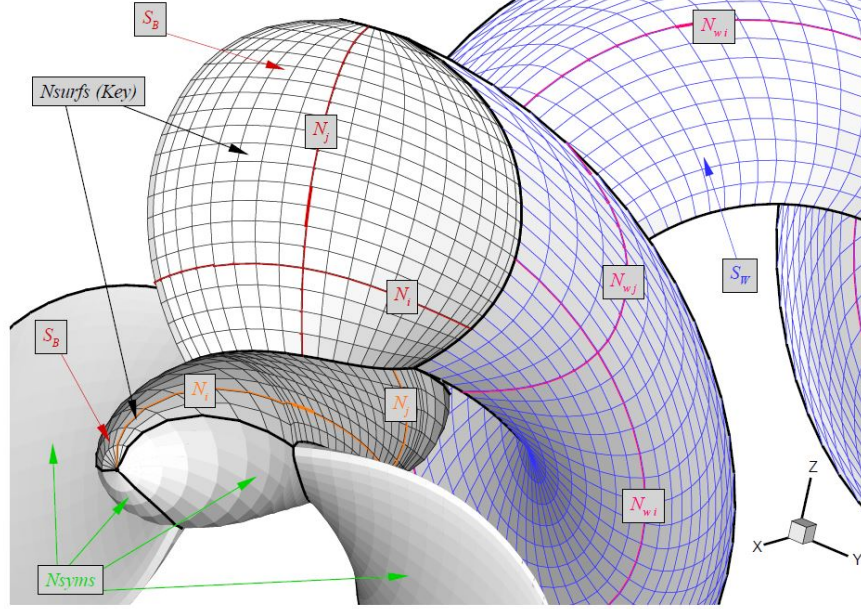


Figure 3.1: Procal surface definitions, from Vaz (2005). [37]

For steady simulations, and an assumed rigid propeller (thus a PROCAL simulation) the Morino formulation from equation 3.10, can be discretized as in equation 3.14.

$$\sum_{isurf=1}^{N_{surfs}} \sum_{isym=1}^{N_{syms}} \left[\sum_{j=1}^{N_j} \sum_{i=1}^{N_i} (D_{nij} \phi_{nij} - S_{nij} \sigma_{nij}) + \sum_{j=1}^{N_{wj}} \sum_{i=1}^{N_{wi}} W_{nij} \Delta \phi_{ij} \right] = 0, n = 1, \dots, N_{total} \quad (3.14)$$

Here, σ_{ij} and ϕ_{ij} are the sources and dipole strengths respectively at collocation point i, j on the body surface. $\Delta \phi_{ij}$ is the dipole strength on the wake surface.

The hydrodynamic influence coefficients are: D_{nij} , S_{nij} and W_{nij} and denote the body surface dipole, body surface source and wake surface dipoles respectively. Their formulation is given in equations 3.15 through 3.17. \mathbf{R}_{ij} denotes the distance as shown in 3.12 and \mathbf{n}_{ij} is the surface's normal.

$$D_{nij} = \begin{cases} -\frac{1}{2\pi} \int_{S_{Bij}} \frac{\mathbf{n}_{ij} \cdot \mathbf{r}_{ij}}{r_{ij}^3} dS_{Bij}, & \text{if } n \text{ does not refer to element } i,j \\ 1 - \frac{1}{2\pi} \int_{S_{Bij}} \frac{\mathbf{n}_{ij} \cdot \mathbf{r}_{ij}}{r_{ij}^3} dS_{Bij}, & \text{if } n \text{ refers to element } i,j \end{cases} \quad (3.15)$$

$$S_{nij} = \frac{1}{2\pi} \int_{S_{Bij}} \frac{1}{r_{nij}} dS_{Bij} \quad (3.16)$$

$$W_{nij} = -\frac{1}{2\pi} \int_{S_{Wij}} \frac{\mathbf{n}_{ij} \cdot \mathbf{r}_{ij}}{r_{nij}^3} dS_{Wij} \quad (3.17)$$

Steady FSI discretization

For steady simulations, the assumption is made that the vortex shedding is time-invariant, which was already stated in the kinematic boundary conditions shown in equations 3.7 and 3.8. The dipole strength ($\Delta \phi_{ij}$) is not different for varying i on a strip of j -panels. Then by using the symmetry properties of the key surfaces, the wake sheet dipole coefficient for the complete propeller W_{nj}^* can be written as:

$$W_{nj}^* = \sum_{i=1}^{N_{wj}} W_{nij}^* \quad (3.18)$$

The same symmetry property can be attributed to the body surface and wake surface dipoles resulting in equations 3.19 and 3.20.

$$D_{nij}^* = D_{nij} + \sum_{isym=2}^{N_{syms}} D_{nij} \quad (3.19)$$

$$S_{nij}^* = S_{nij} + \sum_{isym=2}^{N_{syms}} S_{nij} \quad (3.20)$$

With these simplifications, equation 3.14 can be rewritten to 3.21.

$$\sum_{isurf=1}^{N_{surfs}} \left[\sum_{j=1}^{N_j} \sum_{i=1}^{N_i} D_{nij}^* \phi_{ij} + \sum_{j=1}^{N_{wj}} W_{nij}^* \Delta \phi_j \right] = \sum_{isurf=1}^{N_{surfs}} S_{nij}^* \sigma_{nij}, n = 1, \dots, N_{total} \quad (3.21)$$

To close (ensuring an equal number of equations as unknowns) the Kutta-condition can be discretized to say that the potential of the upper and lower side on the trailing edge equal the wake dipole strength for every strip of j on the propeller. Thus a total of N_{wj} equations in the form of equation 3.22 are added to the system:

$$\Delta \phi_j = \phi_{N_i j} - \phi_{1j} \quad (3.22)$$

This can be written in matrix form as equation 3.23, where the influence coefficient matrices \mathbf{D}^* , \mathbf{W}^* and \mathbf{S}^* are shown, and the matrices \mathbf{I}_u , \mathbf{I}_l and \mathbf{I} only contain ones and zeros to provide the Kutta-condition:

$$\begin{bmatrix} \mathbf{D}^* & \mathbf{W}^* \\ -\mathbf{I}_u + \mathbf{I}_l & \mathbf{I} \end{bmatrix} \begin{bmatrix} \phi \\ \Delta \phi \end{bmatrix} = \begin{bmatrix} \mathbf{S}^* & \mathbf{0} \\ \mathbf{0} & \mathbf{0} \end{bmatrix} \begin{bmatrix} \sigma \\ 0 \end{bmatrix} \quad (3.23)$$

The Coefficients in equation 3.23 can be expressed as one matrix known as the total dipole influence coefficients matrix $[\mathbf{B}^*]$. This is shown in equation 3.24. Now the complete system can be expressed in one formulation as shown in equation 3.25.

$$[\mathbf{B}^*] = [\mathbf{D}^*] + [\mathbf{W}^*] [\mathbf{I}_u - \mathbf{I}_l] \quad (3.24)$$

$$[\mathbf{B}^*] \{\phi\} = [\mathbf{S}^*] \{\sigma\} \quad (3.25)$$

Unsteady FSI Discretization

To extrapolate the discretization of the steady FSI analysis to a formulation that simulates unsteady flow occurrences, the time dependency of all influence coefficients has to follow the formulation as was derived in the unsteady Morino formulation in equation 3.13.

PROCAL executes a number of k time steps, which is the number of time steps during one revolution (blade positions) N_t times the number of time steps necessary for convergence for one revolution N_{revs} . The discretized equation is shown in equation 3.26.

$$\begin{aligned} \sum_{isurf=1}^{N_{surfs}} \left[\sum_{j=1}^{N_j} \sum_{i=1}^{N_i} D_{nij}^k \phi_{ij}^k + \sum_{j=1}^{N_{wj}} W_{n1j}^k \Delta \phi_{1j}^k \right] &= \sum_{isurf=1}^{N_{surfs}} \left[\sum_{j=1}^{N_j} \sum_{i=1}^{N_i} S_{nij}^k \sigma_{ij}^k + \sum_{j=1}^{N_{wj}} \sum_{i=2}^{N_{wi}} W_{nij}^k \Delta \phi_{ij}^k \right] \\ - \sum_{isurf=1}^{N_{surfs}} \sum_{isym=2}^{N_{syms}} \left[\sum_{j=1}^{N_j} \sum_{i=1}^{N_i} D_{nij}^{k isym} \phi_{ij}^{k isym} + \sum_{j=1}^{N_j} \sum_{i=1}^{N_i} S_{nij}^{k isym} \sigma_{ij}^{k isym} - \sum_{j=1}^{N_{wj}} \sum_{i=1}^{N_{wi}} W_{nij}^{k isym} \Delta \phi_{ij}^{k isym} \right] & \quad (3.26) \\ n = 1, \dots, N_{total} \quad \& \quad k = 1, \dots, N_{revs} N_t \end{aligned}$$

3.2.4 Fluid added mass and Hydrodynamic damping

The last step is to obtain closed-form expressions for the added mass and damping matrices which can be used in the structural calculations. The complete disturbance potential Φ can be decomposed into two parts; φ due to vibration velocities of a blade in a non-uniform wake and ϕ for the disturbance of a flexible marine propeller (with all the time-dependencies as discussed in this section).

$$\Phi = \phi + \varphi \quad (3.27)$$

With the use of the method described in this section, the pressure p_ϕ is obtained by solving the potential ϕ and calculating equation 3.28. The non-uniform vibration pressure contribution (φ) is calculated with equation 3.29.

$$p_\phi = -\rho \left(\frac{\partial \phi}{\partial t} + \mathbf{v}_0 \cdot \nabla \phi + \frac{1}{2} |\nabla \phi|^2 \right) \quad (3.28)$$

$$p_\varphi = \rho \left(-\frac{\partial \varphi}{\partial t} - \mathbf{v}_0 \cdot \nabla \varphi \right) \quad (3.29)$$

Similar to equations 3.24 and 3.25, for a flexible blade the potential can be obtained and discretized as in equation 3.30. Here the top equation is used with a constant vortex wake sheet and the bottom one for panels without vortex wake sheets.

$$\{\varphi\} = \begin{cases} [\mathbf{B}^*]^{-1} [\mathbf{S}^*] \left\{ \frac{\partial \varphi}{\partial n} \right\} \\ [\mathbf{D}^*]^{-1} [\mathbf{S}^*] \left\{ \frac{\partial \varphi}{\partial n} \right\} \end{cases} \quad (3.30)$$

A kinematic boundary condition has to be imposed which states that the flow on the deforming blade should have the same vibration velocity as the blade itself, with \mathbf{n} the undeformed blade geometry:

$$\frac{\partial \varphi}{\partial n} = \frac{\partial \delta}{\partial t} \cdot \mathbf{n}(\mathbf{x}) \quad (3.31)$$

Now, with some manipulation which is explained in detail in the works of Vaz and Maljaars ([37], [35]), the hydrodynamic damping matrix \mathbf{C}_h is written as in equation 3.32. In which \mathbf{N} is the transformation matrix that relates the 3D potential velocities to the normal velocity at the surface. \mathbf{T} is the transformation matrix that relates the normal velocities at the nodes to the normal velocity at the collocation points, $\overline{\mathbf{V}}_0$ is the inflow velocity matrix which has been averaged over a revolution and ∇ the gradient operator. Note that to arrive at the damping matrix for a constant vortex wake sheet, $[\mathbf{B}^*]$ in equation 3.32 is simply replaced with $[\mathbf{D}^*]$.

$$[\mathbf{C}_h] = -\rho [\mathbf{T}]^T [\mathbf{N}]^T [\mathbf{A}] [\overline{\mathbf{V}}_0] [\nabla] [\mathbf{B}^*]^{-1} [\mathbf{S}^*] [\mathbf{T}] [\mathbf{N}] \quad (3.32)$$

A similar kinematic boundary condition for the accelerations can be imposed as was done for the blade velocities, this is shown in equation 3.33. And the final product is the discretized representation of the added mass matrix \mathbf{M}_h as shown in 3.34. Here \mathbf{A} denotes the acceleration matrix. Furthermore does equation 3.34 have the same interchangeability between $[\mathbf{B}^*]$ and $[\mathbf{D}^*]$ to change from a constant vortex wake sheet to a simulation without wake sheets.

$$\left\{ \frac{\partial^2 \varphi}{\partial t \partial n} \right\} = [\mathbf{T}] [\mathbf{N}] \{\ddot{\mathbf{u}}\} \quad (3.33)$$

$$[\mathbf{M}_h] = -\rho [\mathbf{T}]^T [\mathbf{N}]^T [\mathbf{A}] [\mathbf{D}^*]^{-1} [\mathbf{S}^*] [\mathbf{T}] [\mathbf{N}] \quad (3.34)$$

3.2.5 Friction Coefficients

As discussed, the friction between fluid and propeller is not modelled in potential flow methods. Therefore corrections are applied to account for this resistance. These friction coefficients are adopted from the International Towing Tank Conference (ITTC) [38]. Equations 3.35 through 3.37 show these viscous correction factors used in PROCAL. For these equations, the Reynolds number Re should be computed with the chord length of the evaluated panel. It should be noted that these friction coefficients are currently not implemented in the ComPropApp.

$$\text{Laminar} : C_f = \frac{1.328}{\sqrt{Re}} \quad (3.35)$$

$$\text{Turbulent} : C_f = \frac{0.044}{Re^{\frac{1}{6}}} - 5.0 \frac{1}{Re^{\frac{2}{3}}} \quad (3.36)$$

$$\text{Roughness} : C_f = \frac{1}{\left(1.89 + 1.62 \log \left(\frac{\text{chord}}{K_p} \right) \right)^{2.5}} \quad (3.37)$$

With these friction coefficients for the different regimes of flow. And the dynamic pressure coefficient (C_{pn}) computed from the solved potential as shown in equation 3.38, finally the total moment (torque) and force (thrust) can be expressed as equations 3.39 and 3.40:

$$C_{pn} = 1 - \frac{|\mathbf{V}|^2}{(nD)^2} - 2 \frac{\frac{\partial \Phi}{\partial t}}{(nD)^2} - 2 \frac{gz}{(nD)^2} \quad (3.38)$$

$$F = \sum_{i=1}^{N_i} \sum_{j=1}^{N_j} \left[\frac{1}{2} \rho (nD)^2 C_{pn_{ij}} \mathbf{n}_{ij} + \frac{1}{2} \rho C_{f,ij} |\mathbf{v}_{ij}| \mathbf{v}_{ij} \right] A_{ij} \quad (3.39)$$

$$M = \sum_{i=1}^{N_i} \sum_{j=1}^{N_j} \left[\frac{1}{2} \rho (nD)^2 C_{pn_{ij}} (\mathbf{x}_{ij} \times \mathbf{n}_{ij}) + \frac{1}{2} \rho C_{f,ij} |\mathbf{v}_{ij}| (\mathbf{x}_{ij} \times \mathbf{v}_{ij}) \right] A_{ij} \quad (3.40)$$

3.2.6 Cavitation modelling in PROCAL/ComPropApp

Cavitation can be modelled in PROCAL, this was the main goal of the Ph.D thesis by G. Vaz [37]. A summary of these working principles can be found in the MSc thesis by K. van de Sanden, who also researched verification and validation on the ComPropApp (2020) [39]. Van de Sanden showed that through PROCAL a cavitation bucket can be constructed for the c4-40 propeller. These results should however be treated with caution as they are quasi-steady computations. They were obtained through calculations with the undeformed propeller geometry. Whilst in reality the deformation (and thus vibration) of the blade have an influence on the cavitation. So, only preliminary conclusions on cavitation can be made with the ComPropApp and PROCAL. But, it should be obvious that for full conclusive cavitation modelling CFD methods should always be the method of choice over BEM.

3.3 Vast/Trident and Finite element method

Real-life objects are complex and continuous. A computer on the other hand has a finite capacity. To calculate the physics in real-life objects, computer models can be made with finite approximations and assumptions. The Finite Element Method is used to calculate structural stresses and deformations of a model by discretizing the model into a finite number of discrete elements. The question of how accurate the finite element model is in comparison with reality, is affected mainly by the number of elements, types of elements and how the elements are structured (the mesh). This can always be validated by doing experiments.

3.3.1 Finite Element Method in General

The simplest form of a structural finite element analysis is shown in equation 3.41. in which \mathbf{u} denotes the displacement vector of all elements within the system, \mathbf{K} the stiffness matrix and \mathbf{f} the applied load to each of the elements. Here no non-linearities, or time dependant properties as acceleration and velocity are present. It does however give a clear picture of how complex systems can be simplified into elemental easier systems.

$$K \{\mathbf{u}\} = \{\mathbf{f}\} \quad (3.41)$$

The usage of structural FEM in modern software packages is far more complex than simple linear deformations as in equation 3.41. It can for example be used for modal analysis. In which the natural frequency and the deformation shapes of models can be computed through a finite element analysis. The standard equation used for this analysis (which is a three-dimensionalized mass-spring system) is shown in equation 3.42.

$$M \{\ddot{\mathbf{u}}\} + C \{\dot{\mathbf{u}}\} + K \{\mathbf{u}\} = \{\mathbf{f}\} \quad (3.42)$$

This can be solved for the natural frequency of the model which is solved by manipulating equation 3.42 to equation 3.43. Here, the eigenvalues and eigenvectors are the natural frequencies and corresponding mode shapes.

$$(K - \omega^2 M) \{\mathbf{u}\} = 0 \quad (3.43)$$

Now, \hat{u} is the real eigenvector belonging to eigenfrequency ω . When this is a non-trivial solution, it can be considered a mode shape. There can be m different mode shapes for a $n \times m$ matrix. Where the mode shapes belonging to the lowest frequencies are the dominant modes of the structure. The solution is formed in the mode shape matrix Ψ with m system modes as shown in equation 3.44.

$$\Psi = [\{\hat{u}\}_1, \{\hat{u}\}_2, \dots, \{\hat{u}\}_m] \quad (3.44)$$

Now, the displacement of the structure can be written as a function of modal displacements in time ($\{q\}(t)$) as in equation 3.45. Here, $\{q\}$ are the modal participation factors, which quantify the interaction between modes and the size of the structural response.

$$\{\mathbf{u}\}(t) = \{\hat{\mathbf{u}}\}_1 q_1(t) + \{\hat{\mathbf{u}}\}_2 q_2(t) + \dots + \{\hat{\mathbf{u}}\}_m q_m(t) = \Psi \{q\}(t) \quad (3.45)$$

Equations 3.42 and 3.45 can be combined with a few manipulations to convert mass matrix \mathbf{M} into a unit matrix \mathbf{I} . Ignoring damping yields that stiffness matrix \mathbf{K} becomes Ω . Rewriting the damping matrix C to a modal damping matrix Z , the decoupled matrix with modal participation factors $\{q\}$ becomes as in equation 3.46.

$$I\{\ddot{\mathbf{q}}\}(t) + Z\{\dot{\mathbf{q}}\}(t) + \Omega\{\mathbf{q}\}(t) = \Psi^T \{\mathbf{f}\}(t) \quad (3.46)$$

Now, time-integration can be applied for a given load $\{\mathbf{f}\}(t)$ which yields a deformation vector $\{\mathbf{u}\}(t)$. By using a Fourier-Transform this can be solved in the frequency domain what is used in the ComPropApp in the unsteady FSI analysis.

3.3.2 FEM in Vast/Trident

In the ComPropApp the finite element method applied is the software package *TRIDENT/VAST*. The theoretical background is given in the ComPropApp manual [40]. Within this FEM software, a version was developed especially for the structural evaluation of marine propellers. For proper results, a couple of linearization requirements have been applied:

- the material behaves in a linear elastic way such that Hooke's law is applied, which is a reasonable assumption for propellers since the propeller's operational domain won't reach plastic behaviour.
- Loads from previous time-steps are applied to the *undeformed structure*, thus some small changes in the directions of loads are occurring. However, since the applied loads are pressures, these directions will always be equal to the normal vector of the propeller surface.

In Trident equation 3.42 is transformed to equation 3.47 to account for the correct loads encountered by a marine propeller. $\{f_h\}(t)$ is the hydrodynamic load which consists of fluid added mass, damping, stiffness and blade deformation effects (obtained loads from the PROCAL analysis). The fictitious forces are added to account for centrifugal forces $\{f_c\}(t)$, and Coriolis forces $\{f_{Coriolis}\}(t)$ which are caused by the orbital motion of a propeller.

$$M\{\ddot{\mathbf{u}}\}(t) + C\{\dot{\mathbf{u}}\}(t) + K\{\mathbf{u}\}(t) = \{\mathbf{f}_h\} + \{\mathbf{f}_{fictitious}\}(t) \quad (3.47)$$

The contribution of the Coriolis force to the damping is considered negligible compared to the hydrodynamic damping. The centrifugal force does need to be incorporated. This force on a point mass m , at location x , is given by equation 3.48.

$$\{\mathbf{f}_c\}(t) = -m(\boldsymbol{\theta} \times (\boldsymbol{\theta} \times x(t))) = m(2\pi n)^2 \mathbf{r}(t) \quad (3.48)$$

Combining equations 3.46 and 3.47 now yields equation 3.49. This gives the dry mode shapes matrix off the propeller. This dry formulation does not take fluid added mass, hydrodynamic damping and fluid stiffness into account.

$$I\{\ddot{\mathbf{q}}\}(t) + Z\{\dot{\mathbf{q}}\}(t) + \Omega\{\mathbf{q}\}(t) = \Psi^T \{\mathbf{f}_h + \mathbf{f}_c\}(t) \quad (3.49)$$

3.3.3 Conversion to frequency domain

Since the solution of the simulation is assumed to be periodic, which makes sense as the propeller blade revolves with a constant rotational speed in the wake field. The computation can be performed in the frequency domain rather than the time domain which saves significant computational time, because convergence to steady-state will be reached faster because each blade position within a revolution can be considered separately, instead of a solution of the previous blade position.

Since each blade position is considered separately, the force term can be chosen at the same blade position in the previous revolution instead of the previous time step. Thus for revolution index k , the equations of motion become as in equation 3.50.

$$I\{\ddot{\mathbf{q}}\}^k + Z\{\dot{\mathbf{q}}\}^k + \tilde{\Omega}\{\mathbf{q}\}^k = \tilde{\Psi}^T \{\mathbf{f}_{total}\}^{k-1} \quad (3.50)$$

When M blade positions per revolution are considered. Then M modal force vectors have to be considered: $\tilde{\Psi} \{\mathbf{f}_0\}, \dots, \tilde{\Psi} \{\mathbf{f}_{M-1}\}$. Which can be converted to Modal force vectors $\{\mathbf{F}_0\}, \dots, \{\mathbf{F}_m\}$ in the frequency domain with the Fourier Transform in equation 3.51:

$$\{\mathbf{F}_m\} = \sum_{l=0}^{M-1} \tilde{\Psi}^T \{\mathbf{f}_l\} \exp(-i2\pi nml\Delta t) \quad (3.51)$$

In which $2\pi n$ is the fundamental blade passing frequency and Δt is the time step. This can be inverse Fourier transformed to a Modal force vector as in equation 3.52. With corresponding modal participation factors q , \dot{q} and \ddot{q} as in equations 3.53 through 3.55:

$$\tilde{\Psi}^T \{\mathbf{f}_l\} = \frac{1}{M} \sum_{m=0}^{M-1} \{\mathbf{F}_m\} \exp(+i2\pi nml\Delta t) \quad (3.52)$$

$$\{q_l\} = \frac{1}{M} \sum_{m=0}^{M-1} \{Q_m\} \exp(+i2\pi nml\Delta t) \quad (3.53)$$

$$\{\dot{q}_l\} = \frac{1}{M} \sum_{m=0}^{M-1} \{i2\pi nm Q_m\} \exp(+i2\pi nml\Delta t) \quad (3.54)$$

$$\{\ddot{q}_l\} = \frac{1}{M} \sum_{m=0}^{M-1} \{-(2\pi nm)^2 Q_m\} \exp(+i2\pi nml\Delta t) \quad (3.55)$$

Equation 3.50 can now be converted to be solved in the frequency domain as well such that the modal participation factors can be solved as in equation 3.56:

$$\{Q_m\}^k = \left(-(2\pi nm)^2 \mathbf{I} + i2\pi nm \tilde{\mathbf{Z}} + \tilde{\mathbf{\Omega}} \right)^{-1} \{\mathbf{F}_m\}^{k-1} \quad (3.56)$$

Now, the time domain solution can be obtained by substituting equation 3.56 into 3.53 through 3.55 to obtain equation 3.57:

$$\{\mathbf{u}\}(t) = \{\tilde{\mathbf{u}}\}_1 q_1(t) + \{\tilde{\mathbf{u}}\}_2 q_2(t) + \dots + \{\tilde{\mathbf{u}}\}_m q_m(t) = \tilde{\Psi} \{q\}(t) \quad (3.57)$$

And finally yield for blade position l at revolution k as shown in equation 3.58:

$$\{\mathbf{u}_l\}^k = \tilde{\Psi} \{q_l\}^k \quad (3.58)$$

3.3.4 Wet mode shapes

If one wants to approach the modes using wet modes. Equation 3.47 is replaced with equation 3.59. In this new form M^a and C^a are the estimated fluid added mass and hydrodynamic damping matrices. Now the wet frequencies ($\tilde{\omega}$) can be derived with the corresponding normalized wet eigenvectors ($\Theta = [\{\tilde{u}_1\}, \{\tilde{u}_2\} \dots \{\tilde{u}_m\}]$) with equation 3.60:

$$(M + M^a) \{\ddot{\mathbf{u}}\}(t) + (C + C^a) \{\dot{\mathbf{u}}\}(t) + K \{\mathbf{u}\}(t) = \{\mathbf{f}_h\}(t) + \{\mathbf{f}_c\}(t) + M^a \{\ddot{\mathbf{u}}\}(t) + C^a \{\dot{\mathbf{u}}\}(t) \quad (3.59)$$

$$(\Omega - \tilde{\omega}^2(I + M^a)) \{\tilde{u}\} = \{0\} \quad (3.60)$$

To obtain the wet mode shape matrix $\tilde{\Phi}$, the eigenvectors are multiplied with the dry mode shape matrix Φ . Now, the same approach as for the dry mode shapes can be executed to obtain the wet results. This is currently not possible in the ComPropApp, but is scheduled to be implemented in the future

$$\tilde{\Phi} = \Theta \Phi \quad (3.61)$$

3.4 FSI and CompropApp

The ComPropApp is the tool combining the BEM (PROCAL) and FEM (Vast/Trident) code to execute the partitioned FSI analysis. The Application mainly controls the separate executables, controls the in- and output of data and ensures the numerical convergence of the coupling procedure. The ComPropApp can execute four types of analyse. They will be discussed separately:

- Steady FSI analysis
- Modal Analysis
- Unsteady FSI Analysis
- Stress Analysis

3.4.1 Steady FSI analysis

In the Steady FSI Analysis, the blade is analyzed in the time domain. The load on the propeller is applied in steps because instantaneous loading results in diverging FEM results. These load steps are applied by gradually increasing the rotational speed and inflow velocity such that the advance velocity remains the same and a equal pressure distribution is applied over all load steps. PROCAL does this without updating propeller geometry, in TRIDENT, the deformation is applied in load steps as well for each load increment iteration for PROCAL. This both happens within one iteration of ComPropApp. After which the full load is applied, the updated geometry obtained from TRIDENT is running one or more iterations (specified by the user) to ensure convergence at full load. The number of load steps to reach the full load condition can be specified by the user as well, the way these two parameters affect the final result will be part of the validation study.

3.4.2 Modal Analysis

In the Modal Analysis, the ComPropApp simply executes Trident/Vast to estimate the mode shapes of the propeller blade. The number of mode shapes to be considered can be determined by the user. The method is as described in section 3.3. The output consists of the mode shapes and corresponding eigenfrequencies. This computation is necessary for the unsteady FSI- and Stress analyses.

3.4.3 Unsteady FSI Analysis

The difference between a steady and unsteady FSI Analysis is that the propeller is vibrating with its structural mode shapes and eigenfrequencies. Since the blade passes at a constant frequency, the solution is periodic as well, the beneficial part of this is that the solution can be calculated in the frequency domain and not in the time domain, which would take significantly longer to converge due to transient phenomena when starting up the simulation in the time domain. Within the ComPropApp the unsteady analysis is done with a geometrically linear finite element procedure. This results in limitations in the magnitude of the deformations of the blade. But this geometric linearization is necessary to enable conversion in the frequency domain [40]. The modal analysis is performed only once before to the unsteady analysis. During the analysis, modal superposition is applied to calculate the deformed blade position at the next position in time. In reality, the deformation of the blade should lead to different mode shapes and frequencies. These are however assumed to be negligibly small.

Thus the load is first applied at all blade positions within a revolution, then using modal superposition the deformation for all blade positions is obtained. Afterwards, the ComPropApp updates the propeller geometry. Now one blade is analyzed in PROCAL at just one blade position with accompanying blade shape in time. This is done for all blade positions in several revolutions until load convergence is obtained for all blade positions. There will however always be a small difference between the structural and hydrodynamic solutions which do not exactly obey the equations of motion. For flexible blades, this can result in rapidly growing errors and thus diverging results. This is solved in the ComPropApp by coupling iterations between loading and deformation by the use of a Quasi-Newton iterative least method (*QN-ILS*) which is explained in section 3.4.5.

3.4.4 Stress Analysis

The Stress Analysis performs the deformation of the blade separated from the ComPropApp. Therefore an input file containing the hydrodynamic pressure history of simulation is required from the unsteady FSI Analysis. This was mainly built to investigate whether the FEM software and the coupling FSI simulation generated similar deformations of the propeller blade. The Stress analysis is executed with an output file from the Unsteady FSI analysis; a .LIN file. This file contains the blade loading for each blade position of the last and converged revolution of the unsteady FSI analysis.

3.4.5 Coupling Procedure

As was discussed, the ComPropApp consists of a partitioned FSI approach where the two independent solutions (structural and hydrodynamical) have to be coupled between each time step. This coupling causes that some information in next time step t_{i+1} , which is calculated from the information of time step t_i is slightly disobeying the equations of motion. This could lead to ever-growing errors in the solution. Therefore coupling iterations have to be used. The same error occurs in the frequency domain where differences occur between revolution k_{i+1} and k_i .

The QN-ILS approach goes as follows: let f_h be the hydrodynamic load, which is determined with a fluid operator F , and a certain displacement vector u as in equation 3.62. This means that the fluid is deformed by the deformation of the structure. So the fluid equation of motions are solved. And the hydrodynamic fluid-structure interaction is solved.

The updated pressure distribution can now from the structural perspective be applied as a certain structural operator S and the hydrodynamic forces f_h . Together, they deform the structure as in equation 3.63:

$$\{f_h\} = F\{u\} \quad (3.62)$$

$$\{u\} = S\{f_h\} \quad (3.63)$$

If in both equations 3.62 and 3.63 the equations of motion are obeyed. Then applying S after F on the displacement $\{u\}$, would exactly yield $\{u\}$. Thus the operators are each other's inverse. This is not exactly true in numerical simulations and some sort of residue is always present. The problem is to minimize or mitigate the problem. This residue is denoted as in equation 3.64 in mathematical notation:

$$R(\{\mathbf{u}\}) = S \circ F(\{\mathbf{u}\}) - \{\mathbf{u}\} = 0 \quad (3.64)$$

The formulation in the frequency domain is denoted with steps k (at revolution position k) this becomes equation 3.65. Where \mathbf{J}^{-1} denotes the inverse Jacobian, which is not known and must be estimated, that is where the QN-ILS method comes in.

$$\{\mathbf{u}\}_{k+1} = \{\mathbf{u}\}_k - \mathbf{J}_k^{-1} R(\{\mathbf{u}\}_k) \quad (3.65)$$

It should be noted that easier coupling methods exist as explained in the manual [40]. But these do not work properly for fluid-structure systems which are *strongly coupled* (big interaction between structure and fluid). This is true for flexible propellers is to some degree. So instead, the QN-ILS method is used in the ComPropApp. This method is shown in equation 3.66:

$$\mathbf{J}_k^{-1} = \mathbf{W}_k R_{k-1} \mathbf{Q}_k^T - \mathbf{I} \quad (3.66)$$

Here, W_k denotes the fluid state, R_{k-1} the residue of the previous time step, Q is an orthogonal matrix to fulfill the QR-decomposition method used and I is a n -degree of freedom identity matrix. It should be noted that in the current ComPropApp version, the residual and relaxation forces are estimated by the complete history of forces, which might be an inefficient method since the first few iterations will be the most fluctuating and prone to errors, so keeping these iterations influencing the more converged last iterations of a simulation might result in a less accurate or longer process. With all separate physical attributes of the ComPropApp explained, and how they are coupled. The complete procedure can be summarized as in figure 3.2.

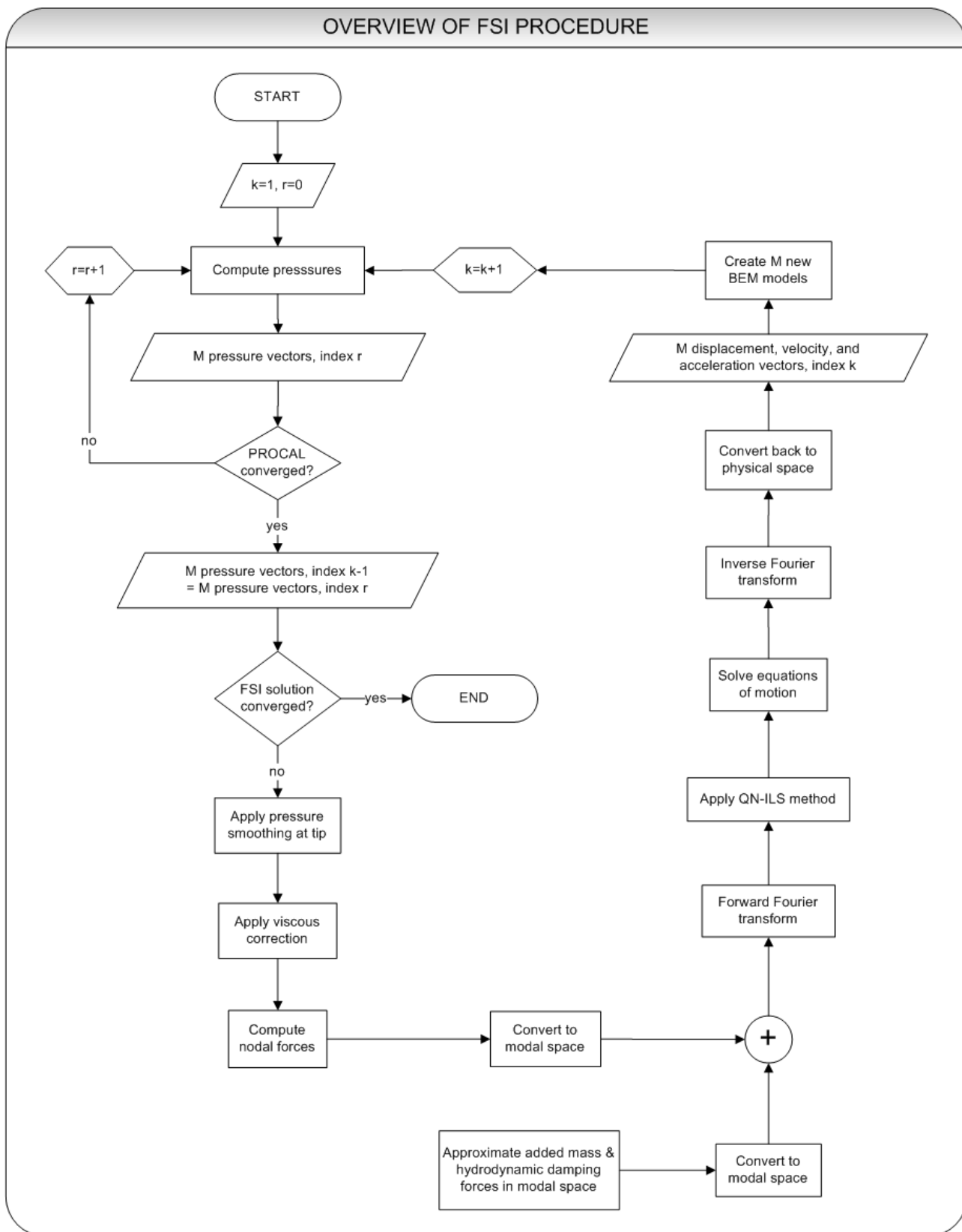


Figure 3.2: Flowchart summarizing the ComPropApp. (source: [40])

4 Grid Study and open water validation study

4.1 Introduction

In this chapter, the working principles of the ComPropApp are validated in open water (meaning no variance of inflow speed over a propeller revolution). This must be done because before possible design studies and conclusions in realistic conditions can be executed, it must be verified that the numerical solution obtained can be adopted with certainty. This will be done with a Wageningen c4-40 propeller, which is shown in figure 4.1. This is the same propeller as was used in the experiments in the COMPROP2 study and has been selected for a couple of reasons:

Firstly, the propeller geometry was known and available to everybody in the CRS working group. Secondly, the propeller has a very applicable geometry which is used by a wide number of ships in the industry. And lastly, the propeller is expected to propel with minimum amounts of vortex generation and flow separation. This is necessary to compare BEM and experimental results as BEM simulations will not capture these complex flow phenomena. The main parameters of the propeller are shown in table 4.1. The flow parameters used in the simulations are shown in table 4.2. Lastly, to calculate deflections, mode shapes and other structural parameters. The material properties are needed. For the validation study, the SikaBlock M980 material properties are used as in table 4.3 which were obtained from data from the manufacturer [41].



Figure 4.1: A wageningen c4-40 propeller with $P/D_{0.7R} = 0.8$, Source: MARIN. [42]

Table 4.1: Main Parameters of the Wageningen c4-40 propeller used in this validation study.

| c4-40 Propeller | symbol | value |
|-------------------------|--------------|--------|
| Number of blades | Z | 4 |
| Diameter [m] | D | 0.34 |
| Hub Diameter [m] | H | 0.0580 |
| Pitch ratio at 0.7R [-] | $P/D_{0.7R}$ | 0.8 |
| Skew [°] | θ_s | 23.6 |

Table 4.2: Flow parameters used in the simulations.

| parameter | symbol | value |
|--|------------|-----------|
| Density [kg/m^3] | ρ_w | 998 |
| Temperature [C] | T | 6.3 |
| Kinematic viscosity [m^2/s] | ν | 1.010E-06 |
| Ambient Pressure [kPa] | p_∞ | 1025 |
| Vapour Pressure [kPa] | p_v | 1.7 |
| Gravitational Constant [m/s^2] | g | 9.81 |

Table 4.3: Material properties SikaBlock M980.

| material Properties M980 | symbol | value |
|------------------------------|--------|-------|
| Young's Modulus [GPa] | E | 4 |
| Density [g/cm ³] | ρ | 1.35 |
| Poisson's Ratio [-] | ν | 0.3 |

The structure of this chapter is as follows. In section 4.2 the influence of the BEM- and FEM grid is analyzed, the influence of the tip cut-off will be discussed through a steady FSI analysis. Later on, in section 4.3, the performance of the ComPropApp, both in steady- and unsteady FSI analyses will be compared with the c4-40 open water diagram found by MARIN (2020) [42]. The convergence criteria of both analyses will be examined as well. In section 4.4, the deformation patterns of the blade will be studied. This all is summarized in section 4.5 with concluding remarks.

4.2 Grid Study

4.2.1 BEM convergence

The first grid study contains the convergence for the BEM grid in PROCAL. This is done for a uniform wake and Steady FSI run with a ship speed $v_s = 4.92$ m/s and a rotation rate of 19.83 rps. The standard setting is 15×30 (450) panels. 15 panels in I -direction (radial) and 30 panels in J -direction (chord), this grid size is increased and decreased and the resulting hydrodynamic characteristics are shown in figure 4.2. As the absolute difference with respect to the previous grid size is plotted (lower difference means more converged), it can be concluded that a 15×30 grid indeed is the best fit. Note that it was chosen to plot the absolute difference instead of the actual values because those differences results in three straight lines, which does not adequately visualizes the convergence. Why the solution seems to diverge at the 700 grid (20×35) is not known, however differences are within 1%, and thus, very small.

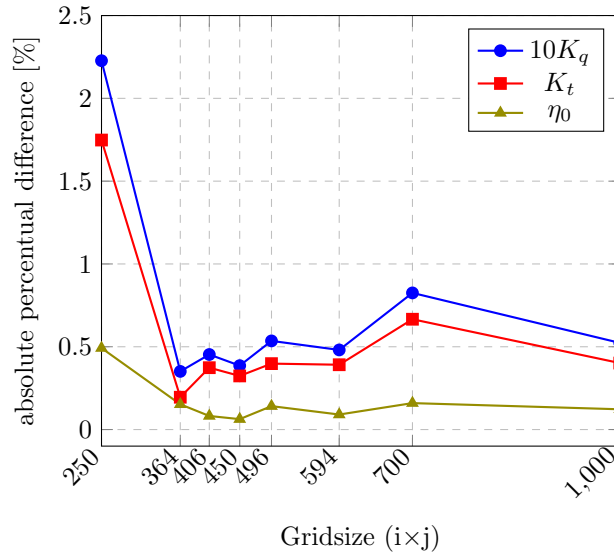


Figure 4.2: Influence of BEM grid on hydrodynamic performance characteristics.

Besides analyzing the hydrodynamic characteristics. The pressure distribution on the blades can be compared for different grids as well. Figure 4.3 shows the suction side pressure distributions for two different grid sizes. It shows that besides refinement no real changes occur by refining the grid. Only a small increase in the minimum pressure coefficient C_p on the blade is noticeable, but this increase is not of significance.

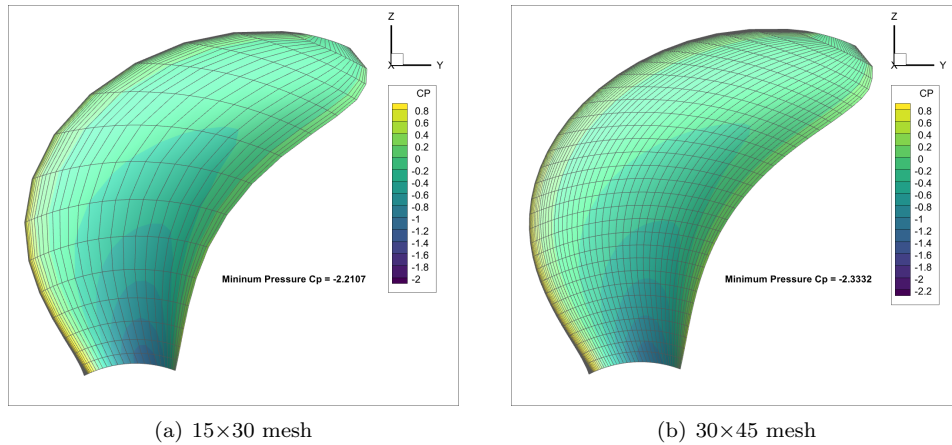


Figure 4.3: Pressure distribution of the suction side for different BEM mesh sizes.

4.2.2 FEM convergence

The second convergence criterion is the FEM convergence. In a similar manner as the BEM convergence study, the grid size of the structural solution is decreased and increased and the changes in the solution are observed. The grid size is increased from 10×10 to 99×99 with the same flow condition of $v_s = 4.92$ m/s and a rotation rate of 19.83 rps. The results are shown in figure 4.4. It shows that very little happens by increasing the grid size, whilst the computational time increases significantly, therefore the FEM grid size adopted hereafter is 50×50 . Besides the hydrodynamic characteristics, it might also be fair to look at the convergence of the tip deflection at an increasing grid size. This is shown in figure 4.5. Some weird increase in the deflection at a 50×50 grid is visible, but this only is a 0.01 mm increase of the tip deflection and is thus not of significance.

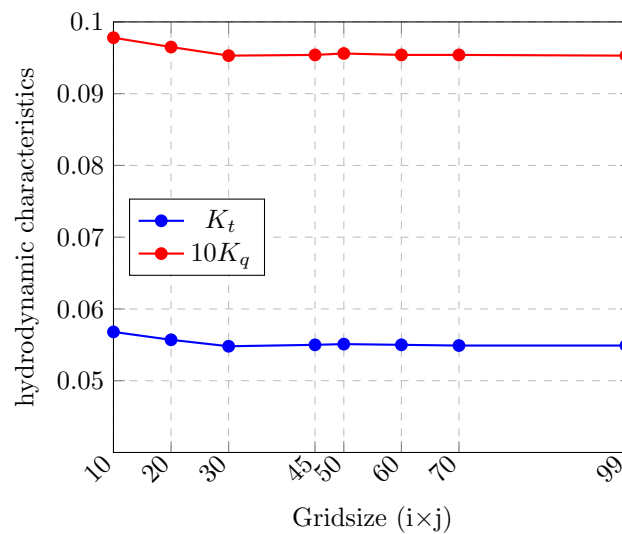


Figure 4.4: Influence of FEM grid on hydrodynamic performance characteristics.

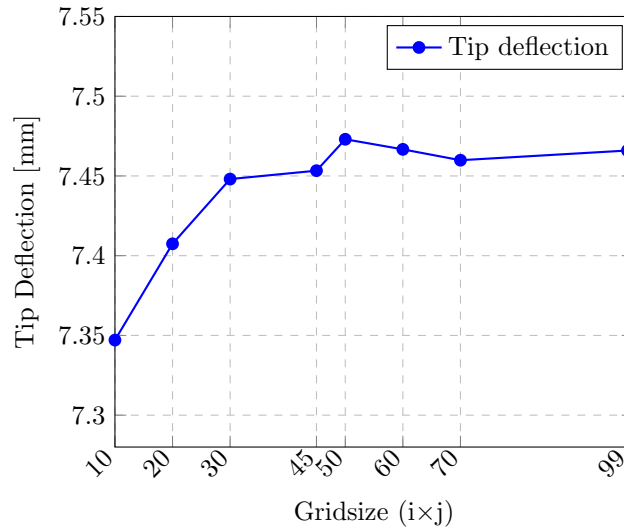


Figure 4.5: Influence of FEM grid on Tip deflection.

4.2.3 Tip Cut-off value

From figure 4.3, especially from the more coarse grid of 15 by 30 panels, it can be seen that the tip of the propeller blade is "Cut-off". This is done because PROCAL does not allow non-zero chord length and thickness at the tip off the propeller. Furthermore are the numerical simulations very unstable at the tip. Therefore, this tip is *cut off*. The standard setting of this tip cut-off value is 0.995 of the non-dimensional length. This means the amount of blade area lost by this method is marginal and is expected to not influence the hydrodynamics characteristics a lot. Figure 4.6 shows the maximum blade deflection for different points of cutting off the blade. It shows that the chosen value of 0.995 is a decent choice as no more significant change in deflection is encountered.

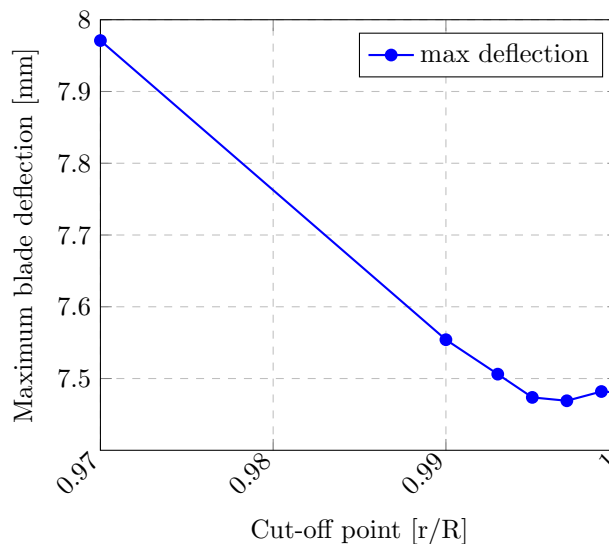


Figure 4.6: Tip deflection for different cut off positions.

With all three convergence parameters studied, from hereon the values as shown in table 4.4 will be applied to future simulations. These should lead to simulations that are independent of the numerical grids.

Table 4.4: Results of executed grid studies.

| Grid | Value |
|--------------------|-------|
| FEM | 50×50 |
| BEM | 15×30 |
| Tip cut-off | 0.995 |

4.3 Open water diagram and convergence

With confidence in the grid established. Now the open water diagram of the c4-40 propeller which is available in the MARIN conference paper (2020) [42], will be studied. First, the convergence parameters of the steady and unsteady FSI are investigated. These convergence parameters determine whether the simulation is converged to a "steady-state" solution. By relaxing this parameter, the solution becomes faster, but also less precise as it allows for fluctuation in the results.

4.3.1 Steady FSI convergence

The steady FSI simulation is driven by two convergence parameters: The number of load steps to reach the full load, and the number of full load iterations. Figure 4.7 shows the results for three different settings. It is clear that no matter what load setting is used, it all converges to the same value. However, the transient behaviour seems to be larger for more increasing load steps. For now, 4 increasing steps and 8 iterating full load steps are adopted in simulations.

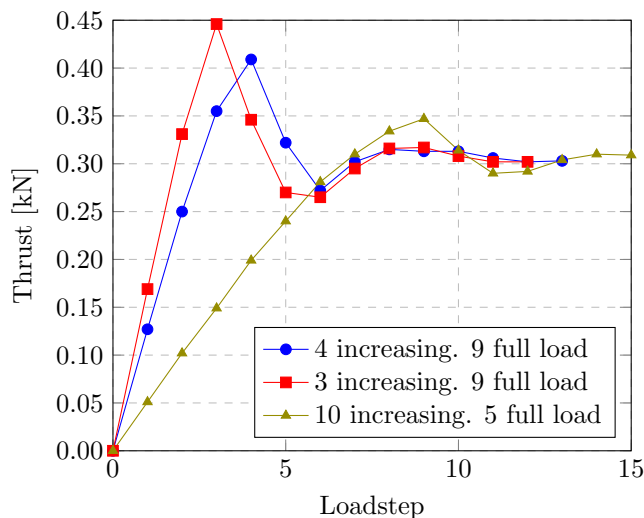


Figure 4.7: Influence of load steps on resulting thrust.

4.3.2 Unsteady FSI convergence

The unsteady FSI simulation is numerically performed by the use of the QN-ILS coupling scheme. This scheme can be controlled by the user with two parameters: Relaxation, the percentage of how much of the forces of the old iterations are used in the new iteration to start up the simulation in the first two iterations. Without this, simulations would diverge quite rapidly as instant complete loading would overload the propeller and divergence issues arise. And secondly, the Tolerance, this quantifies how much convergence should be reached in the simulation. This is known as the Convergence criterion C_c . The ComPropApp logs this data in a separate file. In this file, the convergence criterion for each mode in each iteration is logged. The standard settings are relaxation of 10 %, and tolerance of 1%. The convergence criterion is shown in equation 4.1. F_{res} is the difference (residue) in modal forces between two time steps and F_{rel} is the applied force in the current time step. The convergence criterion is then computed by taking the norm (length) of all modes in all blade positions considered. (For instance, 5 modes are used and the simulation contains 20 blade positions, C_c will compute the length of an error vector of 100 dimensions).

This raises the question of whether this convergence criterion is sufficient. Within a vector of 100 dimensions, one relatively large error on a single blade position could potentially not affect the overall error a lot. This could cause weird instabilities in the supposedly steady solution. It might be better to calculate the norm separately for each blade position considered, which would mean that within a revolution every blade angle is confirmed to be converged. This will probably lead to longer simulation times. As this project will not go into depth in this parameter, it will be deemed out of scope for now whether this convergence criterion could potentially be improved.

$$C_C = \frac{\text{norm}(f_{res})}{\text{norm}(F_{rel})} \quad (4.1)$$

For now, in simple open water cases, The standard values seemed to be decent, as 1 % tolerance is very accurate and lies within the range of the established accuracy of the chosen grid in the simulations. So from

hereon these values will be adopted. 1 % could even be increased to speed up certain comparison studies but this will be explained when those cases arise.

4.3.3 Open water diagram

Now the steady and unsteady FSI analyses will be compared to the open water diagram of the c4-40 propeller. Note that in the article, the shaft speed is 900 rpm, which is 15 revolutions per second. This will be maintained in this section as well (the default setting is 19.83 revolutions per second). Those lower rotational speeds mean slightly different ship speeds to ensure the blade loading in the ComPropApp will resemble the experimental the most. This results in ship speeds as shown in table 4.5

Table 4.5: Investigated advance ratio (J) range for the open water diagram at 900 rpm.

| J [-] | 0 | 0.1 | 0.3 | 0.5 | 0.6 | 0.65 | 0.7 | 0.75 | 0.8 | 0.85 |
|-------------|---|------|------|------|------|-------|-------|-------|------|-------|
| v_a [m/s] | 0 | 0.51 | 1.53 | 2.55 | 3.06 | 3.315 | 3.570 | 3.825 | 4.08 | 4.335 |

Comparison OWD and PROCAL

First will the open water diagram be compared to the steady simulation through PROCAL only, so the blade will be assumed rigid and no fluid-structure interaction is present. This is shown in figure 4.8 and shows that PROCAL accurately predicts the performance of the propeller in the mid-range of advance ratios (from 0.3 to 0.6), beyond these values the numerical prediction is getting worse rapidly. This can for the lower advance ratios be explained by the large flow separation due to high thrust which is not modelled by BEM solvers. And for the high values of J , the viscous forces are not estimated correctly by the friction coefficients as was discussed previously.

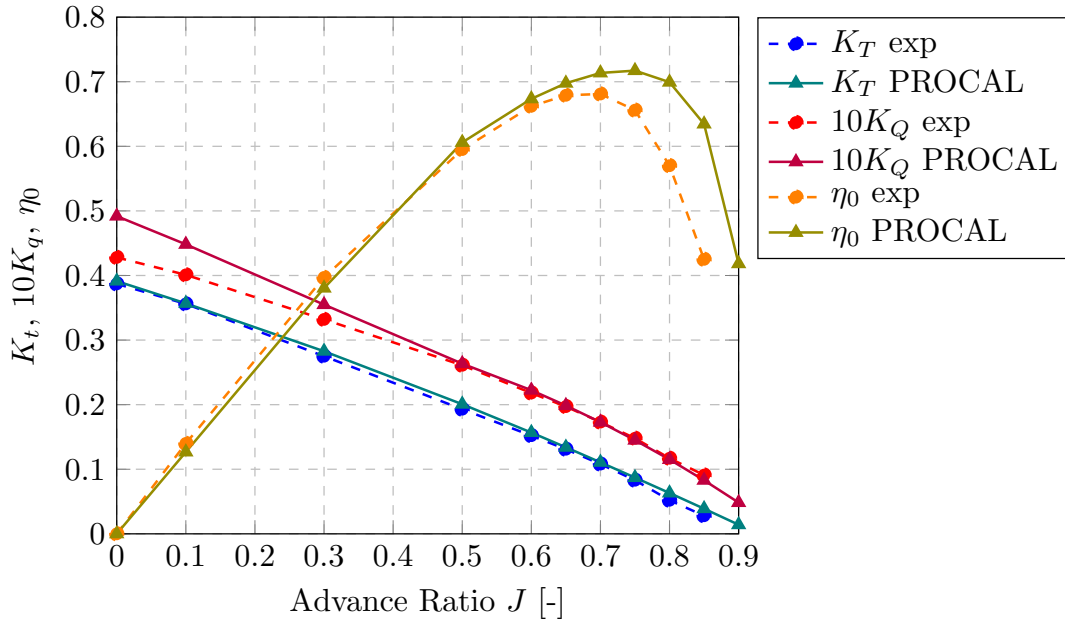


Figure 4.8: Open water diagram of c4-40 propeller ($P/D_{0.7R} = 0.8$) obtained through experiment and BEM simulation.

Comparison experiment and bronze propeller

The PROCAL code is well capable of simulating rigid propeller performance. The next step of validation consists of checking whether the ComPropApp can predict the performance as well. Even though this study will mainly focus on flexible marine propellers with significant deflection, it is also capable of simulating the performance of more rigid propellers. Figure 4.9 shows a comparison between the experimental OWD and a ComPropApp simulation of a bronze propeller with material properties as shown in table 4.6. It shows as expected, agreeing results up to an advance ratio of 0.6. Beyond that value, the viscous forces are becoming dominant and the model is unable to predict the performance accurately.

Table 4.6: material properties of a bronze propeller.

| Material Properties Bronze | value |
|------------------------------|-------|
| Young's Modulus [GPa] | 70 |
| Density [g/cm ³] | 8.73 |
| Poisson Ratio [-] | 0.34 |

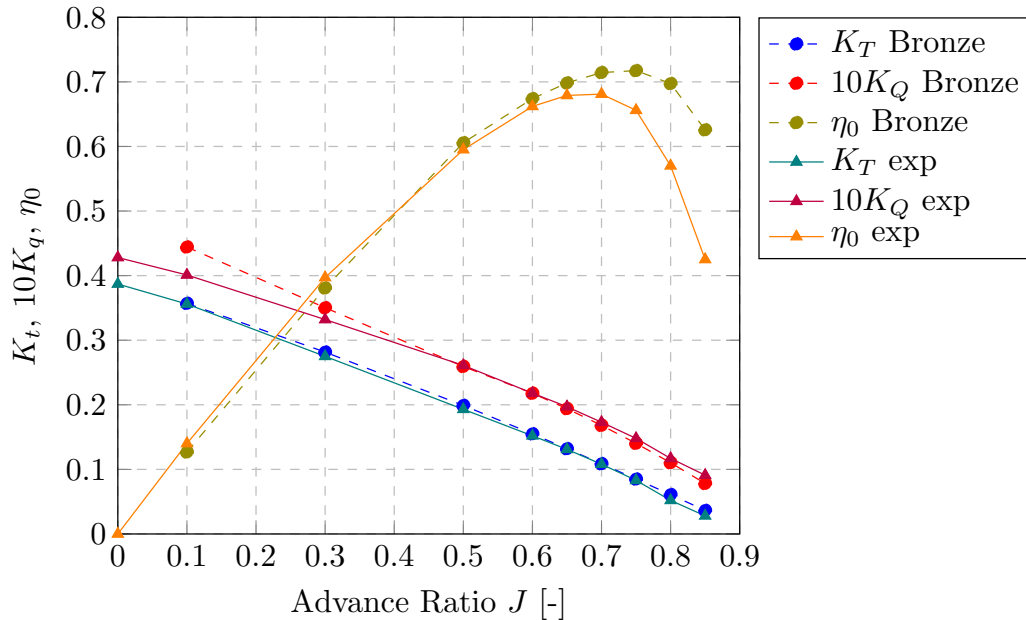


Figure 4.9: Open water diagram c4-40 propeller obtained through experiment and ComPropApp steady FSI simulation for a bronze propeller.

Comparison steady and unsteady FSI results

Up until now, the design advance ratio of $J = 0.73$ was used. Examining figure 4.8 however, shows that this value is too high. This theoretical efficiency optimum at $J = 0.73$ is too high for realistic simulations. As the viscosity errors are becoming larger, no meaningful conclusion can be made here since a flexible propeller will not operate at this design point. Figure 4.10 shows the results for both steady and unsteady simulation. It is visible that up until $J = 0.55$ are in good agreement, and from there the simulations start to deviate a little bit.

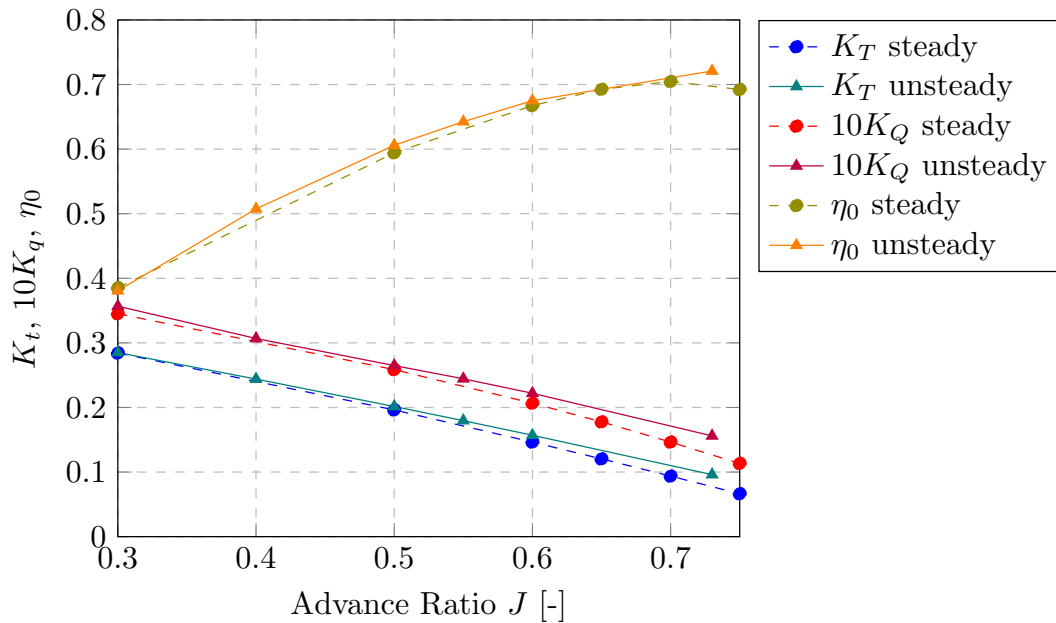


Figure 4.10: Comparison steady versus unsteady FSI hydrodynamic performance.

All three open water diagrams shown in this section gave confidence in using the ComPropApp as a tool to predict the hydrodynamic performance of propellers for medium advance ratios. For now, to ensure comparable and valid data, all simulations hereon after are done with an advance ratio of $J = 0.55$ and a rotation rate of 15 rps. This seems to be the highest advance ratio for which experiment and simulation are in agreement.

4.4 Blade Deformation

With the obtained confidence in the hydrodynamic performance. The next, and most important part concerning the design and application of flexible propellers, is the deformation of the propeller. In this section, the deflection of the blade and the twist angle in a uniform wake field are examined. This twist angle is one of the most important parameters regarding composite propellers. If this parameter can be controlled adequately, one can de-pitch (and consequently unload) the propeller to the desired condition.

First, the blade deformation on mid-chord is plotted for steady and unsteady simulation. This is shown in figure 4.11. It shows that the results are similar for steady and unsteady analysis with a slight (but negligible) larger estimation of deformation through the unsteady-FSI analysis. The same can be done for the twist angle over the blade length, this is shown in figure 4.12. This also shows slightly higher pitch deformation for the unsteady FSI analysis.

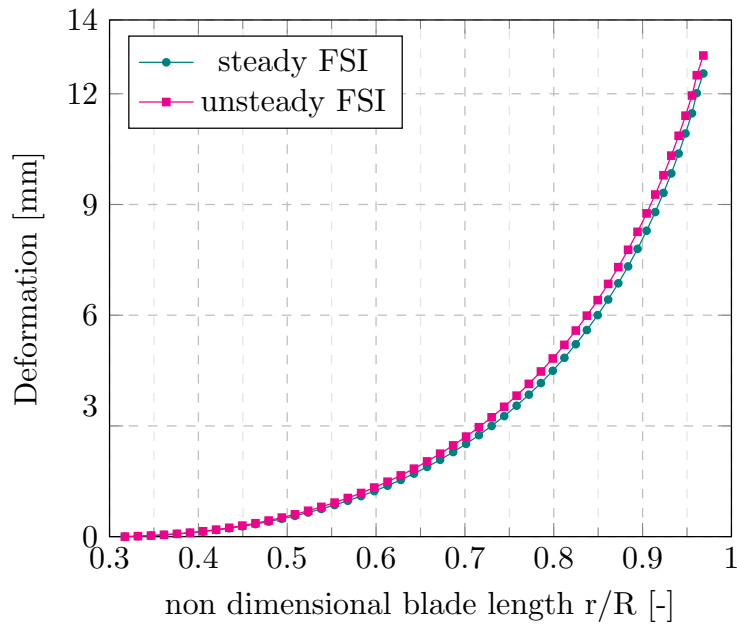


Figure 4.11: Blade deformation comparison steady- and unsteady FSI, $J = 0.55$.

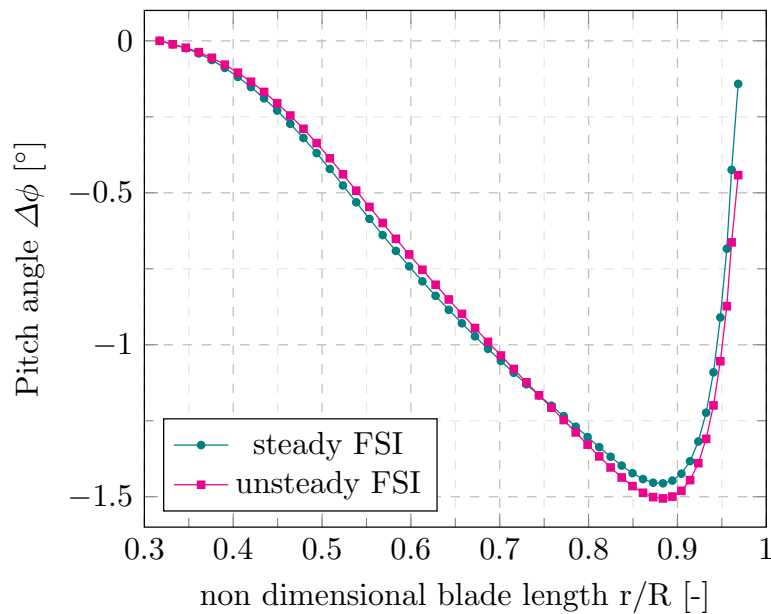


Figure 4.12: Pitch angle deformation comparison steady- and unsteady FSI, $J = 0.55$.

Unfortunately, no experimental data on the blade deformation in open water is present so whether they are both simulated correctly or both simulated wrong can not be stated at this point. What can be executed is a comparison between the deformation patterns for different advance ratios, this is done in figures 4.13 and 4.14. It shows expected larger deformations for lower advance ratios (higher thrust) and somewhat larger pitch deformation as result. The pitch deformations for different advance ratios do indicate the complexity of de-pitching a propeller blade to the desired setting.

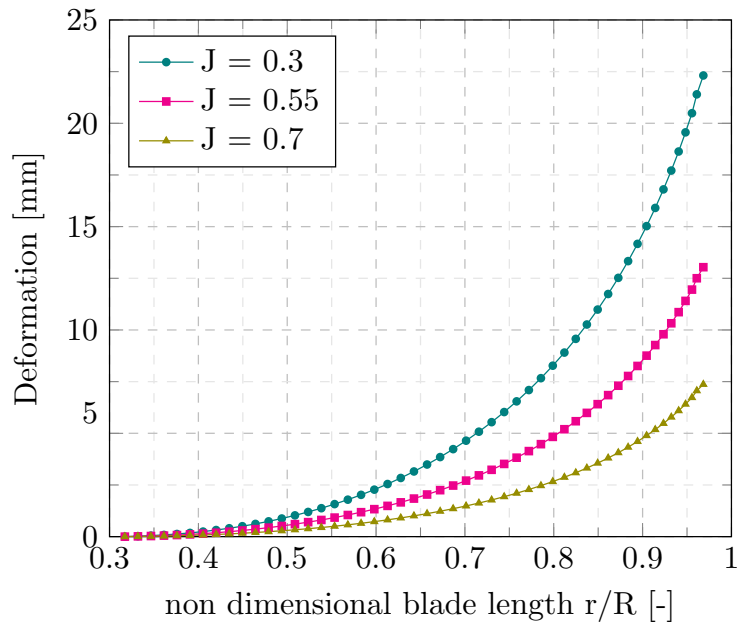


Figure 4.13: Blade deformation comparison for different advance ratios.

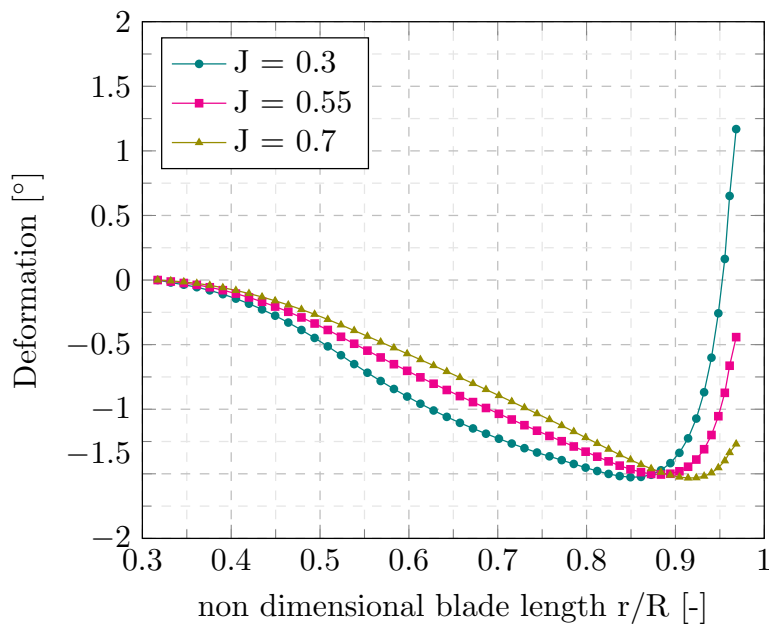


Figure 4.14: Pitch angle deformation comparison for different advance ratios.

4.5 Conclusions

In this chapter first, the numerical grids were investigated and a proper selection of these grids has been established. Afterward, with an open water diagram the working principles of PROCAL have been validated, afterward, the hydrodynamic performance estimation of the ComPropApp, for both the steady and unsteady FSI methods was validated to be working correctly for the mid-range of advance ratios. And lastly, the deformation of the blade in open water was analyzed for both methods and several advance ratios. this complete set of simulations gives the confidence that the tool is well capable of predicting the propeller performance in open water.

In the next chapter, the ComPropApp will be subjected to non-uniform wake fields which a propeller experiences behind a ship. This will first be tested on a fictitious simple varying wake field as a stepping stone towards the validation of the experiments conducted at MARIN as part of the COMPROP2 experiments.

5 Non-uniform wake field validation

In the previous chapter, the hydrodynamic performance and deformation of the steady- and unsteady FSI simulations were found to be comparable for a uniform wake field. The true power of the unsteady FSI tool is to predict the performance of propellers in a realistic non-uniform wake field encountered when a propeller is operating behind a ship.

As a stepping stone towards the final goal of validating the conducted experiments within the COMPROP2 working group, in this chapter the unsteady FSI module is tested with a fictitious, simple sinusoidal wakefield. As shown in figure 5.1:

In section 5.1 the simulations of the ComPropApp are shown with serious bugs, afterwards, in section 5.2 the method to pinpoint the error is discussed and thereafter, in section 5.3, the simulations are discussed after the code was altered is analyzed.

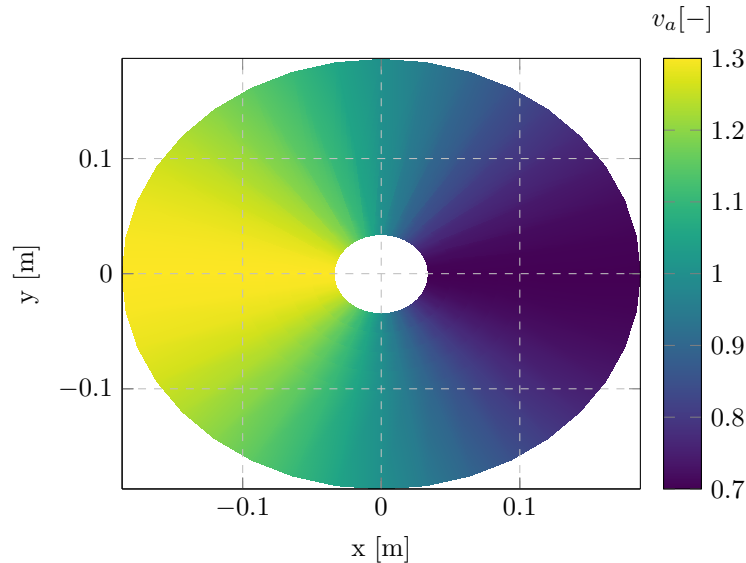


Figure 5.1: Sinusoidal wake field.

5.1 ComPropApp before modifications

The main difference in computations between the steady and unsteady FSI, is that in the unsteady analysis the solution is obtained through modal analysis. This means that the time domain is converted to the frequency domain with the Fourier Transform. This can be done since the non-uniform wakefield can be considered as a periodically forced vibration component. When using a uniform wake field, the unsteady FSI reduces to a quasi-static computation, as no differences exist between different blade positions. When a non-uniform wake field is applied (as the sinusoidal wake field in figure 5.1, there are differences in loading, pressure and deformation between different blade angles.

Within the ComPropApp, two methods exist to analyze the deformation of the blade in a non-uniform wake:

- **Unsteady FSI:** the last (presumably converged) iteration of the unsteady analysis is written as a file which contains data as deformation, velocities and pressures. This is present for every node on every considered blade position.
- **Stress Analysis:** From this last iteration, a .LIN file is written which communicates with the FEM module. This .LIN file consists of the pressure distribution over the blade throughout the last revolution of the unsteady FSI. This is then used to simulate the blade deformation for a user-defined number of revolutions, where this pressure distribution is then considered periodic.

In theory, those two methods should describe the same blade deformation pattern over a revolution. Figure 5.2 shows the results for a simulation with an advance ratio of $J = 0.55$:

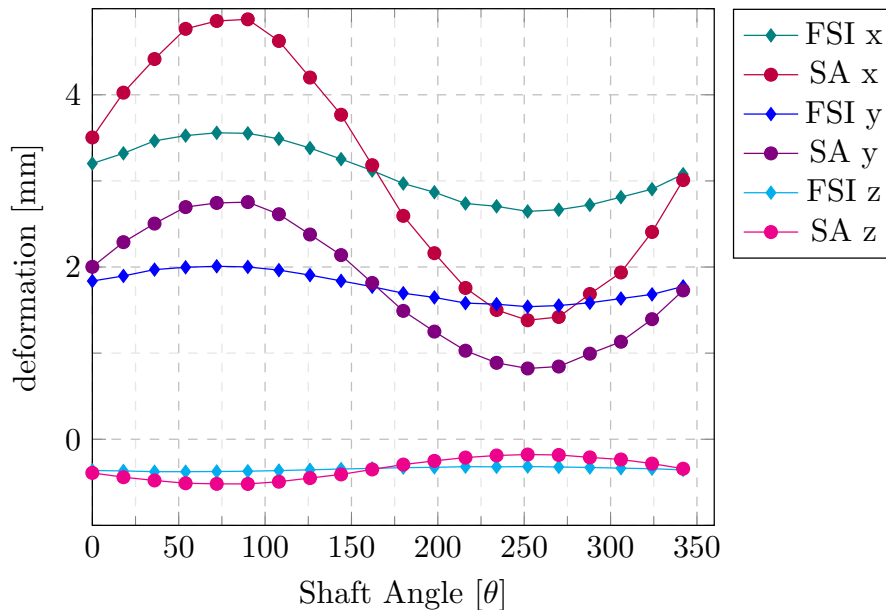


Figure 5.2: Deformation of a blade at 0.7R mid-chord in a sinusoidal wake field. $J = 0.55$, $n = 900$ rpm, $v_a = 2.805$ m/s and $\zeta = 0.1$.

Immediately the amplitude difference of the deformations between the two methods is visible. The Stress analysis results are much larger compared to the unsteady FSI. The following conclusions can be drawn from figure 5.2:

- There is a large difference in the amplitude of the deformations between both methods, for which it is inconclusive to state which resembles reality the best at this point. All three deformation components show a scaling error of approximately 1.375. This hints toward the fact that a scaling error is made somewhere in the code. Especially when considering that the stress analysis is generated from pressure information from the last revolution of the Unsteady FSI solution.
- The average blade deformation is equal for both analyses. This in turn corresponds with the conclusion that the open water deformation for a blade was equal for both the Steady FSI and Unsteady FSI results described in the previous chapter.
- No phase angle difference is present between the two methods.

The question that arises now is: "Which of the two methods predicts the blade deformation correct, or are they both wrong?" Unfortunately, since it contains a fictitious wakefield it can not be validated with experimental data, as it does simply not exist. Therefore, the method chosen to investigate the problem is by performing systematic series of simulations by altering parameters. Changing these important parameters might give insight into where the bug is present.

5.2 Systematic testing of the ComPropApp

Since the unsteady analysis and the stress analysis are both relying on modal analysis it is most likely that the error is somewhere in this code. Therefore systematic modifications to parameters influencing this process will be done to see how both methods respond to those modifications. First, a small recap on the Fourier transform theory is made to ensure it is known which response to the modifications is expected to occur. This topic is written about extensively in Rao (2011)[43].

As the Fourier transform approaches the propeller deformations from a frequency point of view instead of a standard time point of view, it is wise to approach the theory from this same point. In general, the transmissionability (how much deformation is made as a function of the frequency of the system) is expressed as in equation 5.1. This is known as the frequency response function.

$$\frac{1}{\mathbf{F}_m} = \frac{1}{\sqrt{(1 - \frac{\omega_h^2}{\omega_n^2})^2 + (2\zeta \frac{\omega_h}{\omega_n})^2}} \quad (5.1)$$

In which \mathbf{F}_m is the modal force for mode m , if a one degree of freedom system is considered (displacement in only one direction) and one mode is considered. The response function which describes the displacement is dependent on:

- the frequency ratio: ω_h/ω_n , which in this simplified sinusoidal wake is the rotation rate divided by the first natural frequency (which is 184.7 Hz with the material properties as described in table 4.3). Thus: $\omega_h/\omega_n = (15 \text{ rps} / 184.7 \text{ Hz} = 0.081)$.
- the material damping ratio ζ , which is a parameter that influences the damping of the system. In terms of the basic equations of motions, ζ is prescribed as in equation 5.2.

$$\zeta = \frac{c}{2\sqrt{mk}} \quad (5.2)$$

Now, the complete response function can be plotted as a function of the frequency ratio for several damping ratios. this is done in figure 5.3. From this figure, three distinct regions can be defined:

- Stiffness Controlled region: $\omega/\omega_n \ll 1$: Only displacement without frequency is shown in this domain. The transfer function equals one, so no resonance effects are present here. (should be the region of operation for marine propellers as the frequency ratio is only 0.081)
- Damping controlled region: $\omega/\omega_n \cong 1$: The resonance frequency is excited and a much larger transmission of displacement is present. The lower the damping ratio ζ , the higher the resonance.
- Mass controlled region: $\omega/\omega_n \gg 1$: Well above the resonance frequency lower responses are present compared to the static response.

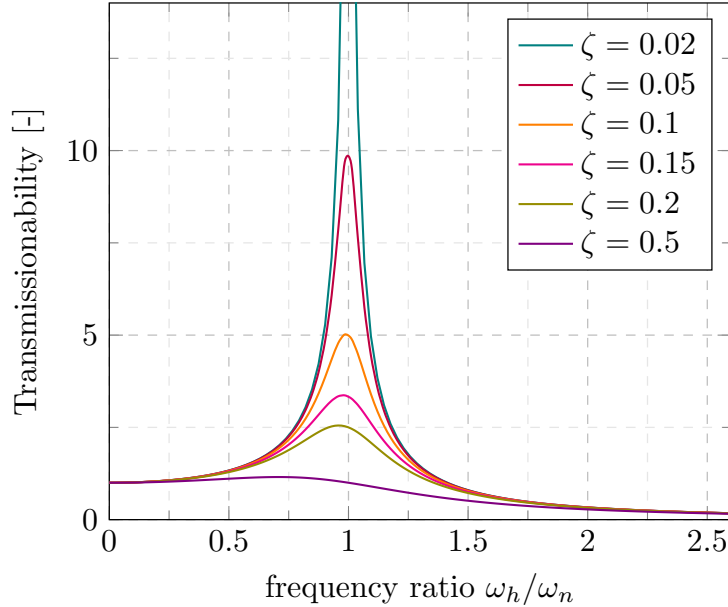


Figure 5.3: Influence of the damping ratio ζ on the transmissionability of the system. ($\omega_n = 184.7 \text{ Hz}$)

Another important feature of modal analysis is the existence of a phase angle ϕ (a difference in time when the peak amplitude is reached). This phase angle is computed as in equation 5.1. And visually represented as in figure 5.4. From this figure can be seen that a larger phase lag is the result of a higher damping ratio (even at low frequency ratios of 0.08). Furthermore is another crucial effect that when a system is overdamped (values larger than $\zeta = 1$), the deformation amplitude also decreases, even for small frequency ratios. This is not visually visible in figures 5.3 and 5.4 but should be remembered to be a physical fact.

$$\phi = -\tan^{-1} \frac{2\zeta \frac{\omega_h}{\omega_n}}{1 - \frac{\omega_h^2}{\omega_n^2}} \quad (5.3)$$

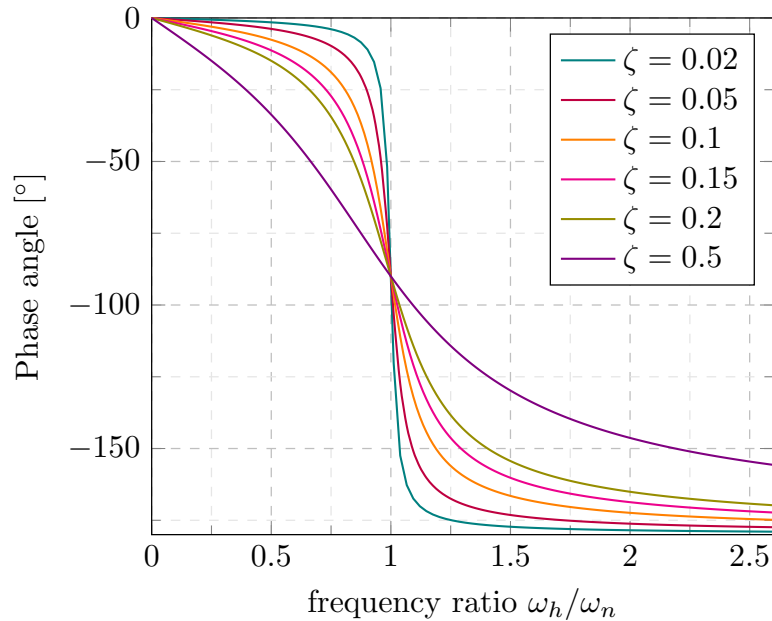


Figure 5.4: Influence of the damping ratio ζ on the resulting phase angle of the system. ($\omega_n = 184.7$ Hz)

With this knowledge in mind, it was selected to alter four parameters:

- **Number of Modes:** should in theory not affect the results besides convergence issues with very few modes. A rule of thumb for engineers is to ensure that 80 % of the modal mass should be accounted for to get accurate enough results. it will be decreased en increased to show the effects
- **Stiffness:** Increasing stiffness (through increasing Young's modulus E) should decrease the transmission-ability as smaller deflections are expected. A secondary effect is that increasing the stiffness also increases the natural frequency. Thus even less damping region effects should be present.
- **Mass:** increasing the mass (through increasing the materials' density ρ) should in contrast to the stiffness, not influence the deflection as it does not affect the total deflection. It only decreases the natural frequency of the system and thus no effects on the deformation amplitude should be present.
- **Damping ratio:** Increasing the damping ratio should cause the most effects, as both phase lag and decreasing amplitude are expected for altering this parameter.

5.2.1 Altering the number of Modes

Figures 5.5 and 5.6 show the simulations for a different number of modes taken into account for the unsteady FSI analysis and the Stress analysis, keeping all other parameters the same. It can be seen be that for 1 and 3 Modes, the solution is incorrect in terms of vibration and deformation amplitude. For 5 modes and more, the stress analysis results are marginally different and 5 modes should be enough for analyzing the sinusoidal wake case. But the unsteady FSI solution seems to vibrate up until 10 considered modes. The difference in amplitude of the deformation is comparable over all simulations and the ratio between the two methods is equal for all modes.

It is important to note that it can not be stated that 5 or 10 modes is enough for all future simulations, since in this simple forces sinusoidal wakefield no resonance is expected. It could very well be that for more complex cases (the in-behind condition in the COMPROP2 experiments for example), more modes are necessary to predict the motion accurately. Furthermore, might twenty blade positions be too few nodes to visualize the motion throughout a revolution.

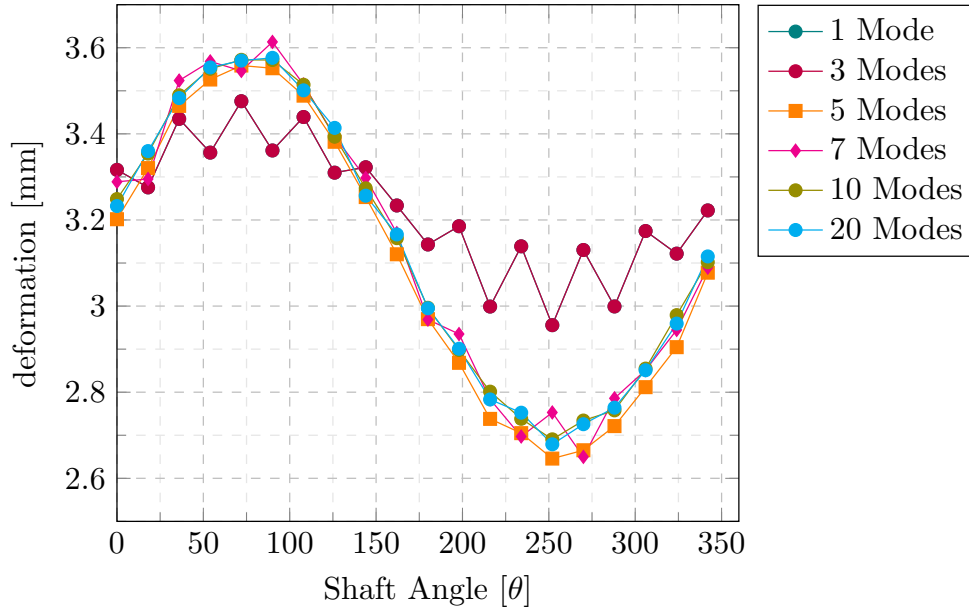


Figure 5.5: Deformation of a blade at 0.7R mid-chord in a sinusoidal wake field for different number of Modes through unsteady FSI. $J = 0.55$, $n = 900$ rpm, $v_a = 2.805$ m/s and $\zeta = 0.1$

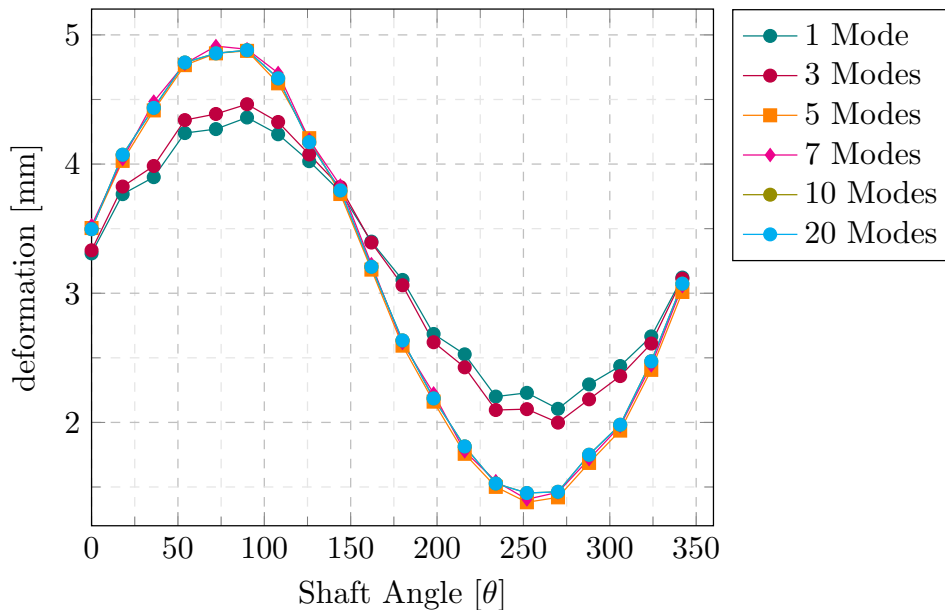


Figure 5.6: Deformation of a blade at 0.7R mid-chord in a sinusoidal wake field for different number of Modes through stress analysis. $J = 0.55$, $n = 900$ rpm, $v_a = 2.805$ m/s and $\zeta = 0.1$.

For now, the conclusions are as follows:

- The difference in amplitude and the phase angle of deformation is unrelated to the number of modes considered for a simple sinusoidal wakefield. The ratio between the two seems to stay around 1.37.
- After 5 modes the Stress analysis results are converged, after 10 Modes the unsteady FSI results are converged. For now, in this comparison study, 10 Modes will be applied to all simulations

5.2.2 Altering Stiffness

figures 5.7 and 5.8 show the different deformations for an increasing Young's modulus. and the difference between the two methods is instantly striking:

Again phase shift is visible in the unsteady FSI analysis, which can not be explained as phase shift should be lower for higher Young's moduli as this increases the eigenfrequency, resulting in a lower frequency ratio. But, the most obvious difference between the two methods is how the deformation develops in the off-peak

at a shaft angle of $\theta = 270^\circ$. The unsteady FSI simulations show that for higher Young's moduli, the steady deflection (mean of the sinus) decreases, the amplitude decreases gradually as well. For the Stress Analysis results, the amplitude at the off-peak seems to be of a fixed value (as if no less deformation is possible at this point). Intuitively the unsteady FSI results seem to be simulation the reality more accurate, but this can not be substantiated with certainty or supported with mathematics. The deformation as shown in figure 5.8 could very well be physical and the result of the complex 3D shape of the propeller blade.

The mean value of both methods does coincide extremely well (the maximum error of the difference in mean displacement in the investigated series is 0.06%). The error of the maximum amplitude did however grow with increasing the stiffness. Ultimately, these systematic series did not construct any conclusions.

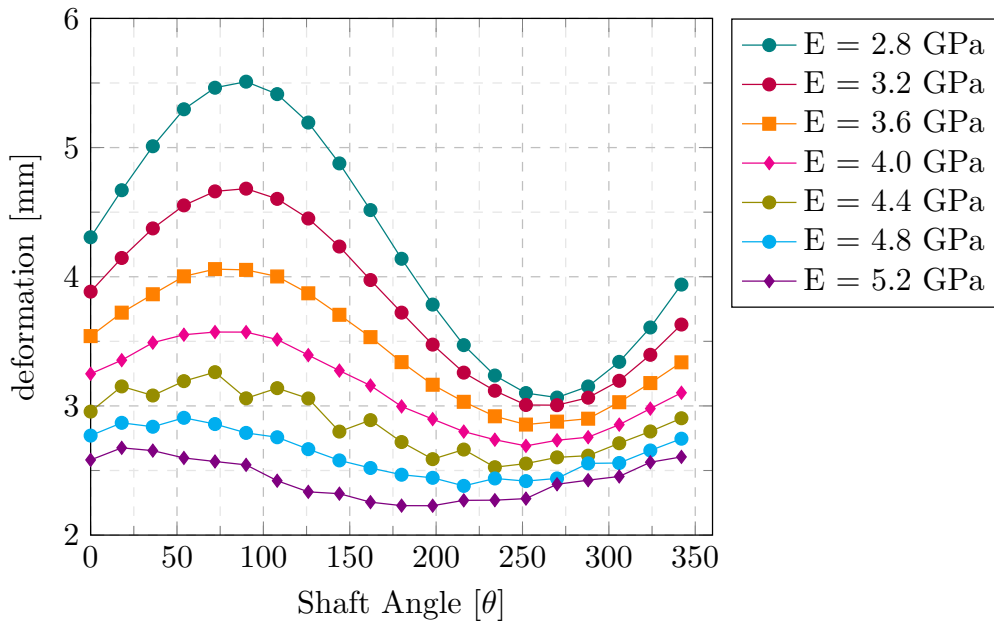


Figure 5.7: Deformation of a blade at 0.7R mid-chord in a sinusoidal wake field for different Young's moduli through unsteady FSI. $J = 0.55$, $n = 900$ rpm, $v_a = 2.805$ m/s, $\zeta=0.1$ and 10 modes.

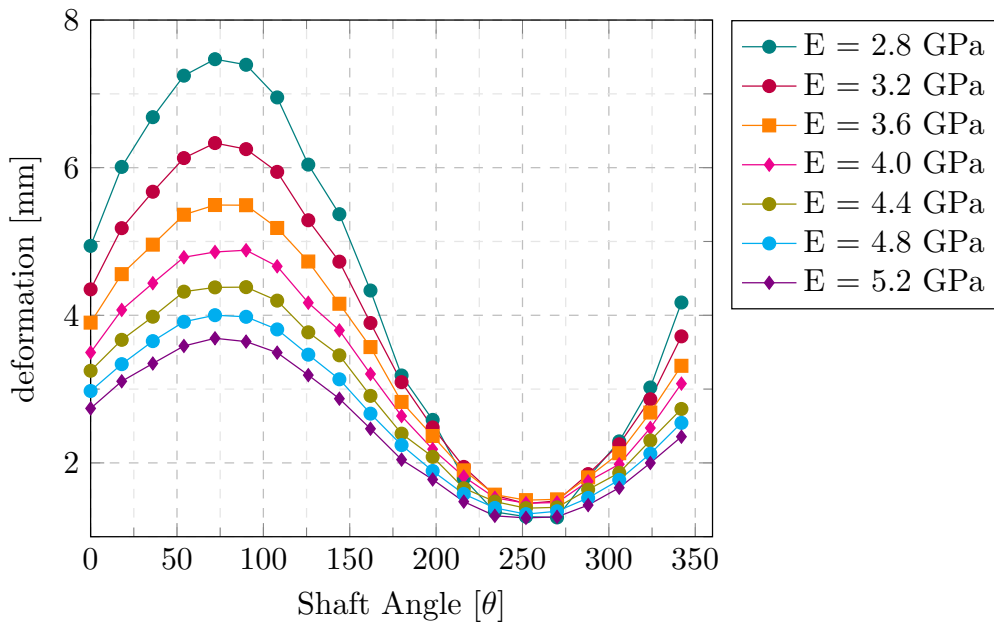


Figure 5.8: Deformation of a blade at 0.7R mid-chord in a sinusoidal wake field for different Young's moduli through Stress Analysis. $J = 0.55$, $n = 900$ rpm, $v_a = 2.805$ m/s, $\zeta=0.1$ and 10 modes.

5.2.3 Altering Mass

Increasing the stiffness has the same effect on the systems' natural frequency as decreasing the material density. However, stiffness influences the 0-frequency component directly (mean displacement). This does not happen for altering mass (or material density).

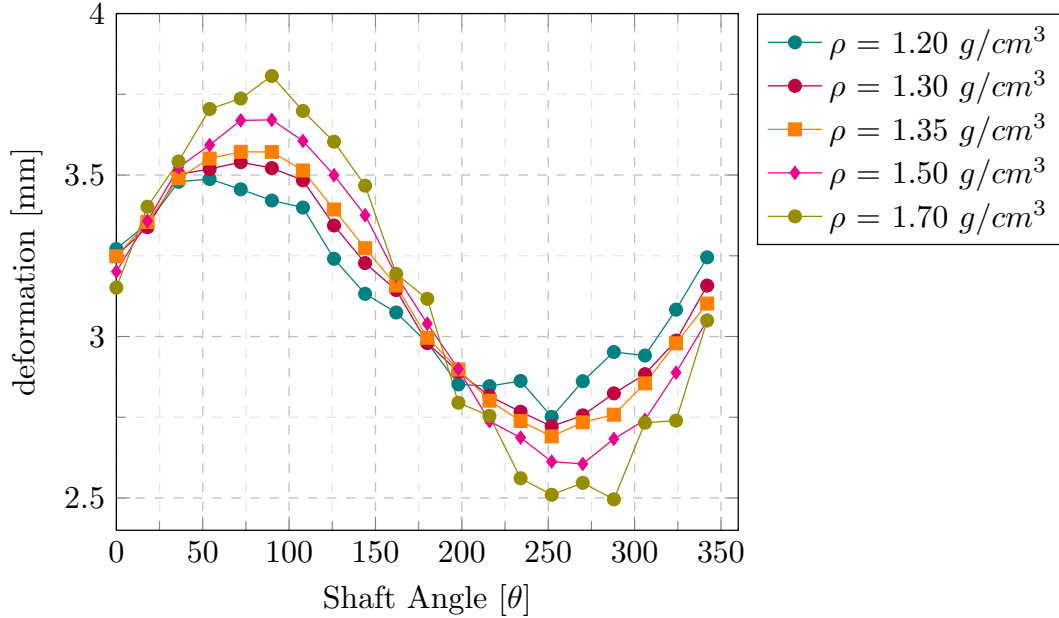


Figure 5.9: Deformation of a blade at 0.7R mid-chord in a sinusoidal wake field for different material densities through unsteady FSI. $J = 0.55$, $n = 900 \text{ rpm}$, $v_a = 2.805 \text{ m/s}$, $\zeta=0.1$ and 10 modes.

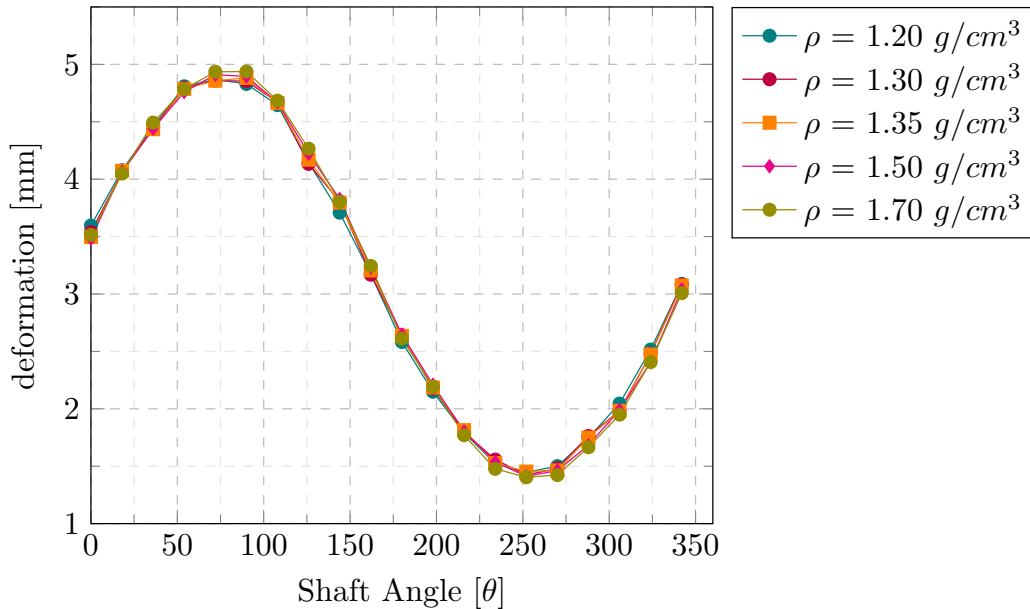


Figure 5.10: Deformation of a blade at 0.7R mid-chord in a sinusoidal wake field for different material densities through Stress analysis. $J = 0.55$, $n = 900 \text{ rpm}$, $v_a = 2.805 \text{ m/s}$, $\zeta=0.1$ and 10 modes.

Figures 5.9 and 5.10 show completely different results. This series is a very useful argument to state that the unsteady FSI analysis is incorrect, as no increase (or decrease) in deformation amplitude should happen. Furthermore are severe convergence issues visible for the unsteady FSI. (For some of the simulations, it is questionable why the ComPropApp even states that a simulation has converged). The stress Analysis, does show the expected similar deformation patterns for different material densities. Even though the results are strikingly different, the mean component of deformation was equal for all simulations.

5.2.4 Altering Damping Ratio

The last examined series are different damping ratios. This one should; as discussed give the best conclusions as the phase lag angle should become visible, accompanied by a lower deformation amplitude. These simulations were chosen to be executed after only *one* iteration in the unsteady FSI module, so fluid-structure interaction is disregarded. As this is calculated after the first iteration, it simply shows complete loading on the blade and which deformation is the result. this was done for two reasons:

- Much faster way of analysis (skips a lot of iterations)
- systems in reality are also damped by water (*Hydrodynamic damping*), This way only damping caused by the material damping ratio ζ , is examined.

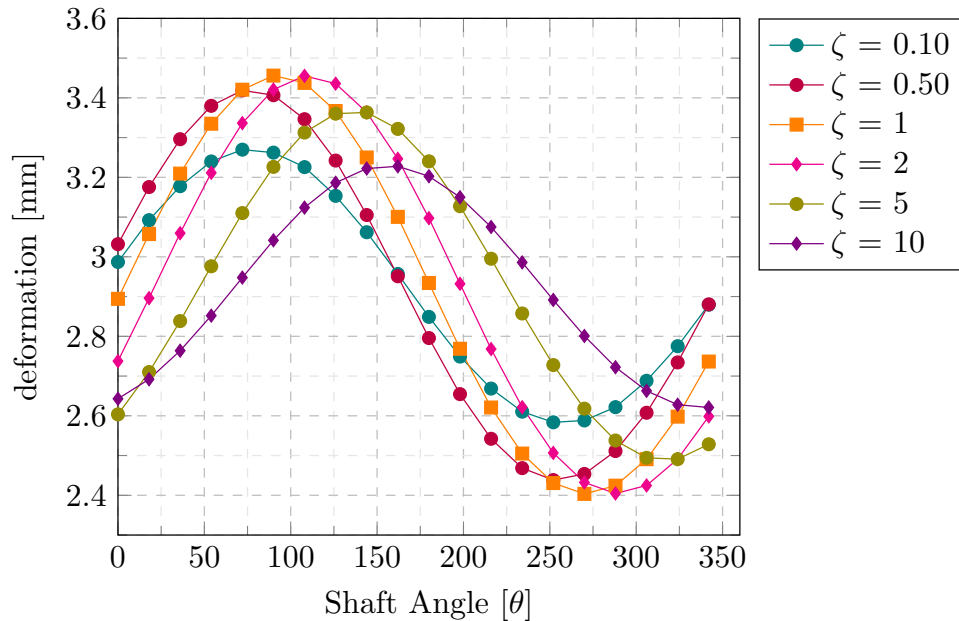


Figure 5.11: Deformation of a blade at 0.7R mid-chord in a sinusoidal wake disregarding fluid structure interaction for different damping ratios through unsteady FSI.

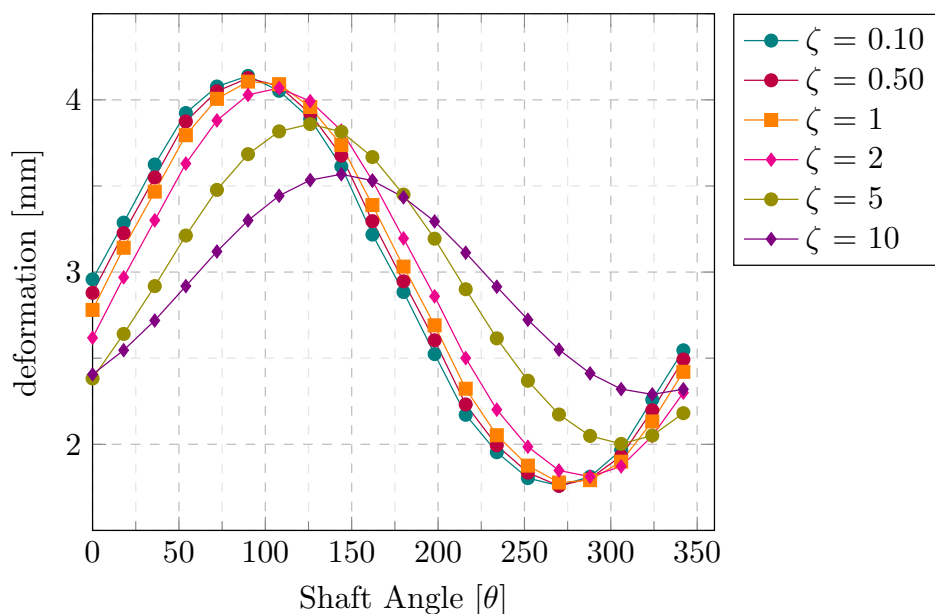


Figure 5.12: Deformation of a blade at 0.7R mid-chord in a sinusoidal wake disregarding fluid structure interaction for different damping ratios through stress analysis.

The results are shown in figures 5.11 and 5.12. The unsteady FSI results do show a correct occurring phase lag, but this only starts at very high damping ratios. This phase lag is simulated quite accurately by the stress analysis. Furthermore, does the stress analysis show the expected decrease in amplitude for high damping ratios. The unsteady FSI analysis on the other hand, first increases significantly in amplitude which should not happen. Again, as with the other series, the mean average displacement component is equal for all simulations.

5.2.5 Conclusions from systematic series

From the performed simulations several conclusions on the ComPropApp can be drawn:

- The Stress Analysis shows more accurate deformations over the revolution compared to the unsteady FSI. This conclusion is substantiated by the following conclusions
 - The phase lag and visible lower amplitude are well described by the stress analysis. The unsteady analysis does not show these phenomena
 - The material density showed to be a large factor in disturbing the results for the unsteady FSI, which hints toward the fact that something is wrong with the modal vectors in the code
 - The number of modes did result in much less convergence for the unsteady FSI results, which also hints towards the modal vectors being incorrect
- The mean displacement components turned out to be equal for all simulations, again hinting that the unsteady FSI code has a bug. If somewhere the complex conjugate vectors are wrong (Modal vectors), this could explain why the mean component is still correct as this is the only component without a complex conjugate.
- Damping ratio ζ , Young's Modulus E and material density ρ all influenced the error between the two simulations.

5.2.6 Code repair

by discovering that the error must be within the Unsteady FSI, the party responsible for the code has indeed found that there was an error within the ComPropApp concerning the Modal analysis. This was happening within the Fourier transform. It turned out that the modal participation factors, which are calculated with equations 3.52 through 3.55, were not declared properly. This led to an error where the complex conjugates were not always linked to their corresponding real counterpart. Thus indeed the hypothesis that the main deflection component of the experiment was not affected because it does not have a complex conjugate vector in the modal analysis was true.

5.3 ComPropApp after modifications

The results after the bug was found are shown in figures 5.14, 5.14 and 5.15 for altering stiffness, mass and damping ratio respectively. It can be concluded that now no more differences between the two methods exist. Thus all physical attributes of the transfer function in equation 5.1 are implemented correctly in both methods. It is now validated that both simulation methods predict the same deformation in a non-uniform wake. It however can not be validated that this fictitious wake field would yield the same deformations in real life. Therefore, in the next chapter, it is time to compare simulations with the non-uniform experiments conducted within the COMPROP2 working group.

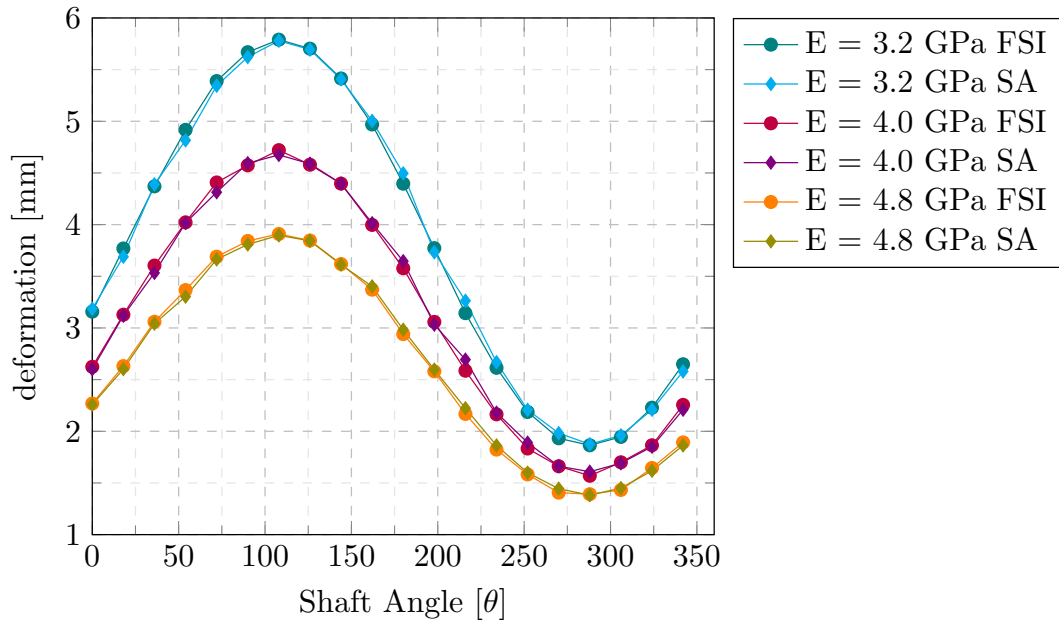


Figure 5.13: Deformation in x-direction of a blade at 0.7R mid-chord in a sinusoidal wake for different Young's moduli, through unsteady FSI and Stress Analysis.

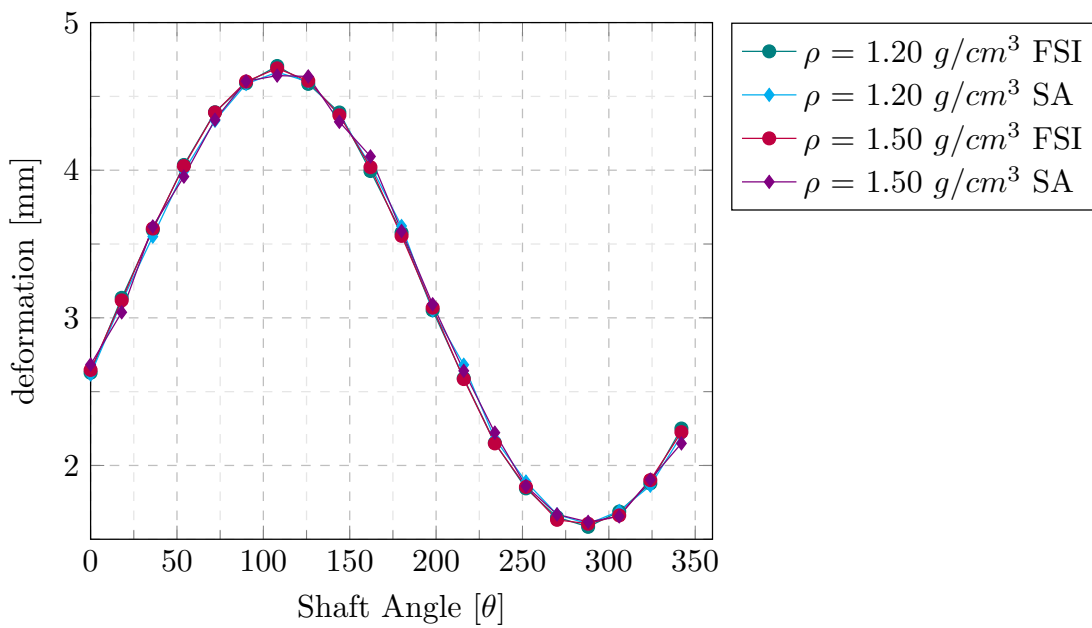


Figure 5.14: Deformation in x-direction of a blade at 0.7R mid-chord in a sinusoidal wake for different material densities, through unsteady FSI and Stress Analysis.

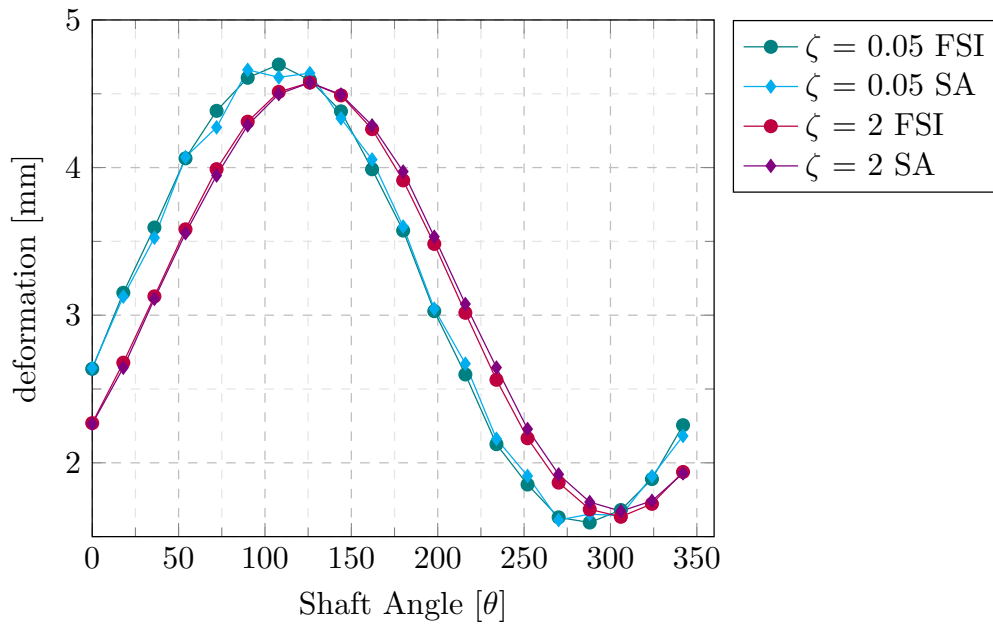


Figure 5.15: Deformation in x-direction of a blade at 0.7R mid-chord in a sinusoidal wake for different damping ratios, through unsteady FSI and Stress Analysis.

6 Validation of the COMPROP2 experiments

In chapter 5 the working principles and method of the modal analysis in a simplified sinusoidal wake field was validated. Now that it is known that the ComPropApp can handle non-uniform wake field computations, it is time to approach the final goal: *Validation of the COMPROP2 experiments*. The numerical simulations become more difficult here because the wake is generating more complex flow compared to the sinusoidal wake field of chapter 5. In the simple sinusoidal field, only forced vibration in the rotational speed is experienced. However, the wake field, as shown in figure 6.1, has a much sharper wake peak which resembles a gondola. This wake field will be described as the gondola wake hereafter. This sharp wake peak causes the possibility of exiting resonance frequencies of the propeller blade.

First, in section 6.1 the methodology of the experiments in MARIN is discussed and how experimental data is retrieved from the experiments. After that, in section 6.2 the material used in the experiments is explained and possible uncertainties which arise from that material are discussed. Thereafter, in section 6.3 the damping ratio of the propeller models is determined using a damping test. Then, in section 6.4 the experimental data is processed into usable data and the uncertainty is discussed. And finally, in section 6.5, the comparison between the experiments and the numerical simulation is made.

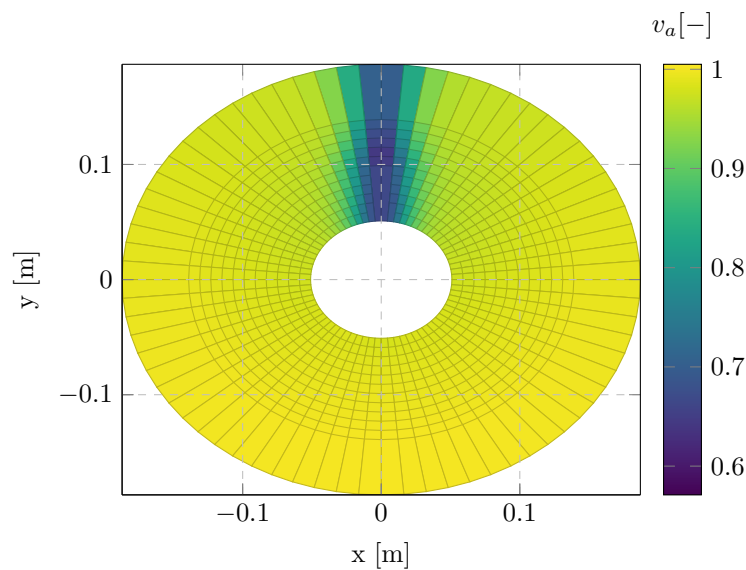


Figure 6.1: Induced wake field velocity in the COMPROP2 experiments.

6.1 Experimental Setup

Within the CRS working group COMPROP2, it was decided to perform experiments concerning flexible marine propellers. This with the aim to verify the ComPropApp. The main particulars of the set-up and information regarding the performed experiments were found in documents by Lloyd's Register [44] and a report by Marin [45]. In total, six experiments at different hydrodynamic conditions were executed with the model c4-40 propeller. They are shown in table 6.1 with their corresponding ID.

Table 6.1: In behind condition experiments conducted at MARIN.

| Experiment ID | V_s [m/s] | n [rpm] | J [-] | T [N] |
|---------------|-------------|-----------|---------|---------|
| C034 | 4.0 | 840 | 0.84 | 29.0 |
| C036 | 4.0 | 960 | 0.74 | -174.8 |
| C038 | 4.0 | 1119 | 0.63 | -478.5 |
| C039 | 5.0 | 1199 | 0.74 | -180.3 |
| C042 | 3.0 | 920 | 0.58 | -460.9 |
| C043 | 3.5 | 980 | 0.63 | -398.4 |

The experiments at MARIN were conducted in a cavitation tunnel (see figure 6.2). In this cavitation tunnel, water is pumped around at the desired speed. And the model propeller is rotated at the desired rate. Furthermore, is the body used to generate the wake field seen in the figure. It is possible to measure the total blade thrust with the use of a force transducer.



Figure 6.2: Cavitation tunnel set up. Left: Open water, Right: with wake generator. [45]

With this setup, it was decided to measure the deformation of the blade with a technique known as DIC (*Digital Image Correlation*). this technique uses stereo camera positioning to three-dimensionally follow points in time. These points are randomly applied with a black marker to the model propellers. In figure 6.3 this is visualized with a model propeller from the earlier executed COMPROP1 experiments. In figure 6.4, a representation is given on how the DIC-system traces those black markings in time: both cameras are capturing the same black dot at a different position on the sensor. This can be mathematically translated to the position of the dot and this is done for each dot for each captured image with an accuracy of the size of a pixel.



Figure 6.3: Model propeller for SikaBlock M700 propellers, with black markings. [45]

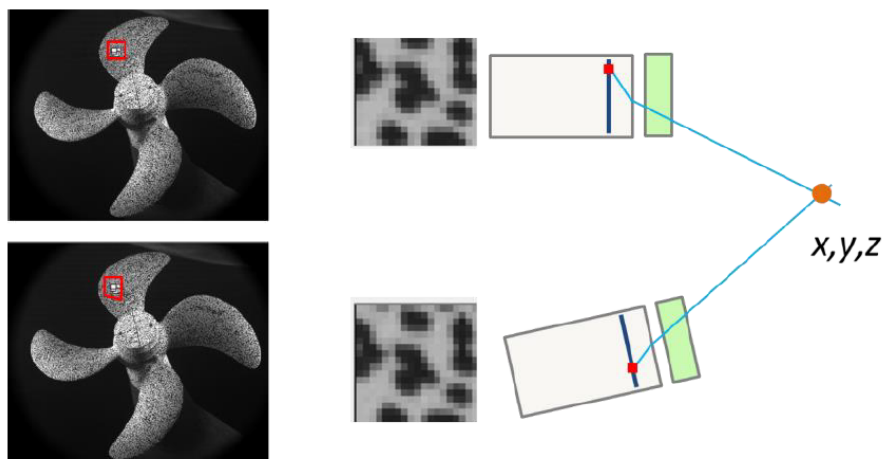


Figure 6.4: Schematic representation of the DIC system. [45]

The DIC method has uncertainty which occurs because of three separate sources:

- Camera accuracy: is as small as the pixel size: the order of camera accuracy is 0.02 mm.
- On top of the camera's accuracy, the deformation is calculated as a difference with a reference image. This difference results in a variation (and error) of 0.13 mm.
- Measurement stability over time. Some variations in accuracy and calibration were observed over the course of the measurements. This was in the order of 0.04 - 0.13 mm.

Those errors are all random in character and can not simply be superimposed to construct a uncertainty band. The errors were however deemed significantly small by MARIN [45] for the purpose of this project.

6.2 Material models

The propellers were milled at MARIN from a single brick of the SikaBlock M980 material for which the material properties were given in table 4.3 in chapter 4. In a preceding CRS Working group (COMPROP1), experiments were conducted as well. Those experiments were executed with a much less stiff material known as SikaBlock M700. For both materials, the properties are shown in table 6.2. This SikaBlock, a polyurethane foam was selected because it had a desirable stiffness and it has good manufacturing properties.

Table 6.2: Material properties as provided by the manufacturer. [46] [41]

| | SikaBlock M980 | SikaBlock M700 |
|---------------------|----------------|----------------|
| Young's Modulus E | 4 GPa | 1 1.1 Gpa |
| Density ρ | 1.35 g/cm^3 | 0.7 g/cm^3 |

6.2.1 SikaBlock M700

The experiments conducted within the COMPROP1 group instantly showed that SikaBlock M700 was way too flexible to obtain any acceptable measurements in the cavitation tunnel. This was the main reason to reject these experiments and proceed with the stiffer SikaBlock M980 material. However, some static testing conducted by DRDC-Atlantic (a partner in the CRS working group) gave some insights into the material. Firstly, the material properties were found to be significantly different from those stated on the tech sheet provided by the material manufacturer. Material specimen testing by LR (Lloyd's register) proved the actual material properties to be as stated in table 6.3. These parameter discrepancies have a significant effect on the simulations in terms of deflection and natural frequency. The specimen tests raise suspicion that there is a slight anisotropic component to the material as well. This is likely to be caused by to rolling process in the manufacturing of the product.

Table 6.3: Material properties as provided by the manufacturer [46] and by specimen testing for SikaBlock M700.

| | Manufacturer | actual |
|---------------------|--------------|---------------|
| Young's Modulus E | 1 1.1 Gpa | 0.8 Gpa |
| Density ρ | 0.7 g/cm^3 | 0.65 g/cm^3 |

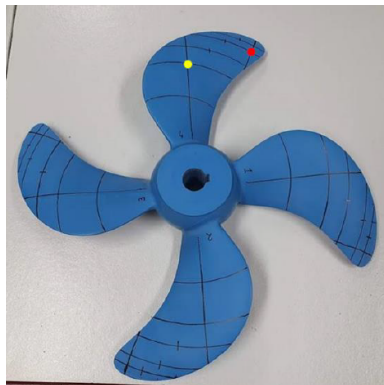


Figure 6.5: Point load conditions. Yellow dot is on 0.7 r/R, red dot is on 0.9 r/R. [44] *Note: this is the SikaBlock M980 propeller, but load points are the same for the M700 propeller*

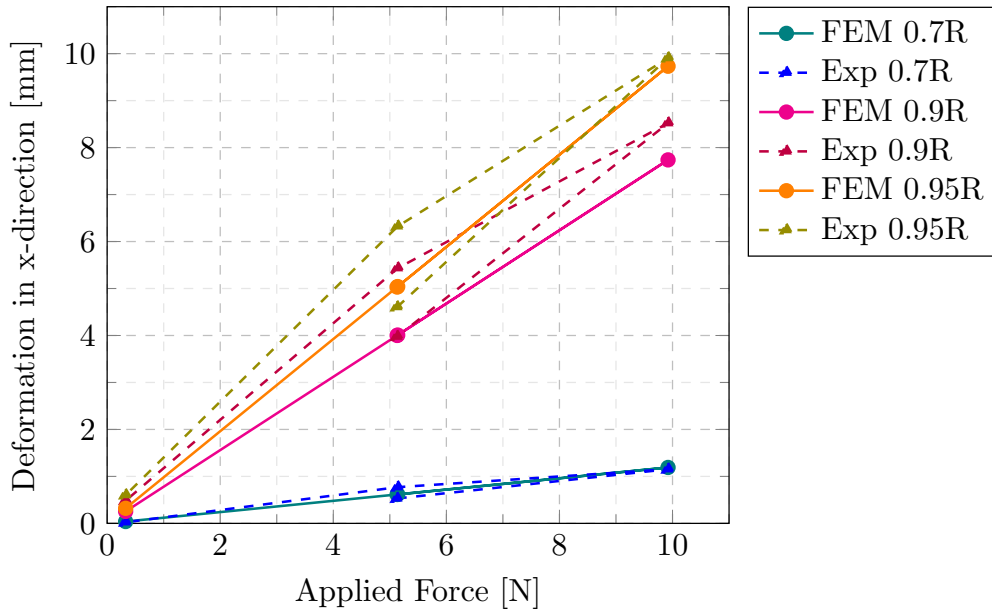


Figure 6.6: Comparison of static blade deformations by FEM and experiment for a SikaBlock M700 Propeller.

Figure 6.6 shows the deformation history of a static point load test in air on three different points on the propeller as shown in figure 6.5. It shows that the deformation of the blade is time-dependent. This is not captured by the linear Hooke's law, as shown in equation 6.1. This non-linear theory can not be modelled in VAST/TRIDENT. It could also be that the material is operating too close to its plastic limit and therefore starts to deform non-linearly. Therefore, together with the fact that the deformations were way to large for the experiments, it was chosen to advance to the COMPROP2 experiments with a much stiffer material: SikaBlock M980.

$$\sigma = E\varepsilon \quad (6.1)$$

6.2.2 SikaBlock M980

As was discussed in the previous paragraph, the material properties turned out to be much lower than was stated on the tech sheet. This same suspicion is present for SikaBlock M980, but the specimen tests have not been carried out yet. Figure 6.7 shows the deformation history of two tested SikaBlock M980 propeller blades subjected to a static loading test.

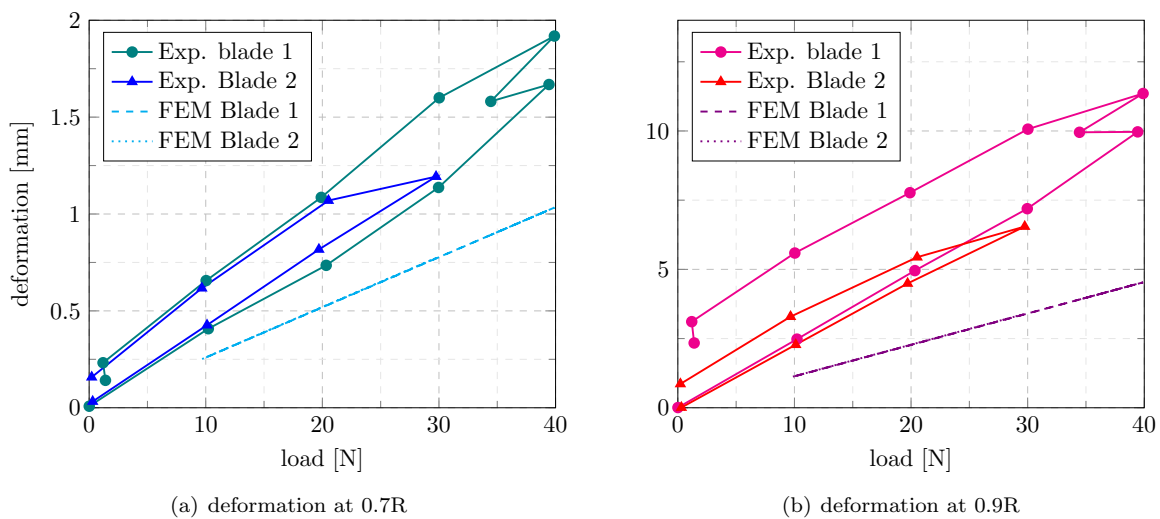


Figure 6.7: Deformation comparison for two different blades, point load at 0.9R.

From both the M700 and M980 static loading tests, several conclusions can be drawn:

- The material stiffness must indeed be significantly lower, as can be concluded from the wrong slope of the experimental and FEM deformation curves.
- Time-dependent deformation is also present in the stiffer SikaBlock M980 material, thus the permanent deformation is not due to the possibility that the SikaBlock M700 material was operating near the plastic regime.
- Besides time dependant deformation, there is also some form of unrecoverable deformation present (creep). This is permanent deformation that is happening because of visco-elastic effects in the material. Why this only happened with the stiffer M980 material is still a mystery.
- Differences exist between two (supposedly) equal propeller blades (see figure 6.7b), which raises concerns on the manufacturing tolerances, as these effects might be even larger for composite marine propellers.

As the current FEM package, does not account for non-linear deformation (and viscoelasticity models), it should be concluded that the material is not a good fit for flexible marine propeller testing. Unfortunately, there are not a lot of candidate materials that could easily replace polyurethane foams without sacrificing costs, manufacturability, or proper flexibility. And might using software with non-linear theory be the best option for the future.

All these subjects could be the foundation for a research study regarding the material properties of the SikaBlock material. In the first place, it is recommended to find a new material that meets the three design criteria: manufacturability, stiffness and cost. However, this is thought to be a difficult task. It could therefore be researched whether these non-linear characteristics can be quantified, neglected, or in some way be mitigated. For this study, this is deemed out of scope.

6.2.3 Manufacturing tolerances

In total, three propellers were constructed, which were expected to be similar and of equally isotropic and linearly elastic material. As stated above, the linearity and isotropy of the material are already suspected to be false. There are manufacturing errors introduced within those models as well, Those errors also introduce fluctuation in the results, both hydrodynamic and structural.

In principle, all propellers were manufactured under the same conditions, with the same CAD input file. The difference in the resulting propellers and even differences per blade is striking. Figure 6.8 shows the error of the model propeller which was measured with an accurate laser measurement system at MARIN. The shown deviation is with respect to the CAD model. It shows how to supposedly equal propellers can perform significantly different. The effects of these deviations were simulated in open water in the ComPropApp by generating .ppg files from those laser measurements by LR [44]). The results are shown in table 6.4. The BT and AT (meaning before testing and after testing) indicate whether this laser measurement and corresponding .ppg files were constructed before or after the propeller was used for cavitation tunnel tests.

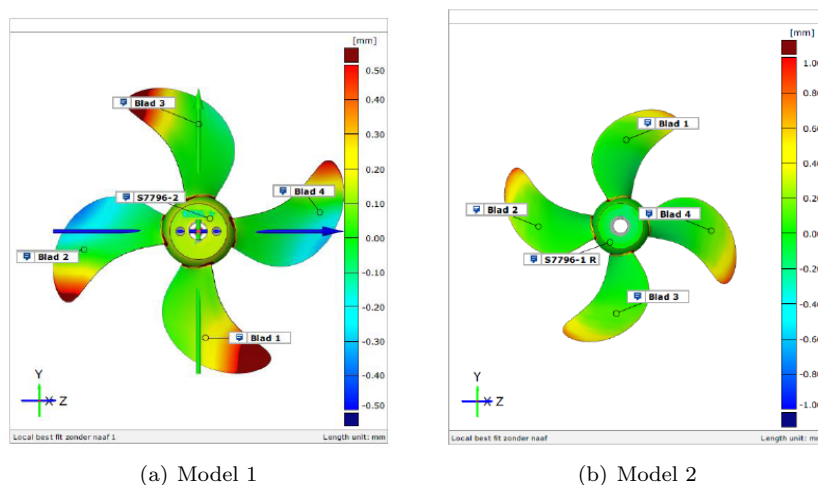


Figure 6.8: Deviation of two model propellers from the same CAD input file. (*Source: Lloyd's Register [44]*)

Table 6.4: Simulated hydrodynamic results and deflections for the SikaBlock M980 blades. (BT = before testing, AT = after testing)

| Blade | Hydrodynamic | | | Deflection [mm] | | |
|--------|--------------|--------|---------|-----------------|------|------|
| | η | K_T | $10K_Q$ | 0.7R | 0.9R | Tip |
| 1 (BT) | 0.6866 | 0.1056 | 0.1716 | 0.35 | 0.99 | 1.38 |
| 2 (BT) | 0.6850 | 0.1043 | 0.1698 | 0.34 | 0.97 | 1.34 |
| 3 (BT) | 0.6873 | 0.1073 | 0.1741 | 0.36 | 1.02 | 1.42 |
| 1 (AT) | 0.6652 | 0.0834 | 0.1395 | 0.23 | 0.66 | 0.94 |
| 2 (AT) | 0.6770 | 0.0964 | 0.1586 | 0.30 | 0.84 | 1.16 |

The results show the sensitivity of the manufacturing errors with respect to the performance. This was also the case for the material properties. This is an interesting topic to investigate in further research: *how sensitive is the performance of a flexible marine propeller towards manufacturing errors and material property deviations?* As for composite propellers, these deviations might be even of more importance due to their complex material properties. This might give insight in which tolerances should always be reduced to a minimum and which deviations are of less importance to the performance. In the study performed by Lloyd's Register, only five data points are present, so in a larger data set this could provide valuable insights into the tolerances of flexible marine propellers.

6.3 Damping ratio and material property determination

As was shown in figure 6.7, the material properties must be different from those stated in the manufacturer's tech sheet. Besides testing the specimen (which is time and cost expensive) there is a rather easy workaround to get a decent estimation: In a damping proof, the blade is excited and the vibration pattern is measured. This way, one can determine the natural frequency of the blade. Then, with the modal analysis tool in the ComPropApp one can simply tweak the Young's modulus to achieve that same frequency. Note that also the material density could be altered to change the natural frequency. But the other main target is to decrease the stiffness to match the deformation slope in figure 6.7 thus it is chosen to only alter the materials Young's modulus)

Two of those damping tests were performed. Experiments C146 and C148 both measured a different blade from the same model propeller. Their free vibration is shown in figure 6.9. Now with a simple Fourier analysis tool in Matlab [47], the eigenfrequency of the signal can be calculated. Note that for that Fourier analysis the loading from zero to maximum deflection of the signal is deleted. The max deflection point has to get timestamp zero. This way both signals are determined to have a natural frequency of around 172 Hz, which is close to the values found by LR (172 Hz). [44].

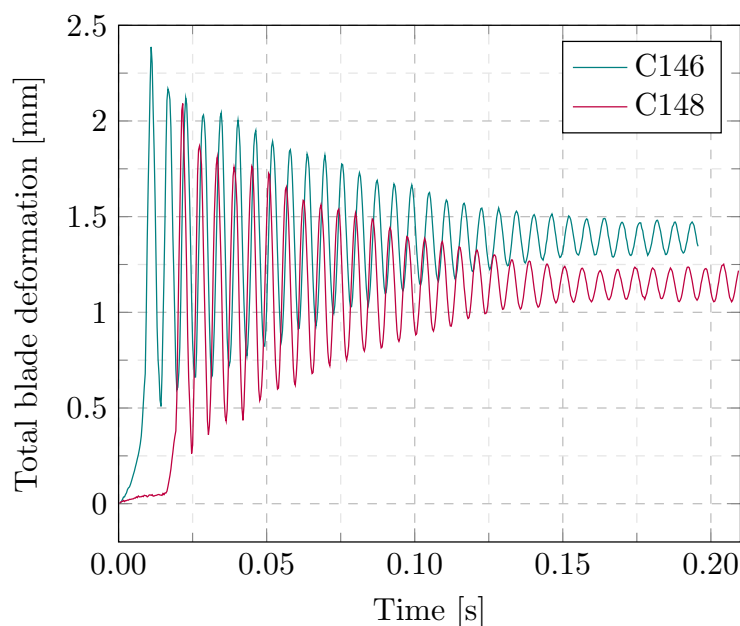


Figure 6.9: Damping test in air, total displacement for two different blades at 0.7R.

Now, the Young's modulus can be lowered until an accurate eigenfrequency is obtained in the ComPropApp.

This was achieved at a Young's modulus of 3.5 GPa. Table 6.5 shows the determined material properties which will be used in the validation compared to the manufacturer's given properties.

Table 6.5: Material properties as provided by the manufacturer [46] and by damping test estimation for SikaBlock M980.

| | Manufacturer | actual |
|--|----------------|----------------|
| Young's Modulus E | 4 Gpa | 3.5 Gpa |
| Density ρ | 1.350 g/cm^3 | 1.350 g/cm^3 |
| natural frequency ω_n | 184.7 | 172.8 |

Another material parameter that can be estimated is the material damping ratio ζ . This was shown to have large effects on the behaviour of the propeller in chapter 5. The method to determine this is with the logarithmic decrement (δ) [48]. As this method is theoretically exactly true for a single degree of freedom system, it was chosen to only use displacement in the x-direction to approach this definition a bit better. formula 6.2 shows the formulation of the logarithmic decrement. in which n is the number of periods considered, $x(t)$ the amplitude at the first measurement point and $x(t + nT)$ the amplitude at n -cycles.

$$\delta = \frac{1}{n} \ln \frac{x(t)}{x(t + nT)} \quad (6.2)$$

In formula 6.3 it is shown how the damping factor is estimated. Here, τ is the time factor (time between the two considered amplitude peaks) and f_d is the frequency of the system.

$$\zeta = \frac{\ln(x(t)/x(t + nT))}{\sqrt{(2\pi f_d \tau)^2 + \ln(x(t)/x(t + nT))}} \quad (6.3)$$

This yield an damping ratio of approximately $\zeta = 0.0160$ (C146 = 0.0158, C148 = 0.160) for both signals when ten revolutions are considered. These seems very low, but in reality there is also a contribution of the water to the system damping (hydrodynamic damping) which should slowly be added to the system through the working principles of fluid-structure interaction. For a better estimate, the same excitation test in water might give a better estimate for the input parameters in water (wet natural frequency and a hydrodynamic damping ratio).

6.4 Experimental Data

In section 6.1 it was discussed how the setup of the experiments was structured. In this section it will be explained how that DIC data is used to construct usable data for validation of the ComPropApp. The method used to determine the blade deformation is known as *Ensemble averaging*. This method works as follows: First, the DIC cameras are taking a picture at shaft angle 0°. Then the propeller rotates a complete revolution and another picture is captured at the same shaft angle. This is repeated 40 times before the cameras moves the point where this process of capturing 40 pictures is repeated at a shaft angle of 1°. Thus in total for 360 shaft angles, 40 pictures are taken. Then the DIC system calculates the displacement compared to the undeformed position for all pictures. And for each shaft angle, the average deformation components are calculated.

This method was chosen over an actual time signal since real-time signal time tracing required a too sensitive camera which would generate a lot of uncertainty. Note; for a rotational rate of 15 Hz, a camera with 5400 Fps would be required to calculate the deformation. The disadvantage is that the signals obtained through signal averaging are only an average of 40 deformation values. So no conclusions can be made on resonance phenomena within a revolution as it could very well be a distortion caused by minor fluctuations of the wake field per separate revolution.

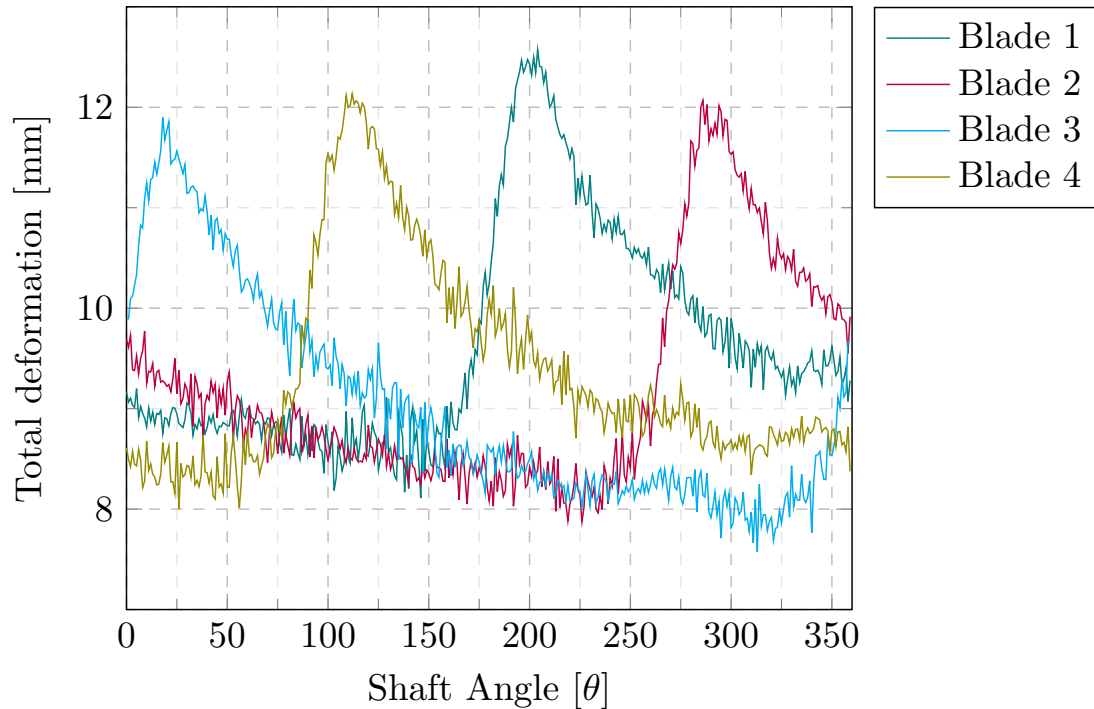


Figure 6.10: Blade deformation of four blades over one revolution of experiment C038. ($J = 0.63$, $n = 1119$ rpm, $v_a = 4$ m/s)

Figure 6.10 shows the raw data of experiment C038 for four blades. And the noise on the signal is visible. It can also be seen that the minor manufacturing tolerances has a serious influence on the deformation. (the difference in peak deformation values of blade 1 and 3 is significant). Later on, it was verified that blade 3 of this experiment was used in the static load tests from section 6.2. So, blade 3 was not representative for propeller c4-40 as it already contained deformation.

Since the values in figure 6.10 are a mean value of 40 values, they also bear some uncertainty with them. This is expressed in the two standard-deviation interval (2σ -interval). Within this interval, there is 95 % certainty that the actual value lies within those bound. This is visualized for a deformation signal of experiment C039 in figure 6.11. It shows that the most uncertainty is right before the wake peak. This area of large uncertainty is most likely caused by the fact that the experimental uncertainties (rotational rate, water velocity and pressure) are the largest in this area of the revolution. That uncertainty combined with the actual change in inflow velocity which caused the blade to deform makes that larger uncertainties are present here.

Again, it would be meaningful to also capture real-time data of these experiment. This makes in possible to investigate the deformation of the blades through this area before the wake peak. With the current available data it can not be concluded whether blades are vibrating in this area, or that the deformation component is simply highly random in character.

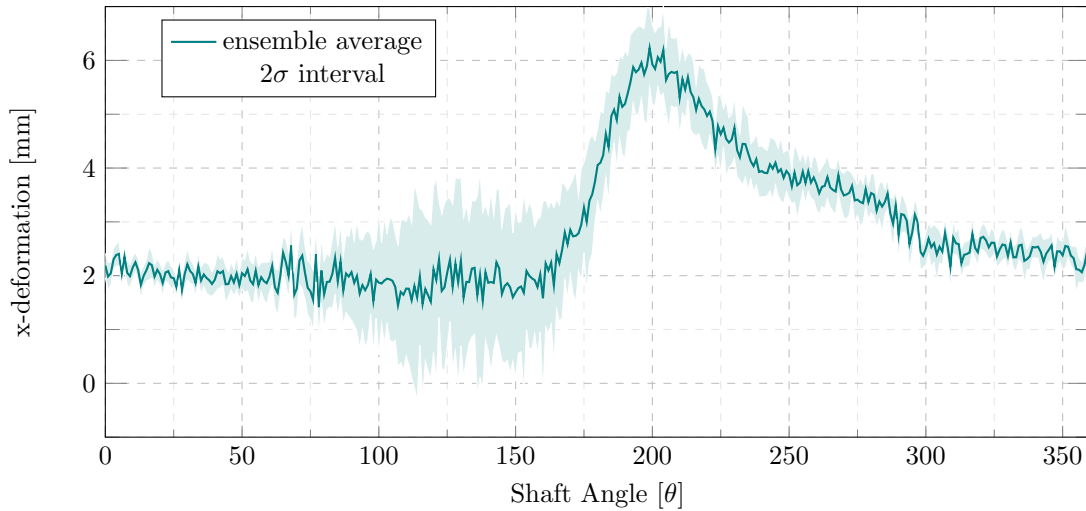


Figure 6.11: Blade deformation in x-direction with uncertainty bounds for experiment C039. ($v_a = 5$ m/s, $J = 0.7$, $n = 1200$ rpm)

For all six experiments from table 6.1, for all four blades, the displacement in x-,y- and z-direction, and their corresponding standard deviations are given at 0.5R, 0.7R, 0.9R and 0.95R of the blade length. This data can be used to the main goal of this validation study: validation of the simulations using the experiments.

6.5 Comparison experiment and simulation

6.5.1 Convergence issues

For the cases in chapters 4 and 5, the unsteady FSI simulation times were approximately 15 minutes. Some outliers were present with computational times of approximately one hour. For these more complex cases, the simulation time and convergence are becoming much more problematic. This is firstly caused by the fact that 20 blade positions per revolution is not sufficient anymore when one wants to capture the vibrations within a revolution. Increasing the number of blade positions exponentially increases the calculation time. This is caused by the program P4C which is used to calculate the deformed blade geometries for each new FEM iteration. Secondly, for more blade points, the convergence also becomes much slower as more vibrations are introduced into the simulations. This combined with the low damping ratio found in section 6.3 of 1.6 % leads to the fact that it takes a very long time to get converged simulations. (A COMPROP2 experiment with 72 blade positions took 7 hours and still was not converged within the 1% error norm.)

A method to overcome this problem in the future might be a quasi-static approach. This was also addressed by the preceding graduate K. van den Sanden [39]: First, the average wake velocity is taken and a steady FSI simulation is performed. Then this converged deformed geometry could be used as input for the unsteady FSI tool to account for the non-uniform wake field and resulting periodic dependant deformations within a revolution. From chapter 4, it should be valid to apply this method as the final deformation and hydrodynamic performance comparison between the steady and unsteady FSI showed the agreement between the two methods. One problem which has to be overcome is that this initial steady FSI calculation produces internal stresses in the propeller which affect the eigenfrequency, mode shapes and deformation behaviour of the blade. Those are currently not accounted for if one would use the deformed geometry as input for the unsteady analysis. This is an interesting topic for possible future research as the benefits in terms of computational time could be enormous.

6.5.2 Open water wake validation

As was shown in section 6.3, the damping ratio was obtained through a damping proof test. Now, applying a uniform wake simulation to the propeller model, the simulation should obtain that same damping ratio. By performing this test, it is also possible to check whether the added mass is applied correctly and causes hydrodynamic damping. The wet natural frequency of the blade should be significantly lower compared to the dry natural frequency. When analyzing signals with Fourier transforms to determine frequencies one should be certain that enough data points are present to make conclusions. To accurately visualize a sinusoidal signal, there should at least be four data points per period, with the determined dry frequency of 172 Hz. This means at least 688 data points per second should be present. The analyzed signal has a rotational rate of 15 rounds per second, so if 48 blade positions per revolution are considered, the signal contains (15×48) 720 data points per second. This should be sufficient to analyze the dry natural frequency of the simulation.

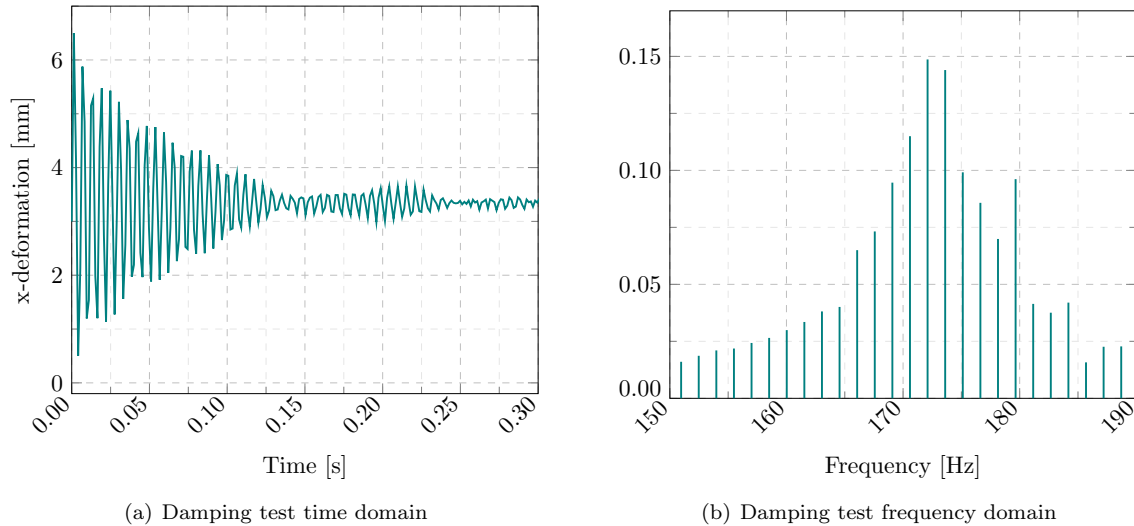


Figure 6.12: Open water test excitation in (a) time and (b) frequency domain.

Figure 6.12 shows the results for the damping test in the time- and frequency domain. In figure 6.12a it is visible that a lot of vibration is still present. This is caused by allowable errors within PROCAL and in the Unsteady FSI. In figure 6.12b, a close-up of the Fourier transform is shown with the peak at approximately 172 Hz. This is equal to the dry eigenfrequency. Thus added mass is somehow not added to the system. Otherwise, hydrodynamic damping would have resulted in a lower (wetted) frequency. A method might be to first estimate the wetted eigenfrequencies of the blade (as described in the ComPropApp manual [40]) This is not done or allowed yet in the current version of the ComPropApp. It however may be necessary to estimate this, since now the system keeps vibrating at dry frequencies, which is not physical.

6.5.3 Validation of experiment C038 (smallest deflection)

In the previous section it was concluded that the experimental data is not sufficient to make conclusions about the vibrations within a revolution due to the ensemble averaging method. This combined with the above-mentioned problems with convergence for complex simulation gives the preference to first solely validate the deformation component and disregard the potential vibrations.

The first experiment to be examined is C034, which is expected to have the smallest deformations and consequently, the smallest computational time. It should be noted that for these simulations a damping ratio of $\zeta = 0.10$ was taken since the actual damping ratio led to divergence in PROCAL. This is an indication that still something is wrong in the code because the added mass is not adding hydrodynamic damping to the system. However, when only analyzing the mean deflection component, this fictitious damping ratio does not significantly influence the results. (the phase lag and decreased amplitude only start to affect the simulation after an overdamped value of $\zeta = 1$). The raw data looks as in figure 6.13. From this figure, it is clear that there is some sort of error in the definition of the displacement components of the experimental data since it makes no sense that negative displacement from the origin is reached in a revolution.

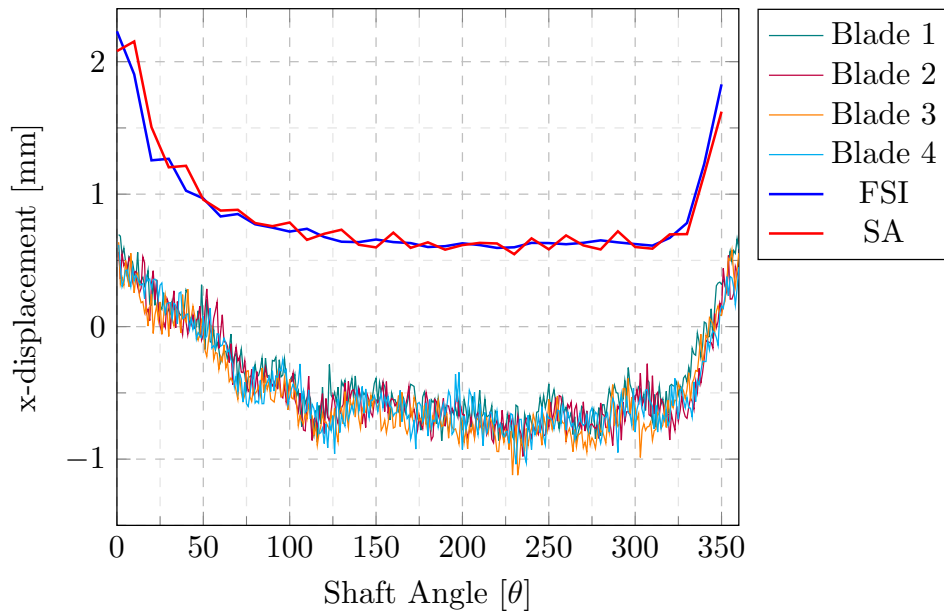


Figure 6.13: Blade deformation in x-direction of C034 through FSI, SA and experiment. ($V = 4$ m/s, $J = 0.84$, $n = 840$)

It is unknown how the axis and measured distances are defined in the experimental data. To obtain better comparable data, the experimental data is shifted upwards with a factor equal to $\mu(\text{SA}) - \mu(\text{exp})$. This ensures that the average deformation component of the experimental data is set equal to that of the stress analysis simulation. With this correction, a comparison as in figure 6.14 is obtained. The results of the experimental deformations and both simulations are in quite good agreement.

A final visualization is given in figure 6.15 where only one blade is compared with the experimental deformation and its uncertainty bounds. Both figures 6.14 and 6.15 give confidence in the capability of the ComPropApp to predict the deflection pattern of the blade over a revolution. It should however be noted that now the mean components have been set equal as no other method or data has been found on how to interpret the deflections given in the experimental data. C034 is the experiment with the smallest deflections. So the next step is the validation of C038 in table 6.1. This experiment has much larger deformations.

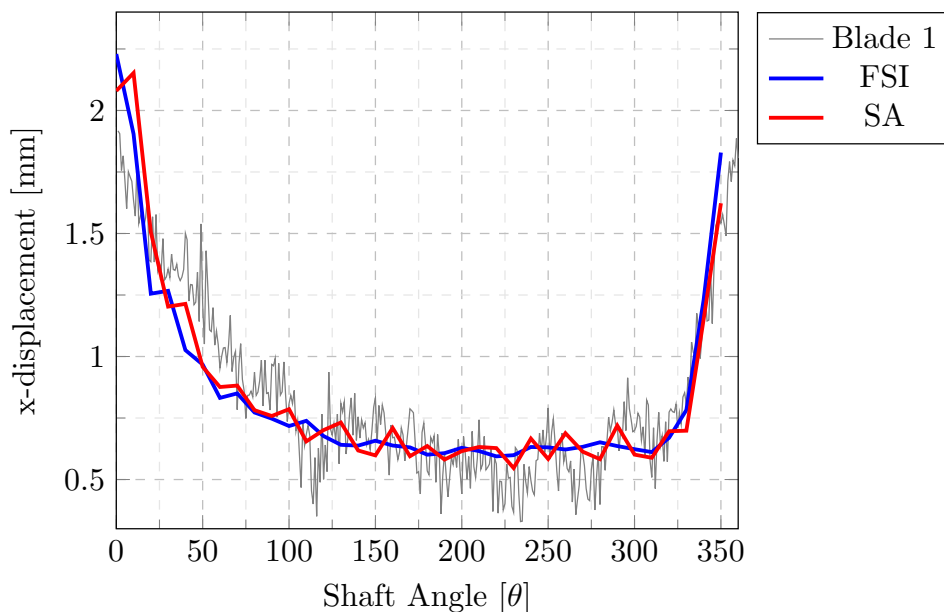


Figure 6.14: Blade deformation in x-direction of C034 through FSI, SA and experiment. ($V = 4$ m/s, $J = 0.84$, $n = 840$)

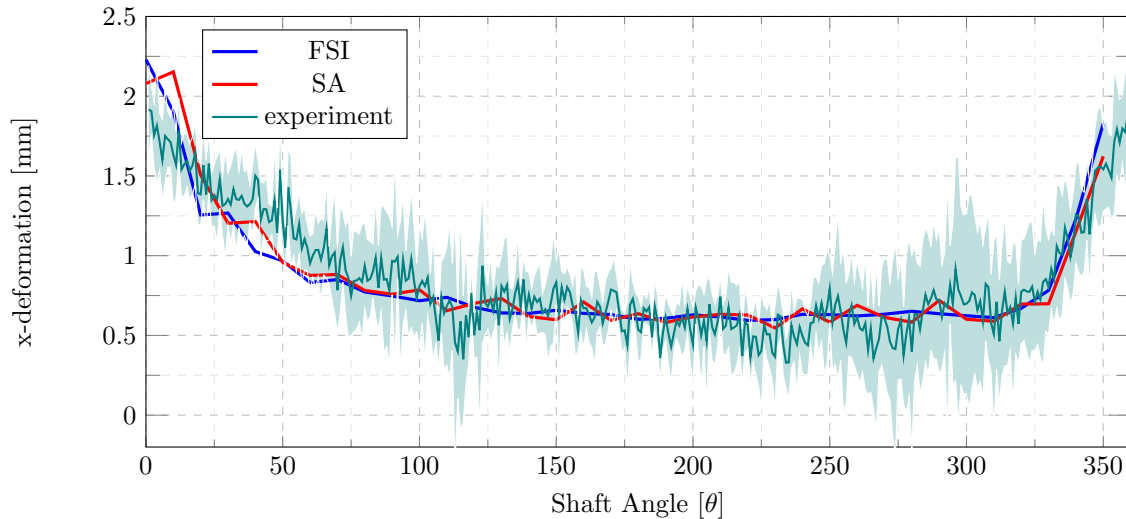


Figure 6.15: Blade deformation in x-direction of C034 through FSI, SA and experiment with uncertainty bounds. ($V = 4$ m/s, $J = 0.84$, $n = 840$)

6.5.4 Validation of experiment C038 (Largest deflection)

Experiment C038 has the largest deflection. The question is whether both ComPropApp simulation methods are still able to predict the performance accurately. Figure 6.16 shows the comparison between the simulations and the experimental deflection. The wake peak seems to be overestimated by both simulations, whilst the rest of the revolution is in good agreement. It is visible by comparing figures 6.14 and 6.16 that the noise on the signal has become much larger. This means that the uncertainty is mainly based on differences in the flow and not caused by uncertainty from the measurement (which would have led to approximately the same 2σ -interval for each simulation). This is also visible when plotting a single blade with its measured 2 standard deviation interval as in figure 6.17. The uncertainty interval of the less deformed blade in experiments C036 and C034 (see figures 6.11 and 6.15) did not show the large uncertainty after the wake peak, only before the wake peak. This might indicate that for higher loads, the blade does start to vibrate after the wake peak excitation, but can not be stated with any certainty. Therefore a real-time signal experiment has to be executed.

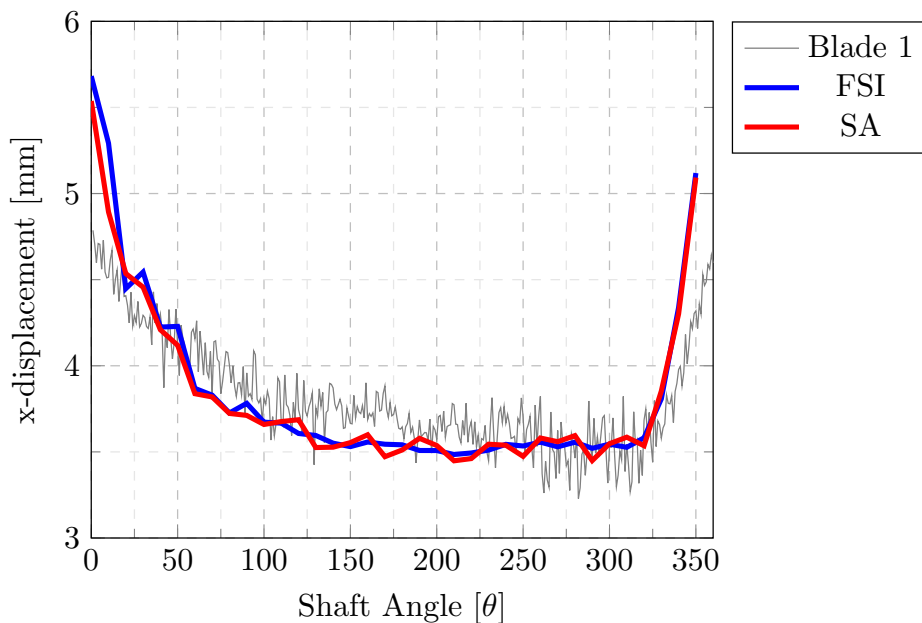


Figure 6.16: Blade deformation in x-direction of C038 through FSI, SA and experiment. ($V = 4$ m/s, $J = 0.63$, $n = 1119$)

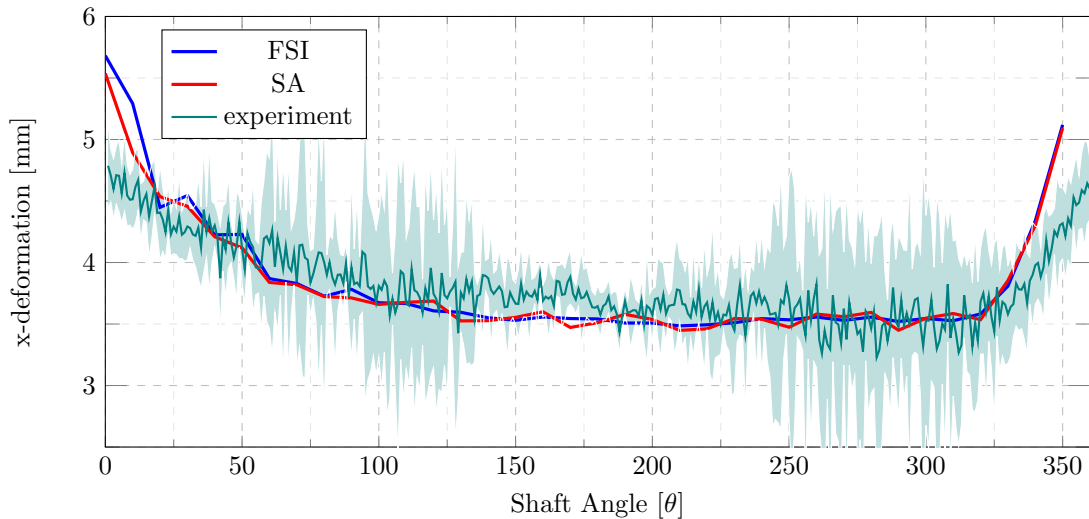


Figure 6.17: Blade deformation in x-direction with uncertainty bounds for experiment C038. ($v_a = 4$ m/s, $J = 0.63$, $n = 1119$ rpm)

The fact that the simulations both overestimate the deformation in the wake peak could be caused by the fact that too few blade positions (36) were considered. More blade positions might be necessary to gradually encounter this flow difference. Therefore, a simulation with more (72 blade positions must be performed). With the knowledge that the deformation with the smallest deformation was predicted accurately and the simulation with the largest deformations had issues in estimating the deflection in the wake peak. It is decided to validate one more COMPROP2 experiment with a middle range value. This will be experiment C036.

6.5.5 Validation of experiment C036 (medium deflection)

In figure 6.18, the results for experiment C036 (medium deflection) are shown. Again, it is visible that the simulations overestimate the wake peak deflection. This is as mentioned before, probably caused by the deficit in blade positions. It is also noticeable in figure 6.19 that the uncertainty region after the wake peak has become much smaller compared to experiment C038. This might indicate that the conditions in experiment C038 were a reason for the blade to resonate. In C038 Much higher thrust and rotational frequency are encountered compared to the other two simulations.

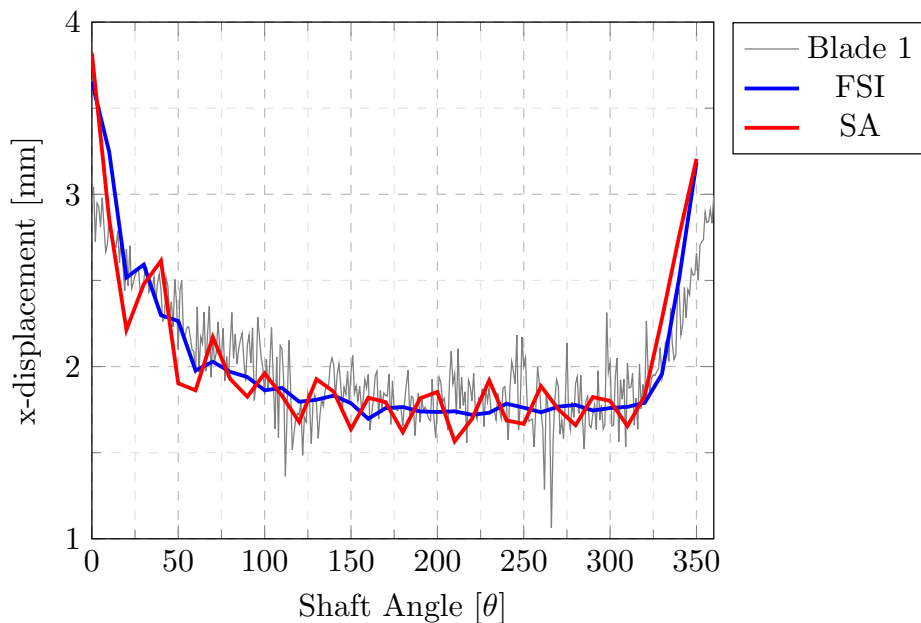


Figure 6.18: Blade deformation in x-direction of C036 through FSI, SA and experiment. ($V = 4$ m/s, $J = 0.74$, $n = 960$)

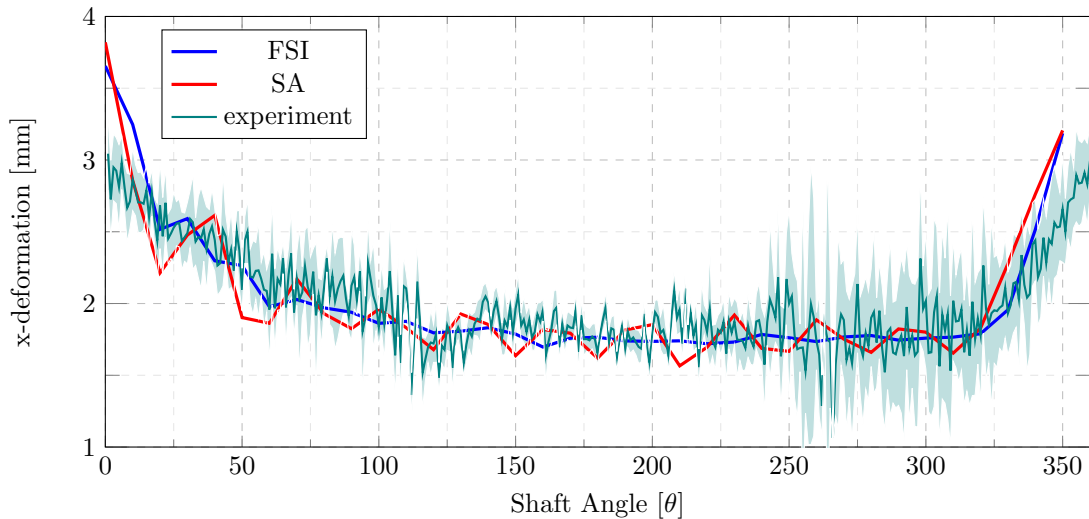


Figure 6.19: Blade deformation in x-direction with uncertainty bounds for experiment C036. ($v_a = 4$ m/s, $J = 0.74$, $n = 960$ rpm)

6.5.6 More blade positions in experiment C036

It was shown that the larger the thrust and torque on the blade get, the bigger the error between the simulations and experimental blade displacement got. One potential cause for this expanding error might be that the number of blade positions considered is too low to encounter the wake peak properly. This could cause abnormally and instantaneously high blade loading in the simulations. To investigate this hypothesis, experiment C036 is repeated with a double number of blade positions. As stated, the ComPropApp becomes increasingly divergent and time-consuming by increasing the number of blade positions. The simulation of experiment C036 with 72 blade positions took 12 hours and was still at an error norm of 20 %. (1 % is considered converged) After these 12 hours, the simulation was terminated due to a maximum number of iterations that was reached. The simulations containing 36 blade positions took approximately 3 hours to reach the 1 % error norm, thus this exponential time consumption is a serious issue.

If several FEM iterations (a complete Unsteady FSI loop) are analyzed, this 20 % error makes also little sense, as is shown in figure 6.20. It shows that the variation between the iterations is marginal so a 20 % error norm makes not much sense. Thus a study into a deeper understanding of the convergence criterion and how the QN-ILS process influences the simulations is a wise idea to fully understand why this convergence issue exists and how it could be resolved.

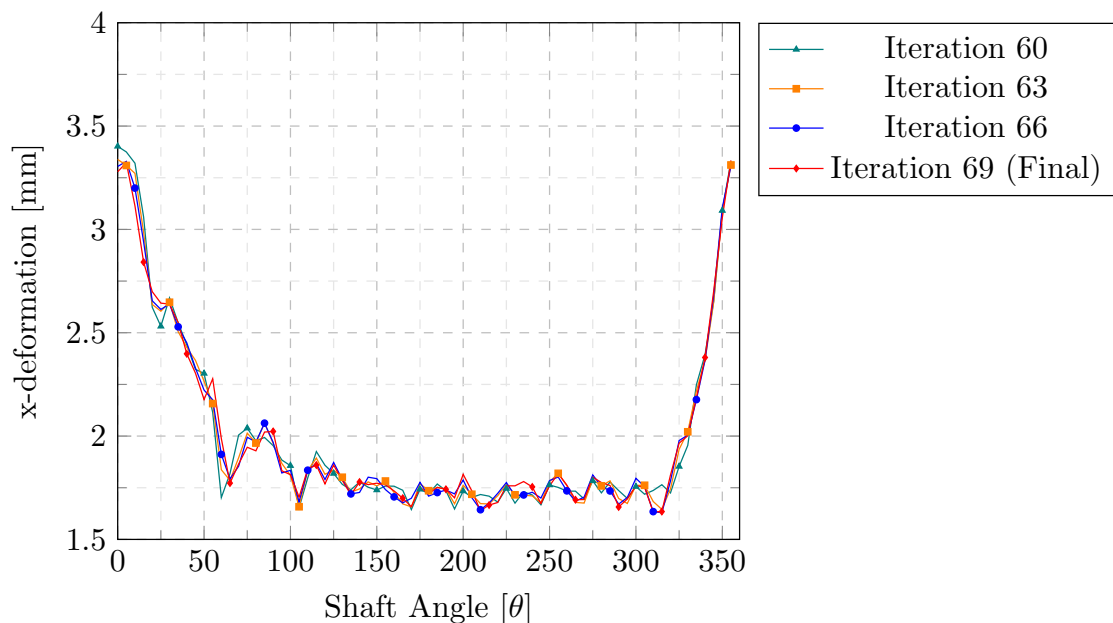


Figure 6.20: Blade deformation in x-direction for several iterations of experiment C036. ($v_a = 4$ m/s, $J = 0.74$, $n = 960$ rpm)

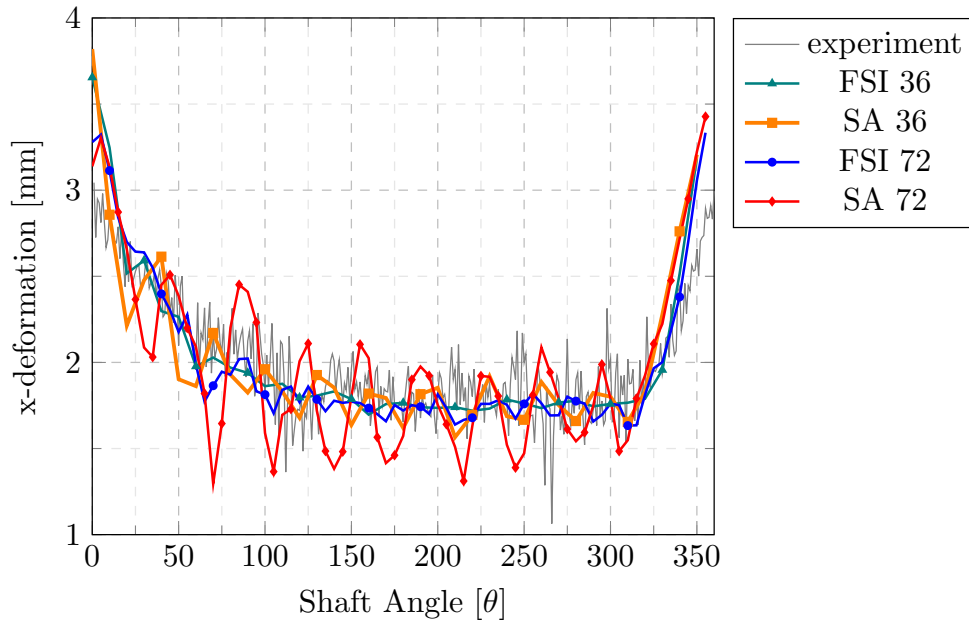


Figure 6.21: Effect on results for different number of blade positions for experiment C036. ($v_a = 4$ m/s, $J = 0.74$, $n = 960$ rpm)

As the results still look similar to that of the C036 simulations with 36 blade positions. It is still possible to determine whether the deflection in the wake peak got smaller. Figure 6.21 shows the effect of a different number of blade positions. It can be seen that the unsteady FSI results are not influenced that much aside from the difference in the vibration magnitude, even though the 72 blade positions simulation was far from being converged. The stress Analysis results do show a much larger difference in the vibration magnitudes. As the simulation was not converged, it can not be said whether this is an actual vibration happening in reality, or a numerical artifact which smoothens over more iterations.

Figure 6.21 does show that the error at the wake peak did actually get smaller (FSI and SA are much lower at shaft angle $\theta = 0$). But the error is still present. So more precise simulations are needed find out if this error at the wake peak decreases to zero by adding even more blade positions. The next check must be to double the number of blade positions again. For now, this does not make sense to perform as the 72 blade position case already diverged. One can imagine what happens with 144 blade positions.

6.6 Conclusions and recommendations

In this and the two previous chapters, it was validated that the ComPropApp is well capable of numerically predicting the deformation of flexible propellers. For simple open water conditions, the steady fluid-structure interaction module is sufficient. In terms of hydrodynamic performance and deflection this is in good agreement with experimental results. If on the other hand, one is interested in a more realistic non-uniform wake field that a propeller encounters in reality, the unsteady fluid-structure interaction module is necessary. In chapter 5 it was shown that through modifications of the code, this module is also capable of predicting the non-uniform performance. In chapter 6 the tool was shown to accurately predict the deformation of experiments executed in a cavitation tunnel for minor deformations. The larger the thrust on the propeller got, the less accurate the simulations became and both simulation tools (unsteady FSI and Stress Analysis) tend to over predict the deformation in the wake peak. It was also shown that the added mass is somehow not attributed correctly, this was proofed by a numerical damping test which showed that the blade vibrates at the dry eigenfrequency. Furthermore did this small found damping ratio of $\zeta = 0.016$ contribute to convergence issues.

The tool is not yet capable to prove how the blade vibrates within a revolution. And whether the sharp wake peak excites resonance frequencies. This has a couple of reasons:

- The experimental method known as *Ensemble averaging* turned out to be unsuitable to measure those vibrations as only average deformations over a large number of revolutions are known. If one is interested in studying those resonance vibrations, one must use an experimental setup where the deformations are traced real-time.
- From the numerical perspective, the simulations became too time-consuming due to the geometry construction package P4C. For adding more data points per revolution, which was deemed necessary, the

simulation became too lengthy. From a BEM flow solver perspective, this time consumption is unwanted, as the elegance of the BEM method over CFD methods is its computational speed.

- Convergence issues arose hand in hand with the above-mentioned point. It would be wise to consider developing a quasi-steady approach where first through a steady FSI simulation the mean deformation is quickly calculated and converged before the non-uniform wake field is applied. This might seriously speed up operations.
- experiments with a less sharp wake peak might be useful. A more gradually developing peak would decrease excitation in the wake peak. It would probably lower uncertainties in the experimental data as well. Finally, would it also help speed up the simulations as less blade position points have to be considered for accurate results.
- Examining the convergence criteria and the QN-ILS method in general might improve the program. The more complex the cases got, the more serious the convergence issues were. Especially with small damping ratios, the vibrations seem not to be resolved by the QN-ILS method. A possible solution might be to apply the criterion on each blade position, instead of on a combined error on all modes. Then would each considered blade position be checked separately. This would also provides the user with more information of why a case is diverging.

With the confidence in the steady FSI module and the lessons learned from the unsteady FSI- and Stress Analysis modules. The second goal of this project can be executed. In all previous cases, the simulations were executed with the c4-40 propeller. Thus an equal simulation leads to equal results. The real question regarding flexible propellers is: *What geometry parameters influence the design of flexible marine propellers?*

Before this design space is explored, in the next chapter the theory found in literature regarding propeller design is discussed.

7 Design study: design of flexible propellers

7.1 Introduction

In chapter 2, a literature study was done to understand the parameters that control propeller performance. In chapters 4 through 6, the ComPropApp was validated as a tool to study the deformation and hydrodynamic performance of marine propellers now completed. It can be used to study how a flexible propeller can be designed to be efficient and relieve the pressure on the blade, whilst considering the deformation throughout the simulations. As the unsteady FSI module was unable to efficiently simulate propellers in terms of computational time, it was chosen to only simulate propellers in open water. This does mean that the time-dependent deformation and pressure distributions can not be investigated when the propeller moves to the wake peak.

The goal of this study is to present future researchers in the research group a overview of parameters which were shown to relieve pressure. They will still need to be verified to also relieve pressure adequately in a non-uniform wake field. The main idea behind applying flexible materials is that the propeller can unload itself through deformation to obtain more favourable pressure distributions. Especially in the wake peak where the pressures are much higher compared to the rest of the revolution.

In section 7.2, the parameters that will be used are explained. The methodology used to alter propeller geometry is also explained. Afterwards, in section 7.3, the deformation and pressure distribution of the Wageningen c4-40 is discussed. In section 7.4, the criterion that is used to evaluate the propeller pressure is introduced. In section 7.5, the results for varying single propeller geometries are presented which lead to the final selection of parameters used in the multi-variable analysis. The set-up and methodology of this multi-variate study are discussed in section 7.6. The results of this study are presented in section 7.7. From these results, a quick study is executed into how critical tip pressures could be reduced is presented in section 7.9. And finally, in section 7.10, all lessons learned from this study are presented in a chapter conclusion.

7.2 Parameter identification & Methodology

7.2.1 Parameter identification

From a propeller designer's perspective. There are several parameters which affect the deformation of the propeller blades. The main goal of all these parameters is to affect the distribution of forces and moments on the blade in such a manner, that the blade is unloaded to the desired setting. The parameters which were identified in chapter 2 and several more parameters are discussed in this section. The most important parameter to de-pitch a propeller is pitch itself. By increasing the propeller pitch, the angle of attack increases which in turn results in a higher lift of the blade sections. Thus initially increasing pitch could lead to a deformed blade geometry which is equal to the undeformed standard propeller geometry. These higher lift coefficients could also result in higher pressures. In chapter 2 it was discussed that studies also have shown reduced cavitation for higher pitch settings. It should be studied what the beneficial and disadvantageous effects of increasing the pitch are.

Another parameter which was identified in chapter 2 is propeller skew. Skew influences mostly the propeller geometry and the way forces are distributed along the blade. The effects of skew were mentioned in chapter 2. The effects include improved efficiency and cavitation behaviour. Furthermore does skew highly influences the way in which stress is distributed along the blade.

Where skew introduces initial deflection in the yz -plane; (following the ITTC and Carlton guidelines of coordinates [4] [5]), rake introduces deflection in the xz -plane (either positive or negative). This parameter should influence the way in which the propeller is allowed to deflected in operation and affect the pressure development along the blade. In chapter 2, the observed effects include reduced tip pressures and slight efficiency gains for positive (upstream) rake.

Chord length defines the length from the blade and thus affects the inertia of the blade, the resistance towards bending. It also influences the way a blade tends to deform and bend during operation. This parameter was not defined in the literature study, it is however an important geometry parameter of the propeller thus it will be included as well. Since it influences the bending behaviour, it might therefore be a useful parameter as it could alter the amount of bending per unit of deformation (Bend-twist coupling).

Camber was not yet identified in chapter 2. Camber defines the amount of curvature of the wing-like sections of the blade. No camber denotes an symmetrical foil and high camber means a foil where the upper side (suction side of the propeller) is thicker and more curved. This positive camber is visualized in figure 7.1. In studies into the effects of camber, the results include higher efficiency for marine propellers and decreasing the risk of cavitation by Nouri and Mohaddi (2018) [49]. Furthermore does the shape largely affects the lift and drag coefficients of the foil-like sections. Thus camber is identified as an important parameter.

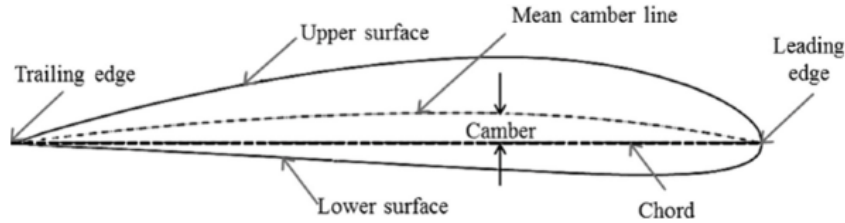


Figure 7.1: Example of an positive camber distribution. Source: Ebrary [50]

The thickness of the blade also plays an important role as it determines how much blade deflection can be achieved. It however might be a fairer parameter to alter the Young's modulus as the blade thickness is a dangerous parameter to alter and investigate with BEM computations. This is dangerous since the effects of tip vortices are not well simulated in BEM-methods whilst the implications on cavitation are large. Together with the Young's modulus, anisotropy of the material is also extremely important. As this also determines how much bending can be obtained. Unfortunately, Trident/VAST is currently unable to model anisotropic solids thus the effects of these cannot be studied in this study. In further research anisotropy should be included as it is the most important parameter in the effects of bend-twist coupling.

7.2.2 PROPART and propeller geometry modification

The program used to alter the propeller geometry is known as PROPART, which is a collection of cooperating MATLAB functions that let the user alter the propeller, analyze the cavitation behaviour and a lot of other tools as well. Within PROPART a .ppg file (the file that communicates the geometry to PROCAL and the ComPropApp), can be loaded and the values for the parameters can be altered. This could be done by hand as well, but PROPART uses Bezier curves to ensure the newly generated propeller geometry is smooth and suitable as propeller geometry. PROPART also uses a user-friendly interface to stay in control of the new propeller geometries. This turned out not to be the case when altering propellers manually. This resulted in unexpected and unrealistic propeller geometries. Within this study, only the *Bezier-Modify* command has been used to deform the c4-40 propeller to new propeller geometries. Besides this Bezier-Modify function, a vast amount of other propeller generation methods are available. To stay in control and due to time limitations. It was chosen to only alter the propellers with this single tool.

7.3 Deformation standard c4-40 Propeller

Before altering parameters which are supposed to change the deformation behaviour. First, the deformation of the standard c4-40 propeller is investigated. This to gather insight into which parameters could be altered to obtain the new propeller. It is also necessary, as there has to be a baseline propeller to which newly generated propellers can be compared with. The final goal is to deform the propeller to a new optimum in terms of efficiency and/or cavitation behaviour. An operating point at $J = 0.66$, $v_a = 3.4 \text{ m/s}$ and $n = 900 \text{ rpm}$ was established (which is slightly below the rigid propeller optimum at $J = 0.73$, but from the results in chapter 4, it was shown that at that advance ratio the ComPropApp was not estimating the performance accurately. From figure 2.5, it was shown that the efficiency rapidly drops right after the theoretical optimum. Thus besides that numerical uncertainty, a realistic propeller always operates slightly below the theoretical optimum to ensure room for inflow variations. It chosen to perform steady FSI calculations, as it was giving equal results as the unsteady FSI module and is quicker in executing open water simulations.

First, in figure 7.2, the chosen coordinate system is explained. Thus the direction of the propeller is forward and the rotation is rightward, in agreement with PROCAL/PropArt definitions.

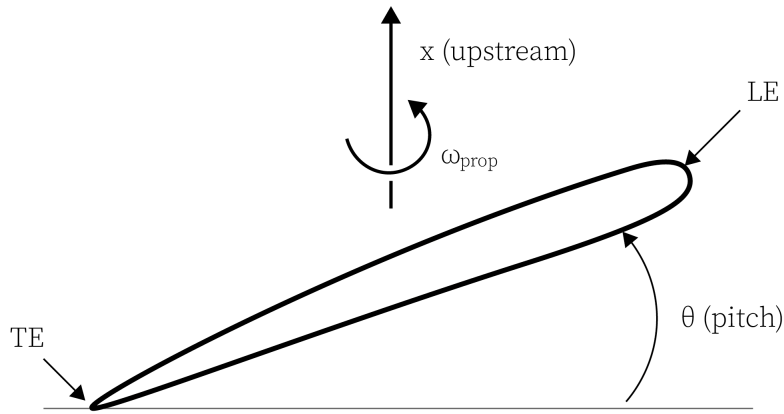


Figure 7.2: Definition of the coordinate system used.

In figure 7.3 the corresponding blade deformation (a), and pitch angle deformation (b) are shown for the standard c4-40 propeller. At this point, the Young's modulus of SikaBlock M980 of 3.5 GPa is used. The question now is, how the above-mentioned propeller geometry parameters alter these deformation distributions. And how those in turn, affect the performance of the propeller.

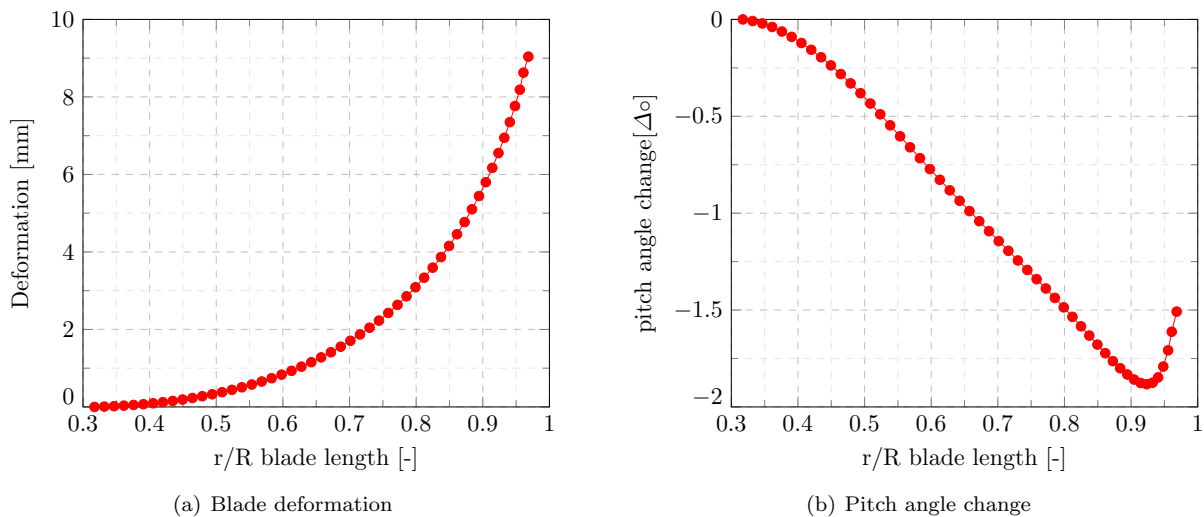


Figure 7.3: Deformation and pitch angle change over the blade length for $J = 0.66$, $v_a = 3.4$ and $n = 900$ rpm.

It might however be a fairer comparison to evaluate the performance of the to-be-designed flexible propeller with its metallic counterpart. The whole idea is to alleviate the pressure loading and thus cavitation of the propeller by exploiting the bend-twist coupling of flexible materials, whilst minimizing the hydrodynamic losses of the propeller. Furthermore, the c4-40 propeller was not intended to be used as a flexible propeller but as a conventional metal propeller. Thus the performance of a flexible c4-40 propeller is not expected to be good. Within PROCAL/ComPropApp there is an calculation option known as *Set Point Iteration*. This method converges to a user defined thrust. This is obtained by altering the propeller speed each iteration. This way the propeller ensures the same propulsive condition as the metal c4-40 propeller. This way, a fairer comparison of the hydrodynamic performance and the pressure distribution with the metal propeller is made.

From a preliminary PROCAL (rigid propeller) simulation, the thrust is determined to be 0.3792 kN at the operating condition. This is also achieved when running a bronze propeller in a deformable simulation. Thus the assumption that metallic propellers are rigid still holds. For the SikaBlock Propeller a slight thrust decrease in thrust and efficiency are observable, as is shown in table 7.1. This is thus caused by the deformation of the much weaker material.

Table 7.1: Thrust and open water efficiency for three different types of computations on the c4-40 propeller.

| | PROCAL bronze | CPA bronze | CPA SikaBlock M980 |
|--------------|---------------|------------|--------------------|
| T [kN] | 0.3792 | 0.3792 | 0.3784 |
| η_o [-] | 0.704 | 0.703 | 0.695 |

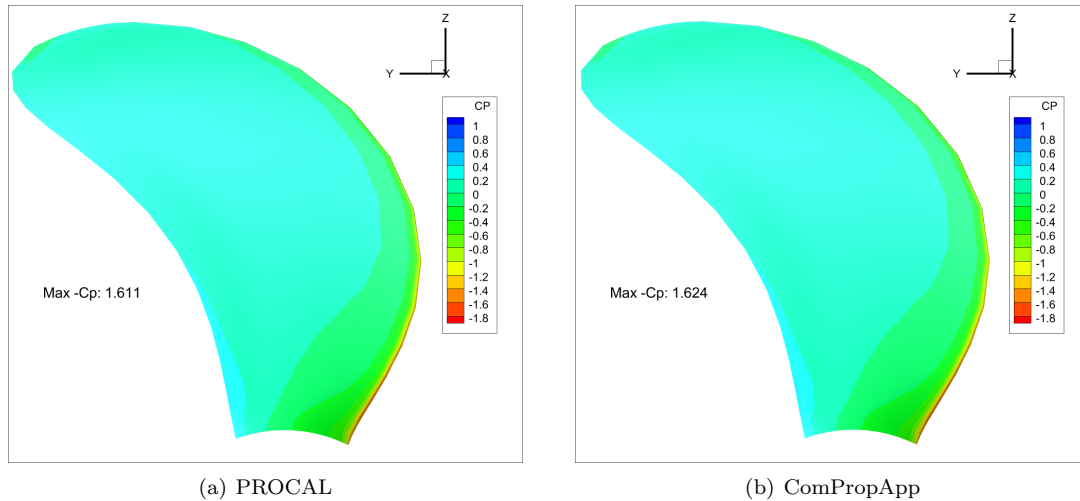


Figure 7.4: Pressure side pressure distribution of the bronze propeller through PROCAL and ComPropApp.

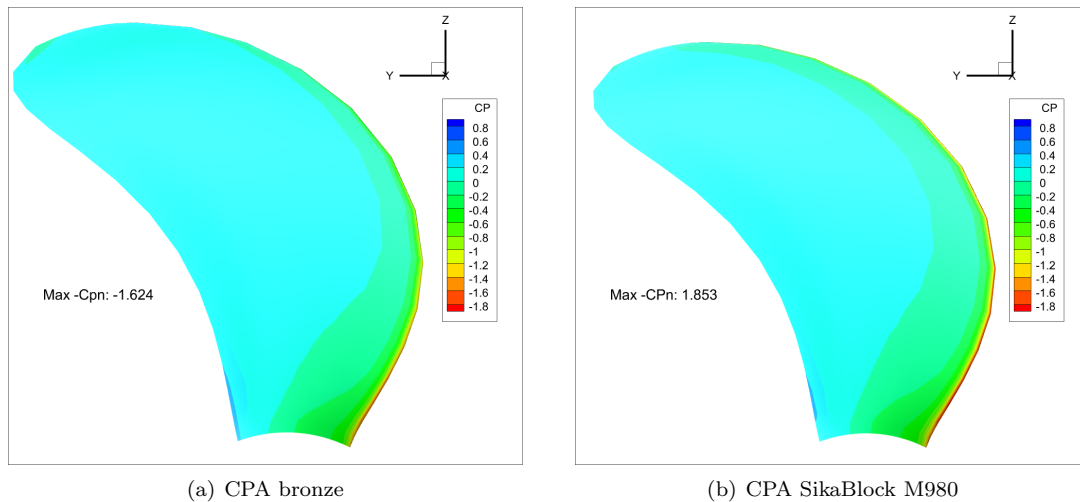


Figure 7.5: Pressure side pressure distribution of the bronze and SikaBlock propeller through ComPropApp simulations.

The bronze propeller shows a pressure distribution through PROCAL and the ComPropApp as shown in figure 7.4. In figure 7.5 the pressure distribution for the bronze and the SikaBlock M980 propeller are visualized. The maximum negative pressure on the blade did increase for the softer material. No significant changes in the pressure distributions did occur by lowering the material's Young's modulus but it does confirm that parameters need to be altered to design a decent flexible marine propeller.

7.4 Cavitation area Criterion

With PROCAL, simulations with cavitation are possible and validated to capture some *stable* forms of cavitation. This was shown in chapter 2. These sums are however much more time-consuming compared to a steady FSI ComPropApp simulation. When propellers are made from flexible materials. The propeller can not be assumed rigid anymore, these vibrations and deformations are affecting the cavitation behaviour of propellers. Thus in initial propeller design studies, this might not be the best method to investigate cavitation risks of propeller

blades. Furthermore is the effectivity of the cavitation module of PROCAL not been validated or verified for flexible propellers. It was therefore chosen not to use cavitating sums in this study.

The ComPropApp does provide the pressure distribution along the blade for each iteration. This is shown for the c4-40 propeller for the suction side (a), and pressure side (b) in figure 7.6.

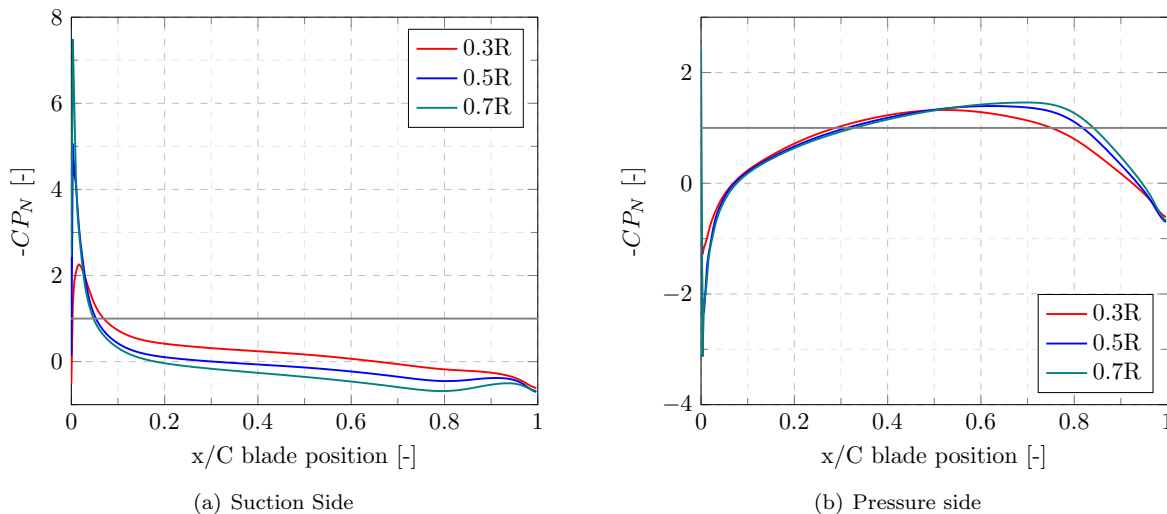


Figure 7.6: Natural Pressure coefficient distribution on the suction- (a) and pressure side (b) of the c4-40 propeller at $J = 0.66$.

In figure 7.6, the pressure distribution at three arbitrary radial stations are shown for clarity. But the output consists of 13 radial stations ranging from the root up to the tip. This natural pressure coefficient C_{PN} is calculated as in equation 7.1. Here p_{shaft} denotes the undisturbed static pressure at the shaft and V_{ref} is the reference velocity which is the propeller tip velocity. It was chosen to use the natural pressure coefficient over pressure coefficient (C_P), as this also includes the effect of the rotational speed of the propeller, which is useful since the *SetPointIteration*-method alters this rotational speed to match an equal thrust for each propeller.

$$C_{PN} = \frac{p - p_{shaft}}{\frac{1}{2}\rho V_{ref}^2} \quad (7.1)$$

Thus a lower pressure coefficient denotes a lower local pressure. Per definition, cavitation occurs when the local pressure drops below the vapour pressure of water. Thus the lower this C_{PN} value gets, the higher the risk of cavitation is. Therefore it makes sense to calculate the area of these negative pressure coefficients visible in figure 7.6a at the suction side, or this negative mid-chord pressure rise in figure 7.6b at the pressure side of the blade. To ensure only relevant negative pressures are considered, a threshold of $C_{PN} = -1$ is used. This negative pressure coefficients can then be integrated over the non-dimensional blade length to obtain a number which tells something about the amount of critical low pressure. It should be noted and remembered, that although this method shows similarities with cavitation number σ , it is nowhere near a final statement on whether the propeller will cavitate or not. It can only be used to compare large numbers of generated propellers as an initial assessment of pressure development and the risk of cavitation.

This number will from here on be denoted as $A_{Cav,Suc}$ or $A_{Cav,Pres}$ and contains the pressure coefficient areas from radial stations 0.3R up to 0.9R. The radial stations outside this region are neglected as the tip and hub regions are very unstable due to numerical errors in these regions. For the bronze c4-40 and the SikaBlock M980 propeller these cavitation area numbers are shown in table 7.2. This table shows that the softer propeller has a higher pressure development on both the suction and pressure side. In the next section, the linear response (systematically altering a single parameter) will be analyzed for several parameters. The main goal is to check whether it is possible to get the cavitation area numbers below the values for the bronze propeller as shown in table 7.2.

Table 7.2: Cavitation area numbers for the c4-40 propeller.

| - | $A_{cav,suc}$ | $A_{cav,pres}$ |
|-----------------------------|---------------|----------------|
| c4-40 Bronze | 0.3287 | 0.7827 |
| c4-40 SikaBlock M980 | 0.6093 | 1.1723 |

7.5 Single parameter variations

Before the multi-variate design space including all parameters and their dependencies/correlations will be investigated, the effect of varying single parameters will be studied. This is to check whether the parameters influence the pressure distributions, and possibly increase the open water efficiency as well. As said, all propellers from hereon after are fixed to deliver the same thrust as the bronze propeller: 0.3792 kN.

7.5.1 Pitch

The first parameter which will be altered is pitch. There are many ways in which the pitch distribution can be altered. For simplicity's sake only the mean pitch will be modified (average pitch found along the blade) by increasing or decreasing the pitch values at the hub and the tip as shown in figure 7.7a.

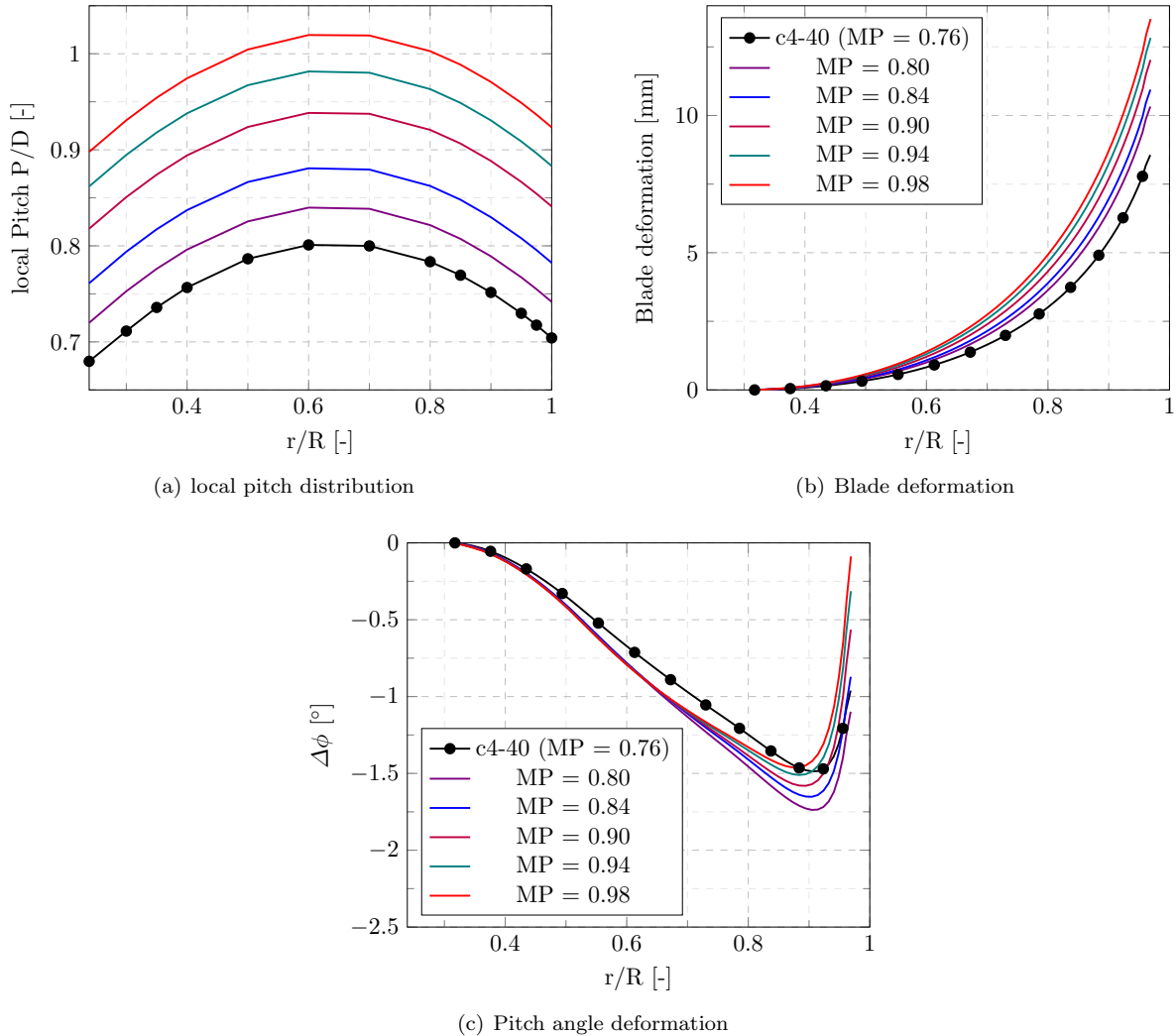


Figure 7.7: Deformation and pitch angle change for different mean pitch propeller geometries.

Figure 7.7b, shows the results one expects when increasing the propeller pitch. By increasing the pitch, the angle of attack increases and thus the loading increases which yields higher deformations. This effect is unexpectedly less present in terms of pitch angle deformation in figure 7.7c. Increasing the pitch angle yields lower pitch angle deflection at the tip (around $0.9R$), where it looks as if the tip is becoming unstable as for all propellers the tip deformation is rapidly decreasing. It could also mean that for too high tip pitch values, the tip becomes overloaded and highly unfavourable effects start to happen here.

Table 7.3: Cavitation area numbers and open water efficiencies for different mean pitch values.

| Prop ID | A_{Suc} | A_{Pres} | η_0 |
|---------------------|------------------|-------------------|--------------|
| c4-40 Bronze | 0.3287 | 0.7827 | 0.704 |
| c4-40 M980 | 0.6093 | 1.1723 | 0.695 |
| Mean Pitch = 0.80 | 0.5867 | 1.4253 | 0.6991 |
| Mean Pitch = 0.84 | 0.5177 | 1.6699 | 0.7064 |
| Mean Pitch = 0.90 | 0.4285 | 2.0562 | 0.7145 |
| Mean Pitch = 0.94 | 0.3597 | 2.3630 | 0.7189 |
| Mean Pitch = 0.98 | 0.3057 | 2.6478 | 0.7220 |

This unfavourable behaviour is also visible in the results in table 7.3. The cavitation area on the pressure side is rapidly increasing for higher pitch ratios. The cavitation area on the suction side and open water efficiency are both changing favourable whilst increasing the mean pitch. Both observations make sense, as the blade deformations cause less pressure on the suction side. Yet for the pressure side pressures, this seems unfavourable. It is wise to analyse these pressure distributions more thoroughly instead of a single number for the complete blade.

The pressure distributions for the propellers with mean pitch 0.80 and mean pitch 0.98 are shown in figures 7.8 and figure 7.9. They show that the suction side cavitation area number is a decent indicator in the pressure distribution as both propellers have the high pressure on the leading edge, which drops whilst increasing propeller pitch. For the pressure side pressures however, the pressure area number becomes less conclusive. It seems as the cavitation area number is too harsh for mid-chord pressure coefficients (it could very well be that a pressure coefficient of $C_{PN} - 1$ is sufficient enough to avoid cavitation. Furthermore it is visible that a sharp leading edge pressure seems to be present for the less pitched propeller. It is however known that BEM codes tend to show numerical instabilities here. It can not be stated whether this high leading edge pressure peak is physical or a numerical artefact.

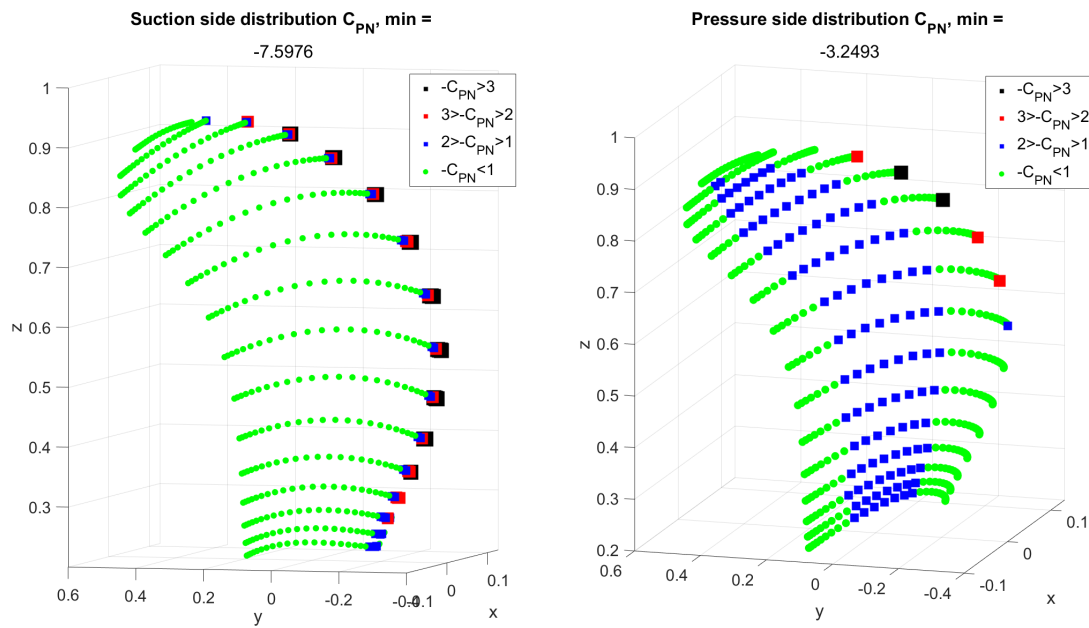


Figure 7.8: Suction and pressure side pressure distribution for mean pitch = 0.80.

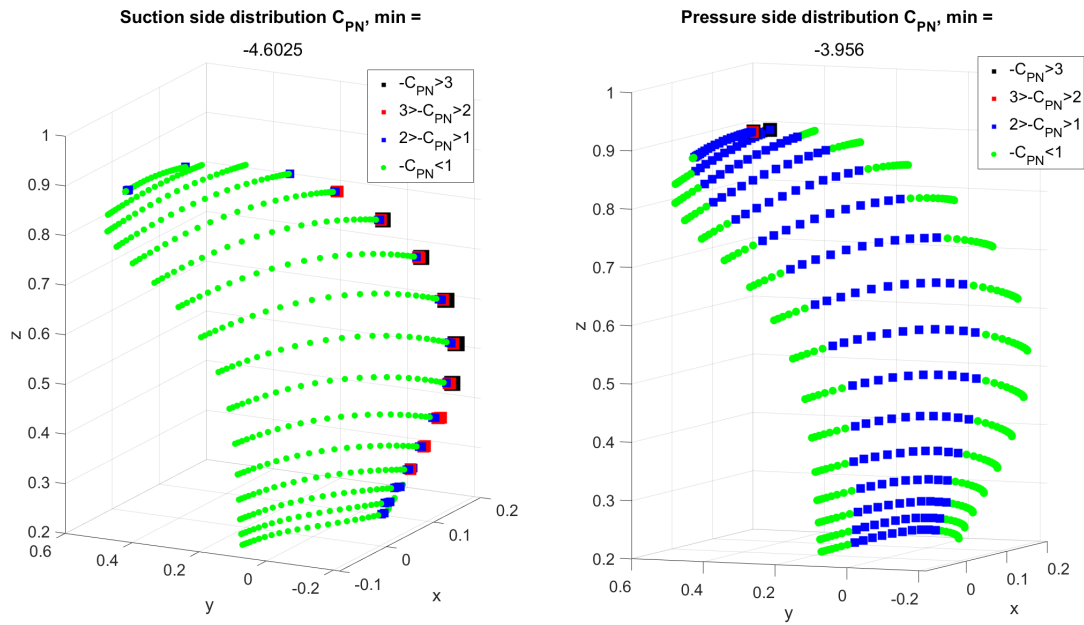


Figure 7.9: Suction and pressure side pressure distribution for mean pitch = 0.98.

7.5.2 Skew

Skew is one of the most influential parameters in propeller design. It completely alters the way forces are distributed over the blade. And thus affects how the flexibility can be used to de-pitch the propeller. Skew can be altered in several ways (maximum skew angle at the tip and skew distribution along the blade construct numerous possibilities). It was chosen to maintain the same skew angles at hub and tip and only alter the skew distribution along the blade.

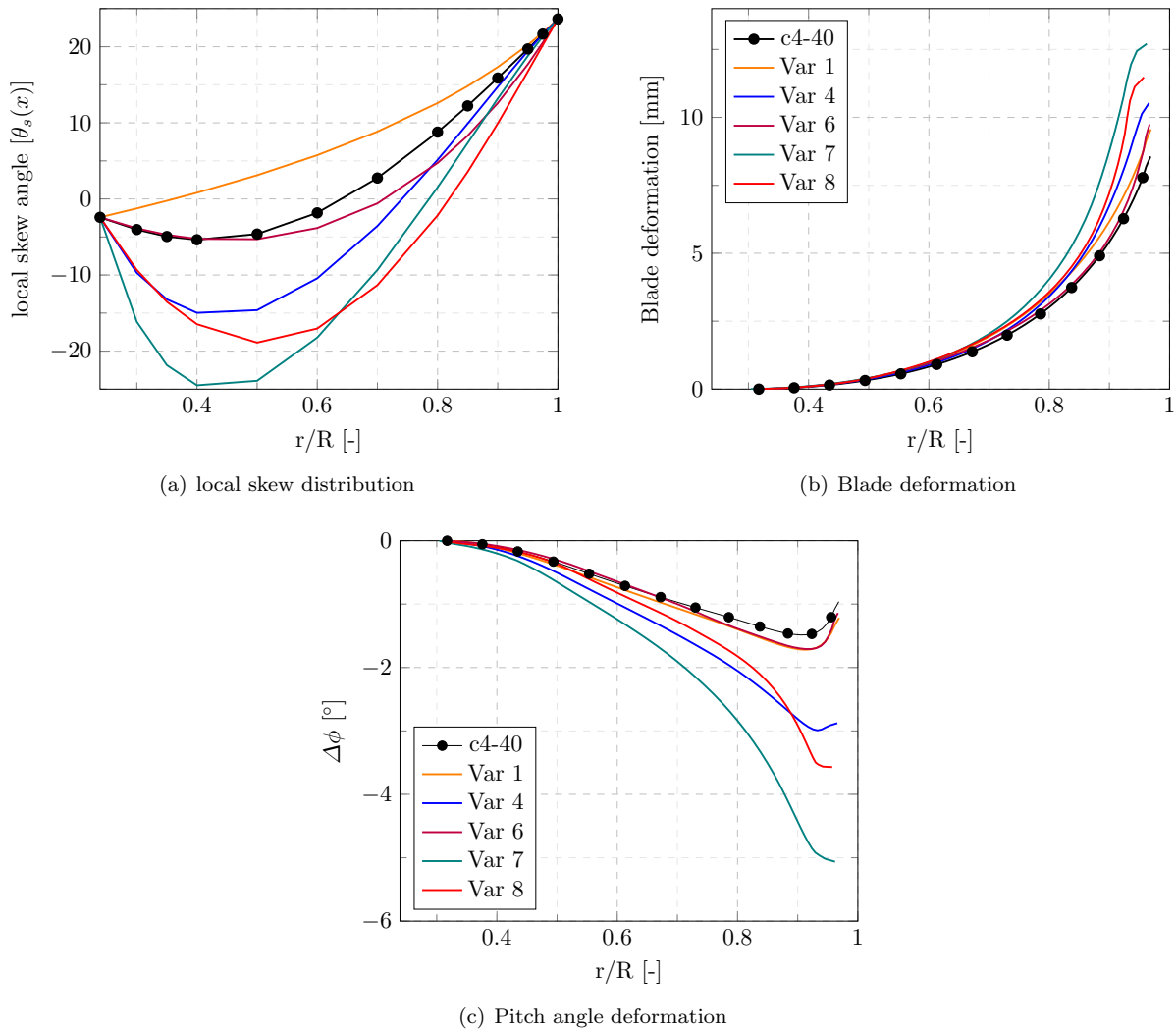


Figure 7.10: Deformation and pitch angle change for different skew distributions.

In figure 7.10, it is visible that more skew towards the leading edge of the blade (biased skew), the deformation and pitch angle deformation are becoming larger. And if the pitch deformations are compared to the pitch deformation that were obtained by increasing the pitch (see figure 7.10c and 7.7c) it is visible that the tip also deforms in a more stable manner.

Table 7.4: Cavitation area numbers and open water efficiencies for different skew distributions. (see figure 7.10a)

| Prop ID | A_{Suc} | A_{Pres} | η_0 |
|---------------------|------------------|-------------------|--------------|
| c4-40 Bronze | 0.3287 | 0.7827 | 0.704 |
| c4-40 M980 | 0.6093 | 1.1723 | 0.695 |
| Skew var 1 | 0.9227 | 1.4065 | 0.6889 |
| Skew var 4 | 0.3138 | 0.5997 | 0.6797 |
| Skew var 6 | 0.6418 | 1.1931 | 0.6927 |
| Skew var 7 | 0.1562 | 0.2833 | 0.6660 |
| Skew var 8 | 0.2721 | 0.5423 | 0.6791 |

This can be further elaborated by table 7.4, where it is visible that this increased skew reduces the cavitation area on both the suction- and pressure side of the blade. This beneficial cavitation behaviour is paid with a penalty on the efficiency which seems to decrease. Besides only examining the cavitation area criterion, the pressure distributions are also visualized to show which regions are affected more with large pressures. This is done for the supposedly best and worse skew variation propellers (variation 8 and variation 1 respectively).

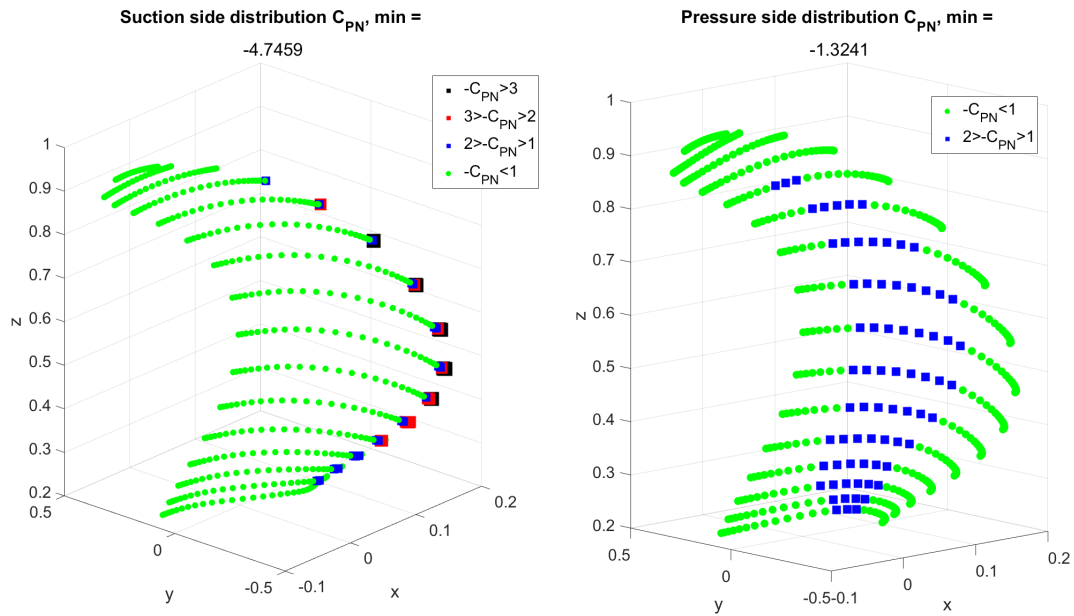


Figure 7.11: Suction and pressure side pressure distribution for skew variation 8.

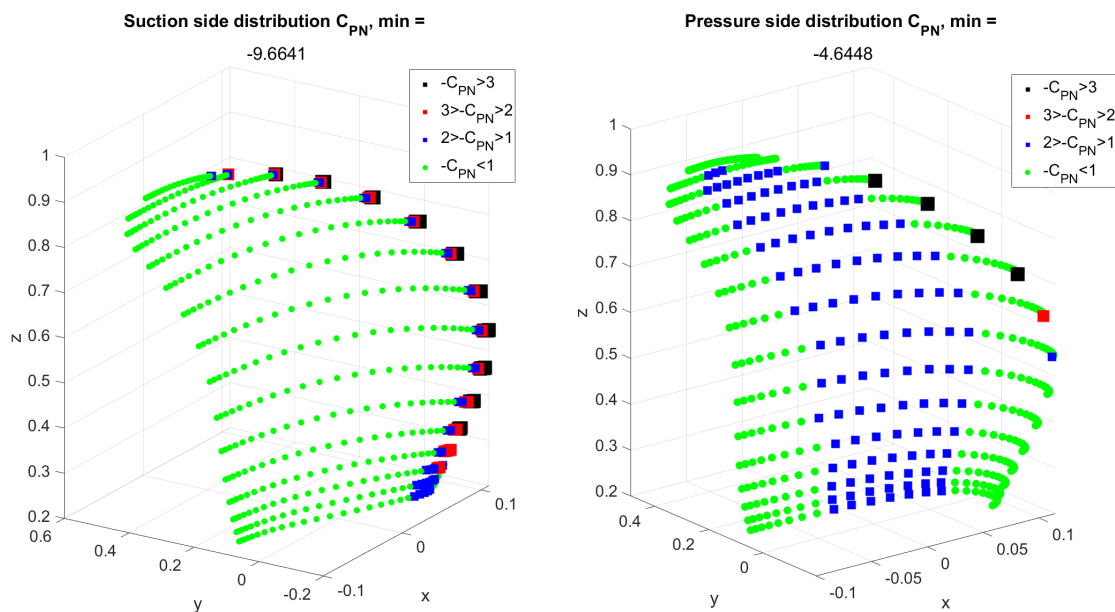


Figure 7.12: Suction and pressure side pressure distribution for skew variation 1.

From these distributions in figures 7.11 and 7.12, it seems that increasing the biased skew of the propeller results in less sharp suction side pressure at the leading edge. The amount of panels having larger minimum pressures than 1 is decreased as well. For the pressure sides, this biased skew seems to have eliminated the leading edge pressures. Again, these leading edge pressures are risky to evaluate with BEM codes but it seems that skew is a mechanism to alleviate leading edge pressures on both sides of the blade. The mid-chord pressure seems to have reduced in number of panels and the amount of negative pressure near the tip. These are both much lower for the higher skewed propeller in figure 7.11.

7.5.3 Rake

From literature, as was discussed in chapter 2, propeller rake was identified as a possible parameter to improve efficiency and relieve the tip pressures. Rake is a much more complex parameter to modify. Firstly, the distribution as shown in figure 7.13a is not as straightforward to modify as the rake distribution is less commonly described in literature. This means that the effects of applying positive- or negative rake are less known. This

leads to a trial-and-error approach which is also shown in the results in terms of deformation in figures 7.13b and 7.13c. Only slightly more deformation is obtained for negative rake (downstream rake). And the pitch deformation seems to be completely unaffected. These inconclusive results are further mystified by the results in table 7.5. The table shows that not a single conclusion can be drawn on the effects of rake modifications. It should be noted that this does not conclude that rake is an ineffective parameter in general. It shows that the generated rake modifications in this study were not effective. This is caused by the fact that little information can be found on how to effectively construct a rake distribution of a marine propeller.

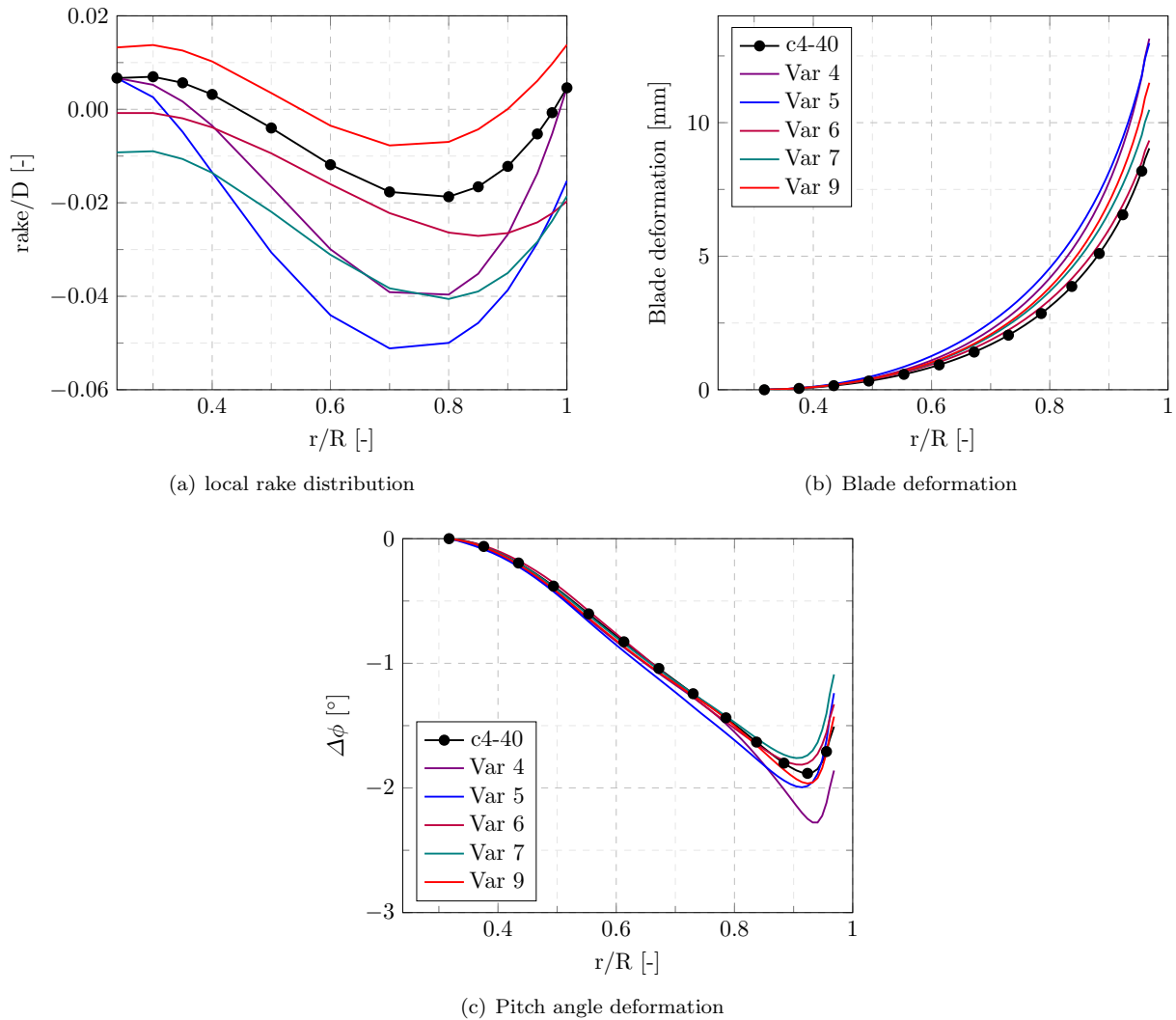


Figure 7.13: Deformation and pitch angle change for different rake distributions propeller geometries.

Table 7.5: Cavitation area numbers and open water efficiencies for different rake distributions. (see figure 7.13a)

| Prop ID | A_{Suc} | A_{Pres} | η_0 |
|---------------------|------------------|-------------------|--------------|
| c4-40 Bronze | 0.3287 | 0.7827 | 0.704 |
| c4-40 M980 | 0.6093 | 1.1723 | 0.695 |
| Rake var 4 | 0.8393 | 1.3939 | 0.6883 |
| Rake var 5 | 0.8585 | 1.4280 | 0.6898 |
| Rake var 6 | 0.5345 | 1.0695 | 0.6865 |
| Rake var 7 | 0.6706 | 1.2441 | 0.6896 |
| Skew var 9 | 0.6366 | 1.1813 | 0.6914 |

7.5.4 Chord length

The chord length is most likely an important parameter in propeller design and has an influence on deformation and consequently on the pressure distributions. In figure 7.14 the results for several chord length distributions

along the blade are shown. In figure 7.14b, the deformations of all variations are shown and it seems as if the chord length has little influence on the deformation which seems odd as a less wide blade should be easier to deform. In figure 7.14c, this hypothesis does hold for the pitch angle deformation. A less wide blade (the teal and blue lines) show much larger pitch angle deformation.

Interestingly enough, chord length variation 7, having a much thicker blade, has higher deformation at the root compared to thinner blades. This can be explained by the fact that wider blades are also capable of being loaded much higher. Furthermore, the method used to generate these propellers does not ensure that on both sides of the neutral length an equal length is present. Thus it could be that the bending moment on this blade has become significantly larger.

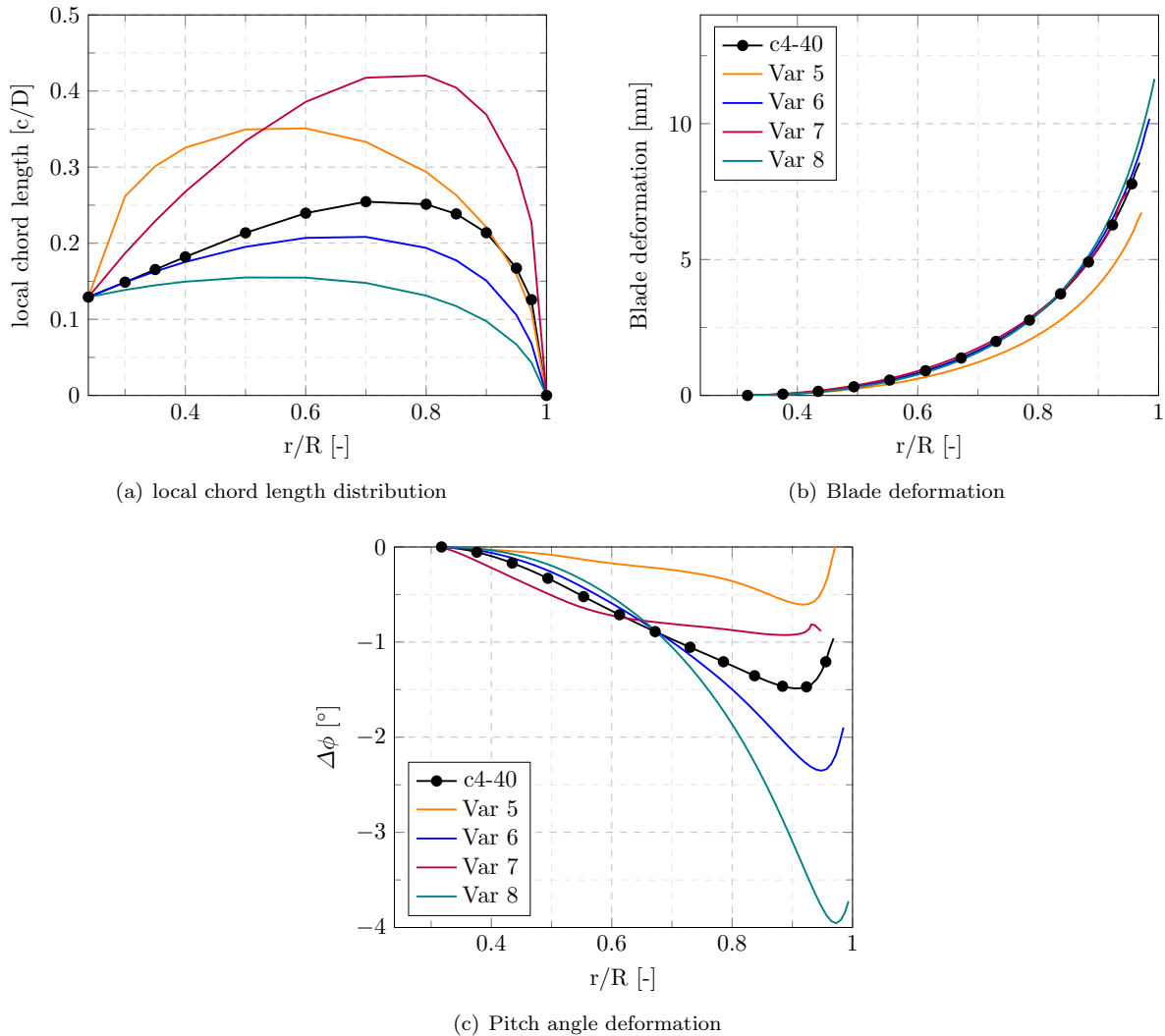


Figure 7.14: Deformation and pitch angle change for different chord length distributions.

The cavitation area criteria and open water efficiencies are shown in table 7.6. It shows that the blades with less wide blades (variations 6 and 8) yield a significant reduction in suction side pressure, but this is paid with the penalty of a much larger pressure side cavitation area. It does seem to improve the propeller efficiency. For wider propellers (variations 5 and 7), the opposite conclusion holds: higher suction side pressures, lower pressure side pressures and lower open water efficiency.

Table 7.6: Cavitation area numbers and open water efficiencies for different Chord length distributions. (see figure 7.14a)

| Prop ID | A_{Suc} | A_{Pres} | η_0 |
|--------------|------------------|-------------------|--------------|
| c4-40 Bronze | 0.3287 | 0.7827 | 0.704 |
| c4-40 M980 | 0.6093 | 1.1723 | 0.695 |
| Chord var 5 | 0.9580 | 0.7585 | 0.6838 |
| Chord var 6 | 0.3820 | 1.7244 | 0.7044 |
| Chord var 7 | 1.4205 | 0.5206 | 0.6453 |
| Chord var 8 | 0.1042 | 3.0618 | 0.7122 |

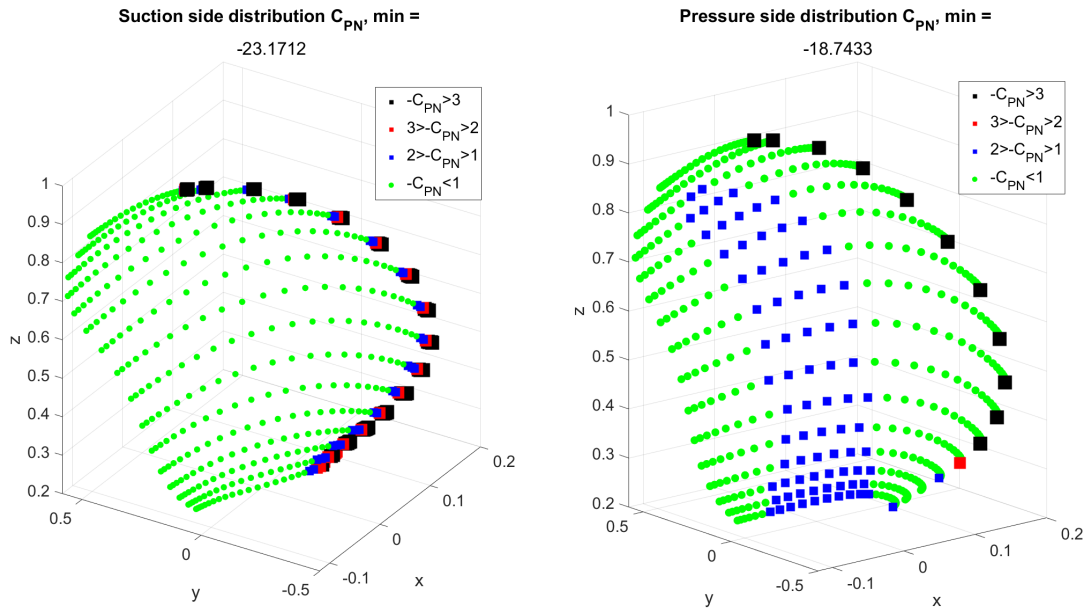


Figure 7.15: Suction and pressure side pressure distribution for chord length variation 7.

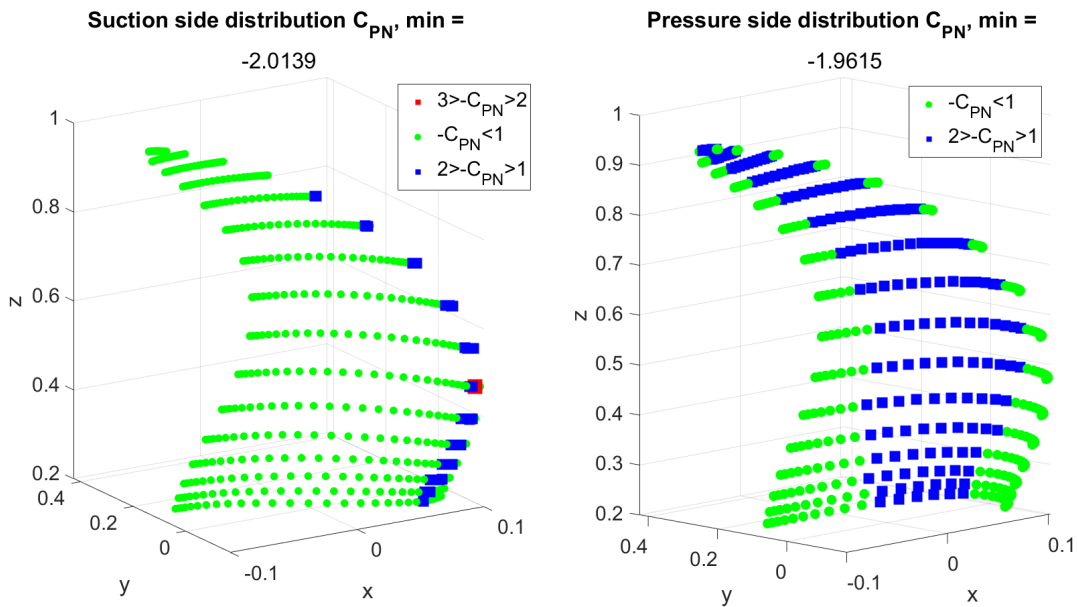


Figure 7.16: Suction and pressure side pressure distribution for chord length variation 8.

In figures 7.15 and 7.16, the development of the pressures is visualized. The propeller with a wider blade section is said to have high suction side pressures, which is verified by comparing the suction side pressures of the

two propellers. Note the extremely high minimum pressure found on the wider blade. This complies with the suction side cavitation criterion. But, the pressure side pressures raises some questions and concern about this cavity area number.

The criterion was much lower for chord variation 7 (figure 7.15) than for chord variation 8 (figure 7.16). But if the pressure along the blade is examined, it is visible that this is caused by relatively low pressures ($-C_{PN} = [1:2]$), whilst this is paid with an extremely large leading edge pressure area number. So decreasing the chord length, increases the risk of mid-chord cavitation. The risk of leading-edge pressures is not captured properly with this pressure side cavitation criteria. It could also be a numerical artefact, this was also noted when discussing the results of altering the skew. It is uncertain how to properly assess these leading-edge pressures with BEM models. It could very well be one of the shortcomings of BEM models. And to properly simulate the leading edge flow, CFD codes might be required. For this study, it will be ignored for the most part as no definite statements can be made on the pressures at the leading-edge.

7.5.5 Camber

Camber defines the amount of curvature in blade sections. As this parameter is less straightforward compared to the previous alterations in terms of how the resulting blade geometry looks like. In figure 7.17 camber variations with high and low camber respectively are plotted at $0.8R$, where the difference in camber is the highest. It clearly shows the difference in cross-section when altering the camber. The advantageous impact of higher camber is an increase in the angle of attack without altering the pitch of the propeller. This results in higher loading at the same propeller pitch angle. In figures 7.18b and 7.18c. this can be seen by the fact that higher camber results in higher deformation and pitch angle change. It also shows that lower camber settings, do not lead to significant smaller pitch angle deformation compared to the c4-40 propeller.

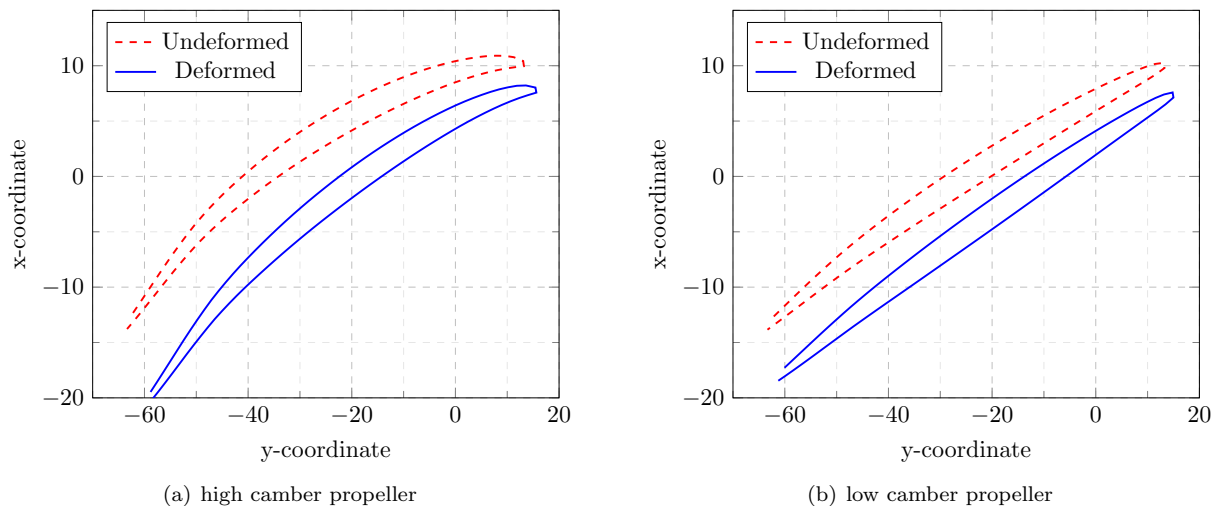


Figure 7.17: Blade cross sections for deformed and undeformed geometries of high (a) and low (b) camber at $0.8R$.

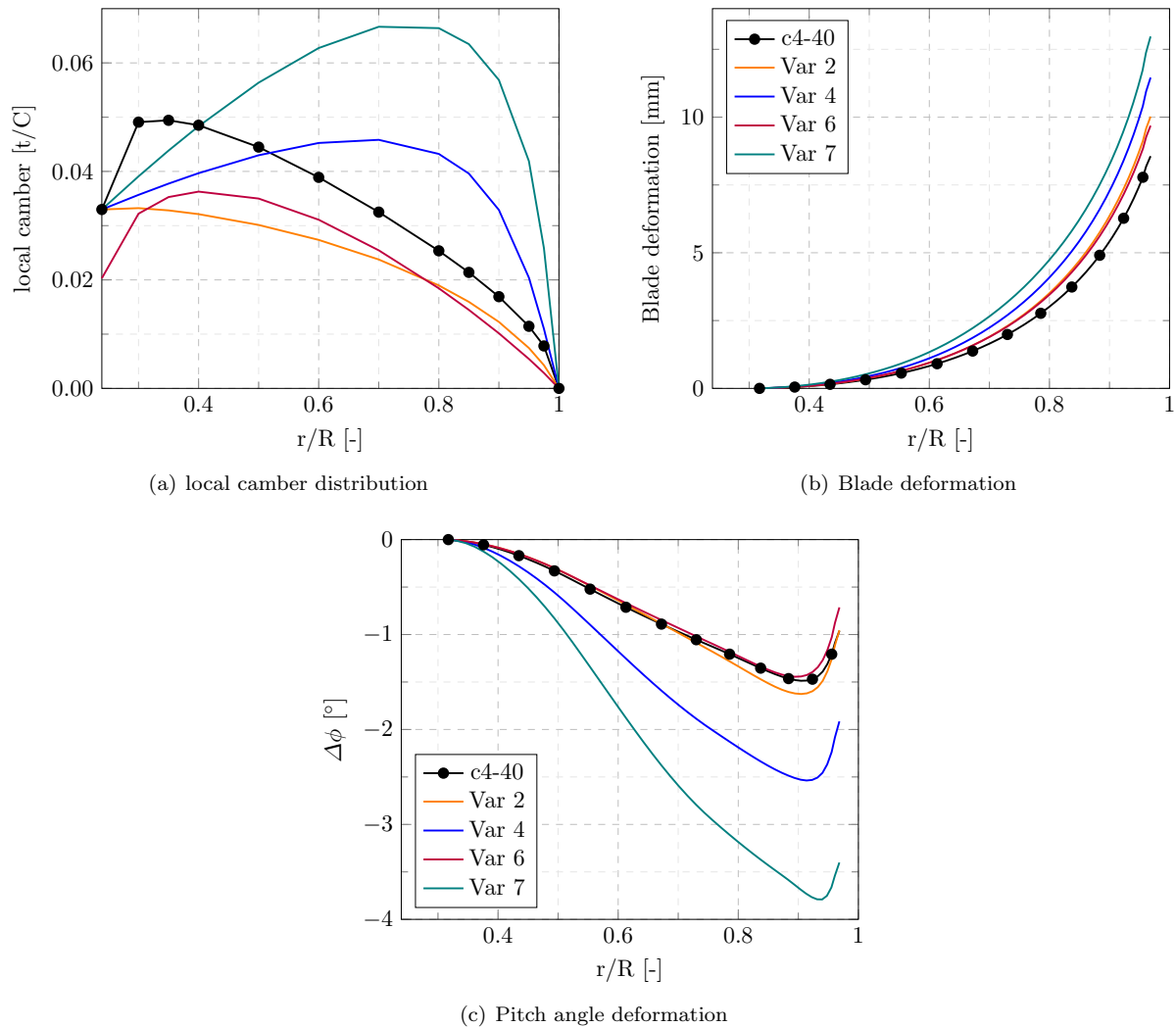


Figure 7.18: Deformation and pitch angle change for different Camber distributions.

Table 7.7: Cavitation area numbers and open water efficiencies for different camber distributions. (see figure 7.18a)

| Prop ID | A_{Suc} | A_{Pres} | η_0 |
|---------------------|------------------|-------------------|--------------|
| c4-40 Bronze | 0.3287 | 0.7827 | 0.704 |
| c4-40 M980 | 0.6093 | 1.1723 | 0.695 |
| Camber var 2 | 0.1678 | 0.4537 | 0.6910 |
| Camber var 4 | 1.4091 | 2.0397 | 0.6820 |
| Camber var 6 | 0.2081 | 0.5355 | 0.6922 |
| Camber var 7 | 3.3294 | 3.9012 | 0.6517 |

In table 7.7 the camber variations are compared in terms of pressure numbers and open water efficiencies. It shows that lower camber (camber variations 2 and 6) have lower cavitation area numbers on both the suction and on the pressure side of the blade. The efficiency is inconclusive at this point as the variations are too small. When the camber is increased (camber variations 4 and 7) both cavitation area numbers are increasing. Indicating disadvantageous pressure on the blade. To visualize the distributions, again the propeller with the most- (variation 2, figure 7.19) and least favourable (variation 7, figure 7.20) cavitation area numbers are plotted. It shows how the cavitation area number is an excellent indicator of the pressure distribution on the blade. For the suction side pressures, the leading edge pressure is drastically reduced. The same goes for the pressure side, where the leading edge pressure is completely alleviated. Even though the leading-edge was deemed uncertain, from a logical point of reasoning, it still seems favourable when they are not present. The mid-chord pressure is drastically reduced. There was also a trend visible where tip pressures were becoming less dominant whilst decreasing propeller camber.

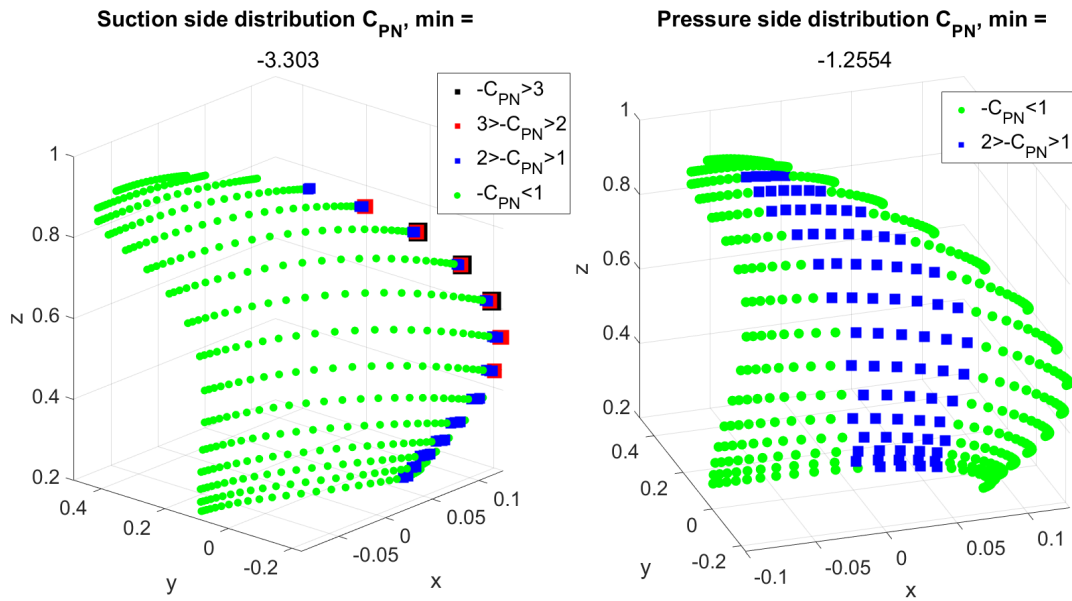


Figure 7.19: Suction and pressure side pressure distribution for camber variation 2.

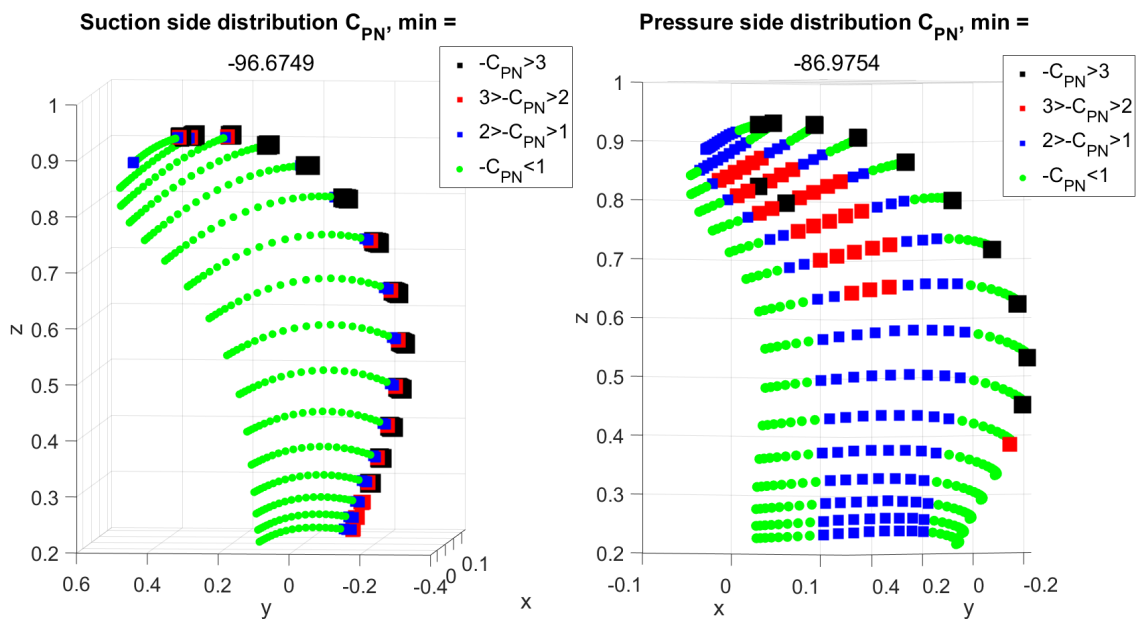


Figure 7.20: Suction and pressure side pressure distribution for camber variation 7.

7.5.6 Young's Modulus

The Young's modulus is an obvious parameter in terms of expected deformation. Higher stiffness will always yield lower deformation and pitch angle deformation. This is shown in figure 7.21. Table 7.8 shows that an increase in Young's modulus gradually decreases the cavitation area numbers and increases the efficiency. This possibly goes up towards the values for the bronze c4-40 propeller. It was initially planned to increase the range of Young's moduli for a more thorough analysis. An unknown convergence issue arises for Young's moduli lower than 2.5 GPa and higher than 5.5 GPa in combination with the set-point iteration. It is suspected that varying the Young's modulus could very much influence the pressure distribution, especially in combination with altering other parameters. But this can unfortunately not be studied due to this convergence issue. As the highest possible Young's modulus yields the best propeller, it was chosen hereon after, to model all propellers with a Young's modulus of 5.5 GPa.

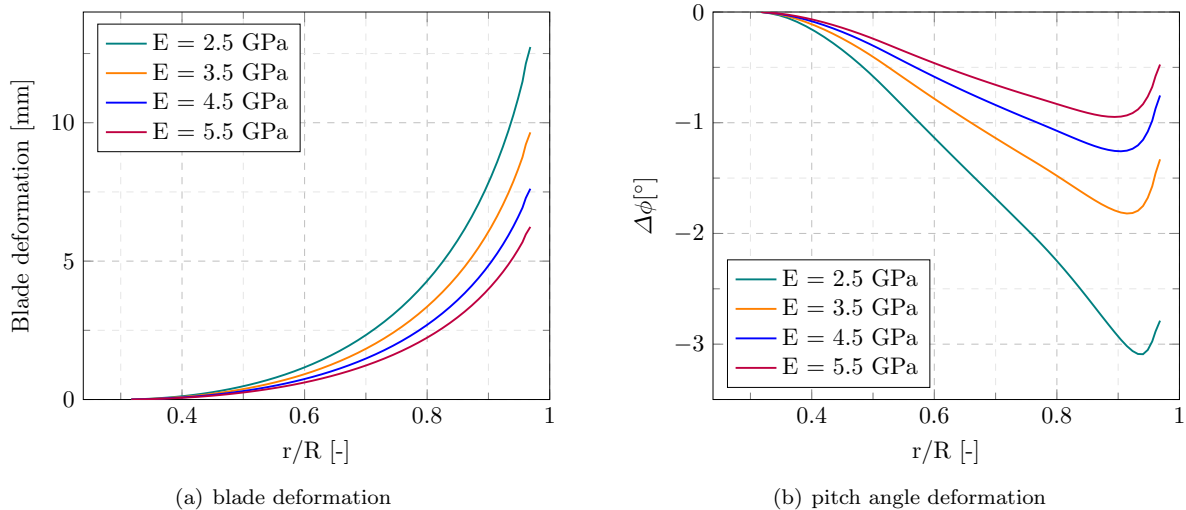


Figure 7.21: Deformation and pitch angle change for different Young's moduli.

Table 7.8: Cavitation area numbers and open water efficiencies for different Young's Moduli. (see figure 7.21a)

| Prop ID | A_{Suc} | A_{Pres} | η_0 |
|---------------------|------------------|-------------------|--------------|
| c4-40 Bronze | 0.3287 | 0.7827 | 0.704 |
| c4-40 M980 | 0.6093 | 1.1723 | 0.695 |
| E = 2.5 GPa | 0.7652 | 1.2580 | 0.6778 |
| E = 4.5 GPa | 0.5716 | 1.1339 | 0.6956 |
| E = 5.5 GPa | 0.5189 | 1.0759 | 0.6981 |

7.5.7 Conclusions

In the previous sections, the effect of individual parameters on propeller performance in terms of deformation, pressure distributions and efficiency has been studied. It showed that the suction side cavitation area number is very well capable of initial assessment of the cavitation risk at the suction side. For the pressure side cavitation side number, this number is insufficient as it over-exaggerates the mid-chord cavitation number and uncertainties due to the leading-edge arise. This problem was present at the pitch-skew and chord series, where an extreme high pressure cavitation area number was present whilst the maximum pressures were not critical. From all performed simulations it was observed that low pressure area number do correspond to favourable pressure side pressure distributions. Extremely high pressure area numbers did not always capture the magnitude of the pressures on this blade side. The reason for these discrepancies is as stated above, that the leading edge pressures gave a large factor of uncertainty of the results. This hints towards the conclusion that for full conclusive results on pressure side cavitation risks, either cavitating calculations in PROCAL must be performed. Or one should perform calculations with CFD codes. As this project is based on a BEM-FEM coupled approach. The best option would be to extend the PROCAL cavitation module (which is validated only for rigid propellers) such that it is applicable with the ComPropApp.

With the performed single parameter studies, it can be concluded that all parameters besides rake (pitch, skew, camber and chord length) do have a significant influence on pressure distributions, deformations and open water efficiency. The question which arises now is: *how do these parameters interact and possibly interfere with each other?*. To explore this design space for flexible marine propellers, the parameters as shown in table 7.9 will be used.

Table 7.9: Parameters to be used in the multi-variable design space study, with their range.

| Parameter | minimum | maximum |
|-------------------------------------|---------|---------|
| Mean Pitch [-] | 0.64 | 0.94 |
| Biased skew angle [°] | 4 | 30 |
| maximum camber t/C [-] | 0.010 | 0.045 |
| maximum chord length f/C [-] | 0.17 | 0.35 |

7.6 Multi variate design space

In the previous chapter, it was studied what the response of several propeller parameters was on the efficiency and pressure distributions. With the four most promising variables (Pitch, Skew, Camber and Chord Length), a study is executed to study how these parameters interact with each other. One could easily set ten values for each parameter and simulate all possible combinations. This would yield 10^4 propellers which is a very inefficient and extremely time-consuming process. Furthermore is it likely that only small sub spaces within this design space are regions of interest, whilst other areas are unrealistic or bad-behaving propellers that one would not want to simulate in the first place. The problem that thus arises is: How can one construct an efficient and wide-reaching sample space to explore the interaction of the parameters in table 7.9. The method chosen is *Latin Hypercube Sampling* (LHS), which divides each parameter into x intervals, where x is equal to the number of simulations one wants to perform. Then it is guaranteed that each interval is matched with other intervals of the other parameters. This way all 4D sample distributions are said to be *orthogonal*, which means that all samples are unique combinations of all sub spaces. In total 50 samples were generated. This is visualized for three parameters in figure 7.22. But this orthogonal distribution is valid for all four parameters.

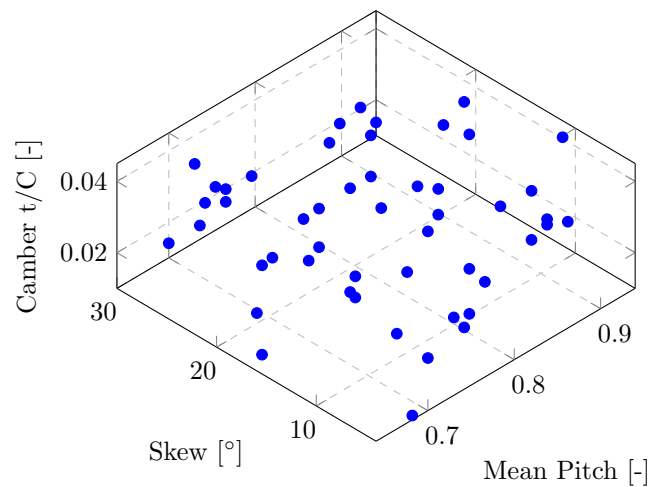


Figure 7.22: Example of the 3D design space for three variables.

A downside of this Latin hypercube sampling space is that it might be difficult to explore the interaction between two parameters as other parameters are varied as well. This can be overcome by refining the grid after a first generation and possibly removing variables from the design space in a second sampling space. Another disadvantageous aspect is due to these unequal intervals for all parameters are the corner points. These corner points contain the extreme values of the design space and are not generated. (Maximum pitch and maximum skew are both in the 50th interval, thus will not be generated for example). The most interesting propellers are likely in these extreme regions.

This can however be overcome by adding the corner points to the generated sample space manually. This is shown in figure 7.23. Where it is shown that extra samples are added in the corner points. In total 50 random samples are generated plus 16 extreme propellers, thus the sample space consists of 66 unique propellers. Their geometry parameters can be found in Appendix A.

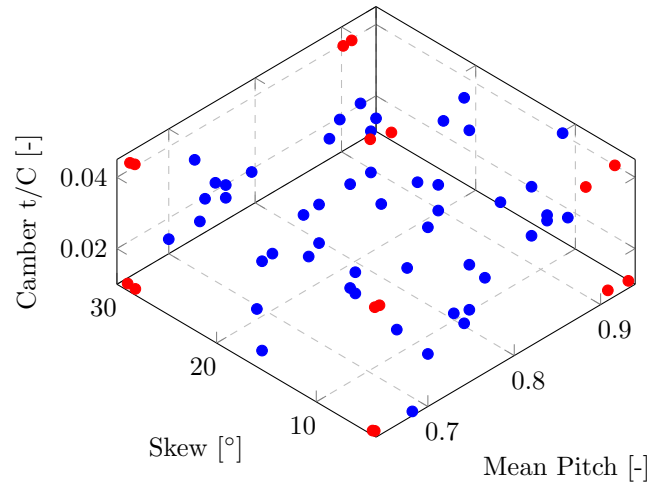


Figure 7.23: Example of the 3D design space for three variables with manually added extreme samples in red.

It should be noted that this study only goes to show which parameters influence the performance of flexible marine propellers and the interaction between those parameters. It is in no way meant as a design study. A design study would never approach design with this method as it would already have a very narrow view of where the to-be-designed propeller would be in terms of geometry parameters and would be tweaked with very little modifications to relieve pressure at certain desired sections of the blade.

This study only tends to show what possible parameters and interactions are in this flexible marine propeller design space which can be used by future propeller design studies. Furthermore are the four parameters altered in a systematic fashion. Whereas skew, chord and camber were examined through various distributions and possibilities (which makes sense if only at certain sections pressure is desired to be reduced or relieved), in this study, they will be altered by only lowering, or increasing the parameter in the same way. Such that the results are easier to interpret. The four modifications that will be investigated are:

- **Pitch:** Mean pitch will be altered by increasing or decreasing the root and tip values accordingly
- **Skew:** Skew will be altered by increasing or decreasing the biased skew. This maximum value will be located at 0.4R.
- **Camber:** Camber will be modified by increasing or decreasing the camber at the root. This way the camber along the blade is modified accordingly.
- **Chord Length:** The chord length is modified by increasing or decreasing the value at 0.8R, this is where the maximum value is located for the c4-40 propeller.

7.7 Results of the multi variate design exploration

Of the 66 generated propellers, 65 simulations were successful and only propeller number 45 had convergence issues, which is odd as it contained no extreme values. The first task is to explore the effects of the parameters whilst the other three are fluctuating now as well.

7.7.1 Open water efficiency

From figure 7.24, it is immediately visible that the efficiency is mainly influenced by increasing the pitch angle of the propeller, and slightly by decreasing the chord length of the propeller. Both observations make sense with the main theory of propeller design: The angle of attack increases and thinner propellers approach the theoretical optimum propeller in the actuator disk theory. The results from camber and skew are very scattered and seem to not affect on the efficiency. Note that also trend lines are plotted with the corresponding root mean square errors (*RMSE*). This is the average squared error of each sample to the trend line. Thus a lower *RMSE* value means a more correlated connection.

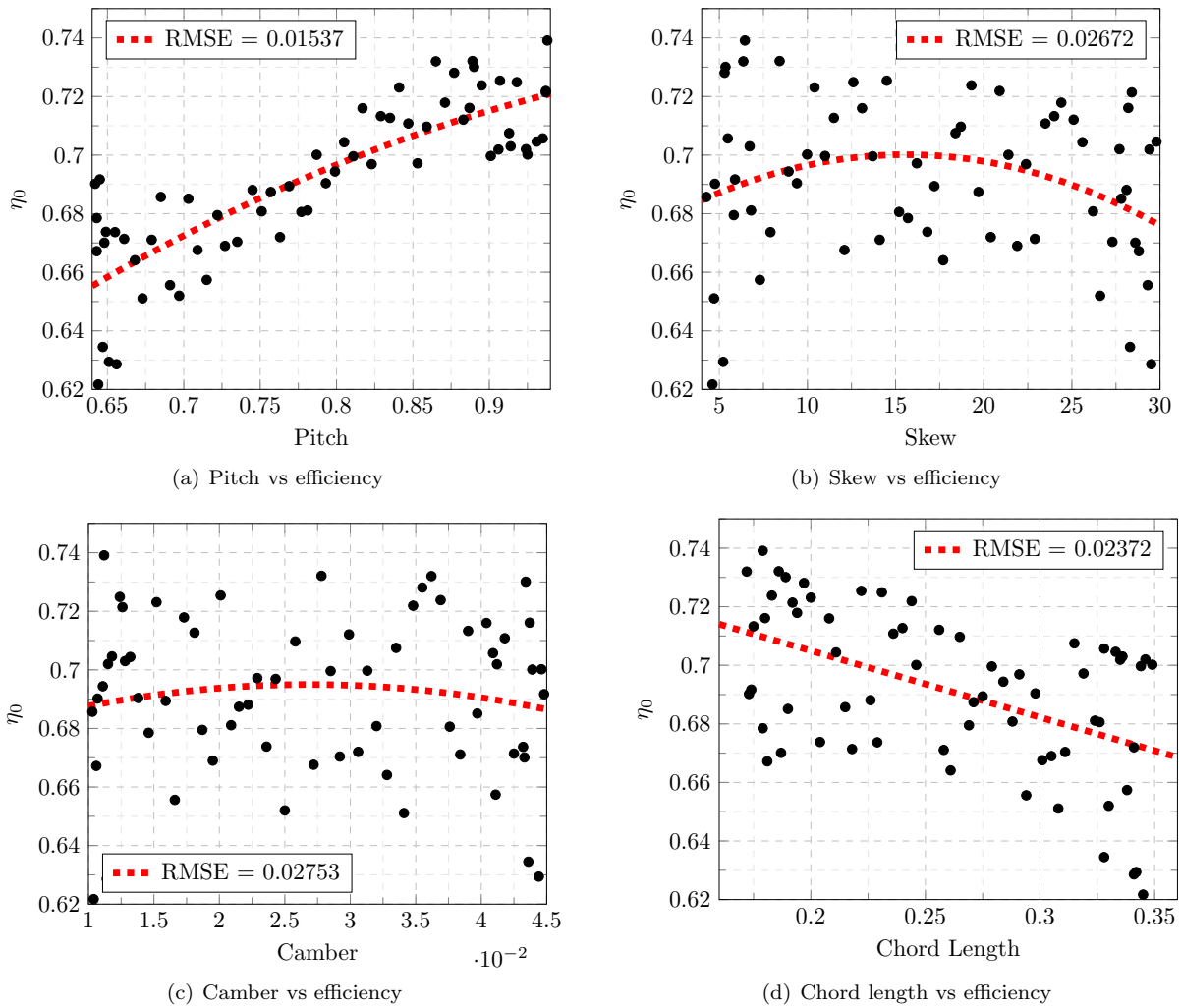


Figure 7.24: Effect of pitch, skew, camber and chord length on open water efficiency.

7.7.2 Suction side cavitation

In figure 7.25, the four parameters are plotted as a function of the suction side pressure number. Again, increasing pitch seems to lower the suction side pressures which was also observed in the single parameter series. The same conclusions can be drawn for skew, camber and chord length. Although the correlation of all four parameters is less pronounced than was observed in the single parameter series. It still can be concluded that suction side cavitation can be fairly easily mitigated for flexible marine propellers.

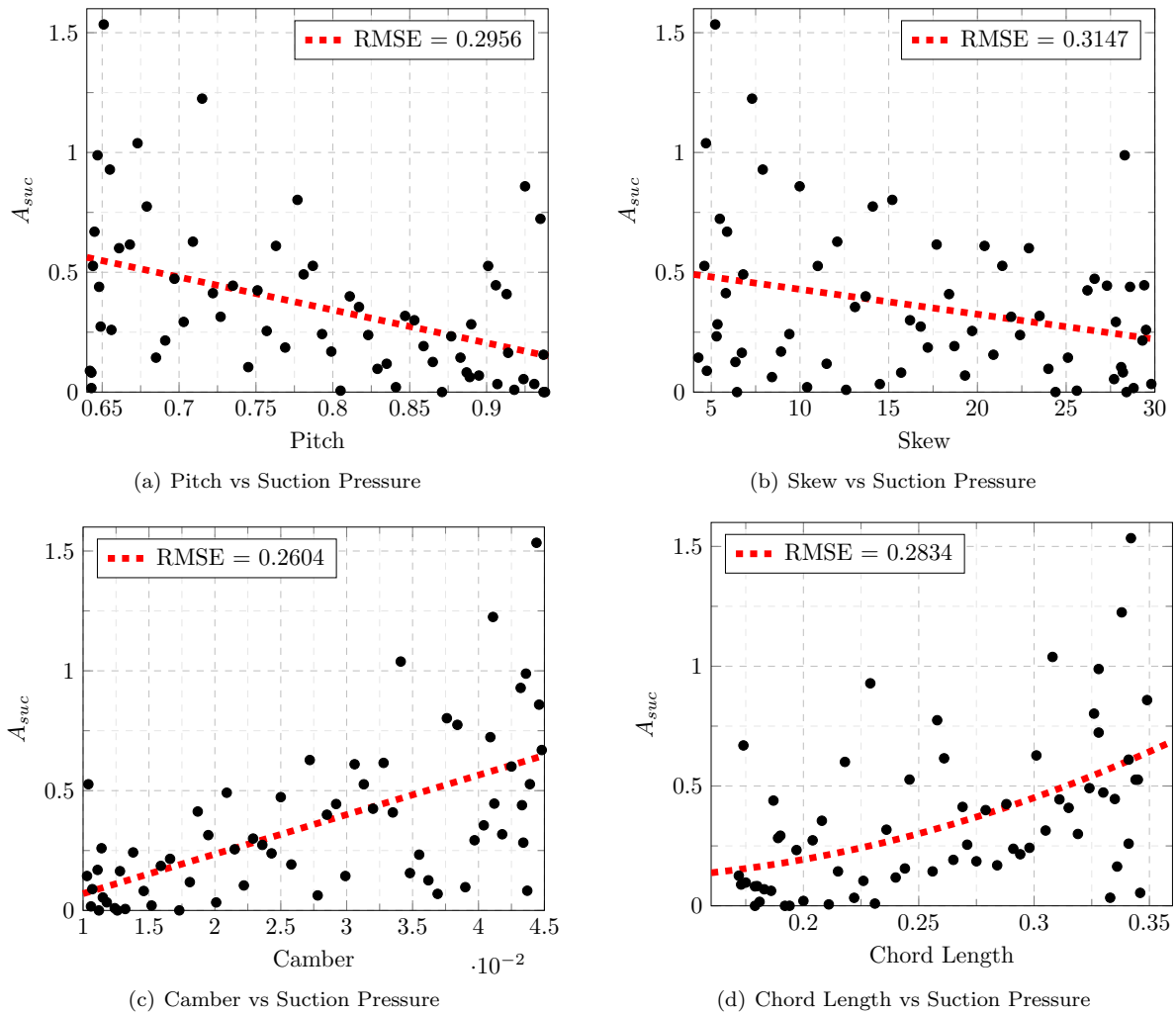


Figure 7.25: Effect of pitch, skew, camber and chord length on the suction side cavitation area.

7.7.3 Pressure side cavitation

In figure 7.26, the link between pressure side area numbers and the four parameters is shown. For pitch the same conclusion as the linear modification is found: higher pitch means higher pressure side pressures. For a higher biased skew, it was shown in section 7.5, that the pressure side pressures dropped significantly. From the results within this 4-dimensional design space, this results becomes less pronounced. The effect of chord length on the pressure side area is visible. Although, outliers which do not show these extreme pressure side pressures are readily present. It was also stated in section 7.5 that this pressure side number still has some shortcomings due to the numerical artefacts at the leading edge. Therefore it is better to visualize the complete distributions as was done in the linear studies as well.

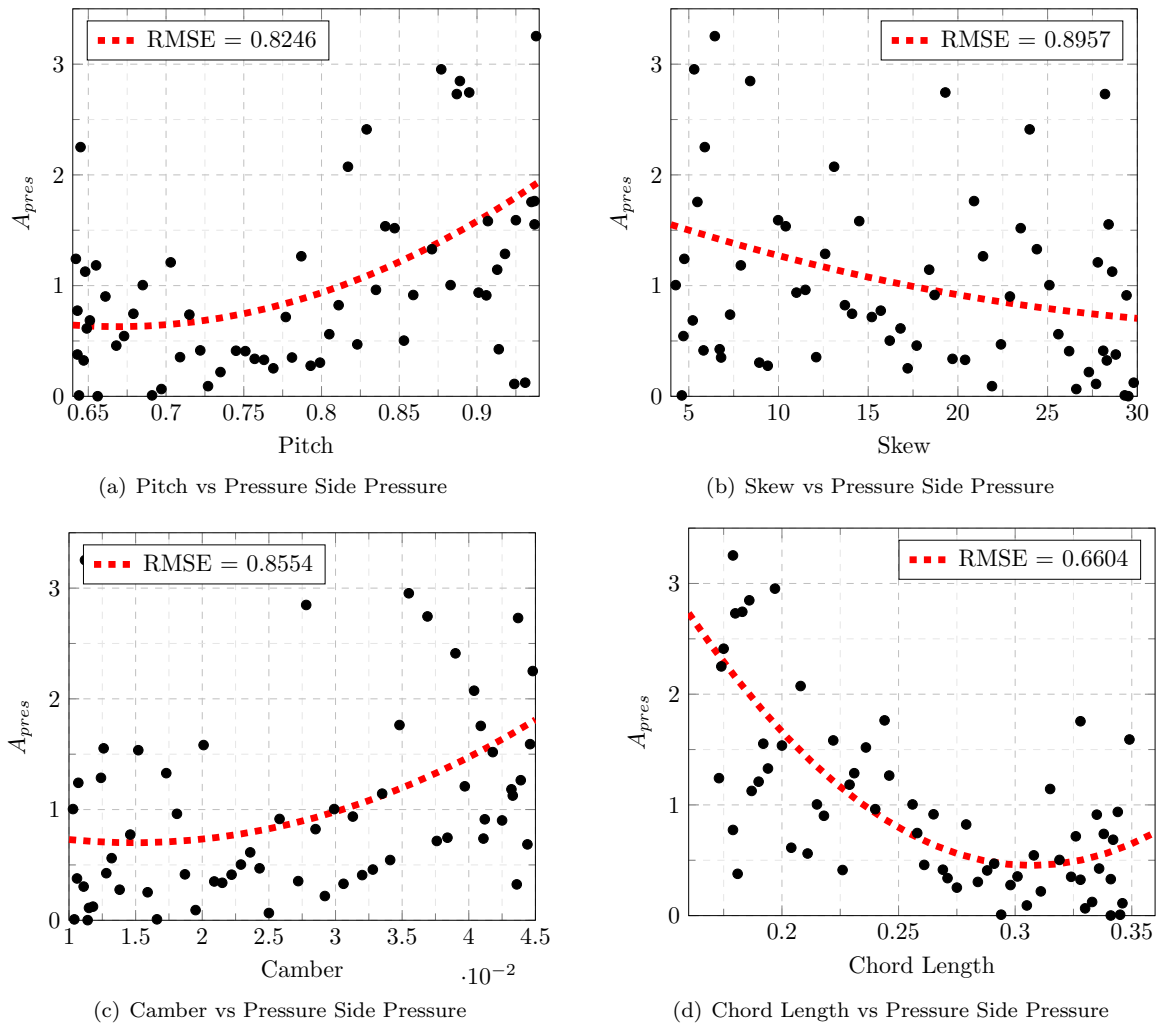


Figure 7.26: Effect of pitch, skew, camber and chord length on the suction pressure side cavitation area.

7.7.4 Maximum Stress

Due to the deformation and bending of the blades, stresses develop in the material. At some point, the stresses become too large and the structure starts to yield. Currently, an imaginary isotropic solid is used without known yielding stress and a Young's modulus of 5.5 GPa. Since the yielding stress is unknown, it is impossible to state whether the propeller is sufficiently strong. What can be done, is using the *Von Mises yield criterion* (σ_{VM}) to compare the developed stresses of all propellers with each other. The Von Mises criterion is given as output by trident and can be used to describe the equivalent maximum stress within the structure as a function of its three principal stress components ($\sigma_1, \sigma_2, \sigma_3$). Mathematically this looks like equation 7.2. In the ComPropApp this computed for every node of the FEM-model.

$$\sigma_{VM} = \sqrt{\frac{1}{2} [(\sigma_1 - \sigma_2)^2 + (\sigma_2 - \sigma_3)^2 + (\sigma_3 - \sigma_1)^2]} \quad (7.2)$$

The maximum Von Mises stress is thus defined as the node with the maximum Von Mises stress. For a vast majority of the propellers, the first node turned out to have the highest stress (leading edge at the hub). It was chosen to remove this first node from selecting the maximum value since this is most likely a numerical singularity in the model as it is clamped at that point. In reality, would smoother blade-hub connections ensure that unallowable stresses will not concentrate at this point. An exemplary stress plot of propeller 21 is shown in figure 7.27. And in figure 7.28 the maximum stress of each propeller is plotted as a function of all four geometry parameters. It is visible that an increase in both pitch and skew tends to increase the maximum Von Mises stress in the propeller blade.

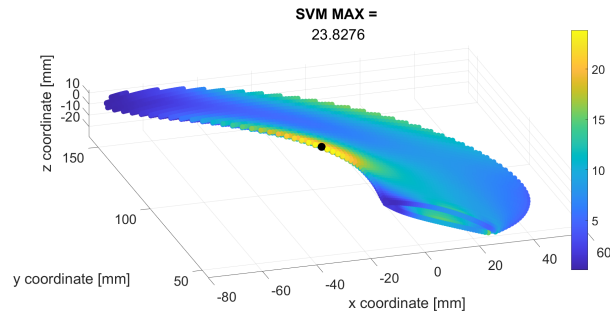


Figure 7.27: Von Mises distribution of Propeller 21, with the maximum stress at the black dot.

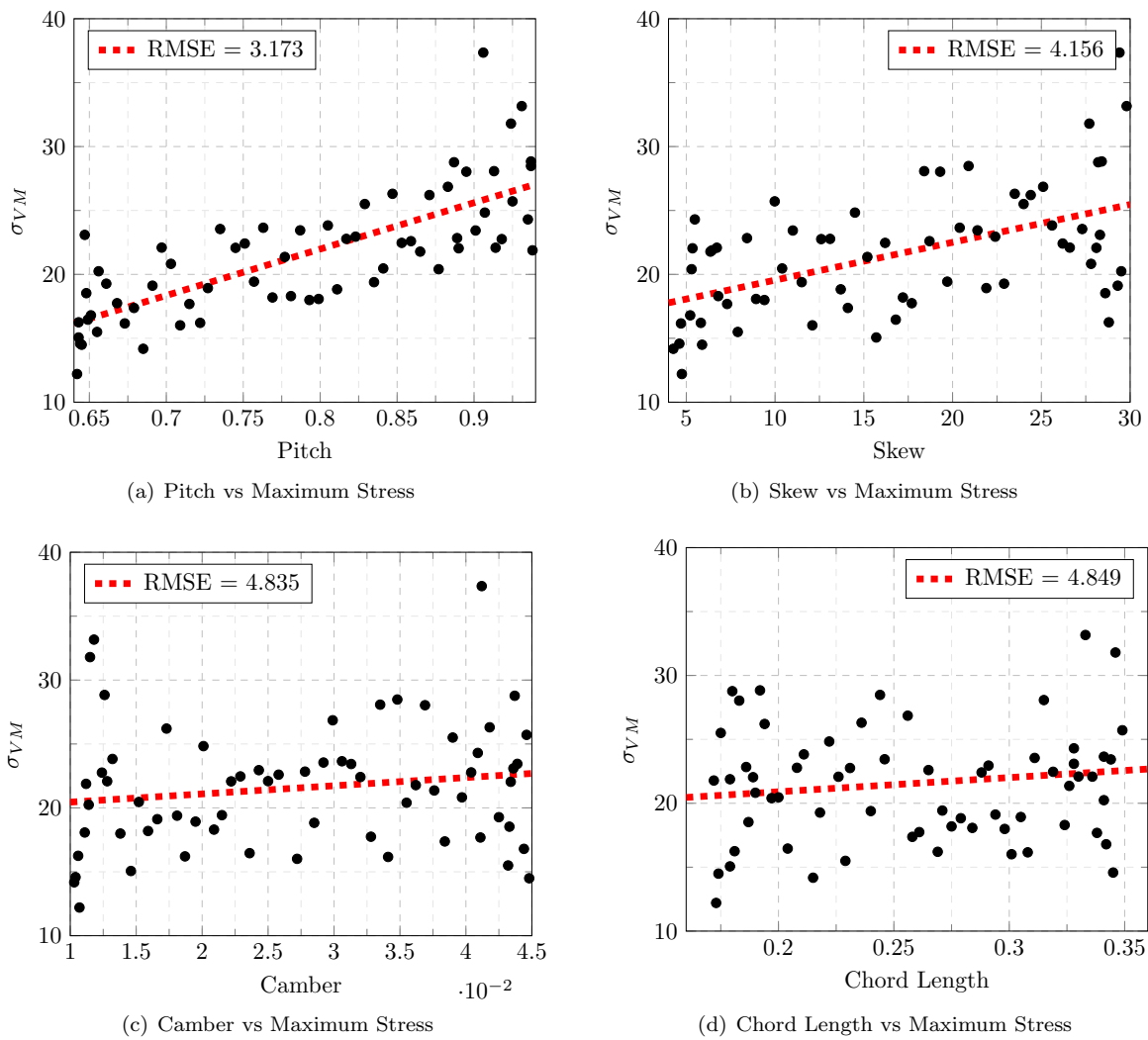


Figure 7.28: Effect of pitch, skew, camber and chord length on the maximum Von Mises stress.

7.7.5 Blade and pitch angle Deformation

Another topic of interest is the amount of deformation obtained in these propellers. Right now, all propellers are still simulated in open water only. But in the future, when flexible propellers will be designed for in-behind ship conditions one wants to know how much deformation is obtainable and how this influences the performance. Figure 7.29 shows the deformation for each parameter. A higher pitch leads to higher deformation as the blade is loaded much higher. Oddly, increasing the skew does not influence the deformation that much. Whilst literature (Carlton for example [4]) states that the stresses are becoming increasingly higher for larger skew angles, which was also shown in figure 7.28. This effect was also visible for only altering skew (see figure 7.10), but apparently, this becomes less evident when other parameters are altered simultaneously. There also is a clear connection between blade deformation and chord length. This is in line with the results of

the pressure side area number (see figure 7.26). Meaning the blade is loaded higher.

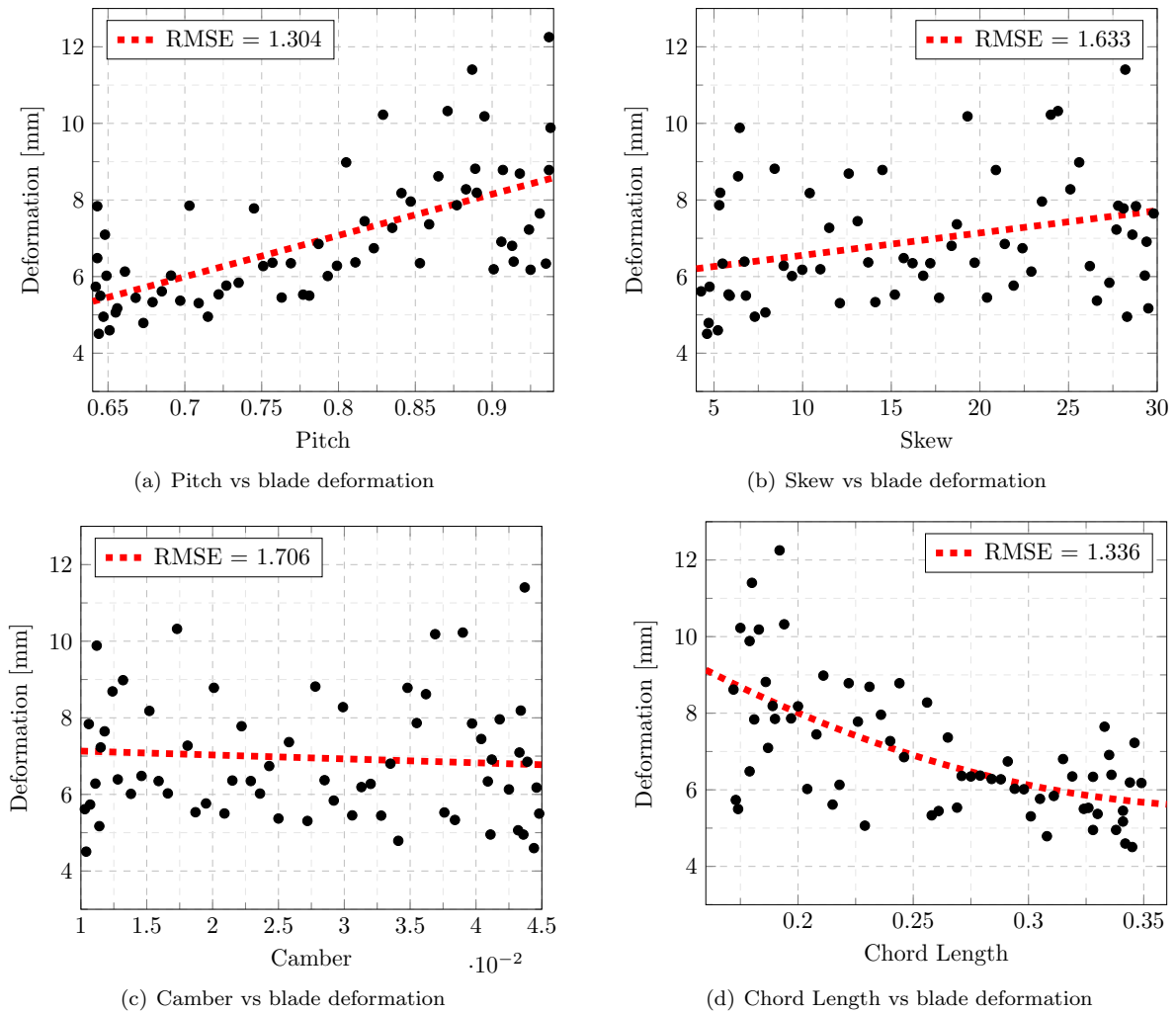


Figure 7.29: Effect of pitch, skew, camber and chord length on the total blade deformation

In figure 7.30, the effect on the maximum pitch angle deformation is shown. Here it is visible, that pitch does not affect the pitch angle deformation, whilst it was the largest factor in determining the blade deformation. The amount of bending possible in blades seems to be affected the most by increasing skew and decreasing chord length.

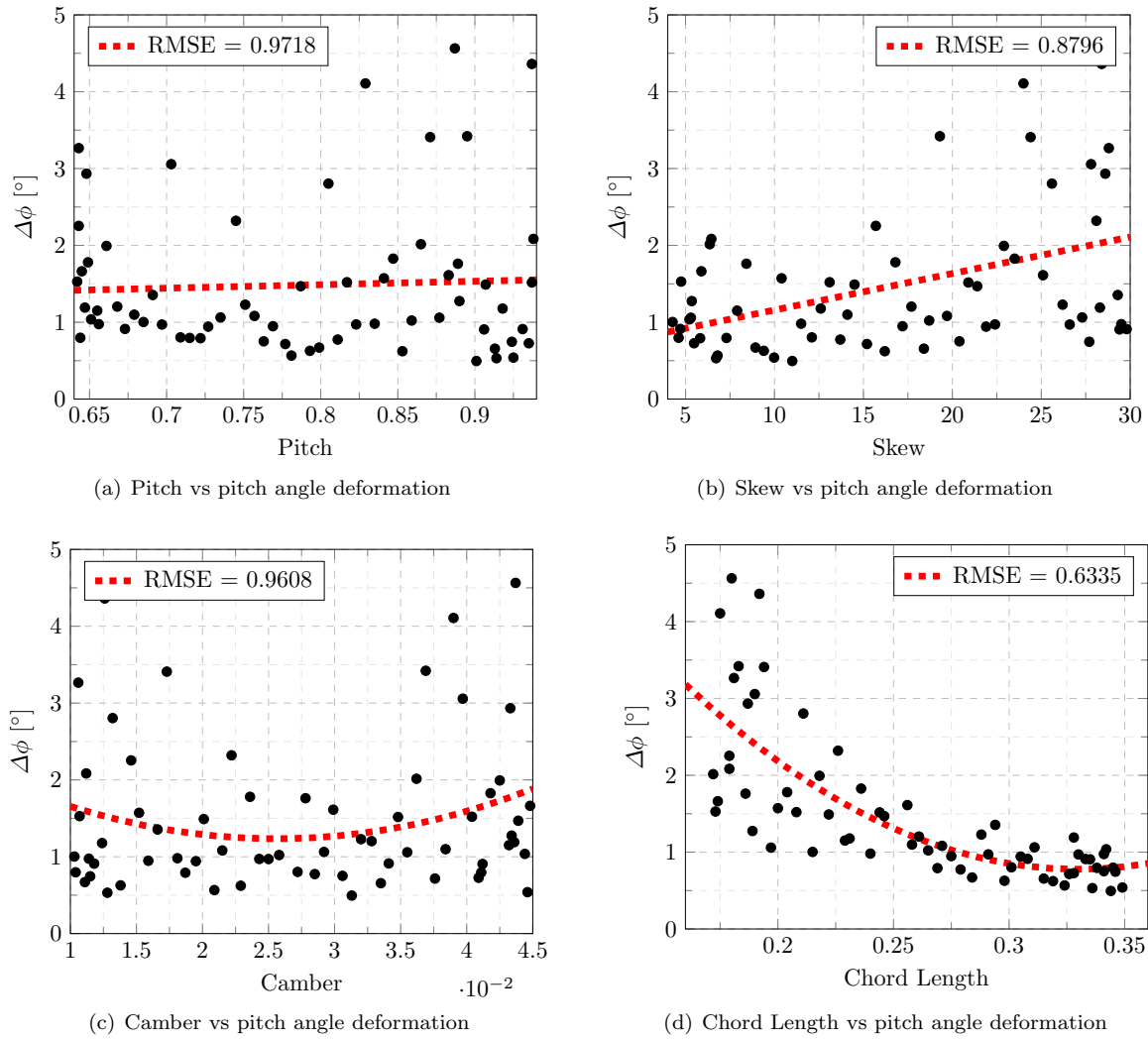


Figure 7.30: Effect of pitch, skew, camber and chord length on the pitch angle deformation.

The last comparison regarding the blade- and pitch angle deformations is to analyze what their connection is to the three design criteria. The relation between the deformations and open water efficiency is shown in figure 7.31. There is a very clear connection between the total blade deformation and the resulting efficiency. This goes hand in hand with an increase in pitch. It seems that there is some sort of maximum in this efficiency increase. At some point, no more efficiency gain can be reached. This makes sense, as at some point the theoretical maximum efficiency must be reached. The pitch angle deformation seems uncorrelated with the efficiency.

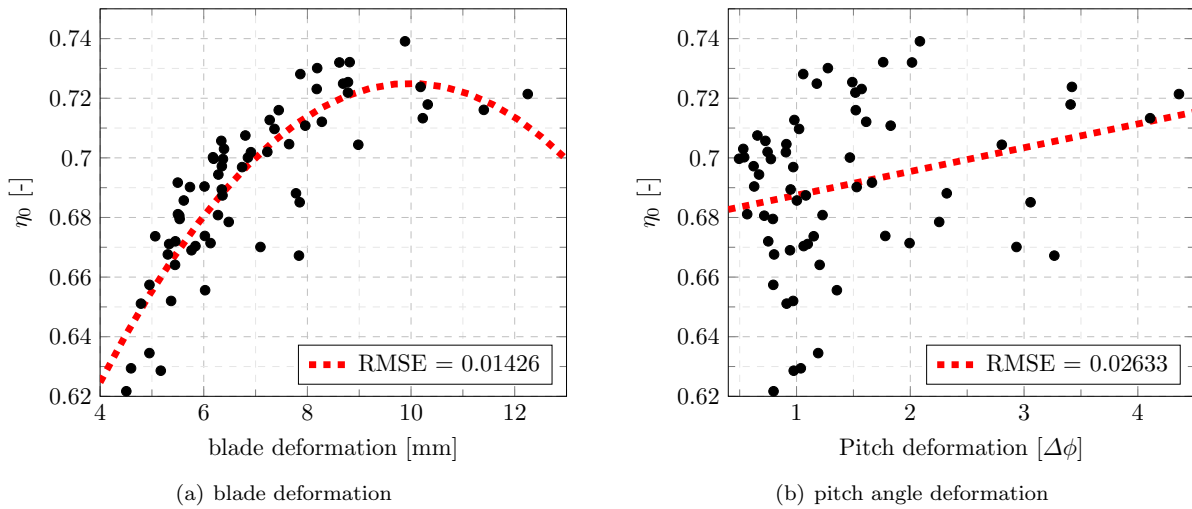


Figure 7.31: Blade- and pitch angle deformation vs. open water efficiency.

In figure 7.32 the connection between the deformations and the suction side area number is shown. It shows that an increase in both deformation components results in a decrease in the suction side pressures. The downside of increased efficiency and suction side improvement is thus linked to larger deformations. Figure 7.33 shows that the opposite is true for the pressure side pressures. This means that for optimal performance, propellers have to be designed with a fine balance between the three criteria.

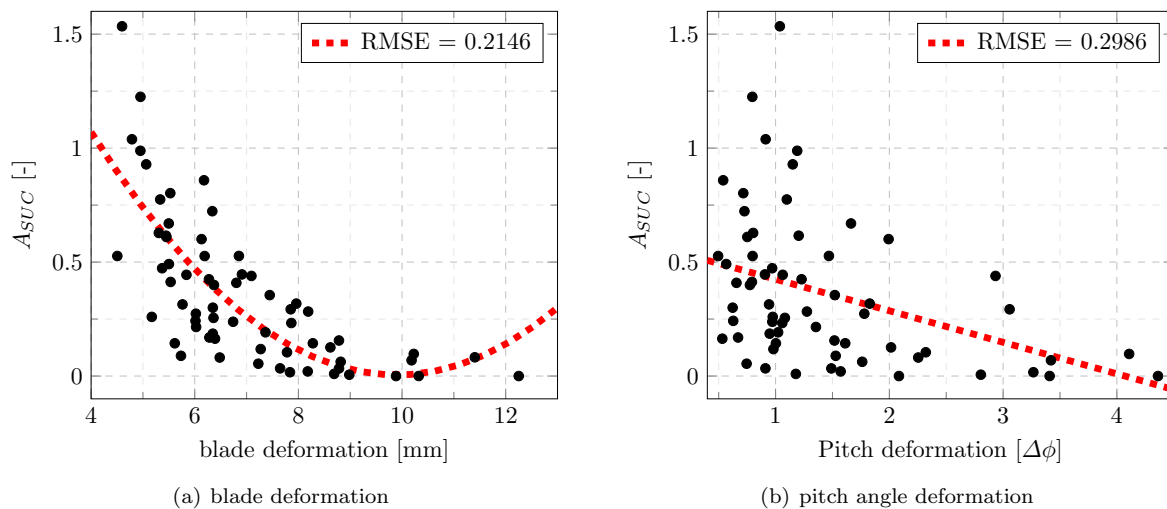


Figure 7.32: Blade- and pitch angle deformation vs. suction side pressure number.

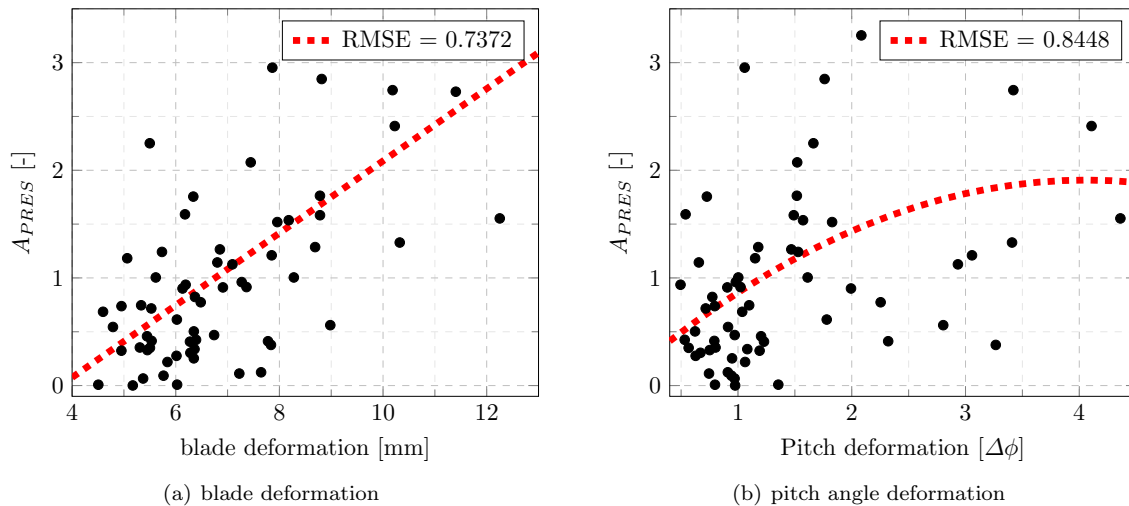


Figure 7.33: Blade- and pitch angle deformation vs. pressure side pressure number.

7.8 Optimum Propellers

Besides looking at the outcomes of the pressures, deformation, stresses and efficiency, as a function of the altered parameter. It is also possible to look at the effect of these outcomes as a function of each other. In figure 7.34, the effect of both pressure area numbers on the efficiency is visualized. From this figure, it becomes visible, that suction side area pressure reduction is linked with higher open water efficiency but the opposite is valid for pressure side area reduction. The higher the efficiency gets, the higher the pressure side area tends to be. The question is, whether there is an optimum propeller randomly generated, which performs well in all three criteria.

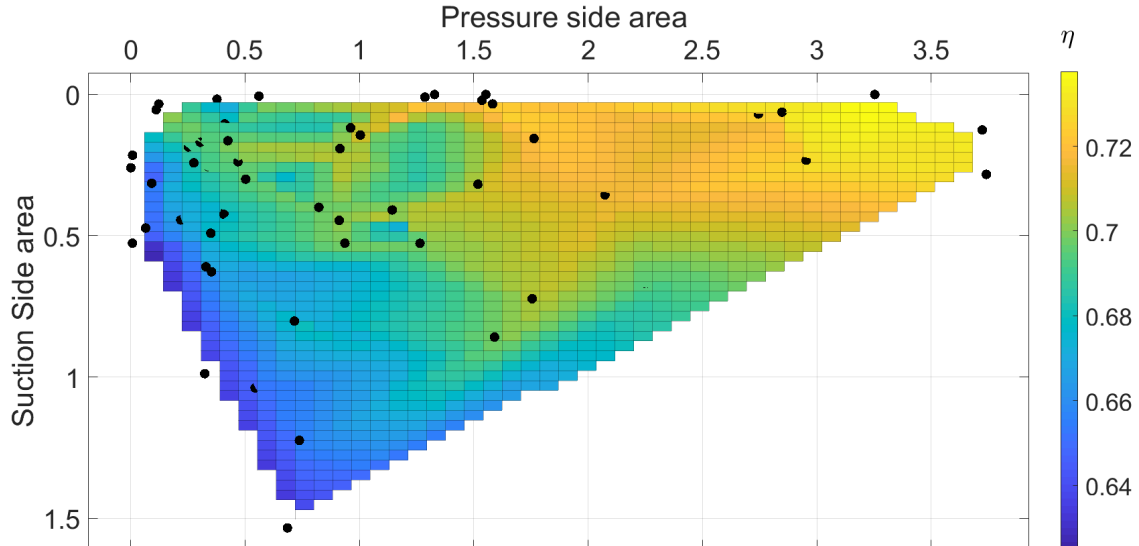


Figure 7.34: Open water efficiency as function of suction- and pressure side cavitation numbers.

It can be investigated whether there is a propeller generated which has a lower suction side cavitation area compared to the bronze c4-40 propeller ($A_{SUC} < 0.3287$), a lower pressure side cavitation area ($A_{PRES} < 0.782$) and a higher propeller efficiency ($\eta_0 > 0.704$). Again it must be stated, that this is in no way a design challenge, or to conclude a better propeller is obtained through this random propeller generation. This is in open water conditions, which is not where the c4-40 was designed for. The performance of all generated propellers might very likely deviate when subjected to a real in-behind ship wake. This study only tends to show which parameters influence design conditions and might be beneficial for real design optimization studies.

Figure 7.35 shows this design space and the two corresponding propellers which met all three conditions: Propeller ID 21 and 23. From this space, it was seen that of the 65 propellers, 32 propellers have a lower suction

side area than the bronze c4-40 propeller, 23 have a higher efficiency and 17 propeller have a lower pressure side number. These have first to be visually inspected because the discrepancies in this pressure area number at the leading edge.

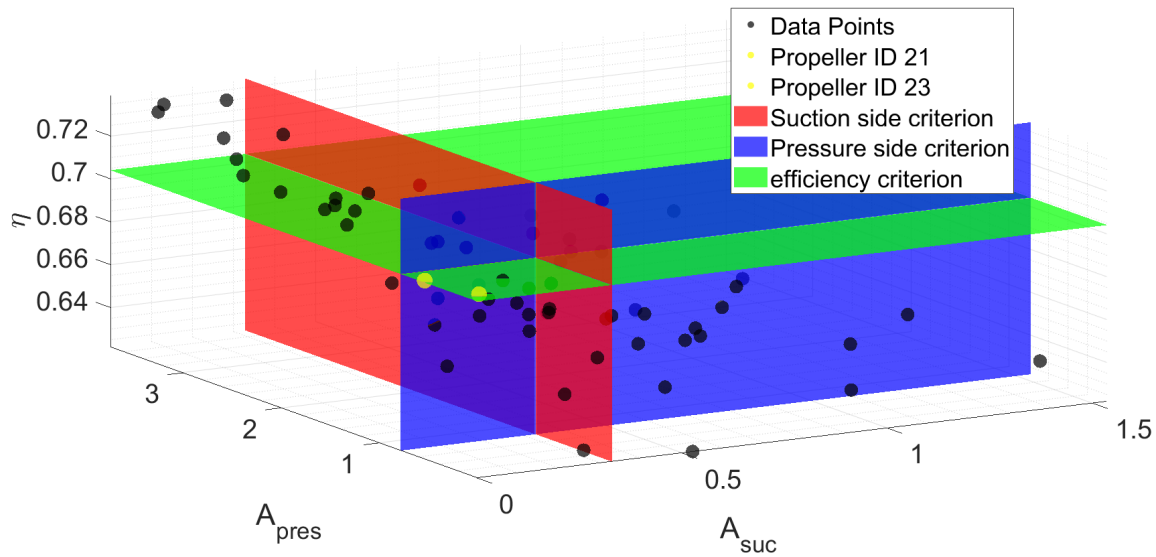


Figure 7.35: Propellers subjected to three design criteria (A_{SUC} , A_{PRES} and η).

Table 7.10 shows the input of propellers 21 and 23 and their performance characteristics. They both have high pitch, high skew and low camber. The only parameter which is very different is chord length. It is also visible that Propeller 21 has a lower pressure side cavitation area compared to propeller. The opposite is true for the suction side cavitation area. Furthermore is it visible that both propellers have relatively large stresses. This is caused by the high skew and pitch.

Table 7.10: Propellers which met all criteria with input parameters and performance indicators.

| Prop | Pitch | Skew | Camber | Chord Length | η_0 | A_{SUC} | A_{PRES} | Max σ_{VM} |
|---------------------|-------|-------|--------|--------------|----------|-----------|------------|-------------------|
| c4-40 Bronze | 0.76 | 10 | 0.330 | 0.250 | 0.7040 | 0.3287 | 0.7827 | 17.8248 |
| Propeller 21 | 0.805 | 25.58 | 0.0132 | 0.2114 | 0.7044 | 0.0337 | 0.1232 | 23.8276 |
| Propeller 23 | 0.931 | 29.8 | 0.118 | 0.333 | 0.7046 | 0.0059 | 0.5610 | 33.1652 |

In figures 7.36 and 7.37, the pressure distributions of Propeller 21 and Propeller 23 are visualized respectively. For Propeller 21, both the suction- and pressure side area number make sense, as the pressure distribution looks favourable on both blade sides, with very low minimum pressures encountered on both sides as well. For propeller 23 however, a very high tip pressure peak becomes visible. This is not accounted for by the current method, as only pressures up to $0.9R$ were integrated in the cavitation area numbers. To see whether this problem exists for more propellers and perhaps tip pressure criteria has to be added. the best- and worst three propellers of each of the three criteria will be investigated.

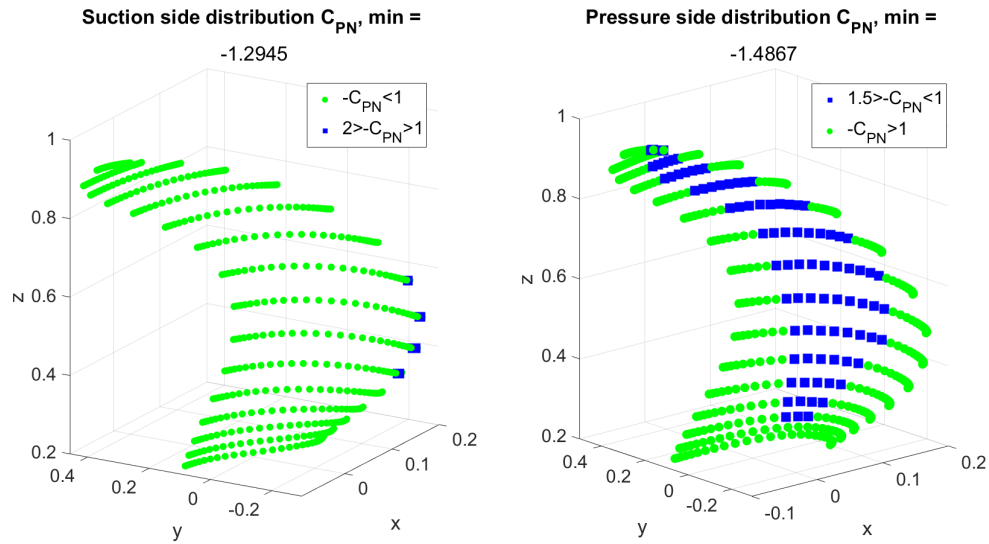


Figure 7.36: Suction and pressure side pressure distribution for Propeller 21.

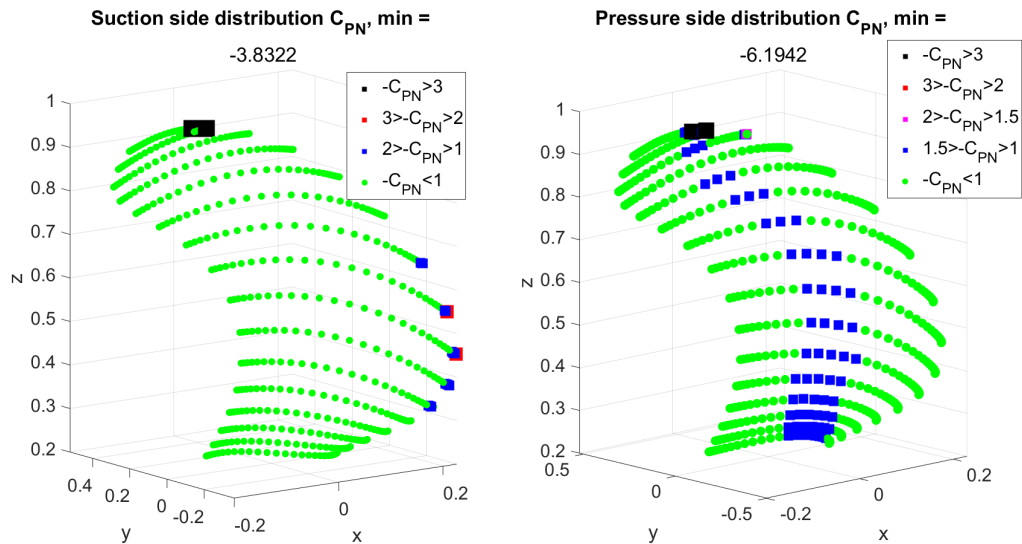


Figure 7.37: Suction and pressure side pressure distribution for Propeller 23.

7.8.1 Best suction side propellers

In table 7.11, the best and worst propellers regarding the suction side pressure area are shown. It shows that increasing pitch and decreasing camber and chord length have a favourable effect on the suction side pressure of the propeller. The effect of skew is not noticeable or at least inconclusive from this table. It does however seem to hint at the fact that increasing skew can decrease the pressure side cavitation area of the propeller. Propeller 59 with little skew, has a significantly higher pressure area number than Propellers 63 and 15, which both have large skew. It also clearly shows the link between reducing this suction side area number and increasing the open water efficiency. Again the effect of skew on the maximum pressure in the blade is visible.

Table 7.11: Top and bottom three propellers on the suction side pressure criterion.

| Prop | Pitch | Skew | Camber | Chord Length | η | A_{SUC} | A_{PRES} | Max σ_{VM} |
|---------------------|-------|------|--------|--------------|--------|-----------|------------|-------------------|
| c4-40 Bronze | 0.76 | 10 | 0.330 | 0.250 | 0.7040 | 0.3287 | 0.7827 | 17.8248 |
| Prop 59 | 0.938 | 6.45 | 0.0112 | 0.179 | 0.7391 | 0.0 | 3.2532 | 21.88 |
| Prop 63 | 0.937 | 28.4 | 0.0126 | 0.192 | 0.7214 | 0.0 | 1.5529 | 28.84 |
| Prop 15 | 0.871 | 24.4 | 0.0173 | 0.194 | 0.7179 | 0.0002 | 1.3288 | 26.21 |
| Prop 54 | 0.651 | 5.22 | 0.0444 | 0.342 | 0.6294 | 1.5344 | 0.6855 | 16.79 |
| Prop 41 | 0.715 | 7.30 | 0.0411 | 0.338 | 0.6574 | 1.2248 | 0.7379 | 17.68 |
| Prop 42 | 0.673 | 4.70 | 0.0341 | 0.308 | 0.6511 | 1.0387 | 0.5442 | 16.16 |

7.8.2 Best pressure side propellers

For a low pressure side pressure distribution, the propellers must have a low pitch, low camber and high chord length. This is directly visible from table 7.12. This would however lead to unwanted propellers, as they all perform very bad in terms of open water efficiency. As skew helped to reduce pressure side pressures whilst optimizing for suction side pressures, this same effect seems to happen for reducing suction side pressures whilst optimizing for pressure side pressures.

Table 7.12: Top and bottom three propellers on the pressure side pressure criterion.

| Prop | Pitch | Skew | Camber | Chord Length | η | A_{SUC} | A_{PRES} | Max σ_{VM} |
|---------------------|-------|------|--------|--------------|--------|-----------|------------|-------------------|
| c4-40 Bronze | 0.76 | 10 | 0.330 | 0.250 | 0.7040 | 0.3287 | 0.7827 | 17.8248 |
| Prop 56 | 0.656 | 29.5 | 0.0144 | 0.341 | 0.6286 | 0.2595 | 0.0010 | 20.24 |
| Prop 52 | 0.644 | 4.61 | 0.0104 | 0.345 | 0.6217 | 0.5266 | 0.0080 | 14.58 |
| Prop 35 | 0.691 | 29.3 | 0.0166 | 0.294 | 0.6556 | 0.2152 | 0.0085 | 19.12 |
| Prop 61 | 0.890 | 5.35 | 0.434 | 0.189 | 0.7301 | 0.2829 | 3.7409 | 22.04 |
| Prop 24 | 0.865 | 6.36 | 0.0362 | 0.172 | 0.7320 | 0.1257 | 3.7228 | 21.78 |
| Prop 59 | 0.938 | 6.45 | 0.0112 | 0.179 | 0.7391 | 0.0 | 3.2532 | 21.88 |

7.8.3 Best efficiency propellers

In table 7.13, the best and worst propellers in terms of efficiency are shown. This clearly shows that efficiency and both pressures are highly linked. Efficient propellers yield high pressure side areas and low suction side areas. They have little skew, small chord lengths and high pitch. Thus the main design question is: *How is a efficient propeller designed with allowable pressure side pressures?*

Table 7.13: Top and bottom three propellers on the efficiency criterion.

| Prop | Pitch | Skew | Camber | Chord Length | η | A_{SUC} | A_{PRES} | Max σ_{VM} |
|---------------------|-------|------|--------|--------------|--------|-----------|------------|-------------------|
| c4-40 Bronze | 0.76 | 10 | 0.330 | 0.250 | 0.7040 | 0.3287 | 0.7827 | 17.8248 |
| Prop 59 | 0.938 | 6.45 | 0.0112 | 0.179 | 0.7391 | 0.0 | 3.2532 | 21.88 |
| Prop 20 | 0.889 | 8.42 | 0.0278 | 0.186 | 0.7321 | 0.0626 | 2.8478 | 22.84 |
| Prop 24 | 0.865 | 6.36 | 0.0362 | 0.172 | 0.7320 | 0.1257 | 3.7228 | 21.78 |
| Prop 52 | 0.644 | 4.61 | 0.0104 | 0.345 | 0.6217 | 0.5266 | 0.0080 | 14.58 |
| Prop 56 | 0.656 | 29.5 | 0.0144 | 0.341 | 0.6286 | 0.2595 | 0.0010 | 20.24 |
| Prop 54 | 0.651 | 5.22 | 0.0444 | 0.342 | 0.6294 | 1.5344 | 0.6855 | 16.79 |

For instance, from tables 7.11 and 7.12, it seems that increasing skew and lowering camber might reduce these pressures. Furthermore could slightly increasing the chord length lead to even more reduction of pressure side pressures with a small decrease of efficiency. In figure 7.38, the pressure distribution of Propeller 20 is shown (reaching the suction side and efficiency criterion, but failing the pressure side criterion). The horrible pressure side distribution is visible.

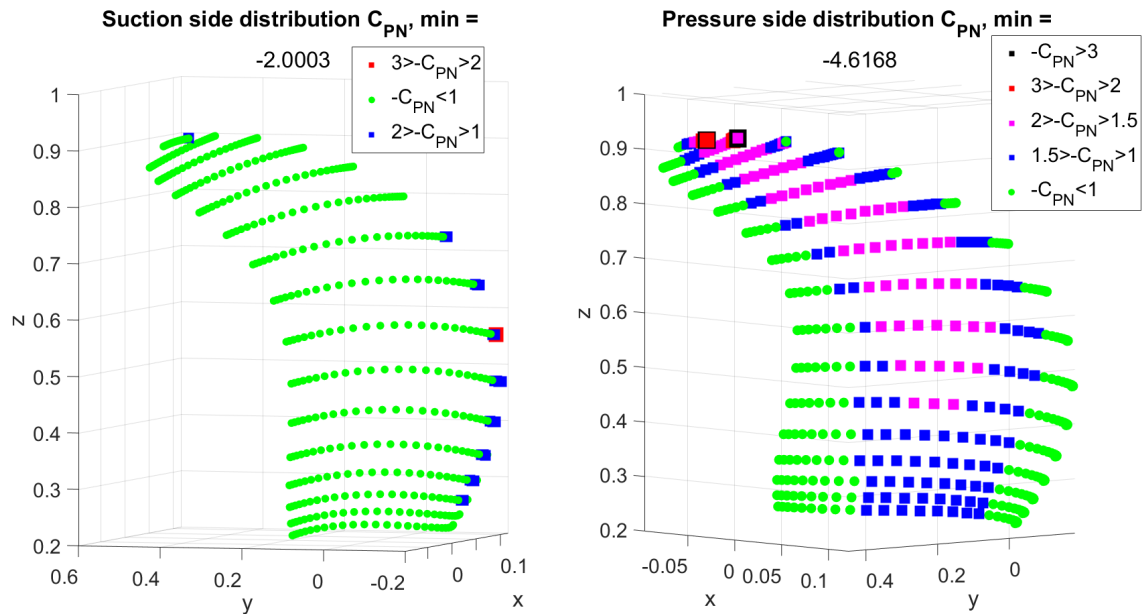


Figure 7.38: Suction and pressure side pressure distribution of Propeller 20.

Now it can be tried to modify this propeller, by increasing the skew, decreasing the camber and increasing the chord length to tailor this pressure side distribution. First, the biased skew angle is increased, afterwards the propeller camber is decreased and finally, the chord length of the propeller is increased. The results for the iterations are shown in table 7.14.

Table 7.14: Propeller 20 with modifications to relieve pressure side pressures.

| Prop | Pitch | Skew | Camber | Chord | η | A_{SUC} | A_{PRES} | Max σ_{VM} |
|------------------------------|-------|------|--------|-------|--------|-----------|------------|-------------------|
| c4-40 Bronze | 0.76 | 10 | 0.330 | 0.250 | 0.7040 | 0.3287 | 0.7827 | 17.82 |
| Prop 20 | 0.889 | 8.42 | 0.0278 | 0.186 | 0.7321 | 0.0626 | 2.8478 | 22.84 |
| Prop 20 Skew = 15 | 0.889 | 15.0 | 0.0278 | 0.186 | 0.7282 | 0.0341 | 2.5249 | 25.50 |
| Prop 20 Skew = 20 | 0.889 | 20.0 | 0.0278 | 0.186 | 0.7245 | 0.0204 | 2.2683 | 26.74 |
| Prop 20 Skew = 25 | 0.889 | 25.0 | 0.0278 | 0.186 | 0.7191 | 0.0107 | 2.0027 | 27.92 |
| Prop 20 Skew = 30 | 0.889 | 30.0 | 0.0278 | 0.186 | 0.7150 | 0.0059 | 1.7999 | 28.21 |
| Prop 20, Cam = 0.02 | 0.889 | 30.0 | 0.0200 | 0.186 | 0.7154 | 0.0000 | 1.5534 | 27.74 |
| Prop 20, Cam = 0.015 | 0.889 | 30.0 | 0.0150 | 0.186 | 0.7155 | 0.0000 | 1.3805 | 27.12 |
| Prop 20, Cam = 0.01 | 0.889 | 30.0 | 0.0100 | 0.186 | 0.7152 | 0.0000 | 1.2624 | 26.64 |
| Prop 20, Chord= 0.2 | 0.889 | 30.0 | 0.0100 | 0.200 | 0.7150 | 0.0000 | 0.9220 | 27.26 |
| Prop 20, Chord= 0.225 | 0.889 | 30.0 | 0.0100 | 0.225 | 0.7129 | 0.0000 | 0.5052 | 27.69 |
| Prop 20, Chord= 0.25 | 0.889 | 30.0 | 0.0100 | 0.250 | 0.7121 | 0.0016 | 0.3474 | 26.70 |

All three parameter modifications lead to a significant reduction of pressure side pressures of the blade, whilst also relieving the suction side pressure of the blade. In figure 7.39, the pressure distribution is shown after increasing the propeller skew. Comparing the pressure distribution with the pressures found on the unmodified Propeller 20 in figure 7.38, it is visible that the pressure build-up at the tip was relieved (in terms of magnitude and size). And the mid-chord pressure is also drastically reduced in size. A secondary beneficial effect is the reduction of pressure at the leading edge of the suction side. Note that this modification does lead to a reduction in open water efficiency. Increasing the skew did raise the maximum blade stress, yet much less than it was expected. Skew was identified as a influential parameter in increasing the stresses in the blade.

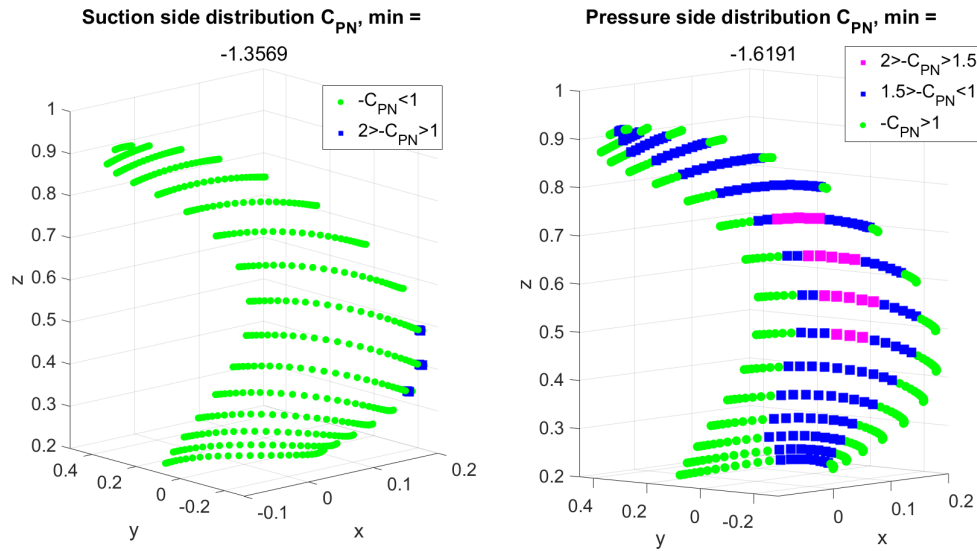


Figure 7.39: Propeller 20 after increasing the biased skew up to 30° .

Afterwards, the camber was decreased which was shown to have possible positive effects as well. The pressure distribution for this modification is shown in figure 7.40. This modification leads to the complete removal of negative suction side pressure ($A_{SUC} = 0.000$). And a further reduction of pressure side pressure. Oddly enough, this modification was not paid with a penalty in terms of efficiency reduction (see table 7.14). At this point, it is as said before inconclusive with the method proposed in this report to state whether these pressure side pressures are allowable or not. The pressure side area number is still relatively large compared to the c4-40 propeller, or compared to the best performing propellers generated under this criterion.

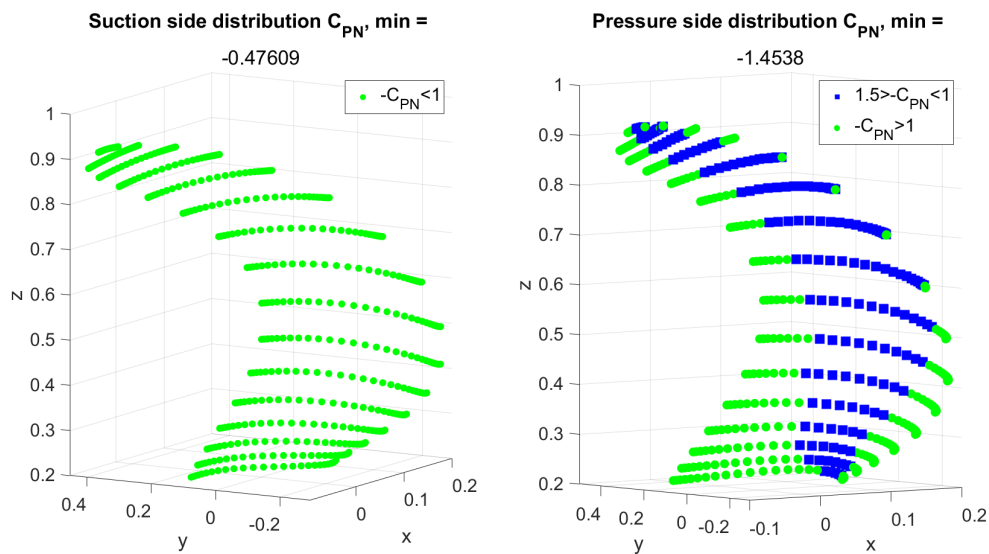


Figure 7.40: Propeller 20 after increasing the biased skew up to 30° and reducing the camber to 0.01.

In table 7.14, it is shown that gradually increasing the chord length distribution of the propeller, does further drop this pressure side area number. If the pressures are visualized, as in figure 7.41, it shows that this lower pressure distribution over the complete blade, is paid with a pressure build up at the tip. These tip pressures will be discussed in the next section. It also shows that as expected, chord length and camber both had very little effect on the maximum stress experienced by the blade.

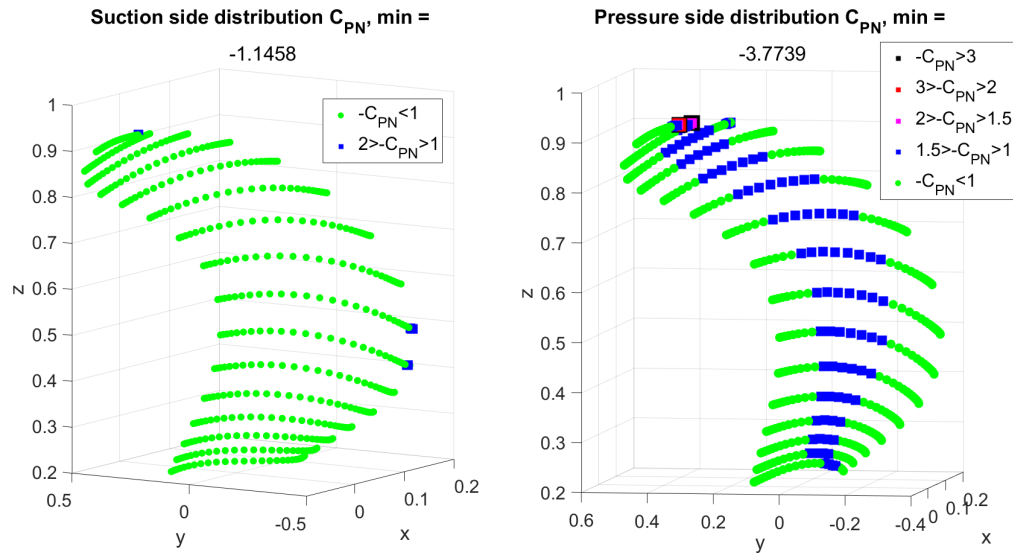


Figure 7.41: Propeller 20 after increasing the biased skew up to 30° , reducing the camber to 0.01 and increasing the maximum chord length to 0.25.

7.9 Tip pressure reduction

This tip pressure can lead to tip vortices, which are large sources of propeller noise emissions and must be avoided. It is possible to only locally lower the pitch in the tip region. This way the pressure side pressures might reduce without affecting the efficiency too significantly. In chapter 2 it was discussed that literature showed the beneficial effects of rake for tip unloading. In section 7.5, the results of applying rake were inconclusive and it was decided to not use it in the design space exploration. Now, it might be beneficial to apply only to the tip to see whether the tip pressures of the modified propeller 20 can be relieved (see the tip pressures in figure 7.41.)

First, the same area measurement can be applied to quantify the pressures encountered there. It was stated that this region is unsuitable for tip cavitation and pressure pulse analysis due to the instabilities. This statement is checked by analyzing the pressure at the radial stations at the tip of propellers 21 and 23 for which the distributions over the complete blade are shown in figures 7.36 and 7.37.

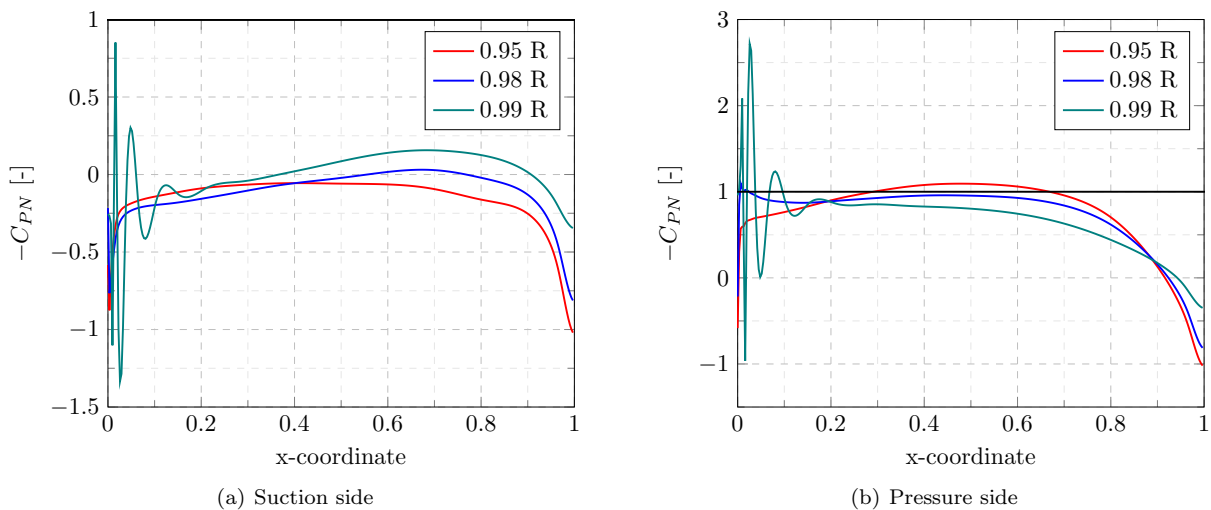


Figure 7.42: Tip pressure distribution for Propeller 21.

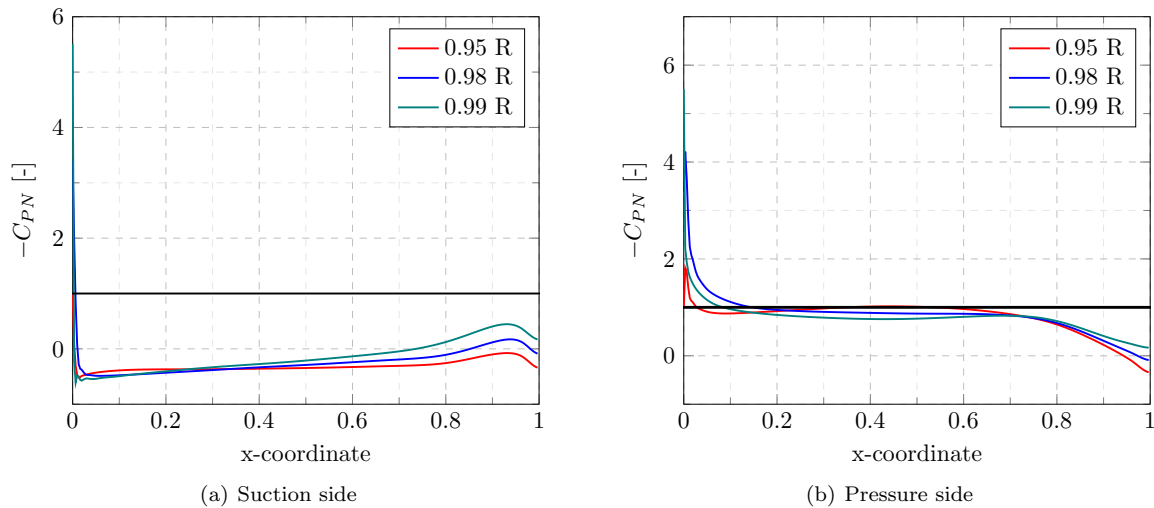


Figure 7.43: Tip pressure distribution for Propeller 23.

The pressure distributions in the tip regions for both propellers are shown in figures 7.42 and 7.43. For Propeller 21, only small tip pressure pulses were visualized in figure 7.36, yet a weird fluctuation in the tip pressure at both sides of the blades at 0.99R is present. This must indeed be a non-physical attribute of PROCAL. It can however not be stated whether the magnitude of this pressure at 0.99R is representing an actual value of leading-edge pressure or is a numerical artefact as well. It could be that only the fluctuations at the tip are numerically unstable, but this leading-edge value makes sense. This can not be concluded and therefore disregarded in this study. the pressure distributions at radial stations 0.95R and 0.98R can be used as a marker of tip pressures.

The results of Propeller 23, which was shown to have quite large tip pressures in figure 7.37. does indeed show larger leading edge tip pressures at both sides of the blade. However can the magnitude not be used due to the uncertainty of the validity of this value. It will be attempted, to see whether this pressure build-up at the tip, can with certain parameters be reduced to lower values. For Propeller 20, which was already relieved from a lot of pressure side pressure, the pressure at the radial stations at the tip is shown in figure 7.44. There was a larger amount of tip pressure visible (see figure 7.41. But these radial pressures seem fairly stable.

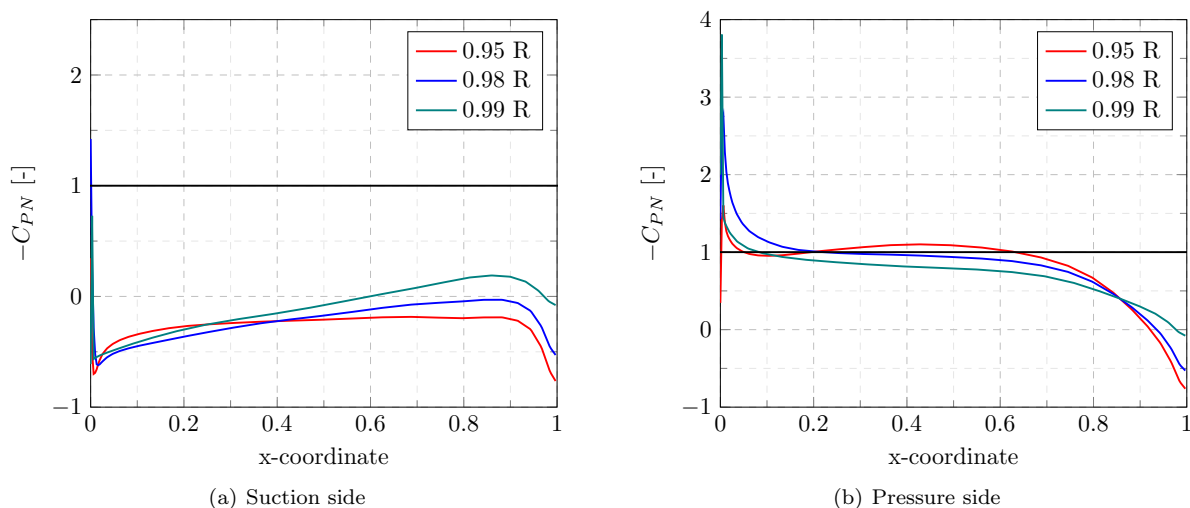


Figure 7.44: Tip pressure distribution for Propeller 20 after increasing the biased skew up to 30°, reducing the camber to 0.01 and increasing the maximum chord length to 0.25.

7.9.1 Lowering pitch at the tip

Although the magnitude is disputable due to numerical instabilities, it can still be stated that larger pressure values in the tip correspond to higher risks of the formation of tip vortices. A method to relieve this pressure could be locally decreasing the pitch at the tip to locally relieve the pressure there without affecting the propeller efficiency significantly. To quantify this pressure, the same area integration method as the overall pressure area

numbers is used for the pressures at 0.95R and 0.98R.

Figure 7.45 shows the pitch distributions of several modifications made to the modified propeller 20. In table 7.15, the obtained tip pressure coefficients are shown. It shows that minor tip pressure reduction is achievable but the efficiency also slightly drops. Furthermore, do the tip area pressure numbers show that the main contribution for tip pressures is in the final 0.99R radial stations, disputing the effectiveness of quantifying tip pressures with this method. In the last row of table 7.15, it is evident that a slight reduction in chord length is more beneficial in reducing the tip pressure at the pressure side of the blade.

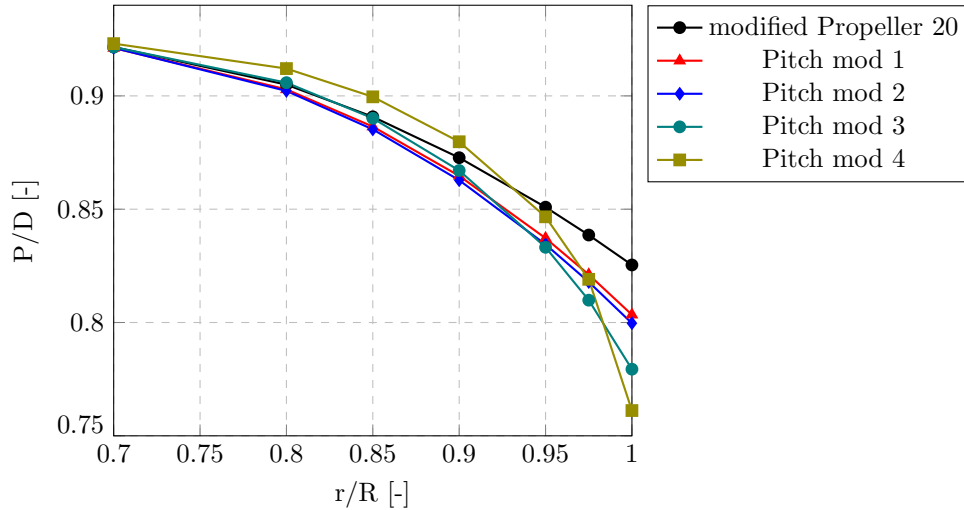


Figure 7.45: Different tip pitch distributions of propeller 20.

Table 7.15: Tip pitch modification iterations.

| Prop ID | A_{Suc} | $A_{\text{Tip,Suc}}$ | A_{Pres} | $A_{\text{Tip,Pres}}$ | η_0 |
|------------------------------|------------------|----------------------|-------------------|-----------------------|----------|
| Prop 20 | 0.0626 | 4.1220e-05 | 2.8478 | 0.9011 | 0.7321 |
| Prop 20, Skew = 30 | 0.0059 | 0 | 1.7999 | 0.1228 | 0.7150 |
| Prop 20, Cam = 0.01 | 0 | 0 | 1.2624 | 0.1173 | 0.7152 |
| Prop 20, Chord = 0.25 | 0.0016 | 2.0765e-04 | 0.3474 | 0.0929 | 0.7121 |
| Pitch Mod 1 | 0.0015 | 3.0845e-04 | 0.3473 | 0.0836 | 0.7113 |
| Pitch Mod 2 | 0.0014 | 2.7154e-04 | 0.3486 | 0.0788 | 0.7112 |
| Pitch Mod 3 | 0.0016 | 2.1535e-04 | 0.3573 | 0.0817 | 0.7113 |
| Pitch Mod 4 | 0.0020 | 3.0066e-04 | 0.3728 | 0.1241 | 0.7121 |
| Prop 20, Chord =0.225 | 0.0016 | 3.8890e-04 | 0.5052 | 0.0752 | 0.7129 |

7.9.2 Rake

Another parameter which could be beneficial is rake, which can be seen as a form of predefining the blade. This alters the way in which a blade experiences pressures during operation. In figure 7.46 several tested rake distributions of propeller 20 are shown.

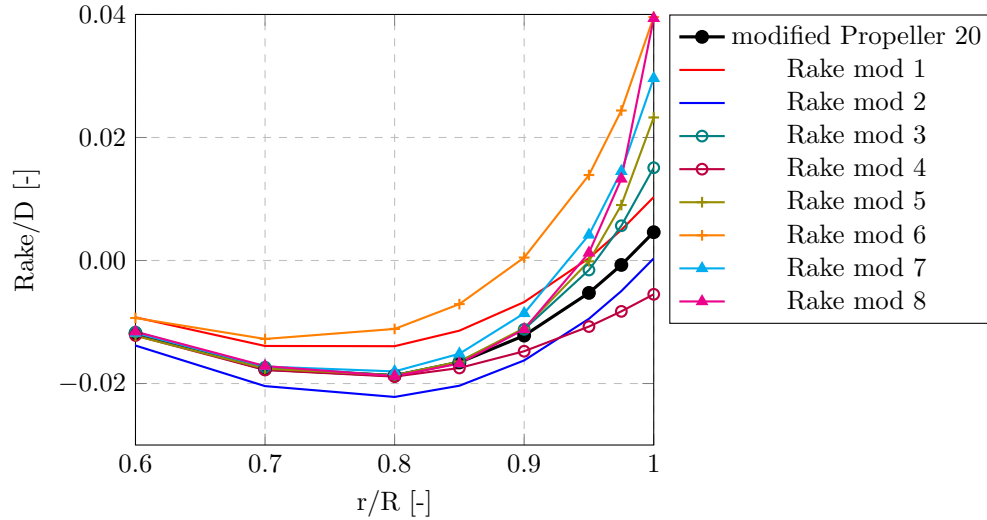


Figure 7.46: Different tip rake distributions of propeller 20.

If the results of these different rake distributions in table 7.16 are analyzed. It is visible that a positive rake (initial bending upstream) has a positive effect on both the total pressure side pressure area and the tip pressure area. This is achieved without affecting the suction side pressure and open water efficiency significantly. For a more negative rake near the tip (rake downstream), the opposite is true, as is shown for Rake modifications 2 and 4.

In terms of tip pressure area, Rake modification 6 reduced this tip pressure area the most. Dropping a staggering 98 % from the modified propeller 20 without rake modification. This is accompanied by a total pressure area reduction of 20.9 %. The pressure distribution is shown in figure 7.47. Note that the tip is completely cleared from pressures besides that single leading-edge tip node. This is very likely to be a numerical instability.

Table 7.16: Tip rake modification iterations.

| Prop ID | A_{Suc} | $A_{\text{Tip,Suc}}$ | A_{Pres} | $A_{\text{Tip,Pres}}$ | η_0 |
|-------------------------------|------------------|----------------------|-------------------|-----------------------|----------|
| Prop 20 | 0.0626 | 4.1220e-05 | 2.8478 | 0.9011 | 0.7321 |
| Prop 20, Skew = 30 | 0.0059 | 0 | 1.7999 | 0.1228 | 0.7150 |
| Prop 20, Cam = 0.01 | 0 | 0 | 1.2624 | 0.1173 | 0.7152 |
| Prop 20, Chord = 0.225 | 0.0016 | 3.8890e-04 | 0.5052 | 0.0752 | 0.7129 |
| Rake mod 1 | 0.0 | 1.0995e-04 | 0.4785 | 0.0528 | 0.7132 |
| Rake mod 2 | 0.0 | 6.6070e-04 | 0.5230 | 0.0921 | 0.7126 |
| Rake mod 3 | 0.0 | 4.9371e-04 | 0.4654 | 0.0293 | 0.7133 |
| Rake mod 4 | 0.0 | 4.7322e-05 | 0.5191 | 0.1073 | 0.7116 |
| Rake mod 5 | 0.0 | 3.8709e-04 | 0.4279 | 0.0124 | 0.7130 |
| Rake mod 6 | 0.0 | 0.0 | 0.3995 | 0.0016 | 0.7134 |
| Rake mod 7 | 0.0 | 8.3376e-06 | 0.4190 | 0.0060 | 0.7135 |
| Rake mod 8 | 0.0 | 4.0047e-04 | 0.3762 | 0.0049 | 0.7129 |

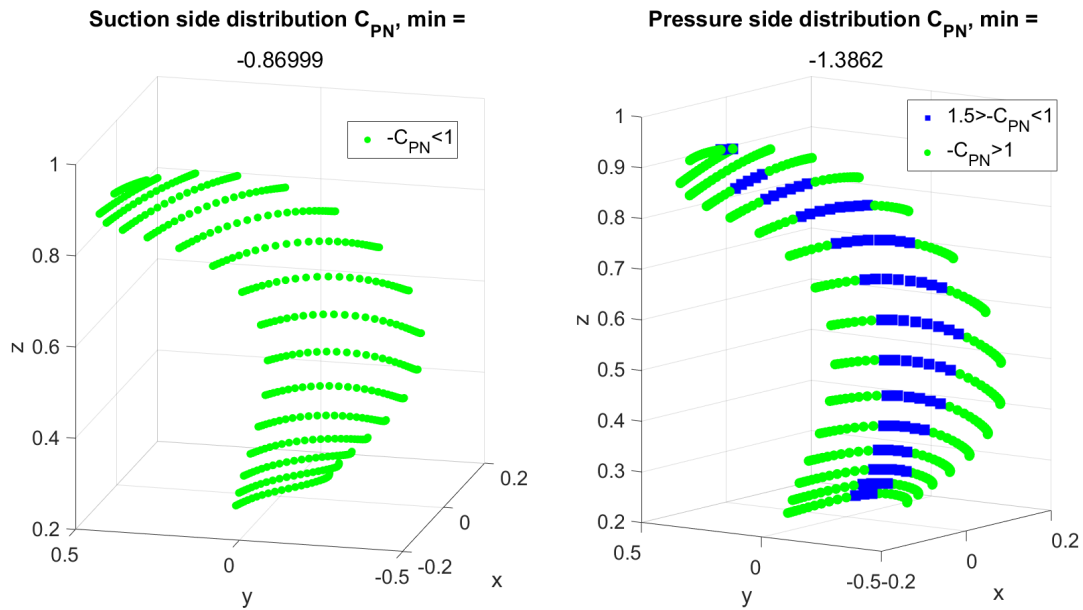


Figure 7.47: Pressure distribution of propeller 20 with rake modification 6. (see figure 7.46)

In terms of total pressure blade side reduction, rake modification 8 has the largest reduction of the pressure area number of 26.2 %. This pressure distribution is shown in figure 7.48. It can be seen that the very last node (leading edge 0.99R) has a higher pressure compared to rake modification 6 (see figure 7.47), but as discussed this pressure is numerically unstable and can not be used for this comparison. But even for the two pressures at radial stations 0.95R and 0.98R which comprise the tip pressure area number is higher for rake modification 8 (0.0049 compared to 0.0016 for rake modification 6).

Even though a lot of uncertainties exist around this tip region. The rake modifications 6 and 8 seem very effective in relieving the tip of negative pressure pulses.

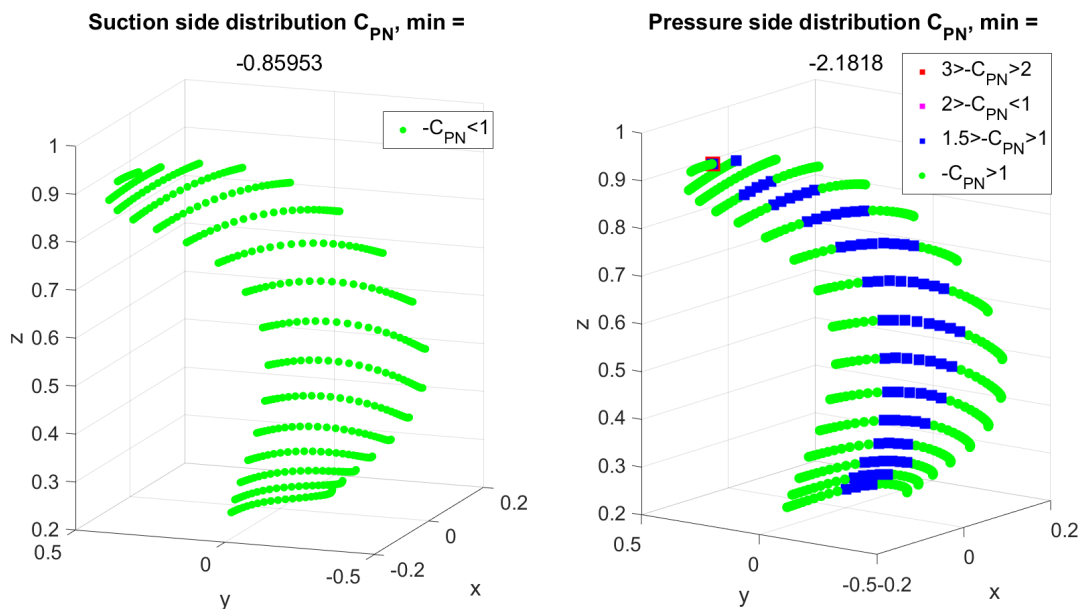


Figure 7.48: Pressure distribution of propeller 20 with rake modification 8. (see figure 7.46)

7.10 Conclusions

In this chapter, a design space exploration of marine propellers has been presented with the focus on which parameters have the potential to be used in the future design of composite marine propellers. increasing the pitch of the propellers results in higher blade deformations which results in higher efficiencies and lower suction side pressure of the propeller. The downside is much larger pressure side pressures. The amount of bending deformation seems largely unaffected, yet larger pitch values showed more instabilities in the tip region. Biased

skew (more skew towards the leading edge) without modifying the tip- and hub skew angles was shown to influence the bending deformation. It also improved the pressure distributions of the blade. Decreasing a propeller's chord length showed no effect on the blade deformation but a large influence on the bending deformation of the blade. This results in much lower suction side pressures, but much higher pressure side pressures. For increasing the chord length, the opposite conclusion is valid. Lastly, a reduction in camber showed much less bending deformation but higher blade deformations. This reduction did lead to favourable pressure distributions on both sides of the blade.

Combining all those parameters in a Latin Hypercube Sampling space, gave room for conclusions about how propeller geometry parameters influence the resulting performance:

- Pitch is the most effective parameter in increasing open water efficiency.
- Increasing pitch and skew are the most effective parameters to reduce suction side cavitation.
- Reducing the risk of pressure side cavitation is best achieved by increasing skew and increasing chord length.
- Almost all propellers with desirable performance had a large skew and high pitch value. The two downsides of this are the larger pressure side pressures. And the higher stresses experienced due to both parameters. These larger pressures can be relieved by reducing camber and increasing the chord length
- Propellers with a large blade deformation have a high pitch setting and low chord length.
- Propellers with a large bending deformation are propellers with a low chord length and high skew, thus for future studies where anisotropy can be applied, this can be exploited to optimize the amount of de-pitching can be achieved.
- Unwanted tip pressures can be reduced by applying a positive rake in the tip region. This results in lower pressure sides pressures on the complete blade. This is achieved without sacrificing the suction side cavitation risk or the efficiency significantly.

Up until now, all propellers have only been subjected to a uniform inflow of water. Thus the effects of deformation in the wake peak are neglected. Mainly due to the problems that still exist with computations in a non-uniform wake field, it was chosen to do this study in open water. To demonstrate the potential of flexible propellers in non-uniform inflow conditions, in chapter 8 a small demonstration of pressure distributions in a wake peak is given.

8 Non-uniform wake field demonstration

8.1 Introduction

As was stated before, it was chosen to perform the design study in chapter 7 in open water conditions with the main reason being time. The time planned in this design study was simply insufficient to execute all propeller generations in non-uniform wake conditions. This combined with the conclusions in chapter 6 that the current version of the unsteady FSI module does not allow an accurate amount of points per revolution, made the uncertainty too large to use that tool.

The findings of the design space exploration showed that there are clear links between deformation, pitch angle change and the performance of the generated propellers. However, up till now, one could have designed the same propeller from a conventional *NAB*-alloy in the deformed state of the flexible marine propeller to reach the same steady-state of performance in open water. This assumption will be tested with two test cases: Propeller 23, which reached better scores on the three criteria (suction side pressure, pressure side pressure and efficiency).

8.2 Wake peak performance

In figure 8.1, the deformation and pitch angle deformation of both the flexible and the predeformed geometry *NAB* propeller are shown relative to the undeformed flexible propeller geometry. It is visible that the bronze propeller now has slightly higher deformations, as it still deforms slightly, regardless of the high Young's modulus. But this deformation can be neglected. In chapter 4, it was concluded that these minor deformations of bronze through the ComPropApp had negligible influence on the propeller efficiency at medium advance ratios (see figure 4.9).

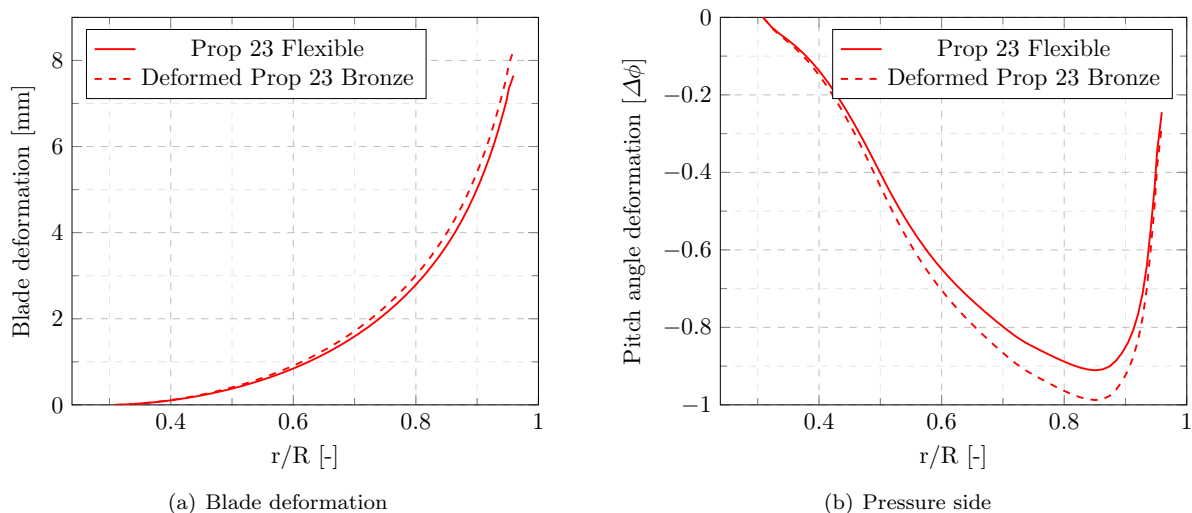


Figure 8.1: Blade and pitch angle deformation for propeller 23 (a) and propeller 23 predeformed bronze.

Table 8.1 shows these results and indeed these are approximately equal performing propellers. It is noticeable that the pre-deformed *NAB* propeller has a better pressure side pressure distribution compared to the flexible propeller, but slightly larger suction side pressure and efficiency coefficients. All explainable by the little extra deformation caused by the very small extra pitch angle deformation. For the PROCAL calculation, the results are even more similar as this is the exact same propeller shape as the propeller 23 after deformation. For the PROCAL simulation, these pressure area numbers can not be computed, but the distribution along the blade can be visualized. The pressure distributions of the flexible propeller 23 and rigid PROCAL propeller are shown in figures 8.2 and 8.3 respectively. And they show an obvious striking resemblance.

Table 8.1: Performance of flexible and predeformed *NAB* Propeller 23.

| Prop | A_{suc} | A_{pres} | $A_{\text{Pres,tip}}$ | η_0 | K_T |
|-------------------------------------|------------------|-------------------|-----------------------|----------|--------|
| Flexible 23 | 0.0059 | 0.5610 | 0.1107 | 0.7046 | 0.1544 |
| Predeformed Bronze 23 CPA | 0.0357 | 0.1271 | 0.1008 | 0.7039 | 0.1538 |
| Predeformed Bronze 23 PROCAL | - | - | - | 0.7044 | 0.1542 |

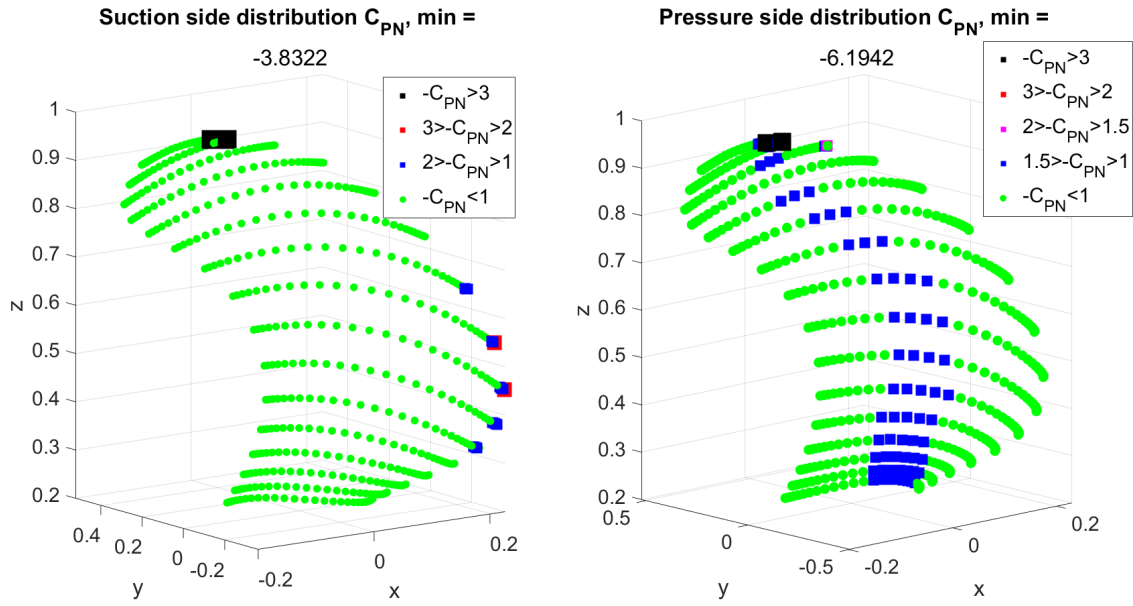


Figure 8.2: Pressure distributions for flexible propeller 23 through the ComPropApp.

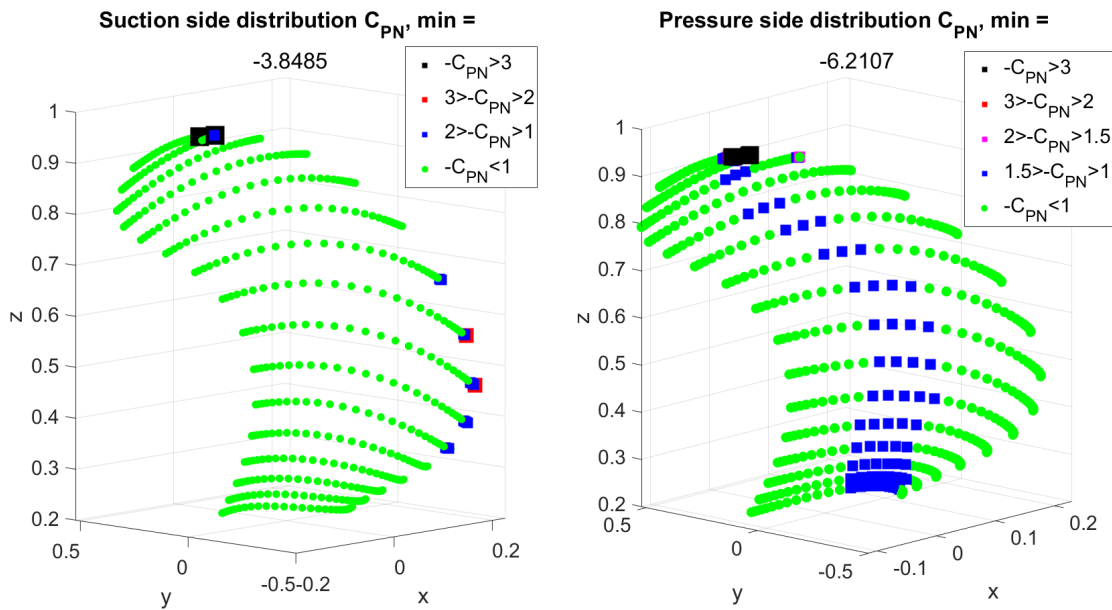


Figure 8.3: Pressure distributions for rigid propeller 23 through PROCAL.

The real elegance and benefits of a flexible marine propeller is that it potentially leads to a favourable deformed geometry in the peak of wake through deformation and bend-twist coupling. Thus relieve the cavitation of the blade, in the rest of the wake field it stays in its less deformed state. Thus even though it was shown in chapter 7 that through parametric modification of propeller geometries, efficiency and pressure gains are achievable. It is in no way a statement that the designed propellers are performing better in a realistic non-uniform wake condition.

What can be done instead of full unsteady FSI simulations is performing some indicative simulations on lower or higher advance ratios to gather insight into how the propeller would perform when it is assumed that there is a wake peak inflow velocity ($0.6v_s$) and a lower inflow velocity (v_s), which were the values found in the COMPROP2 validation wake field.

It will be evaluated whether the generated propellers that were performing well in open water (Propeller 21, Propeller 23 and the modified Propeller 20) also hold in a non-uniform wake. A small study can be done without the unsteady FSI module. The blades can be simulated at another inflow velocity, to simulate the deflection in the wake peak in a separate simulation. Note that this still performs steady computations, so whether a blade critically vibrates whilst deforming through the wake peak can not be concluded. But it does show how different

geometries deform for different flow velocities. Another simplification is that no tangential velocity components are considered in this analysis, which are present in realistic in behind ship wake fields. Propellers 20,21 and 23 were all simulated with the *Set-Point Iteration method*, which means they all delivered the same thrust (0.3792 kN) in the design condition of $J = 0.66$. When other advance ratios are considered, for a more realistic method, this set point iteration is removed. The propellers are then simulated with the constant rotational speed found at their design condition. All simulation setups are shown in table 8.2. furthermore, all propellers will also be simulated as the deformed last iteration from a NAB-material. This is done to show whether the predeformed rigid geometries will be behaving different in the wake peak.

Table 8.2: Lower or higher advance ratio simulations.

| Propeller | J [-] | n [rps] | v_a [m/s] |
|---------------------|-------|---------|-------------|
| c4-40 Bronze | 0.5 | 15.00 | 3.400 |
| c4-40 Bronze | 0.66 | 15.00 | 2.550 |
| c4-40 Bronze | 0.9 | 15.00 | 4.590 |
| Prop 20 | 0.5 | 15.16 | 2.577 |
| Prop 20 | 0.66 | 15.16 | 3.400 |
| Prop 20 | 0.9 | 15.16 | 4.639 |
| Prop 21 | 0.5 | 16.13 | 2.740 |
| Prop 21 | 0.66 | 16.13 | 3.400 |
| Prop 21 | 0.9 | 16.13 | 4.940 |
| Prop 23 | 0.5 | 13.57 | 2.307 |
| Prop 23 | 0.66 | 13.57 | 3.400 |
| Prop 23 | 0.9 | 13.57 | 4.152 |

Table 8.3: Performance of propellers in lower and higher inflow conditions.

| Propeller | J [-] | n [rps] | v_a [m/s] | A_{SUC} | $A_{SUC,TIP}$ | A_{PRES} | $A_{PRES,TIP}$ | η_0 | σ_{VM} |
|---------------------|-------|---------|-------------|-----------|---------------|------------|----------------|----------|---------------|
| c4-40 Bronze | 0.66 | 15.00 | 3.400 | 0.3287 | 0.0 | 0.7827 | 0.0059 | 0.7040 | 17.82 |
| Prop 20 | 0.66 | 15.16 | 3.400 | 0.0 | 0.0 | 0.3995 | 0.0016 | 0.7134 | 29.87 |
| Prop 21 | 0.66 | 16.13 | 3.400 | 0.0337 | 0.0 | 0.1232 | 0.0272 | 0.7044 | 23.83 |
| Prop 23 | 0.66 | 13.57 | 3.400 | 0.0059 | 0.0073 | 0.5610 | 0.1107 | 0.7046 | 33.17 |
| c4-40 Bronze | 0.5 | 15.00 | 2.550 | 0.0019 | 0.0987 | 1.6742 | 1.4684 | 0.6051 | 28.13 |
| Prop 20 | 0.5 | 15.16 | 2.577 | 0.0 | 0.0070 | 1.3935 | 0.3957 | 0.6127 | 44.12 |
| Prop 21 | 0.5 | 16.13 | 2.740 | 0.0 | 0.0019 | 1.2787 | 0.5848 | 0.6342 | 38.60 |
| Prop 23 | 0.5 | 13.57 | 2.307 | 0.0283 | 0.7326 | 1.6949 | 4.0250 | 0.5413 | 45.38 |
| c4-40 Bronze | 0.9 | 15.00 | 4.590 | 2.1474 | 0.6784 | 0.4590 | 0.0343 | 0.3922 | 9.17 |
| Prop 20 | 0.9 | 15.16 | 4.639 | 0.5114 | 0.3311 | 0.0836 | 5.1265e-04 | 0.6479 | 10.35 |
| Prop 21 | 0.9 | 16.13 | 4.940 | - | - | - | - | - | - |
| Prop 23 | 0.9 | 13.57 | 4.152 | 0.4299 | 1.7680e-05 | 0.0554 | 0.0295 | 0.6948 | 16.71 |

In table 8.3, it is visible that for simulations in a lower inflow velocity at $J = 0.55$ propeller 20 and Propeller 21 both have lower suction and pressure side pressure numbers and significantly reduced tip pressures. Also are slightly higher efficiencies reached in the off-design condition compared to the c4-40 propeller. It also shows that Propeller 23 has far worse performance. Thus a better propeller performing in open water does not always create a better propeller in the wake peak condition. In the bottom rows of table 8.3, it can be seen that all propellers have horrible performance. Thus a propeller can best be designed for the high inflow velocity and aim to improve the performance in the wake peak than the other way around. In figures 8.4 through 8.7, the pressure distributions for all four propellers at $J = 0.5$ are visualized.

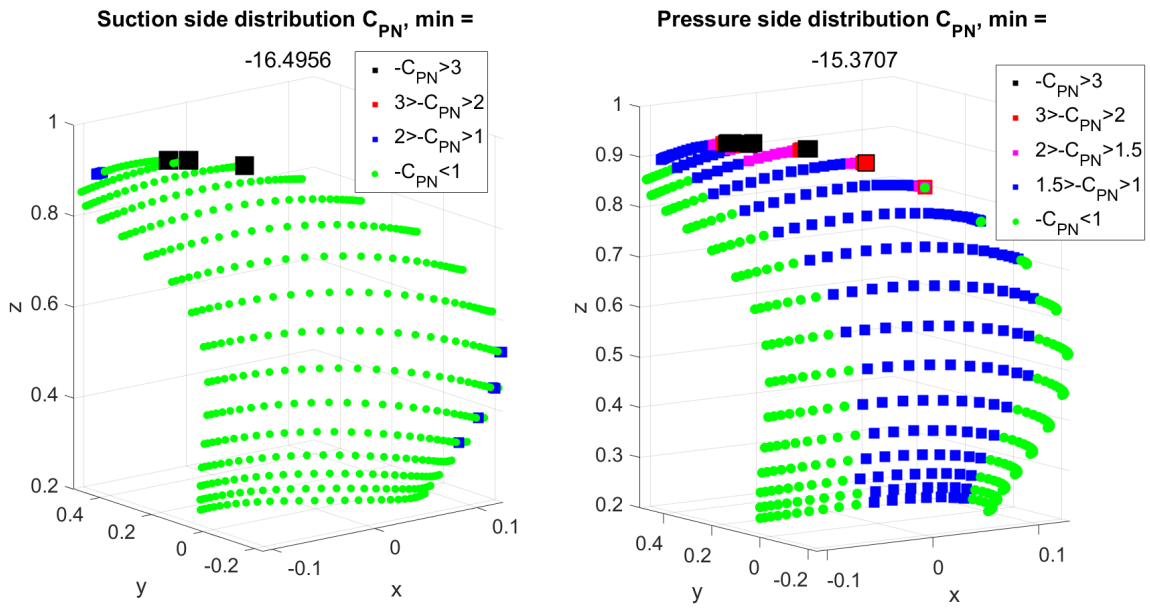


Figure 8.4: Pressure distribution of propeller c4-40 at $J = 0.5$.

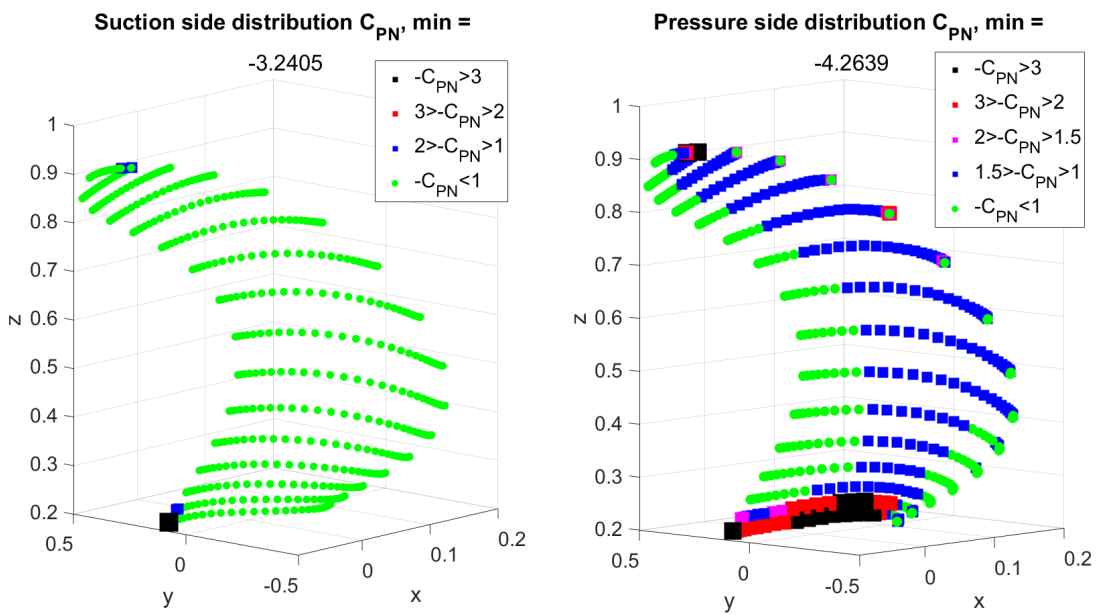
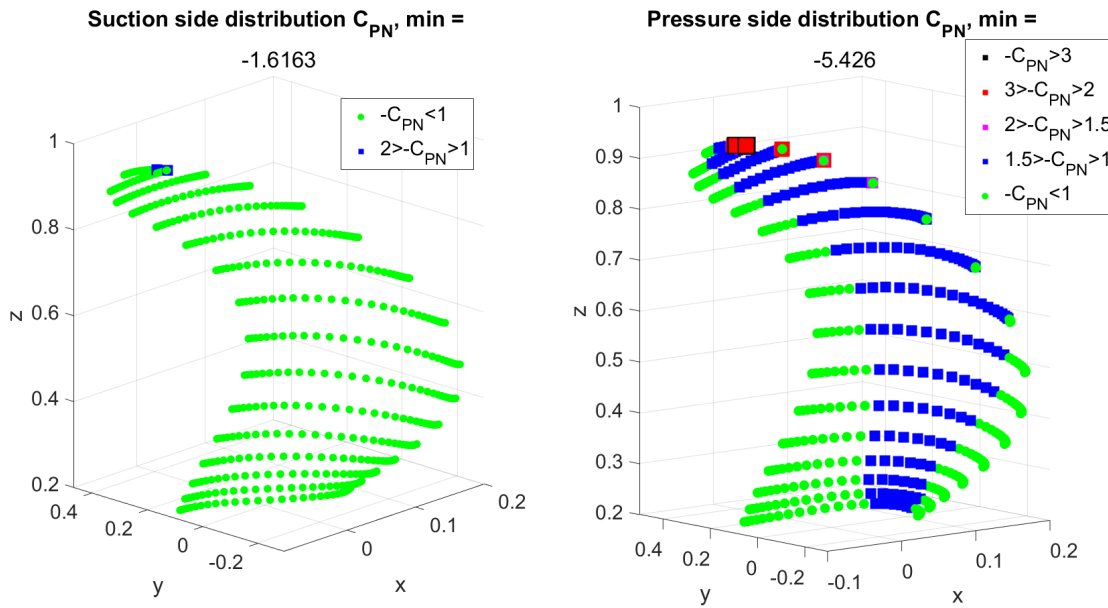
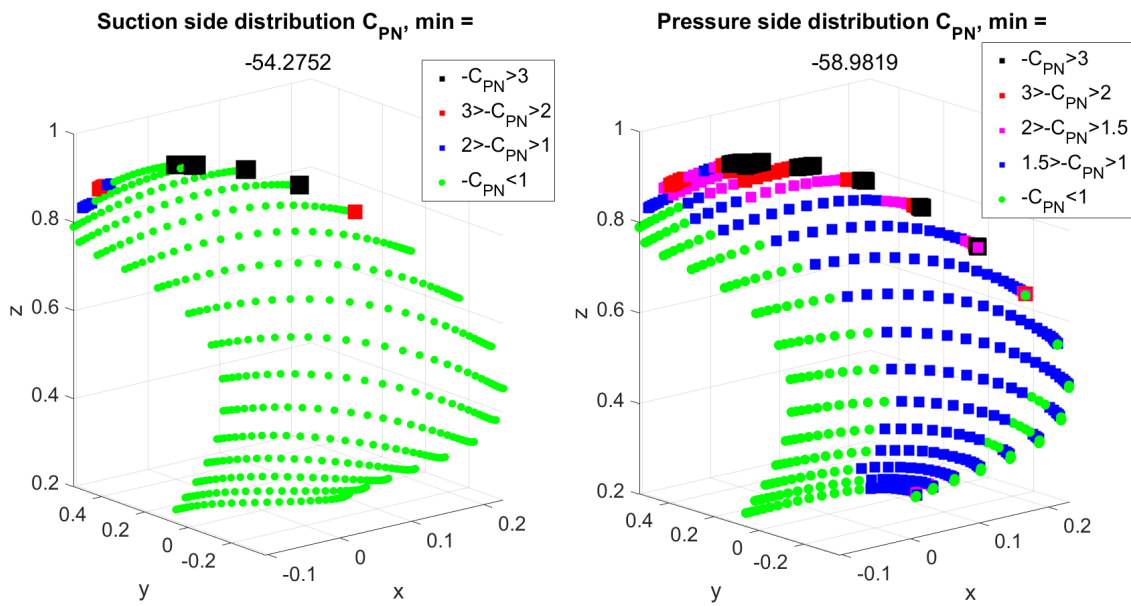


Figure 8.5: Pressure distribution of propeller 20 at $J = 0.5$.

Figure 8.6: Pressure distribution of propeller 21 at $J = 0.5$.Figure 8.7: Pressure distribution of propeller 23 at $J = 0.5$.

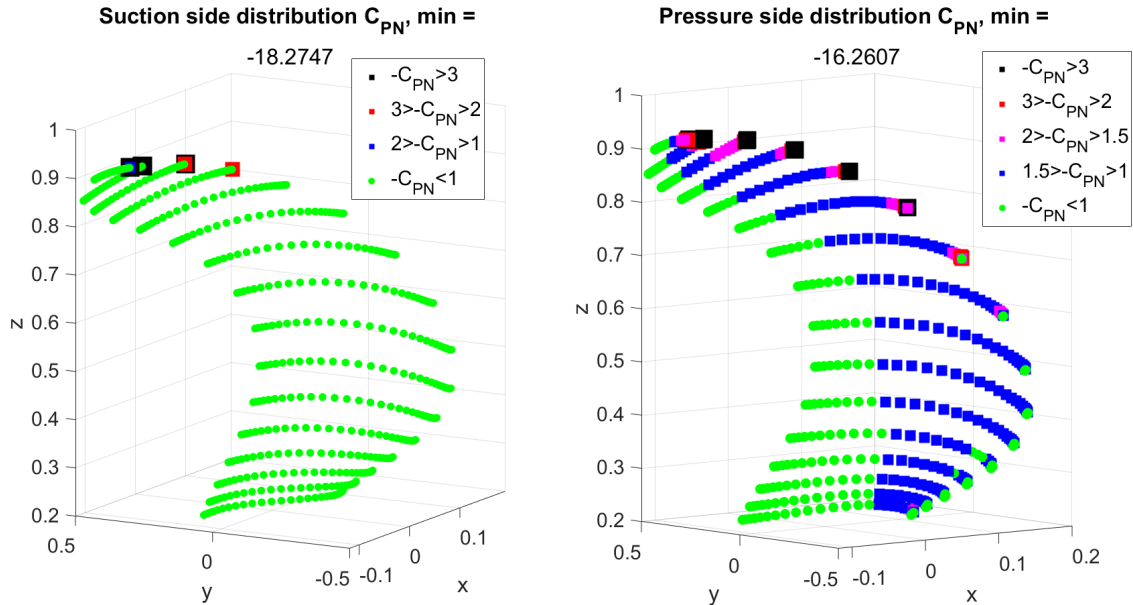
For propeller 20 (figure 8.5) which had better tip and pressure side numbers, the horrible pressures at the hub of the propeller are visible. Pressures up to $0.3R$ were disregarded in A_{PRES} since PROCAL is known to have weird results in this region but from inspecting figure 8.5, one should have serious doubts of this pressure distribution. As this study is not aiming to identify and mitigate numerical instabilities of PROCAL, these hub pressures will not be studied further. Propeller 21 seems to be favourable over propeller 20 in terms of pressures. As was presented in the pressure numbers for propeller 23, figure 8.7 confirms the horrible behaviour. The only downside of flexible propellers seems to be the far worse stresses experienced due to the flexible bending in the blade.

The last check will be to check whether the pre-deformed NAB-propellers perform differently from the flexible propellers that deformed due to operation in this wake peak condition at $J = 0.5$. Unfortunately, the bronze propellers did not all converge, so for this propeller (Propeller 21), this check can only be limited to a visual comparison (PROCAL does not allow computing the pressure area numbers) and the efficiencies.

Table 8.4: Comparison flexible- and preformed NAB propellers at wake peak velocity $J = 0.50$.

| Propeller | A_{SUC} | $A_{SUC,TIP}$ | A_{PRES} | $A_{PRES,TIP}$ | η_0 | σ_{VM} |
|------------------|-----------|---------------|------------|----------------|----------|---------------|
| Prop 20 Flexible | 0.0 | 0.0070 | 1.3935 | 0.3957 | 0.6127 | 44.11 |
| Prop 20 Bronze | 0.0058 | 0.1928 | 1.9342 | 1.2729 | 0.6033 | 51.02 |
| Prop 21 Flexible | 0.0 | 0.0057 | 1.3757 | 0.7926 | 0.6342 | 38.6037 |
| Prop 21 Bronze | - | - | - | - | 0.6364 | - |
| Prop 23 Flexible | 0.0452 | 0.5823 | 1.5328 | 3.1487 | 0.5490 | 41.63 |
| Prop 23 Bronze | 0.0283 | 0.7326 | 1.6949 | 4.0250 | 0.5413 | 45.37 |

These results are shown in table 8.4. For propeller 20, it seems that the flexibility played a key part in the propeller performance. The flexible propeller has significantly lower pressure area numbers compared to its NAB-preformed counterpart. Looking at the pressure side pressure distributions of both propellers in figures 8.5 for the flexible propeller and 8.8 for the preformed bronze it shows that the horrible hub pressures are not present in the NAB propeller but the higher pressures have shifted towards the tip of the propeller. In follow-up research this is an interesting topic as for now it seems arbitrary how this shift in pressure distribution has shifted from hub to tip. But it has to do with the flexibility of the material, as that is the only altered parameter. Another unexpected but very interesting result is the reduced Von Mises stress experienced by the blade for the flexible propeller. So even though the deformations and bending are much higher, the blade encounters smaller stresses. One would expect that larger deformations (ε) results in larger stresses.

Figure 8.8: Pressure distributions of preformed bronze propeller 20 at $J = 0.50$.

Propeller 21 could for some reason not be simulated within the ComPropApp when constructed from bronze as some unknown errors occurred in the FEM software. What can be done is a simulation of this preformed propeller 21 through PROCAL (so neglecting the minor deformations happening). Figure 8.9 shows this pressure distribution. Comparing these pressures with the flexible propeller 21 in figure 8.6, it is evident that the pressure distribution for the flexible variant is better as the tip pressures seem much lower.

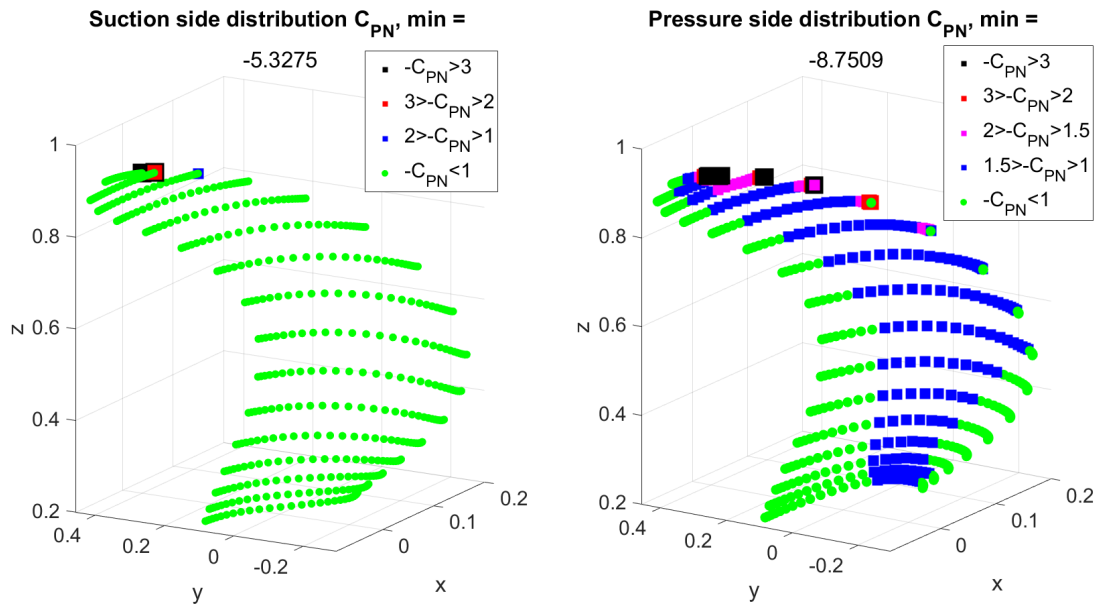


Figure 8.9: Pressure distributions of preformed bronze propeller 21 at $J = 0.50$.

The last propeller is Propeller 23, for which the flexible variant performed horribly in the wake peak. The pressure distribution of the bronze variant is shown in figure 8.10. The pressures seem to have reduced slightly which is also evident from the pressure numbers in table 8.4. Still the propeller performs far worse compared to propellers 20 and 21. The main difference between propeller 23 and the other two propellers is the increased chord length. So it seems that reduced chord length is an important parameter to allow the propeller to de-pitch in the wake peak. This is further substantiated by figure 8.11. Here it is visible that propeller 23 does not succeed in de-pitching the blade in the wake peak, which results in poor the pressure distributions.

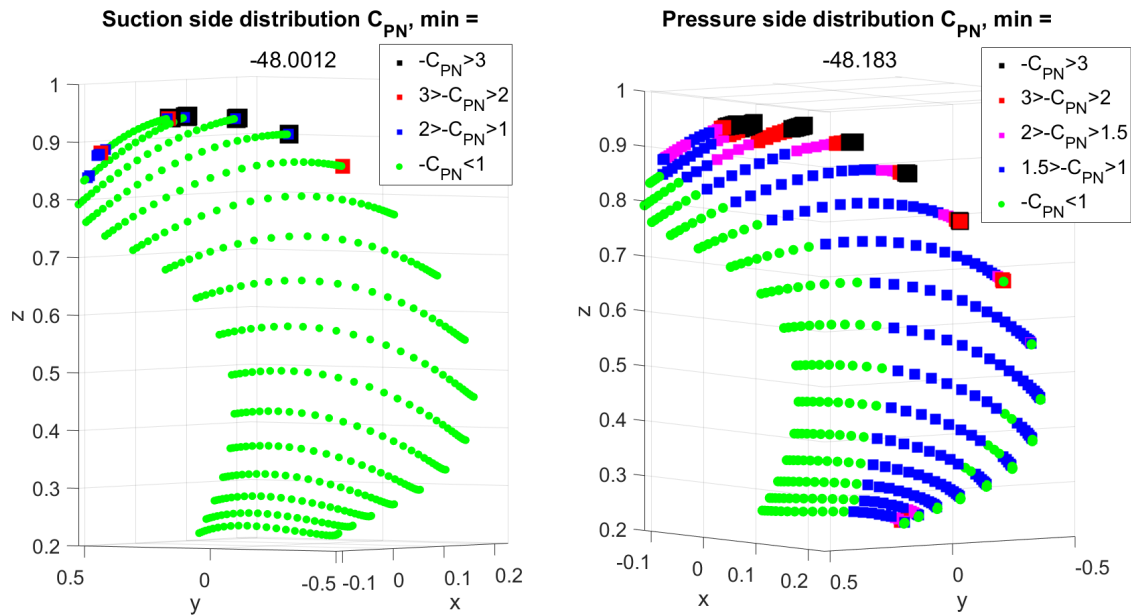


Figure 8.10: Pressure distributions of preformed bronze propeller 23 at $J = 0.50$.

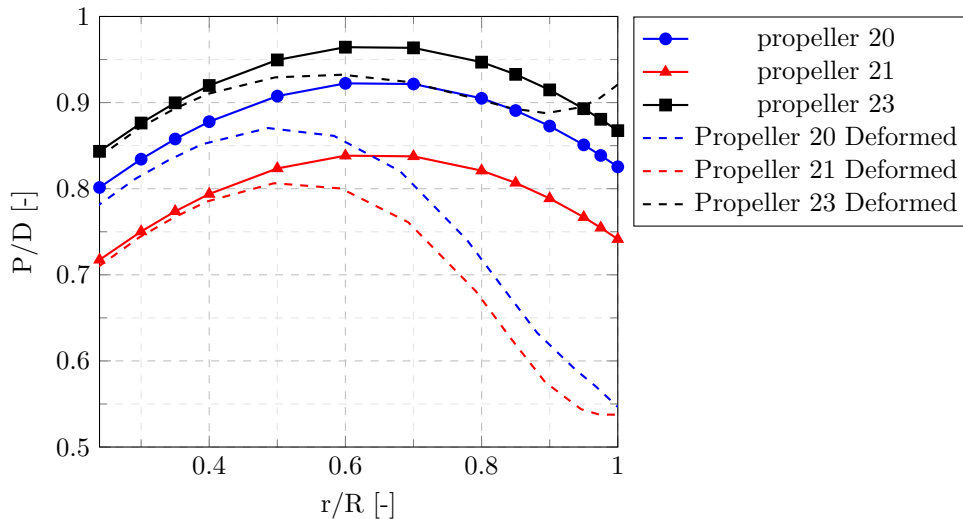


Figure 8.11: Pitch distributions and deformed pitch distributions at $J = 0.5$.

8.3 Conclusion

In this chapter, it was demonstrated that there is potential in the application of composites as a material to relieve pressure in the wake peak whilst maintaining a slightly higher efficiency as well. One of three propellers (propeller 21) was identified as a candidate since it performed better in the design conditions compared to the c4-40, and it showed improvements in the wake peak as well. For propeller 20, a serious increase in pressure at the hub was seen, but overall the pressure area number did increase compared to the bronze propeller. These hub pressures can not be evaluated due to numerical instabilities, so this propeller is inconclusive. The last propeller, propeller 23, showed degraded performance. It was seen that the only significantly different parameter of propeller 23 was a longer chord length, which resulted in a propeller which was unable to de-pitch in the wake peak thus the conclusions that can be drawn from this study are as follows:

- A well-designed flexible propeller for open water does not necessarily yield a propeller with good pressure distributions in the wake peak.
- The de-pitching of the propeller seems to be of importance as the two propellers showing this characteristic had much lower pressure area numbers. A small chord length seems to allow a propeller to de-pitch.
- No time-dependent conclusions can be made based on this study. The propeller which was deemed the best could potentially still resonate much more whilst deforming.

9 Conclusions

In chapters 4 through 6 the Composite Propeller application has been validated. In chapter 4, the first steps were to verify all grid sizes and meshes used in the ComPropApp. It was shown that the ComPropApp is well capable of predicting the performance of a propeller in open water by comparison of simulations with an open water diagram.

Afterwards, in chapter 5 the real power of the ComPropApp was shown where it uses a Fourier transform to analyze the performance of propellers in non-uniform inflow conditions in the frequency domain. When the project started there was serious concern about the tool as large deviations existed between the two methods used to evaluate the propeller deformation within a revolution. Through systematically testing and analysis of both methods it was deduced that the error had to occur within the modal analysis section of the unsteady FSI module. This conclusion was drawn after non-physical behaviour was observed in this module whilst altering the damping ratio (ζ), the density (ρ) and the Young's modulus (E) of the material. This error in the code was found by the supervisor of this project. After the code was modified, it was observed that both methods compared perfectly.

In chapter 6, the main task of the validation part of this project is performed: validation of the experiments performed on behalf of the CRS working group. These experiments were performed at MARIN in their cavitation tunnel. Firstly, the material (SikaBlock M980, a polyurethane foam) was analyzed and it showed inexplicable results in the material behaviour. Data from static loading tests performed at MARIN and DRDC showed that some form of unrecoverable deformation (material creep) is present. As this is not possible to model in the current FEM package of the ComPropApp, this is an unwanted material property which should be avoided. Even if another FEM tool, which could model this material property was to be selected. It should still be considered as it is an unwanted property for propeller construction. It was also deduced from these tests that the material had a significantly different Young's modulus and thus different material natural frequency (which probably differs per specimen of the SikaBlock). This also substantiates the conclusion that the material should in future experiments be avoided.

After the material was investigated, the experimental data is analyzed. It is shown that the largest contribution of uncertainty in the experimental measurements is present right before the wake peak. For the rest of the revolution, not much deviation from the mean value is present in the experimental deformation of the propeller blades. This uncertainty of the data is most likely to be happening due to slight differences per revolution in inflow velocity, model construction errors and measurement uncertainties. Those are the largest when the blade is just entering this area where the inflow velocity decreases, and thus the blade starts to deform.

Due to the method of capturing the blade deformation (Ensemble averaging), no firm conclusion can be made on the blade vibrations happening within a revolution (which could potentially also happen in this large area of uncertainty). Only the main deformation component can be analyzed and compared with the simulations of the ComPropApp.

From a simulation in the ComPropApp, it was observed that the blades happen to vibrate at a frequency very close to the *dry* natural frequency of the propeller blade. In reality, a propeller blade should vibrate lower in water due to added hydrodynamic damping. Due to the diverging nature of these experiments, it could not be checked whether this added hydrodynamic damping is slowly added to the system, or if it is not happening at all. In further research, this should be fixed to analyze the vibration patterns of propellers operating in water. For this project, it was not deemed critical, as only the main deformation component of the experiments could be observed in the first place.

In total three experiments with different advance ratios were compared with an unsteady FSI computation in the ComPropApp. It showed that there was a weird discrepancy in the definition of the origin of the experimental deformation data. This discrepancy was dealt with by shifting the experimental data up with a factor equal to the difference in average experimental- and simulated deformation. After that, the experiments and simulations compared rather good for all three scenarios. An overestimation of the wake peak through both methods was observed (which grows for larger deformations). This is most likely due to a deficit in the number of points per revolution considered, this leads to large instantaneously loading of the blade. Unfortunately, adding more data points led to unacceptable computational times and diverging simulations. In further research the mathematical algorithm (QN-ILS method) must be more thoroughly investigated as it is suspected that lots of profit can be gained there in terms of both computational time and convergence stability of the simulations.

In the second part of this report, from chapter 7 onwards, the design space of propellers is explored. Due to the fact that the unsteady FSI module was currently too time-consuming it was chosen to first explore this space in open water. First, parameters were systematically altered to explore the effect of those parameters in terms of hydrodynamic performance, deformation and pressure distributions. It was shown that great profit in several of those classes can be gained by increasing or decreasing propeller pitch, skew, chord length and propeller camber. To make initial statements on the cavitation performance, the numbers A_{PRES} and A_{SUC}

are introduced which integrate all negative pressure coefficients over the pressure or suction side of the blade to make quick assessments of cavitation risks of these propellers.

The conclusions from these single parameter series are that efficiency can easily be increased by increasing the propeller pitch or reducing the chord length. Suction side pressures are also easily controlled by all four parameters and by increasing the deformation of the blade. The hardest parameter to control turned out to be pressure side pressures. This can be slightly decreased by increasing skew or propeller camber.

After these single parameter series, the effect of all parameters on each other is investigated. This was done with Latin Hypercube Sampling in which 66 propellers were generated and it showed that the effects of these parameters greatly influence each other. The link between modifying a parameter and resulting performance were less clear compared to the single parameter modifications. Nevertheless, the LHS study did provide conclusions about the design space of flexible propellers:

- Pitch is the most effective parameter in increasing open water efficiency.
- Increasing pitch and skew are the most effective parameters to reduce suction side cavitation.
- Reducing the risk of pressure side cavitation is best achieved by increasing skew and increasing chord length.
- Almost all propellers with desirable performance had a large skew and high pitch value. The two downsides of this are the larger pressure side pressures. And the higher stresses experienced due to both parameters. These larger pressures can be relieved by reducing camber and increasing the chord length.
- Propellers with a large blade deformation have a high pitch setting and low chord length.
- Propellers with a large bending deformation are propellers with a low chord length and high skew, thus for future studies where anisotropy can be applied, this can be exploited to optimize the amount of de-pitching can be achieved.
- Unwanted tip pressures can be reduced by applying a positive rake in the tip region. Besides drastically reducing the tip pressures, it also results in lower pressure side pressures on the complete blade. This is achieved without sacrificing the suction side cavitation risk or the efficiency significantly.

It was shown that A_{SUC} turned out to be an excellent indicator of pressures on the suction side of the blade. The pressure area number for the pressure side (A_{PRES}) however, did not contain all information needed to assess the propellers adequately in terms of pressure side cavitation risk. It was observed that large leading-edge-, tip- and hub pressures could occur. These regions are known to be numerically unstable due to the limitations of the BEM code. Since these pressures do not occur on each propeller it is unclear whether they are physical or numerical artefacts. Even if they are real, it is unknown how to assess these pressure areas.

It was possible to assess the tip pressures. The same integration scheme was applied to the pressure distributions of 0.95R and 0.98R. It was shown that these distributions were stable enough to use, only 0.99R was very unstable. This area was named $A_{TIP,PRES}$. It turned out to be a critical design criterion. Tip pressures are a critical source of underwater noise emission and cavitation and could thus not be neglected. In the future, more knowledge must be obtained on why these numerical instabilities occur and how they can be properly assessed. This way these interesting hub- and leading-edge pressures could be quantified to construct a better assessment on pressure side cavitation risk.

Up to this point, these propellers could have also been constructed from NAB-alloys where the propeller geometry is equal to the deformed geometry of its flexible counterpart. The real elegance lies in the possible favourable bending of flexible propellers in the wake peak which can not be achieved by conventional metal propellers. In chapter 8, it is verified that these predeformed metal propellers do indeed reach the same performance as the flexible propellers in terms of efficiency and pressure distributions.

As the method used was open water simulations since the unsteady FSI was deemed unsuitable yet for time-dependent analyses, in this report it is not shown how these parameters influence the pressure distributions over a complete non-uniform inflow revolution. To demonstrate the possible benefits of flexible propellers, three of the best performing propellers in open water were also simulated at a lower advance ratio to imitate the condition a propeller might experience in a wake peak. The study showed that two of the three propellers were experiencing much lower pressures at this lower advance ratio compared to a metal c4-40 propeller, this was accompanied by a slightly higher efficiency as well. The third propeller showed a drastic increase in the risk of cavitation.

It was also validated that this same benefit was not obtained when the designed propellers were made from NAB-alloys, which do not reach the desired depitched position anymore, as the material becomes much stiffer. The main difference between the two propellers which did relieve the pressure in the wake peak and the one that did not was a much higher chord length. Thus a small chord length was identified as an important parameter to allow the propeller to de-pitch itself in the wake peak.

10 Further research and recommendations

This thesis was split in two parts, it make sense to split the further research and recommendations topics in two sections as well:

1. Validation of the Unsteady FSI and Stress Analysis module of the Composite Propeller Application by comparing experiments with simulations.
2. An exploration of the design space of geometry parameters of flexible marine propellers.

10.1 the Composite Propeller Application

In chapters 4 through 6, it was shown that the ComPropApp is very well capable to predict the deformation of propellers in open water and non-uniform inflow conditions as well. Comparing the experiments with simulation did raise a number of questions/errors which could be answered in follow-up research.

First, the numerical scheme which controls the stability of the program, the Quasi Newton - Iterative Least Square method was treated mostly as a black box of the ComPropApp. Mainly since the demarcation of the scope of this project has to cut some topics. It is however believed that serious improvements might be gained if a deeper understanding of this numerical method is reached. It was shown in chapter 6, that for doubling the number of points in the unsteady FSI module the program becomes increasingly divergent which leads to unacceptable computational times. It seemed that these divergence issues arise since the numerical vibrations simply do not want to settle.

Another known issue is the incapability of adding hydrodynamic damping to the system. It was shown that the dry frequency was exited whilst vibrating in water. Currently, the mathematics should allow for this added hydrodynamic damping to slowly enter the system over time, this was observable for some computations but very slowly. This was visible as a slight phase lag over iterations. It could be that over more iterations this phase lag settles as a lower wet eigenfrequency. It could also be that these vibrations smoothen out over time. It is also possible to estimate the wet eigenfrequencies before hand. It is interesting to see how those two methods simulate the blade deformation in a follow-up study.

Due to these two issues, and combined with the fact that P4C also was inherently slow it was decided to not compute any simulations with more data points per revolution. Therefore the discrepancy at the wake peak between experiment and simulation could not be elaborated on any further. The hypothesis now is, is that this overestimation in the simulations is caused due to the too small step size considered and this wake peak deformation has some overshoot. This must be investigated when improvements on the ComPropApp have been done.

As was stated by the preceding graduate on this topic in his thesis, K. van der Sanden [39] came up with another possible method to speed up the process: Quasi-steady simulations. Firstly, with the steady FSI module the ComPropApp could simulate the average inflow velocity in open water. Afterwards with this deformed geometry and internal developed stresses (which is the missing part right now) the unsteady FSI computation can be started. It is believed that this will save large amounts of computational time.

Only if their is more certainty developed of this wake peak deflection and the program has been sufficiently cleaned up in terms of hydrodynamic damping and computational times. The ComPropApp is ready to use in a comparison with experimental real-time deflection tracing. In the current experimental setup, this real time deformation can not be traced. This turned out to not be crucial for this report as the ComPropApp cannot simulate that currently. But if in the future, one would like to experimentally capture vibrations within a revolution, one should not use the ensemble averaging method. To simulate these vibrations in the ComPropApp, much more data points should be considered.

Lastly, was the polyurethane foam SikaBlock discussed. It turned out to raise more questions than answers. Firstly, do all specimens have the same magnitude of anisotropy, discrepancy in Young's modulus and levels of nonlinear behaviour? All these material properties could be studied in a study into the material properties of SikaBlock. And possibly be modelled into more extensive finite element models (ABAQUS and ANSYS are for example able to model creep and time-dependent deformation for example), but it could also turn out to be negligible. the question thus is how valuable this information would be from the point of view of a hydrodynamic perspective. Even from the marine structural engineering perspective, this information might be of little use, as this material would only ever be used in model scale and never in real life. (The material was selected only to get deformations in model scale which were large enough so that the measurement uncertainties were negligible).

Another topic of material science which is more interesting in terms of research with respect to the design of composite marine propellers and which fills the gap between the structural- and hydrodynamic side of the project is to investigate the tolerances of propellers to minor manufacturing and material errors. In chapter 6, it was shown that there were minor milling errors present in all propeller models, which led to significant

differences in hydrodynamic performance when simulated. This combined with the observed material discrepancies (time dependant deformation, anisotropy and Young's modulus) could be the starting point of a study into the manufacturing uncertainties of composite propellers. It is expected that these tolerances will be even more crucial for composite propellers, as even more degrees of freedom are introduced. Matrix stiffness, fibre stiffness, orientation and ply thickness for example.

10.2 Design of flexible marine Propellers

The most obvious, and most important follow-up study would be to perform a design study as in chapter 7, but now in a non-uniform wake. All parameters identified in this study showed that great improvement in pressure distributions is achievable, but in chapter 8 it was also demonstrated that a propeller with lower pressures in the design conditions does not lead to a better pressure distribution in the wake peak automatically. Therefore the same connections between geometry parameters and pressure reductions have to be drawn whilst the propeller deforms through the wake peak.

Another to be studied topic is to check when and why propellers show numerical artefacts at the leading edge, hub and tip. Since sometimes it does occur and sometimes it does not it could be wise to study this more in-depth to improve the value and certainty of PROCAL and the ComPropApp. It could very well turn out to be an unavoidable downside of BEM computations. And only with more lengthy CFD computations, these flow phenomena can be captured accurately.

The pressure area numbers in this study were used only to give a fast initial assessment of the cavitation risk of the propeller blades. It should be validated that these numbers do indeed make sense as an identifier of cavitation risks of flexible marine propellers.

In PROCAL, it is possible to execute cavitating sums. One could simulate the deformed flexible propeller in PROCAL, but it is expected that the vibrations and corresponding velocities and pressures play a large role in the cavitation behaviour of the propeller. Thus this deformed rigid propeller does not make sense. This cavitating simulation module of PROCAL has to be extrapolated to a version which is valid for the ComPropApp as well. This way, the pressure area numbers could be validated, and if necessary, modified. The same computations could also be executed with a CFD-FEM simulation. These are much lengthier than BEM-FEM simulations but capture much more complex flow phenomena.

A Latin Hypercube Sampling design space

Table A.1: Propeller generation 1 through 33

| Prop ID | Mean pitch | Max Skew Angle | Camber | Chord Length |
|---------|------------|----------------|--------|--------------|
| 1 | 0.835 | 11.5 | 0.0181 | 0.240 |
| 2 | 0.895 | 19.3 | 0.0369 | 0.183 |
| 3 | 0.697 | 26.6 | 0.0250 | 0.330 |
| 4 | 0.901 | 11.0 | 0.0313 | 0.344 |
| 5 | 0.722 | 5.82 | 0.0187 | 0.269 |
| 6 | 0.668 | 17.7 | 0.0328 | 0.261 |
| 7 | 0.745 | 28.1 | 0.0222 | 0.226 |
| 8 | 0.777 | 15.2 | 0.0376 | 0.326 |
| 9 | 0.937 | 20.9 | 0.0348 | 0.244 |
| 10 | 0.877 | 5.30 | 0.0355 | 0.197 |
| 11 | 0.735 | 27.3 | 0.0292 | 0.311 |
| 12 | 0.918 | 12.6 | 0.0124 | 0.231 |
| 13 | 0.907 | 14.5 | 0.0201 | 0.222 |
| 14 | 0.787 | 21.4 | 0.0439 | 0.246 |
| 15 | 0.871 | 24.4 | 0.0173 | 0.194 |
| 16 | 0.703 | 27.8 | 0.0397 | 0.190 |
| 17 | 0.763 | 20.4 | 0.0306 | 0.341 |
| 18 | 0.925 | 9.98 | 0.0446 | 0.349 |
| 19 | 0.799 | 8.93 | 0.0111 | 0.284 |
| 20 | 0.889 | 8.42 | 0.0278 | 0.186 |
| 21 | 0.805 | 25.6 | 0.0132 | 0.211 |
| 22 | 0.655 | 7.90 | 0.0432 | 0.229 |
| 23 | 0.931 | 29.8 | 0.0118 | 0.333 |
| 24 | 0.865 | 6.36 | 0.0362 | 0.172 |
| 25 | 0.829 | 24.0 | 0.0390 | 0.175 |
| 26 | 0.817 | 13.1 | 0.0404 | 0.208 |
| 27 | 0.793 | 9.40 | 0.0138 | 0.298 |
| 28 | 0.709 | 12.1 | 0.0272 | 0.301 |
| 29 | 0.823 | 22.4 | 0.0243 | 0.291 |
| 30 | 0.679 | 14.1 | 0.0384 | 0.258 |
| 31 | 0.811 | 13.7 | 0.0285 | 0.279 |
| 32 | 0.661 | 22.9 | 0.0425 | 0.218 |
| 33 | 0.727 | 21.9 | 0.0195 | 0.305 |

Table A.2: Propeller generation 34 through 66

| Prop ID | Mean pitch | Max Skew Angle | Camber | Chord Length |
|----------------|-------------------|-----------------------|---------------|---------------------|
| 34 | 0.649 | 16.8 | 0.0236 | 0.204 |
| 35 | 0.691 | 29.3 | 0.0166 | 0.294 |
| 36 | 0.841 | 10.4 | 0.0152 | 0.200 |
| 37 | 0.847 | 23.5 | 0.0418 | 0.236 |
| 38 | 0.751 | 26.2 | 0.0320 | 0.288 |
| 39 | 0.913 | 18.4 | 0.0335 | 0.315 |
| 40 | 0.643 | 15.7 | 0.0146 | 0.179 |
| 41 | 0.715 | 7.30 | 0.0411 | 0.338 |
| 42 | 0.673 | 4.70 | 0.0341 | 0.308 |
| 43 | 0.859 | 18.7 | 0.0258 | 0.265 |
| 44 | 0.883 | 25.1 | 0.0299 | 0.256 |
| 45 | 0.739 | 28.6 | 0.0264 | 0.251 |
| 46 | 0.685 | 4.27 | 0.0103 | 0.215 |
| 47 | 0.757 | 19.7 | 0.0215 | 0.271 |
| 48 | 0.769 | 17.2 | 0.0159 | 0.275 |
| 49 | 0.781 | 6.80 | 0.0209 | 0.324 |
| 50 | 0.853 | 16.2 | 0.0229 | 0.319 |
| 51 | 0.642 | 4.75 | 0.0107 | 0.173 |
| 52 | 0.644 | 4.61 | 0.0104 | 0.345 |
| 53 | 0.645 | 5.89 | 0.0448 | 0.174 |
| 54 | 0.651 | 5.22 | 0.0444 | 0.342 |
| 55 | 0.643 | 28.8 | 0.0106 | 0.181 |
| 56 | 0.656 | 29.5 | 0.0114 | 0.341 |
| 57 | 0.648 | 28.6 | 0.0433 | 0.187 |
| 58 | 0.647 | 28.3 | 0.0436 | 0.328 |
| 59 | 0.938 | 6.45 | 0.0112 | 0.179 |
| 60 | 0.914 | 6.72 | 0.0128 | 0.336 |
| 61 | 0.890 | 5.35 | 0.0434 | 0.189 |
| 62 | 0.935 | 5.48 | 0.0409 | 0.328 |
| 63 | 0.937 | 28.4 | 0.0126 | 0.192 |
| 64 | 0.924 | 27.7 | 0.0115 | 0.346 |
| 65 | 0.887 | 28.2 | 0.0437 | 0.180 |
| 66 | 0.906 | 29.4 | 0.0412 | 0.335 |

References

- [1] A. Mouritz, E. Gellert, P. Burchill, and K. Challis, “Review of advanced composite structures for naval ships and submarines,” *Composite Structures*, vol. 53, no. 1, p. 21–42, 2001.
- [2] P. Kellett, O. Turan, and A. Incecik, *1 st International Meeting - Propeller Noise & Vibration*.
- [3] “Propeller in composite material,” Tech. Rep. NI 663 DT R00 E, Bureau Veritas, 8 cours du Triangle, Paris, France, 2020.
- [4] J. S. Carlton, *Marine propellers and propulsion*. Kidlington, Oxford: Butterworth-Heinemann, 2019.
- [5] *International Towing Tank Conference 7.5 – 01 02 – 01, Model Manufacture, Propeller Models Terminology and Nomenclature for Propeller Geometry*, p. 1–16. 1999.
- [6] A. Vrijdag, D. Stapersma, and T. van Terwisga, “Control of propeller cavitation in operational conditions,” *Journal of Marine Engineering & Technology*, vol. 9, no. 1, pp. 15–26, 2010.
- [7] M. Motley, Z. Liu, and Y. Young, “Utilizing fluid–structure interactions to improve energy efficiency of composite marine propellers in spatially varying wake,” vol. 90, pp. 304–313, oct 2009.
- [8] Z. Liu and Y. L. Young, “Static divergence of self-twisting composite rotors,” vol. 26, pp. 841–847, jul 2010.
- [9] R. J. Boswell and G. G. Cox, *Design and model evaluation of a highly-skewed propeller for a cargo ship*. Naval Ship Research and Development Center, 1973.
- [10] L.-Z. Wang, C.-Y. Guo, Y.-M. Su, and T.-C. Wu, “A numerical study on the correlation between the evolution of propeller trailing vortex wake and skew of propellers,” *International Journal of Naval Architecture and Ocean Engineering*, vol. 10, no. 2, pp. 212–224, 2018.
- [11] H. Ghasseni and P. Ghadimi, “Numerical analysis of the high skew propeller of an underwater vehicle,” *Journal of Marine Science and Application*, vol. 10, no. 3, p. 289–299, 2011.
- [12] Y. Young, “Time-dependent hydroelastic analysis of cavitating propulsors,” vol. 23, pp. 269–295, Feb. 2007.
- [13] A. N. Hayati, S. M. Hashemi, and M. Shams, “A study on the effect of the rake angle on the performance of marine propellers,” vol. 226, pp. 940–955, Sept. 2011.
- [14] S. Gaggero, J. Gonzalez-Adalid, and M. P. Sobrino, “Design and analysis of a new generation of clt propellers,” *Applied Ocean Research*, vol. 59, p. 424–450, 2016.
- [15] Kang, Kim, Kim, and Shin, “Study on propulsion performance by varying rake distribution at the propeller tip,” vol. 7, p. 386, oct 2019.
- [16] unknown, “Blade area ratio defined,” tech. rep., HydroComp Inc., 2007.
- [17] E.-J. Foeth and F. H. Lafeber, *Systematic propeller optimization using an unsteady Boundary- Element Method*. 2013.
- [18] J. B. D. Rijpkema, B. Starke, “Numerical simulation of propeller-hull interaction and determination of the effective wake field using a hybrid rans-bem approach,” in *Third international symposium on Marine Propulsors*, SMP, (Launceston, Australia), 2013.
- [19] *Various types of cavitation*. Jan 2015.
- [20] A. S. E. v. W. J. Bosschers, G. Vaz, “Computational analysis of propeller sheet cavitation and propeller-ship interaction,” in *RINA Conference ”Marine CFD2008”*, RINA CFD, (Southampton, UK), MARIN, March 2008.
- [21] J. B. M. Abdel-Maksoud, K. Hellwig, “Numerical and experimental investigation of the hub vortex flow of a marine propeller,” in *25th Symposium on Naval Hydrodynamics*, (St. John’s, Canada), Duisburg-Essen University, August 2004.
- [22] C. Ma, H.-p. Cai, Z.-f. Qian, and K. Chen, “The design of propeller and propeller boss cap fins (pbcf) by an integrative method,” *Journal of Hydrodynamics*, vol. 26, no. 4, p. 586–593, 2014.
- [23] J. Hu, W. Zhang, C. Wang, S. Sun, and C. Guo, “Impact of skew on propeller tip vortex cavitation,” *Ocean Engineering*, vol. 220, 2021.

-
- [24] A. Ebrahimi, A. Razaghian, A. Tootian, and M. Seif, “An experimental investigation of hydrodynamic performance, cavitation, and noise of a normal skew b-series marine propeller in the cavitation tunnel,” *Ocean Engineering*, vol. 238, p. 109739, Oct. 2021.
- [25] A. Šarc, T. Stepišnik-Perdih, M. Petkovšek, and M. Dular, “The issue of cavitation number value in studies of water treatment by hydrodynamic cavitation,” *Ultrasonics Sonochemistry*, vol. 34, pp. 51–59, Jan. 2017.
- [26] H. Ghassemi, M. G. Saryazdi, and M. Ghassabzadeh, “Influence of the skew angle on the hydroelastic behaviour of a composite marine propeller,” *Proceedings of the Institution of Mechanical Engineers, Part M: Journal of Engineering for the Maritime Environment*, vol. 226, no. 4, p. 346–359, 2012.
- [27] R. Vijayanandh, K. Venkatesan, M. Senthil Kumar, G. Raj Kumar, P. Jagadeeshwaran, and R. Raj Kumar, “Comparative fatigue life estimations of marine propeller by using fsi,” *Journal of Physics: Conference Series*, vol. 1473, no. 1, p. 012018, 2020.
- [28] L. C. Burrill, *Underwater Propeller Vibration Tests*. North east coast institute of engineers and shipbuilders, 1949.
- [29] E. Loukogeorgaki, C. Michailides, and D. C. Angelides, “Dry” and “wet” mode superposition approaches for the hydroelastic analysis of floating structures. 2014.
- [30] J. Li, Y. Qu, and H. Hua, “Hydroelastic analysis of underwater rotating elastic marine propellers by using a coupled BEM-FEM algorithm,” *Ocean Engineering*, vol. 146, pp. 178–191, Dec. 2017.
- [31] H. Lin and J. Tsai, “Analysis of underwater free vibrations of a composite propeller blade,” vol. 27, pp. 447–458, Jan. 2008.
- [32] C.-C. Lin, Y.-J. Lee, and C.-S. Hung, “Optimization and experiment of composite marine propellers,” *Composite Structures*, vol. 89, no. 2, p. 206–215, 2009.
- [33] P. T. Maung, B. G. Prusty, A. W. Phillips, and N. A. St John, “Curved fibre path optimisation for improved shape adaptive composite propeller blade design,” *Composite Structures*, vol. 255, p. 112961, 2021.
- [34] J. P. Blasques, C. Berggreen, and P. Andersen, “Hydro-elastic analysis and optimization of a composite marine propeller,” *Marine Structures*, vol. 23, no. 1, p. 22–38, 2010.
- [35] P. J. Maljaars, *Hydro-Elastic Analysis of Flexible Marine Propellers*. PhD thesis, 2018.
- [36] L. Morino, L.-T. Chen, and E. Suci, “Steady and oscillatory subsonic and supersonic aerodynamics around complex figurations,” *AIAA Journal*, vol. 13, no. 3, 1975.
- [37] G. Vaz, *Modelling of sheet cavitation on hydrofoils and marine propellers using boundary element methods*. PhD thesis, 2005.
- [38] “Recommended procedures resistance uncertainty analysis,” International towing tank conference, 2002.
- [39] K. van de Sanden, “Validation & Verification of Hydro-Elastic analyses for Marine Propellers,” Master’s thesis, Delft University of Technology, the Netherlands, 2020.
- [40] E. van Wijngaarden, *ComProppApp User’s Guide*. MARIN, 1.0.3.6 beta ed., 8 2021.
- [41] SikaBlock, *SikaBlock M980 Werkzeugplatte - dimensionsstabil und hochabriebfest*, 2020.
- [42] J. Dang, H. van den Boom, and J. Ligtelijn, *The wageningen C- and D-Series Propeller*. 2020.
- [43] S. S. Rao and Y. F. Fah, *Mechanical vibrations; 5th ed. in SI units*. Singapore: Prentice Hall, 2011.
- [44] T. Koko, “ComPropApp Validation Support,” tech. rep., Lloyds’ Register Applied Technology Group, 05 2021.
- [45] G.-J. Zondervan, “Comprop 2 flexible propeller measurements,” Tech. Rep. Report No. 31188-1-PaS, MARIN, August.
- [46] SikaBlock, *SikaBlock M700 Temporary Product Data Sheet*, 2020.
- [47] M. M. Dr. Kochetov, “Fourier transform via fft matlab function,” 2008.
- [48] “Extracting damping ratio from dynamic data and numerical solutions,” *ntrs.nasa.gov*, Sep 2016.
- [49] N. M. Nouri and S. Mohammadi, “Numerical investigation of the effects of camber ratio on the hydrodynamic performance of a marine propeller,” *Ocean Engineering*, vol. 148, pp. 632–636, Jan. 2018.
- [50] “Electric aircraft propeller design.”